UNIVERSITY OF SOUTHAMPTON

THE SOURCES OF VARIABILITY IN THE STATISTICAL ENERGY ANALYSIS OF TWO RECTANGULAR PLATES

by

Woo Sun Park

Institute of Sound and Vibration Research
Faculty of Engineering and Applied Science

Thesis submitted for the degree of
Doctor of Philosophy

January 2003

UNIVERSITY OF SOUTHAMPTON

ABSTRACT

FACULTY OF ENGINEERING AND APPLIED SCIENCE

INSTITUTE OF SOUND AND VIBRATION RESEARCH

Doctor of Philosophy

THE SOURCES OF VARIABILITY IN THE STATISTICAL ENERGY ANALYSIS OF TWO RECTANGULAR PLATES

by Woo Sun Park

Statistical Energy Analysis (SEA) is widely used for the high frequency analysis of vibro-acoustics problems whereas conventional deterministic methods, *e.g.* Finite Element Method and Boundary Element Method, are applied to lower frequency problems. Between low and high frequencies, however, there exists a mid frequency range where neither deterministic methods nor SEA can be used reliably. In this frequency range, the wavelengths are short so that deterministic methods require excessive computation, while the SEA predictions are unreliable due to large uncertainty in the results.

With in SEA, the Coupling Loss Factor (CLF) is a statistical quantity defined in terms of the average behaviour of an ensemble of similar systems. The 'effective' CLF for a given realisation differs from the ensemble average. Significant fluctuations with frequency are observed in the low frequency region. Accordingly, the CLF is the main parameter expected to determine the confidence intervals in the SEA prediction.

In this research, the sources of variability in SEA coupling are systematically investigated and appropriate parameters are established to determine the variability of the effective CLF in the mid to high frequency range. Finally the effect of the variability in the CLF on the resulting response is investigated and the confidence intervals of the SEA predictions are discussed.

A system consisting of two rectangular plates is considered and the exact dynamic response of the system is investigated by using the dynamic stiffness method (DSM). The effective CLF for a particular realisation of the system is evaluated by a ‘numerical experiment’ using the SEA power balance equations and compared with the CLFs obtained from various methods.

The influence of the modal behaviour of the source or the receiver subsystem or both on the energy transmission between the two subsystems is investigated by considering various analytical models, which include an infinite source plate coupled to a finite receiver plate or *vice versa*. For these models, the transmission efficiency or the effective CLF are evaluated using the wave approach and/or the DSM.

The variability of the effective CLF is investigated by a series of systematic parameter variations in the DSM model. An empirical model is derived for the confidence interval of the effective CLF, in terms of the modal overlap factor and the number of modes in a frequency band. The model for the variability of the CLF has then been validated using an experimental study. The reliability and accuracy of this empirical model is discussed in comparison with previously published models. The sensitivity of the resulting SEA prediction due to the variation of the CLF is subsequently investigated by Monte Carlo simulation.

Table of Contents

APPENDICES

Acknowledgements

I would like to acknowledge my sincere gratitude to my supervisors, Dr. David. J. Thompson and Dr. Neil. S. Ferguson for their academic guidance and continuous encouragement. Their enthusiasm and patience made the successful completion of this project possible.

For their valuable advice and useful comments, I wish to express thanks to Dr. Brian R. Mace and Professor Michael J. Brennan. Acknowledgement is also given to my external examiner Professor Barry M. Gibbs of the University of Liverpool who gives me essential discussions in the thesis review.

Many thanks are extended to all ISVR staff and colleagues including Professor Frank J. Fahy and Dr. Nick Lalor as well as Dr. W. Variyart, Mr. A. Thite and Dr. Y.S. Lee for assisting me in the experimental work.

In particular, I gratefully acknowledge the financial support by Daewoo Motor Company and British Chevening Scholarships funded by the Foreign and Commonwealth Office.

I would like to share my pleasure with all members of the Korean Society of Southampton University and their families who have given me their interest and advice.

Finally, I would like to thank my parents, mother-in-law and all families for their sincere concern. I am greatly indebted to my wife Eui-Sook and two lovely daughters Soojin and Eyunjin for their self-sacrifice, patience and continuous encouragement during my PhD study.

List of Symbols

a_n	Fourier coefficient of $\cos(n\pi y/b)$
b	Width of rectangular plate
b_n	Fourier coefficient of $\sin(n\pi y/b)$
c_b	Phase velocity of bending wave
c_g	Group velocity
c_L	Longitudinal wavespeed
d	Bolt spacing
e_j	Theoretically expected number in the interval if the distributions are normal
f	Frequency ($=\omega/2\pi$)
f_c	One-third octave centre frequency
$f_{\text{cut-on}}$	Cut-on frequency
f_l	Lower frequency of band
f_n	Natural frequency
f_u	Upper frequency of band
$f(y)$	Forcing function
h	Thickness of plate
j	Complex operator $\left(=\sqrt{-1}\right)$
k	Wavenumber
k_n	Trace wavenumber ($=n\pi/b$)
k_{nr}	Four complex roots of free flexural vibration of plate
k_f, k_L, k_T	Flexural, longitudinal and transverse wavenumbers for plate
m_i	Total mass of subsystem i
n	Fourier component; Number of samples
$n(\omega)$	Modal density
p	Distributed force
p_j	Probability in the interval
r	Reflection efficiency
s	sin θ; Standard deviation of energy ratio
t	Time

u	Translational displacements in x direction
v	Translational displacements in y direction; Velocity amplitude at the excitation point
w	Translational displacements in z direction
x, y, z	Global Cartesian coordinates
x_j	Interval of sample
A_{in}	Complex amplitude of propagating incident wave
A_r	Complex amplitude of propagating reflected wave
A_{nr}	Constants of integration; Complex amplitude of nearfield wave
A_{nt}	Complex amplitude of non-propagating nearfield wave
A_t	Complex amplitude of propagating transmitted wave
B	$E/2(1+\mu)$
B_i, C_i	Constants
C_{nr}	Constants of integration
D	Flexural rigidity $(=Eh^3/12(1-\mu^2))$
E	Young's modulus; Energy
E_{kin}	Kinetic energy
E_{strain}	Strain energy
$\overline{E}$	Time averaged energy
F	Applied force
F_0, F_n	Amplitude of force
G	Shear modulus
K	Number of intervals
L	Length of plate
M	Modal overlap factor $(=\eta\omega n(\omega))$
M_{comb}	'Combined' modal overlap factor $(=2M_1M_2/(M_1+M_2))$
M_n	Amplitude of bending moment
N	Longitudinal force; Number of modes in a frequency band; Number of samples; Number of bolts
N_{comb}	'Combined' number of modes $(=2N_1N_2/(N_1+N_2))$
N_n	Amplitude of longitudinal force
P_{diss}	Dissipated power

P_{in}	Input power
P_{inc}	Incident power
P_{12}	Transmitted power from subsystem 1 to subsystem 2
R_{ij}	Transmission loss
S_i	Area of plate of plate i
S_n	Amplitude of vertical shear force
T	Transverse force
T_n	Amplitude of transverse force
U_n, V_n, W_n	Amplitude of longitudinal, transverse and vertical displacement
Y	Input mobility; Point mobility
$\hat{Y}$	Peak mobility
$\breve{Y}$	Minimum value for mobility
Y_∞	Point mobility for infinite system
Z	Input impedance

$\mathbf{b}$	Constant vector
$\mathbf{p}_{1n}$, $\mathbf{p}_{2n}$, $\mathbf{r}_{1n}$, $\mathbf{r}_{2n}$	Matrix for plate used in dynamic stiffness matrix
$\mathbf{u}_{nf}$, $\mathbf{u}_p$	Displacement vector

$\mathbf{A}_n$	Constant vector of integration for flexural vibrations
$\mathbf{C}_n$	Constant vector of integration for in-plane vibrations
$\mathbf{F}$, $\mathbf{F}_n$, $\mathbf{F}_{nf}$, $\mathbf{F}_{ni}$, $\mathbf{F}_p$	Force vector
$\mathbf{H}$	Diagonal scaling matrix
$\mathbf{K}$	Dynamic stiffness matrix
$\mathbf{K}_n$, $\mathbf{K}_p$	Dynamic stiffness matrix of plate
$\mathbf{K}_{nf}$	Dynamic stiffness matrix for flexural motion of plate
$\mathbf{K}_{ni}$	Dynamic stiffness matrix for in-plane motion of plate
$\mathbf{K}_r$	Reduced dynamic stiffness matrix of plate
$\mathbf{T}_{tot}$	Global dynamic stiffness matrix

β	$2/\pi M$
χ	$\sqrt{h_1/h_2}$
γ	$(1+\mu)/(1-\mu)$; Coupling parameter

γ_1	Skewness
γ_2	Kurtosis
δ	Dirac delta function; Coupling parameter
ε	Strain
η	Hysteretic damping constant, Damping Loss Factor (DLF)
η_{ij}	Coupling Loss Factor (CLF)
$\eta_{ij,\,ens}$	Ensemble average Coupling Loss Factor
$\eta_{ij\infty}$	Coupling Loss Factor based on two semi-infinite structures
$\hat{\eta}_{ij}$	'Effective' Coupling Loss Factor
λ_b	Flexural wavelength
λ_{nr}	Four roots of free in-plane vibration of plate
μ	Poisson's ratio; Mean value
μ_i	Reflectance
θ	Angle of incidence
ϕ	Rotational displacement in y direction
ϕ_n	Amplitude of rotational displacement
ρ	Material density; Correlation coefficient
σ	Stress; Standard deviation of CLF
ψ	$(h_1/h_2)^2$
ψ_i	Mode shape of subsystem i
τ, τ_{ij}	Transmission efficiency
$\tau_{ij,\,d}$	Diffuse field transmission efficiency
ω	Circular frequency
ω_i	Resonance frequency
$<\overline{v^2}>$	Temporally and spatially averaged mean square velocity
$<\eta_{ij}>$	Frequency averaged Coupling Loss Factor
Δ	Average modal spacing (Hz)
Φ	Values of distribution function

CHAPTER 1

INTRODUCTION

1.1 General introduction

Noise and vibration present major challenges that must be overcome in order to promote the welfare of human beings in most industries, such as transportation, construction and home appliances. As modern science and technology are developing, mechanisms are getting more and more complex and manufacturers are endeavouring to meet customers' various demands. Recent trends in the automotive industry, for example, are towards making vehicles more comfortable and also lighter, due to environmental and economic considerations. By minimising the weight of a car, the fuel economy can be improved and the production cost can be reduced. Simultaneously, a good design should produce a quiet and comfortable environment as well as satisfying the various performance requirements. Unfortunately, these two objectives, economy and low noise and vibration, are often conflicting.

Reducing the noise and vibration levels on existing designs is often very difficult, if not impossible, and will often involve high expenditure and an increase in weight. It is therefore necessary, during the design process, to be able to predict the dynamic response of a structure due to several broadband sources of noise and vibration so that potential problems, such as excessive vibration levels, resonances, failure due to acoustic and dynamic fatigue and noise, can be avoided.

There are a number of methods available for determining the dynamic response of structures. These range from analytical and numerical methods to experimental methods. Different methods are more suited to the low frequency or the high frequency region. The characteristic of the dynamic response depends upon the frequency of the excitation which can be categorized generally as (i) low frequency, (ii) mid frequency and (iii) high frequency. The actual frequency range associated with each of these categories is dependent on the structure itself.

At low frequencies the dynamic behaviour of the structure is mainly dominated by its lower order modes of vibration. The resonance frequencies and mode shapes of these low order modes are generally less sensitive to small changes in the geometric and physical properties than those of higher order modes.

For a specific set for values of the structural properties, the Finite Element Method (FEM) and Boundary Element Method (BEM) can give a deterministic solution in this frequency range. The former is specifically applicable to both structural and acoustical analyses whist the latter is primarily used for acoustic analysis. These are very useful methods to predict the dynamic response of the structure if a real structure is not available, especially in the early design stage. These methods have been applied, for example, to the prediction of the low frequency booming noise (below 200Hz) of a passenger car through coupled structure-fluid analysis of the vehicle structure and compartment cavity [1-3].

In addition, the experimental modal analysis technique is usually used at low frequencies to investigate the dynamic characteristics of existing structures, *e.g.* natural frequency, damping and mode shape, and to validate or update a numerical model.

At high frequencies the higher modes of vibration of the structure are excited and the characteristic wavelength of the structural deformation is much smaller than the overall dimensions of the structure. Under the assumption of a constant loss factor, for example, the vibrational modes of the structure have a wider bandwidth as frequency increases. Consequently the resonant peaks overlap each other and the resulting dynamic response is much smoother than that at low frequencies. The dynamic response at any frequency is no longer dominated by a single mode. Using conventional methods, *e.g.* FEM and BEM, large computational effort may be required to obtain good accuracy. Moreover, there are difficulties in using such a model to represent real structures, because the results are sensitive to small changes in parameters. The model represents merely one member of an ensemble and the results are valid for that model only. These methods are inefficient at high frequencies due to the excessive number of degrees of freedom of the model. They are also unreliable due to statistical uncertainties in structural properties or in defining boundary conditions at the coupling between different parts of the structure. Thus simple methods giving qualitative characteristics are required.

Such an alternative approach is to use Statistical Energy Analysis (SEA) (or the Power Flow method) which has been developed over the past 40 years. SEA is based on simple power balance equations for the system. Using SEA it is possible to predict the spatially and frequency-averaged energy or power of the system. Since the SEA equations are relatively simple and energy and power outputs can provide great insight to the dynamic system, SEA can provide useful guidance for noise and vibration control at high frequencies. Currently SEA is widely used for the high frequency analysis of vibro-acoustics problems where FEM and BEM cannot be applied, *e.g.* ships [4], building acoustics [5] and automotive vehicles [6, 7]. Analytical SEA has been applied to the prediction of structure-borne sound transmission in large welded ship structures [4] and for vibration transmission in a small passenger car [6].

Between low and high frequencies, however, there exists a mid frequency range where neither deterministic methods, *e.g.* FEM and BEM, nor SEA can be used reliably. In this frequency range, short wavelength vibration occurs so that deterministic methods require excessive computation, while the SEA predictions are unreliable due to large uncertainty in the results.

During last two decades, other energy-based methods have been developed to overcome some of the difficulties and limitations of the SEA method in the mid and high frequency regions. These include Energy Flow Analysis (EFA) [8-13], Power Flow Finite Element Analysis (PFFEA) [14] or Energy Finite Element Analysis (EFEA) [15] and a hybrid Finite Element Analysis (FEA) method [16, 17]. However, these methods are not yet widely used for practical applications because the exact energy equations for real structures are quite complex.

More recently Wave Intensity Analysis (WIA) [18, 19], Advanced SEA (ASEA) [20] and Statistical Modal Energy Distribution Analysis (SMEDA) [21, 22] have been developed to overcome some of the drawbacks of SEA. Other theoretical and experimental techniques and applications have been introduced [23, 24] and more recent research and applications of SEA have been reported by the SEANET thematic network [25, 26]. These developments will be discussed further in Section 1.2.2.

One method that can be used to predict the dynamic response of a particular structure irrespective of frequency is the so-called ‘Dynamic Stiffness Method’ (DSM) [27-30]. It can be used for high frequency analysis, to which the conventional FEM cannot be applied, as well as low frequency analysis. However, this method also has some limitations on the geometry and boundary conditions of the structure.

Since each method has its specific advantages, disadvantages and limitations, an appropriate analysis technique should be chosen for the frequency range to be considered. An ESDU report [31] provides a good set of guidelines on how to choose an appropriate method for prediction of the dynamic response of a structure subjected to particular kinds of excitation. Some methods for the mid to high frequency analysis are discussed in more detail in the following section which includes a description of the assumptions, developments and limitations.

The motivation of this project is to assist in providing a particular methodology to predict the interior noise and vibration of a passenger car in the mid to high frequency range where conventional FEM and BEM cannot be applied. Although they are widely used in the automotive industry, these methods have especially been applied to the prediction of low frequency noise and vibration problems. In practice, they are not applicable to high frequency where the wavelengths are short. Instead SEA is increasingly used for the high frequency analysis of cars. A number of commercial computer programmes, *e.g.* AutoSEA (www.vasci.com), SEAM (www.seam.com), SEADS (www.lms.be), have been developed for the SEA application and are widely used in the industry. There are, however, many uncertainties and potential errors in the low to mid frequency range that unwary users have to contemplate. The objective of this project is therefore to quantify these uncertainties in particular cases and to develop a model that can be used to estimate confidence intervals for SEA predictions.

1.2 Literature review on mid to high frequency analysis techniques

1.2.1 Statistical Energy Analysis

SEA was initiated in the early 1960s for predicting the high frequency response of aerospace vehicles. Lyon and Maidanik [32] published the earliest paper in this field on power flow between linearly coupled oscillators. The basic theory of SEA and procedures for engineering applications are presented in the textbook by Lyon and DeJong [33].

Before discussing further references, some description of SEA terminology is useful. 'Statistical' in SEA denotes that a system to be analysed is assumed to be drawn from a population of an ensemble[*1] of similar systems distributed randomly. 'Energy' refers to the quantity that is used to describe the dynamic response of the system. The energy of the system can be transformed into other physical quantities, *e.g.* displacement, pressure, etc. 'Analysis' accentuates that SEA is a framework rather than a rigidly-defined method.

The SEA procedure is performed by three steps [33]; (i) define the system model, (ii) evaluate the model parameters and (iii) evaluate the response variables. The system model contains a group of subsystems[*2]. Subsystems are coupled by physical connections between the components. The SEA solution consists of a single value of the average energy for each subsystem and each frequency band, because lumped parameters are used to represent a continuous system. The parameters needed for each subsystem are the modal density or the number of modes in a frequency band, the damping loss factor (DLF), and the input power. The modal overlap factor is also an important parameter. This is a measure of the degree to which resonant behaviour dominates the response. It can be obtained from the modal density and the DLF. The coupling between connected subsystems is specified by the coupling loss factor (CLF), which relates the power flow between connected subsystems to the stored energy in the transmitting subsystem. A general introduction to SEA is given in numerous references [33-39] which include discussion on the background theories, assumptions and applications of SEA.

[*1] an 'ensemble' is defined as a collection of notionally similar structures or systems, the properties of which have a certain probability distribution; *e.g.* the dynamic properties of cars produced in the same production line are not same due to manufacturing tolerances and fabrication imperfections.

[*2] a 'subsystem' in SEA is different from an element in an FEM model which represents a small physical part of the system. A subsystem can be defined as a collection of similar modes within a physical component of the system; *e.g.* only the bending modes or only the in-plane modes in a plate. The physical size of the subsystems may be different for different mode (or wave) types; *e.g.* for in-plane modes several plates may be combined into a single subsystem.

Woodhouse [34] argued that SEA, as a statistical approach, can be identified with a thermal analogy; modal density corresponds to thermal capacity of the element, damping of the vibration modes corresponds to radiative loss and a measure of the strength of the mechanical coupling of the subsystems corresponds to conductivity or loss by coupling. It was demonstrated [34] that three assumptions are made in standard SEA modelling; (i) the rate of energy dissipation by a subsystem is proportional to the energy of that subsystem, (ii) the rate of power flow from one subsystem to another is proportional to the difference in their average modal energies and (iii) the driving forces on the different subsystems are statistically independent so that one can add the energy responses of a given subsystem produced by these different driving forces to obtain the total mean modal energy of that subsystem.

Burroughs *et al.* [35] reviewed the basic principles behind SEA and the development of SEA, presented examples of the application of SEA and discussed input parameters. It was summarised that in order to obtain accurate predictions using SEA the models must (i) be capable of predicting the input power, (ii) represent all important mode types which occur within the subsystems in the frequency range of interest, (iii) have valid CLFs for all mode types which interact at junctions of subsystems and (iv) provide the output energies or derived vibration levels for those modes of interest.

Fahy [36] gave a brief account of the origins, rationale, principles and some applications of SEA and presented a brief survey of recent research objectives. In another paper [37], he reviewed the origins of SEA and limitations of deterministic methods and accounted for the validity of the use of probabilistic energetic models for high frequency vibration prediction. He also discussed the general advantages and weaknesses of SEA, investigated the current state of development of SEA and pointed out areas for future research.

A more general introduction covering the basic concepts and the application of SEA, rather than a specific discussion of its theoretical background, was provided by ESDU [38]. A guide for potential SEA users has been produced by SEANET [40].

1.2.1.1 Assumptions in SEA

According to references [33, 35, 38], the underlying assumptions to be considered in the development of SEA models are usually outlined as follows.

- The subsystems are weakly coupled. The modal energy of the source subsystem is therefore significantly greater than that of any other subsystem[*].
- Each mode of a given subsystem within a particular frequency band contributes equally to the energy of the subsystem, *i.e.* equipartition of vibrational energy between the modes of a subsystem.
- For a particular frequency band each subsystem generally contains a minimum number of modes between three and seven.
- The DLF is equal for each mode within a subsystem and frequency band. This assumption is not necessary but it simplifies the formalism and tends to be nearly true for reasonably complex subsystems.
- The input forces are independent of frequency within a frequency band, *i.e.* broadband excitation.
- Energy is not generated or dissipated in the couplings between subsystems, *i.e.* conservative coupling.
- The coupling power is proportional to the difference in average modal energy.

The first three assumptions were presented in terms of a modal approach. These are equivalent to the following descriptions in terms of a wave approach. These two approaches describing the structural motion are equivalent to each other, which is referred to as 'wave-mode duality'.

- The transmission efficiency is small at the boundary between subsystems or the damping is sufficiently high so that most of energy input is dissipated within the source subsystem.
- The wavefield in a subsystem is diffuse so that waves propagate equally in all directions.
- The structural and acoustic wavelengths are significantly less than the dimensions of the subsystem.

---

[*] Although stated in [33, 35, 38] as a usual condition, this is not a necessary condition for the application of SEA [41].

1.2.1.2 Advantages and disadvantages of SEA

Some advantages and disadvantages of SEA, that have been found by the previous investigators [31, 33, 42], are summarised as follows.

The advantages of SEA:

- It can allow a response prediction to be made at high frequencies for which FEM and BEM, etc., cannot be used.
- Complex systems are represented in terms of a small number of gross parameters. This allows estimates to be made at an early stage of the design.
- The method involves relatively few degrees of freedom in the model compared with deterministic models so it is possible to perform parameter studies with little computational effort.
- The resulting expressions for stored energy are explicit and easily interpreted in physical terms.

The disadvantages of SEA:

- The accuracy of the predicted result for the average energy is not guaranteed. Also there can be considerable scatter around the average value in both a frequency and an ensemble sense.
- It is not possible to predict the degree to which variations in physical features are likely to cause the behaviour of individual physical systems to deviate significantly from that of the idealized model.
- It does not account for the variation in the energy density within subsystems.
- SEA is not capable of modelling local behaviour.
- The difficult part of an SEA procedure lies in the specification of the CLF that determines how much energy is transmitted from one subsystem to another.

1.2.1.3 Uncertainties in SEA predictions

Since statistical approaches give statistical answers, they are always subject to some uncertainty. The degree of uncertainty in the SEA prediction will depend on many parameters such as the geometry and material properties, the fabrication tolerances, the number of modes of the subsystem, the DLF and CLF, and the modal densities. As discussed by Fahy [37] there is no generally applicable procedure for making estimates of confidence intervals in the SEA prediction. Many uncertainties and potential errors in using SEA have been reviewed previously [33, 41-47].

A useful discussion on the uncertainty of SEA predictions is given by Lyon and DeJong [33]. They developed estimates of variance in the mean square response and presented methods for calculating the variance and confidence levels of the response variables. As an example, a modal analysis for a beam-plate system was used to calculate variance and confidence intervals. The variations due to the input power, the calculated energy distribution in the SEA model and the modal response in each subsystem were presented and these factors were assumed statistically independent. However, these results are rather delicate to apply to a complex system because they contain a certain amount of speculation and implicitness.

The uncertainty of the predictions due to subsystem geometry was studied by Fahy and Mohammed [42, 43]. They presented the results of an attempt to evaluate the effects of random geometric perturbation for coupled beams and plates. The results showed that the modal overlap factors of the uncoupled subsystems and the number of coupled modes of the total system are the two main parameters which control the variability of power flow and the associated CLF.

The potential errors in the SEA prediction at low frequencies were also investigated by Craik *et al.* [44]. It was shown that the vibration level difference between two coupled building structures, such as walls and floor, fluctuates considerably since building structures have few modes at low frequencies. They observed that the fluctuations in the point mobility of the receiving subsystem, relative to that for an infinite structure, are reflected in fluctuations in the CLF. Upper and lower bounds for the CLF were derived in terms of maxima and minima of the point mobility. They also asserted that for the power flow between plates the confidence interval is affected only by the properties of the receiving subsystem. The confidence limits for SEA predictions derived by Lyon [33] were shown to overestimate the actual error considerably, at least for building structures.

Mace investigated the ensemble average power flow and the statistics of the power flows between two continuous one-dimensional subsystems [45, 46], the power flow between two coupled beams [47], and the SEA of two continuous one-dimensional subsystems [41] by using a wave approach. Uncertainties due to the subsystems, the coupling, and the excitations, were considered by assuming that these parameters are drawn from ensembles. The properties of the ensemble were specified by a joint probability density function which defines the probability of occurrence of a combination of parameters. The ensemble power flow statistics were discussed in a number of cases and applications [45-47]. The variation of the ensemble mean, maximum and minimum power flows, normalized by unit incident power, was investigated at various coupling strengths. It was shown that in the general case the ensemble mean power flow may be less than or greater than that expected from a normal SEA approach, due to the strength of coupling. These results were extended to the SEA of two continuous one-dimensional subsystems in reference [41]. The strength of coupling and the features of the ensemble average coupling power and the ensemble average CLF were investigated.

1.2.1.4 Coupling Loss Factor (CLF)

The use of SEA to predict the response of vibro-acoustic systems relies on good estimates of the DLFs of subsystems and the CLFs between them. Damping is usually estimated from measurement data. The CLFs are normally the main parameters that are difficult to evaluate either experimentally or numerically.

There are many methods, numerical, analytical or experimental, to evaluate the CLF. Conventionally, the CLF between two structures, such as two plates, is obtained by analysing the wave transmission between semi-infinite structures [33, 48, 49] or by a modal approach [33]. For two infinite subsystems coupled along a line or at a surface, the wave transmission efficiency, τ, is defined as the ratio of the transmitted power to the incident power. By integrating over all possible angles of incidence, the diffuse incidence transmission efficiency can be determined. The CLF estimates determined from these transmission efficiencies, for infinite subsystems, are taken as representative of ensemble averages of finite subsystems.

An ensemble average CLF for two edge-coupled rectangular plates was investigated using a wave approach by Wester and Mace [50]. This ensemble average CLF, which is exact for all strengths of coupling, was compared with the traditional estimate of CLF from semi-infinite plates. It was shown that the ensemble average CLF and the semi-infinite results are identical if the plates are weakly coupled whilst the former is generally very much less than the latter if the coupling is strong. This is quantified by Wester and Mace using a parameter referred to as the reflectance which describes the attenuation of waves within a subsystem.

FEM has also been used to study the CLF or 'effective' CLF for specific finite systems at low modal overlap by several authors [51-53]. The term 'effective' CLF is used in this thesis when a deterministic approach is used and to distinguish it from the ensemble CLF used in SEA. Thus the effective CLF refers to a single member of the ensemble.

Simmons [51] presented the numerical calculation of the spatially averaged vibrational energies of plates forming L and H shaped structures at discrete frequencies between 10 and 2000 Hz. The energy ratio between two plates was obtained from an FEM model and was compared with experimental results. It was suggested that the CLF can be calculated from the FEM results using the energy ratio between two plates and an estimate of the ratio of their modal densities. However, it was concluded that an ensemble average estimate of the CLF with respect to the different boundary conditions was not satisfactory and required further study.

Steel and Craik [52] investigated the vibration transmission between walls in a building by using FEM. The effective CLF was obtained from the energy ratio of two walls, averaged over 20 excitation points. The effective CLF was compared with the CLF obtained from semi-infinite plates and with the effective CLF predicted using an empirical relationship. At low frequencies the results from the FE model showed large fluctuations compared with the other estimates.

Similarly Fredo [53] applied FEM to the evaluation of the effective CLF, which he referred to as the Energy Flow Coefficient (EFC), between two rectangular plates coupled in an L shape. The effective CLF was influenced by the subsystems' shapes and boundary conditions. 'Rain-on-the-roof' excitation was approximated in the finite element model by uncorrelated forces acting at every node in the respective subsystems.

Using FEM to calculate the CLF is time consuming and Maxit and Guyader [54] developed a new approach, which allows a rapid CLF calculation without solving the equations of motion. A general expression for the CLF was derived using the basic SEA power flow and generalizing a dual modal formulation suggested by Karnopp [55]. The dual modal formulation is a similar approach to that used to study the coupling between structures and acoustic cavities. The structure is subdivided into an uncoupled-blocked subsystem of displacement field and an uncoupled-free subsystem of stress field. The eigenvalue problems for the two independent fields are solved by using the equations of motion, constitutive law and boundary conditions. The CLF is obtained from the FEM results for each uncoupled subsystem, *i.e.* the natural frequencies, the generalized mass and the mode shapes. In a companion paper [56], this approach was applied to estimate the CLF for two numerical examples of coupled beams and coupled plates. The CLF results for two beams showed a good agreement with other FEM results and some differences less than 5 dB were identified for an extreme case with two identical beams. The CLF estimates were investigated for two coupled plates in an L shape where the thinner plate was regarded as the uncoupled-blocked subsystem and the thicker plate as the uncoupled-free subsystem. The results for two coupled plates of different dimensions also showed a good agreement with other results. However it was stated that this approach could not be used for two plates of the same thickness; the method proposed by Wester and Mace [50] is therefore more appropriate.

The above method [54] can reduce the computing time required to obtain the CLF. Although the approach could be used to consider the uncertainty in the coupling by using an ensemble average of the coupling factors, it is subject to the common limitation of FEM. FEM is amenable to model any arbitrary geometry and boundary conditions but the CLF results evaluated strictly apply only to the single case considered unless an ensemble average estimate is considered. In these studies, although differences between the effective CLF and the ensemble average are observed, these have not been quantified consistently.

For the experimental evaluation of the CLF, Bies and Hamid [57] considered the vibrational energy distribution between two coupled plates. Inversion of the power balance equations was used to determine the DLF of each plate and the CLFs *in situ*. The input power was measured sequentially at five randomly chosen points to ensure effective statistical independence of modes. The response of both plates was measured at ten points chosen at random and mean values obtained. This method, which is usually referred to as

Power Injection Method (PIM), is widely used in experimental SEA but a considerable amount of time is required to obtain the necessary measurements. Bharj *et al.* [7], in a recent paper, proposed a new method for calculating CLFs directly from vibration or sound pressure measurements. Although the CLF calculated from a single point measurement in each subsystem showed up to 10 dB difference with that based on an average of 10 points, the errors in the interior sound pressure level of an automotive cabin were less than 3 dB.

At low modal overlap, which usually corresponds to low frequency, the actual energy transfer between subsystems can differ considerably from that predicted using the CLF estimates determined from the power transmission efficiencies for semi-infinite structures. These fluctuations are in part due to the particular realisation of the subsystems within the notional ensemble. Underlying the fluctuations are the modal properties of the subsystems. Their damping also plays a role in determining the extent of the fluctuations.

Yap and Woodhouse [58] investigated the effects of damping on energy sharing in coupled structures. They used FEM and a matrix inversion approach [33] to investigate the CLFs. It was shown that damping is an important factor, affecting the statistical variations of the SEA parameters such as mean power flows, mean energies, CLFs, etc. In particular the values of the CLFs are strongly dependent on damping and the wave method tends to overestimate the CLFs, except when it is sufficiently high, as shown by Fahy and Mohammed [42] and Steel and Craik [52]. It was inferred by Yap and Woodhouse [58] that the SEA predictions of the CLFs for an ensemble of lightly damped systems will be subject to a high variance about the mean value at low modal overlap.

A useful estimate of the degree of variability of the CLF, in terms of upper and lower bounds for the CLF, is proposed by Craik *et al.* [44]. These were based on an empirical expression (that the fluctuations in the CLF are very similar to the fluctuations in the real part of the spatially averaged point mobility) and the bounds for the mobility given by Skudrzyk [59]. These upper and lower bounds will be discussed in more detail in Chapter 3.

1.2.2 Alternative methods including SEA variants

A number of approaches have been investigated to develop an alternative method or a combined method (normally referred to as a hybrid method) in order to overcome the limitations of the existing energy based methods in the mid and high frequency ranges.

1.2.2.1 Wave Intensity Analysis (WIA)

One alternative method to improve the applicability of SEA, which is referred to as Wave Intensity Analysis (WIA), has been developed by Langley [18]. This yields good estimates in situations where the SEA assumption that the vibrational wavefield is diffuse does not hold. The wave energies are expressed in the form of a Fourier series over angle of incidence. If each wave field is diffuse and a single Fourier component is used, the method reduces to the standard SEA formulation. In addition, this method considers the non-direct coupling terms, *i.e.* where two subsystems can be coupled even though they are not physically connected, by partitioning the energy expression. In reference [19] this method was applied to two example structures, a chain of fifteen plates and a flat row of six plates. By comparison with the exact results obtained using the DSM [28], the WIA approach showed a better estimate of the response than conventional SEA. The SEA predictions tended to underestimate the response and this was explained by the wave filtering effect at junctions [19]; waves that are nearly normal to the junctions tend to have a high transmission coefficient in comparison with other wave headings and thus the wavefield becomes less and less diffuse as the vibration travels down the structure. In both the WIA and SEA predictions in [19] the junction transmission coefficients calculated for semi-infinite plates by Langley and Heron [60] were adopted.

An attempt to improve the WIA prediction has been investigated by Nishino and Ohlrich [61]. The original WIA approach [19] was applied for simplified plate models of ship-type structures, which consist of stiffened plates and line junctions between plates. The results of WIA predictions showed good agreement with the exact results determined from the DSM in most frequency bands, especially in the high frequency range where the modal overlap factor exceeds a value of one. The standard SEA results, however, tended to overestimate the results. Moreover the WIA predictions were slightly larger than the DSM results at mid frequencies. A modified transmission coefficient was introduced in order to improve the WIA results in the low modal overlap region. The influence of the DLF and the reflection of waves for a finite receiving plate were considered using a DSM model of a semi-infinite source plate coupled to a finite receiver plate. For a model of two coupled rectangular plates, the modified transmission coefficient was incorporated in the WIA approach and, from the results of the energy ratio, it was observed that the predictions had been improved in the low modal overlap region, especially for a low value of damping.

1.2.2.2 Advanced Statistical Energy Analysis (ASEA)

In some SEA applications consisting of complex systems, the subsystems are indirectly coupled and the SEA predictions may exhibit errors if this is ignored. Heron [20] discussed this and referred to it as 'tunnelling'. A high-frequency theory to account for these effects, referred to as Advanced Statistical Energy Analysis (ASEA), was developed by Heron [20]. The new theory is based on the fundamental assumption that the total energy of an SEA subsystem can be separated into two parts, 'free energy' that is available for transport to other subsystems and 'fixed energy' that is not available for transport to other subsystems. The standard SEA power balance equations were extended to two matrix equations by including the above two energies. A procedure was demonstrated to calculate the elements of the matrices for a beam network and a plate network. The theory was interpreted as a series of mathematical models, the first model is identical to conventional SEA and subsequent higher order models converge to an exact result. The convergence of the higher order models was shown for an example model of an in-line rod assembly consisting of six rods.

1.2.2.3 Statistical Modal Energy Distribution Analysis (SMEDA)

The equipartition of modal energy is a key assumption of SEA. However, it is unrealistic in some cases, for example the assumption does not hold for low damping where SEA overestimates the power flow exchange. In order to overcome this assumption in SEA, Maxit and Guyader [21] investigated a modified SEA method, referred to as Statistical Modal Energy Distribution Analysis (SMEDA). This method was expressed by the classical power flow equations incorporating a less restrictive assumption in which the modal energy distribution of each subsystem is decomposed in terms of a set of shape factors. If the degree of freedom (d.o.f.) thus attributed to each subsystem mode is set to a single value, this reverts to the assumption of modal energy equipartition. A numerical study was performed for a system consisting of two beams coupled by a rotational spring [21]. Two different types of excitation, a 'rain-on-the-roof' excitation (which is necessary for classical SEA to respect the equipartition assumption) and a localised excitation, were investigated. The energy ratio predicted from SEA was overestimated for the lower value of the DLF, whilst that from SMEDA showed a good agreement with the exact result. In a companion paper [22], another numerical example was studied consisting of four coupled plates with the two end plates having high modal density and the two intermediate plates having low modal density. The results obtained from the SMEDA approach, for which the modal energy equipartition was not assumed, tended to coincide with exact results. In fact, this method can be used as an extension of SEA, as it is capable of being used for localised excitation and at low frequency as well as for low modal density.

1.2.2.4 Energy Flow Analysis (EFA) / Energy Finite Element Analysis (EFEA)

SEA does not account for the local behaviour within subsystems, which is one of its disadvantages. EFA, based on a wave approach, allows the spatial variation of the frequency-averaged energy density and energy flow to be predicted. Thus it may give improved predictions of the dynamic behaviour of a system in the high frequencies.

Wohlever and Bernhard [8] and Bouthier and Bernhard [9, 10] derived the governing equations for beams, membranes and plates by an energy balance, a damping model and a simplified energy transmission relationship. The energy balance equation was derived from continuum mechanics, the damping relationship from the loss factor model of energy dissipation and the energy transmission equation from energy density and intensity simplified by a smoothing operation. The energy transmission relationship, where the flux of energy is assumed to be proportional to the spatial derivative of the energy density, is analogous to the heat conduction equation in thermal problems. The application of EFA was presented for simple structures, *e.g.* rods and beams [8], membranes [9] and plates [10]. The broadband response was obtained using a plane wave model for a membrane [9] and the approximate energy distributions, although smoothed, compared well with the exact modal analysis results. For a plate [10], the governing equation for energy was derived using a plane wave approximation in the far field region only (neglecting the near-field region) and the predictions were performed for a distributed pressure excitation at a single frequency. The approach was applied to the EFA of beams and plates for discrete random excitations and random distributed loading by Han *et al.* [12, 13]. The EFA results were shown to be a good approximation of the exact solutions except near boundaries, because EFA does not consider the near-field wave.

Carcaterra and Sestieri [11] have also considered the 'thermal' energy flow approach to represent the possibility of modelling the spatial distribution of energy density at high frequencies. However, they assert that the thermal analogy is questionable for a general structure. They derived the exact power balance in a general elastic medium using Navier's equation and showed that the thermal analogy does not hold and the exact power balance equation differs from the expression considered in reference [8]. The energy density and power flow equations in beams and plates were determined and these equations did not represent any thermal behaviour.

A further investigation on the energy transmission in vibrating structures was presented by Carcaterra and Adamo in two companion papers [62, 63]. The constitutive relationships for the energy transmission in beams and plates were derived theoretically [62] and a particular non-dimensional parameter, 'the ratio of the characteristic finite size to the characteristic wavelength', was introduced to explain the energy transmission. Two types of wave energy, 'the coincident wave energy' (generated by waves proceeding in the same direction) and 'the incident wave energy' (produced by the intersection of travelling waves propagating along different directions), was used to indicate whether the mechanical energy transmission has a thermal form. The vibrational conductivity was found to be valid for one-dimensional systems (beams) but not for two-dimensional systems (plates). The experimental validation for a beam and a plate was performed using a scanning laser vibrometer and was presented in reference [63]. The experimental results showed that the energy behaviour of the beam and the plate are significantly different from each other. For the beam an error that is related to the power flow transmitted by the non-thermal component of the transmission potential, rapidly reached an asymptotic limit, whilst the error for the plate did not reach such a limit even when the non-dimensional parameter is considerably high.

A similar investigation into the 'vibrational conductivity approach', was performed by Langley [64] for two-dimensional structures such as plates, where the approach is more difficult to justify. The vibrational conductivity equation, which is a generalization of the SEA techniques, was derived. A further assumption that the intensity is the same at each wave heading was introduced and the boundary conditions are expressed by the CLF. A critical assessment was given of the underlying assumptions and it was pointed out that the usefulness of the vibrational conductivity equation is open to doubt. The results for a single plate and two coupled plates were presented to assess the performance of the method. The vibrational conductivity method yielded a good estimate of the averaged energy density of the plate, although for heavily damped, point loaded structures it overpredicted the energy density near the plate boundary. The energy ratios obtained from the vibrational conductivity method were compared with the previous WIA results [18] for two coupled plates. The vibrational conductivity approach produced identical results to SEA, whereas the WIA results, allowing for the wave directionality and junction filtering effects, gave results that were closer to the exact result. It was also noted that the scatter in the results over the different load positions was not predicted by the vibrational conductivity method as it effectively averages over the phase of the response, like most energy flow-based methods.

Since EFA can only be applied to simple structures, EFA itself is difficult to apply to a complex system. EFA can be implemented using a finite element (FE) model and the resulting EFEA allows high frequency predictions using FE models developed for low frequency structural predictions. As an example, Vlahopoulos and Zhao [15] investigated the application of EFEA to power transfer coefficients (reflection and transmission coefficients) for spot-welded joints. They discussed the mathematical formulation of the EFEA equations based on the EFA energy equations, the finite element formulation, and the derivation of the energy transferred and EFEA power transfer coefficients. The EFEA power transfer coefficients for three pairs of plates were predicted and compared with test results.

Although EFA and EFEA are alternative approaches to SEA, these methods are not yet widely used and implementation appears difficult.

1.2.2.5 Hybrid method

In the mid-frequency range, since EFEA or SEA cannot capture the resonance effects of a system, a hybrid FEA method was demonstrated by Zhao and Vlahopoulos [16] for three co-linear beams (long-short-long beams). They formulated three sets of equations: FEA model to consider energy information for a short member, a relationship between power input from short to long members and the corresponding energy density at the joint, and compatibility equations at the interfaces. The results obtained by this hybrid FEA method showed good agreement with analytical results and captured the energy and resonant effects of the short members as well as the overall response of the system. In addition, the hybrid FEA results showed a significant improvement compared with the EFEA results at high frequencies.

A hybrid method based on SEA, the theory of structural fuzzy [65] and the Belyaev smooth function, has been presented for the dynamic analysis of complex systems by Langley and Bremner [66]. They found it to yield good results for two coupled rods although the application to more complex systems is still required.

1.2.2.6 DSM and Spectral FEM

For certain continuous elements it is possible to derive the dynamic properties of a structural component exactly in the form of a dynamic stiffness matrix. The dynamic stiffness matrix is a function of frequency and contains not only stiffness information but also mass and damping information. The equations of motion, relating nodal displacements to the forces, can be solved to yield the dynamic response of the structure in any selected frequency range. For example, Langley [28-30] examined the free and forced vibration of a row of rectangular panels, the power flow in beams and frameworks and the vibration analysis of stiffened shell structures. The DSM can be viewed as providing an exact solution for the response of an idealised structure, whereas the main restriction for this method is that, for plate structures, each system must be simply supported on two parallel opposite edges. This restriction is necessary to be able to formulate the response of the plate analytically by separation of variables.

The Spectral FEM (SFEM) presented by Finnveden *et al.* [67-69] is a combination of the direct DSM and the FEM. The SFEM uses an exponential function as a basis function along the length of the structure as in the DSM, and the spectral elements of the cross-section are formulated and assembled as in the standard FEM. The spectral element size is limited by geometrical boundaries and the number of d.o.f. can be reduced while accuracy is increased. Thus the applicability of the DSM may be increased using the SFEM incorporated with the standard FEM. Another investigation for the SFEM was studied by Ahmida and Arruda [70]. They reviewed a Timoshenko beam spectral element and predicted the structural intensity in beams. The SFEM was shown to be a more suitable method than the FEM to model higher frequency propagation problems.

1.3 Aims and scope of thesis

Although there are many alternatives and variants, SEA remains the most commonly used method for high frequency analysis. SEA is based upon the power balance equation for a system which is made up of subsystems. Once the subsystems have been defined and the respective CLFs are correctly obtained, then SEA is very straightforward. Typically these subsystems are drawn from populations of similar members for which the ensemble average is predicted by the SEA model. Variations from the ensemble are expected for any particular realisation taken from the whole population. However SEA does not provide a standard means of estimating confidence intervals. Rather, an estimate is made of the mean value of the response.

It should be realised that the CLF is a statistical quantity and is defined in terms of the average behaviour of an ensemble of similar systems. The ‘actual’ CLF is defined in terms of an ensemble average and as such it is not uncertain once this ensemble of systems is defined. However the power balance equations also hold for individual realisations, in which case the CLFs are replaced by ‘effective’ CLFs (to distinguish them from the ensemble average CLFs). The effective CLF for a given realisation differs from the statistical average. Usually theoretical estimates of the CLF, based on the wave transmission between infinite subsystems, are used. The CLF obtained from the wave approach generally overestimates the actual value at low frequencies (low modal overlap) [42-44, 50, 58]. Significant fluctuations with frequency are also observed in this low frequency region. Accordingly, the CLF is the main parameter expected to determine the confidence intervals in the SEA prediction.

The main aims of the thesis are therefore

- To investigate systematically the sources of variability in the coupling between two subsystems.
- To establish appropriate parameters to determine the variability of the effective CLF.
- To investigate the effect of the variability in the effective CLF on the resulting response for two subsystems and to quantify the confidence intervals of the SEA predictions.

These are achieved by considering extensive parameter variations using a DSM model of two rectangular plates as an example, for which exact dynamic characteristics of the system can be investigated using the DSM.

The effects of varying damping, thicknesses and areas of two plates coupled in an L shape, as well as the effects of the type and position of the excitation, were considered by Boisson *et al.* [71]. However they did not evaluate the CLF but the energy ratio between the two plates. Their theoretical results, based on modal analysis, showed only the minima and maxima of the energy ratio as a quantitative description of the frequency dependence and compared these with experimental results. A number of other studies of a two plate system have previously been performed, although most of them have been limited to plates of the same thickness [42, 43, 53]. The present study considers a wide range of parameter variations including the ratio of the plate thicknesses.

The chapters of this thesis are arranged as follows.

Chapter 2 presents the equations of motion governing the flexural and in-plane vibrations for a plate, the theory of the DSM and the dynamic stiffness matrices for a uniform plate and two coupled plates. The dynamic response to a point force is obtained and calculation methods for the strain energy and power are described. Numerical simulations for a single plate and two coupled plates are performed and the analytical models are validated with particular emphasis on the power balance between the input power and the dissipated power. The analysis procedure is subsequently used in the parametric study to evaluate the SEA parameters in Chapters 5 and 6.

Chapter 3 introduces the power flow between two subsystems and the SEA framework. Various methods to evaluate the effective CLF, the ensemble average CLF and the CLF derived from semi-infinite plates, are discussed. Theoretical upper and lower bounds for the CLF from [44] are presented, which are compared in Chapter 5 with the variability of the effective CLF.

Chapter 4 deals with analytical models for the coupled behaviour of two plates. The various analytical models considered are: (i) two finite plates coupled along a line, (ii) two semi-infinite plates of finite width, (iii) an infinite source plate coupled to a finite receiver, and (iv) a finite source plate coupled to an infinite receiver. These models are considered in order to investigate the influence of the modal behaviour of the source or the receiver plate or both. For the first model the sensitivity is studied to the number and location of forcing points, when a rain-on-the-roof excitation is applied, and the effective CLFs obtained from a 'numerical experiment' are evaluated using different methods. The energy transmission between two subsystems and the effect of the modal characteristics are examined. For the other three analytical models, the transmission efficiency or the effective CLF is investigated using the wave approach and/or the DSM. The influence of the modal behaviour and the effect of the damping of the finite source or the finite receiver plate are discussed.

Chapter 5 presents an initial parametric study for the effective CLF obtained by varying the following parameters: the plate thickness ratio, the length ratio, the length-to-width ratio of the two plates and the DLFs. The effective CLFs for finite plates are investigated for these parameter variations and compared with the semi-infinite plate results. The ratio between these two results is compared with the upper and lower bounds introduced in Chapter 3 and the variability of the effective CLF in terms of the appropriate value of the modal overlap factor is discussed.

Chapter 6 discusses the variability of the effective CLF, quantified by means of a systematic parameter study in which the modal overlap factor and the frequency bandwidth are varied independently. These results are used to derive an empirical formula for the confidence interval of the effective CLF in terms of the modal overlap factor and the number of modes in a frequency band. This empirical model is compared with the previously published models of Mohammed [43] and Lyon and DeJong [33], and the previous parameter variations obtained in Chapter 5. In order to test the form of the statistical distribution of the effective CLF, some statistical investigations (a Chi-square test, skewness and kurtosis) are carried out. The inter-dependence of the CLF from subsystem 1 to subsystem 2 and that from subsystem 2 to subsystem 1 is discussed and the correlation coefficients examined to determine whether they are independent each other.

Chapter 7 describes an experimental validation of the empirical model obtained in Chapter 6. The experimental investigations were carried out on two coplanar plates joined by bolts with all outer edges having free boundary conditions. This arrangement was used for simplicity in the experiments instead of the two rectangular plates coupled at right angles with opposite edges simply supported, as used in the development of the empirical model. Consequently, although the experiments do not provide a validation of the DSM modelling (this is considered unnecessary), they provide validation of the effectiveness of the empirical model in a different situation. An analytical study of the coplanar bolted joint is also presented, in which the DSM is again used to predict the effective CLF. In the experimental study, the vibration of the source and receiver plates is measured when a point force is applied, first to one plate and then to the other. The measured vibrations are averaged over ten forcing points and ten response points on each plate. The DLF for the two uncoupled plates is obtained using the decay rate method. The experimental and analytical CLFs are investigated and are discussed in relation to the empirical model for CLF variability developed in Chapter 6.

Chapter 8 discusses the consequences for SEA predictions of the variation in the effective CLF. In order to investigate the sensitivity of the resulting SEA prediction, a Monte Carlo simulation is applied. The energy ratio between the receiver plate and the source plate obtained by the SEA prediction is compared with the exact analytical DSM results.

The most important results and conclusions drawn from the work are summarised in Chapter 9. Some areas for future research are also identified and discussed.

CHAPTER 2

DYNAMIC STIFFNESS METHOD

2.1 Introduction

This chapter describes theoretical predictions of the dynamic response of a uniform plate and two coupled plates to an applied harmonic point force, using the dynamic stiffness method (DSM). Computer simulations, using MATLAB [72, 73], are included to illustrate the method and to validate the analytical models. The power balance between the input power and the dissipated power for these models is also investigated as a check on the consistency of the model.

2.2 Single plate investigations using DSM

2.2.1 Equations of motion

2.2.1.1 Flexure

For a uniform plate lying in the *x*-*y* plane, the equations of motion consist of partial differential equations in two space dimensions and time. The differential equation governing the flexural vibrations may be written as [28, 74]

$$D\nabla^4 w + \rho h \ddot{w} = p(x,y,t), \tag{2.1}$$

where w is the out-of-plane deflection, D is the flexural rigidity ($D = Eh^3/12(1-\mu^2)$, E is the Young's modulus, h is the thickness of the panel and μ is the Poisson's ratio), ρh is the mass per unit area [kg/m^2], and $p(x,y,t)$ represents a distributed pressure load. In equation (2.1), ∇^4 is the bi-harmonic operator of fourth order,

$$\nabla^4 = \nabla^2\nabla^2 = \frac{\partial^4}{\partial x^4} + 2\frac{\partial^4}{\partial x^2 \partial y^2} + \frac{\partial^4}{\partial y^4}, \tag{2.2}$$

where ∇^2 is the two-dimensional Laplace operator,

$$\nabla^2 = \frac{\partial^2}{\partial x^2} + \frac{\partial^2}{\partial y^2}. \tag{2.3}$$

Consider a rectangular plate of length L and width b. The plate is considered to be simply supported along two opposite longitudinal edges ($y = 0$ and $y = b$), as shown in Figure 2.1. This means that the displacements and bending moment are zero along these edges; *i.e.* $u = w = 0$ and $M_x = -D\frac{\partial^2 w}{\partial x^2} = 0$. The deflection of the plate may therefore be expressed in the form

$$w(x, y, t) = \sum_{n=1}^{\infty} W_n(x,t) \sin\left(\frac{n\pi y}{b}\right), \tag{2.4}$$

where W_n is the n^{th} component of the out-of-plane displacement and n is the number of half-sine waves along the transverse edge.

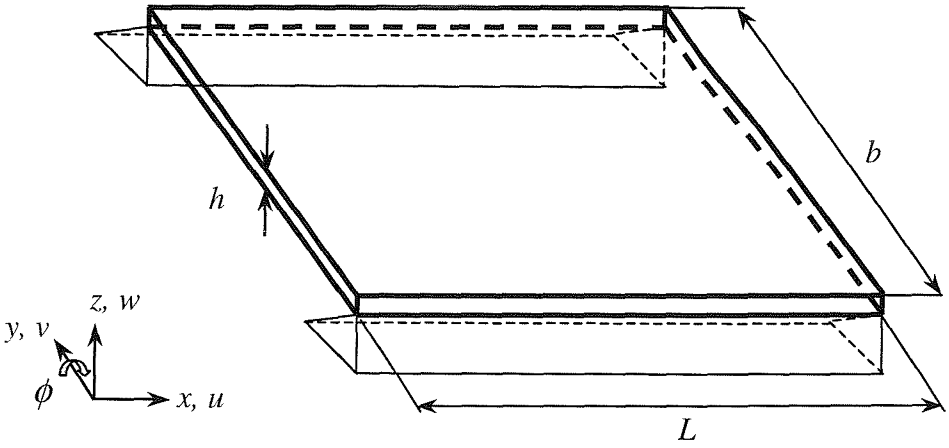

Figure 2.1. Single plate

From equation (2.4),

$$\begin{aligned} &\frac{\partial^4 w}{\partial x^4} = \sum_{n=1}^{\infty} W_n'''' \sin\left(\frac{n\pi y}{b}\right), &&\frac{\partial^4 w}{\partial y^4} = \sum_{n=1}^{\infty} W_n \left(\frac{n\pi}{b}\right)^4 \sin\left(\frac{n\pi y}{b}\right), \\ &\frac{\partial^4 w}{\partial x^2 \partial y^2} = -\sum_{n=1}^{\infty} W_n'' \left(\frac{n\pi}{b}\right)^2 \sin\left(\frac{n\pi y}{b}\right), &&\frac{\partial^2 w}{\partial t^2} = \sum_{n=1}^{\infty} \ddot{W}_n \sin\left(\frac{n\pi y}{b}\right) \end{aligned} \tag{2.5}$$

where $''$ and $''''$ denote the second and fourth derivatives with respect to x.

Substituting equations (2.5) into equation (2.1), then

$$\sum_{n=1}^{\infty}\left[DW_n''''-2D\left(\frac{n\pi}{b}\right)^2W_n''+D\left(\frac{n\pi}{b}\right)^4W_n+\rho h\ddot{W}_n\right]\sin\left(\frac{n\pi y}{b}\right)=p(x,y,t). \qquad (2.6)$$

Writing $k_n = n\pi/b$, multiplying by $\sin(m\pi y/b)$, and integrating over y gives

$$DW_n''''-2Dk_n^2W_n''+Dk_n^4W_n+\rho h\ddot{W}_n=\frac{2}{b}\int_0^b p(x,y,t)\sin(k_n y)dy, \qquad (2.7)$$

since, on the left-hand side, the integral of $\sin(m\pi y/b)\sin(n\pi y/b)$ is zero for $m \neq n$ and $b/2$ for $m = n$. Assuming harmonic time dependence $e^{j\omega t}$, equation (2.7) may be rewritten as follows, if there is no excitation,

$$DW_n''''-2Dk_n^2W_n''+\left\{Dk_n^4-\rho h\omega^2\right\}W_n=0, \qquad (2.8)$$

where $W_n(x)$ represents a complex amplitude. Solutions are sought of the form

$$W_n(x)=W_{n0}e^{k_{nr}x} \qquad (2.9)$$

for some wavenumber k_{nr}. Substituting this into equation (2.8), there are four possible solutions for k_{nr}. Hence the general solution to equation (2.8) is of the form

$$W_n(x)=\sum_{r=1}^{4}A_{nr}e^{k_{nr}x}, \qquad (2.10)$$

where A_{nr} are four unknown constants of integration, which can be found by ensuring that the solution satisfies the boundary conditions at the transverse edges, $x = 0$ and $x = L$, and k_{nr} are the four complex roots of the following equation;

$$Dk_{nr}^4-2Dk_n^2k_{nr}^2+\left(Dk_n^4-\rho h\omega^2\right)=0, \qquad (2.11)$$

$$k_{n1,n2}=\pm\sqrt{k_n^2+k^2},\ k_{n3,n4}=\pm\sqrt{k_n^2-k^2}\ \text{and}\ k^4=\rho h\omega^2/D. \qquad (2.12)$$

Here k is the plate flexural wavenumber. The first two terms of equation (2.10) have real values of k_{nr} and represent non-propagating waves which decay exponentially in space. These waves do not usually transmit energy and they may be called 'near field waves'. On the other hand, if $k > k_n$, the last two terms represent true flexural waves which have a sinusoidal distribution in space and propagate from left to right or from right to left. These waves transmit energy and they may be called 'far-field waves' [75].

The solution to equation (2.1) thus includes all four different k_{nr} terms in the following form

$$w=\sum_{n=1}^{\infty}\sum_{r=1}^{4}A_{nr}e^{k_{nr}x}\sin\left(k_n y\right)e^{j\omega t}. \tag{2.13}$$

2.2.1.2 In-plane motion

The differential equations for free in-plane vibrations of a plate are given by [74, 76]

$$B\left(1+\gamma\right)\frac{\partial^2 u}{\partial x^2}+B\frac{\partial^2 u}{\partial y^2}+B\gamma\frac{\partial^2 v}{\partial x\partial y}-\rho\ddot{u}=0, \tag{2.14}$$

$$B\left(1+\gamma\right)\frac{\partial^2 v}{\partial y^2}+B\frac{\partial^2 v}{\partial x^2}+B\gamma\frac{\partial^2 u}{\partial x\partial y}-\rho\ddot{v}=0, \tag{2.15}$$

where $B = E / 2(1+\mu)$, $\gamma = (1+\mu) / (1-\mu)$, ρ is the material density [kg / m^3], u is the longitudinal deflection, and v is the transverse deflection, as shown in Figure 2.1. These equations are uncoupled from the flexural deflection.

If the boundary conditions are simple supports along the longitudinal edges, the in-plane deflections, u and v, may be expressed as [77]

$$u\left(x,y,t\right)=\sum_{n=1}^{\infty}U_n\left(x,t\right)\sin\left(k_n y\right), \tag{2.16}$$

$$v\left(x,y,t\right)=\sum_{n=1}^{\infty}V_n\left(x,t\right)\cos\left(k_n y\right), \tag{2.17}$$

where $k_n = n\pi/b$ as before. Assuming a harmonic response, solutions are sought for U_n and V_n of the form

$$U_n\left(x,t\right)=U_{n0}\,e^{\left(\lambda_{nr}x+j\omega t\right)}, \tag{2.18}$$

$$V_n\left(x,t\right)=V_{n0}\,e^{\left(\lambda_{nr}x+j\omega t\right)}. \tag{2.19}$$

Using equations (2.16) and (2.17), the differential equations (2.14) and (2.15) can be rewritten as

$$B(1+\gamma)U_n'' - B\gamma k_n V_n' - Bk_n^2 U_n - \rho\ddot{U}_n = 0\,, \tag{2.20}$$

$$BV_n'' + B\gamma k_n U_n' - B(1+\gamma)k_n^2 V_n - \rho\ddot{V}_n = 0\,. \tag{2.21}$$

Substituting equations (2.18) and (2.19) into the differential equations (2.20) and (2.21)

$$B(1+\gamma)\lambda_{nr}^2 U_{n0} - B\gamma k_n \lambda_{nr} V_{n0} - Bk_n^2 U_{n0} + \rho\omega^2 U_{n0} = 0\,, \tag{2.22}$$

$$B\lambda_{nr}^2 V_{n0} + B\gamma k_n \lambda_{nr} U_{n0} - B(1+\gamma)k_n^2 V_{n0} + \rho\omega^2 V_{n0} = 0\,, \tag{2.23}$$

which can be solved for λ_{nr}. The four roots of λ_{nr} for a given n, are

$$\lambda_{n1,\,n2} = \pm\sqrt{k_n^2 - k_L^2} \text{ and } \lambda_{n3,\,n4} = \pm\sqrt{k_n^2 - k_T^2}\,, \tag{2.24}$$

where $k_L^2 = \rho\omega^2(1-\mu^2)/E$ and $k_T^2 = 2\rho\omega^2(1+\mu)/E$. k_L and k_T are the in-plane longitudinal and transverse shear wavenumbers of the plate.

The general solutions for the in-plane displacements may be written as

$$u(x,y,t) = \left\{ \begin{bmatrix}\lambda_{n1} & \lambda_{n2}\end{bmatrix} \begin{bmatrix} C_{n1}e^{\lambda_{n1}x} \\ C_{n2}e^{\lambda_{n2}x} \end{bmatrix} + \begin{bmatrix}k_n & k_n\end{bmatrix} \begin{bmatrix} C_{n3}e^{\lambda_{n3}x} \\ C_{n4}e^{\lambda_{n4}x} \end{bmatrix} \right\} \sin(k_n y)e^{i\omega t}\,, \tag{2.25}$$

$$v(x,y,t) = \left\{ \begin{bmatrix}k_n & k_n\end{bmatrix} \begin{bmatrix} C_{n1}e^{\lambda_{n1}x} \\ C_{n2}e^{\lambda_{n2}x} \end{bmatrix} + \begin{bmatrix}\lambda_{n3} & \lambda_{n4}\end{bmatrix} \begin{bmatrix} C_{n3}e^{\lambda_{n3}x} \\ C_{n4}e^{\lambda_{n4}x} \end{bmatrix} \right\} \cos(k_n y)e^{i\omega t}\,, \tag{2.26}$$

where C_{nr} are four unknown constants of integration which can be found by ensuring that the solution satisfies the boundary conditions at the ends of the plate.

2.2.2 Dynamic stiffness matrix

2.2.2.1 Flexure

Equation (2.10) may be used to derive a relationship between the displacements and forces at the ends of the plate, $x = 0$ and $x = L$, and thus to obtain the dynamic stiffness matrix of the plate for flexural vibrations with transverse modeshape $\sin(k_n y)$ for each n.

Upon introducing the flexural displacement vector for order n

$$\mathbf{u}_{nf}^T = \{W_n(0) \quad W_n'(0) \quad W_n(L) \quad W_n'(L)\}, \tag{2.27}$$

then from equation (2.10)

$$\begin{aligned} W_n(0) &= A_{n1} + A_{n2} + A_{n3} + A_{n4} \\ W_n'(0) &= k_{n1}A_{n1} + k_{n2}A_{n2} + k_{n3}A_{n3} + k_{n4}A_{n4} \\ W_n(L) &= A_{n1}e^{k_{n1}L} + A_{n2}e^{k_{n2}L} + A_{n3}e^{k_{n3}L} + A_{n4}e^{k_{n4}L} \\ W_n'(L) &= k_{n1}A_{n1}e^{k_{n1}L} + k_{n2}A_{n2}e^{k_{n2}L} + k_{n3}A_{n3}e^{k_{n3}L} + k_{n4}A_{n4}e^{k_{n4}L} \end{aligned}, \tag{2.28}$$

or in matrix form

$$\mathbf{u}_{nf} = \mathbf{p}_{1n}\mathbf{A}_n, \tag{2.29}$$

where $\mathbf{A}_n^T = \{A_{n1} \quad A_{n2} \quad A_{n3} \quad A_{n4}\}$ and

$$\mathbf{p}_{1n} = \begin{bmatrix} 1 & 1 & 1 & 1 \\ k_{n1} & k_{n2} & k_{n3} & k_{n4} \\ e^{k_{n1}L} & e^{k_{n2}L} & e^{k_{n3}L} & e^{k_{n4}L} \\ k_{n1}e^{k_{n1}L} & k_{n2}e^{k_{n2}L} & k_{n3}e^{k_{n3}L} & k_{n4}e^{k_{n4}L} \end{bmatrix}. \tag{2.30}$$

The components of vertical shear force $S_n(x)$ and bending moment $M_n(x)$ along the free edges for order n may be written as [28, 74]

$$S_n = -D\left[W_n''' - (2-\mu)k_n^2 W_n'\right], \tag{2.31}$$

$$M_n = -D\left[W_n'' - \mu k_n^2 W_n\right]. \tag{2.32}$$

The restoring force vector $\mathbf{F}_{nf}$ is now introduced

$$\mathbf{F}_{nf}^T = \{-S_n(0) \quad M_n(0) \quad S_n(L) \quad -M_n(L)\}, \tag{2.33}$$

where $$-S_n(0) = D\left[\sum_{r=1}^{4} k_{nr}^{\ 3} A_{nr} - (2-\mu)k_n^2\left\{\sum_{r=1}^{4} k_{nr}A_{nr}\right\}\right], \tag{2.34}$$

$$M_n(0) = -D\left[\sum_{r=1}^{4} k_{nr}^{\ 2} A_{nr} - \mu k_n^2 \sum_{r=1}^{4} A_{nr}\right], \tag{2.35}$$

$$S_n(L) = -D\left[\left\{\sum_{r=1}^{4} k_{nr}^{\ 3} A_{nr} e^{k_{nr}L}\right\} - (2-\mu)k_n^2\left\{\sum_{r=1}^{4} k_{nr}A_{nr}e^{k_{nr}L}\right\}\right], \tag{2.36}$$

$$-M_n(L) = D\left[\sum_{i=1}^{4} k_{nr}{}^{2} A_{ni} e^{k_{nr}L} - \mu k_n^2 \sum_{i=1}^{4} A_{ni} e^{k_{nr}L}\right]. \tag{2.37}$$

Equations (2.34 - 37) can be written in matrix form

$$\mathbf{F}_{nf} = \mathbf{p}_{2n}\mathbf{A}_n \tag{2.38}$$

where

$$\mathbf{p}_{2n} = D\begin{bmatrix} k_{n1}{}^{3} - (2-\mu)k_n^2 k_{n1} & k_{n2}{}^{3} - (2-\mu)k_n^2 k_{n2} & k_{n3}{}^{3} - (2-\mu)k_n^2 k_{n3} & k_{n4}{}^{3} - (2-\mu)k_n^2 k_{n4} \\ -k_{n1}{}^{2} + \mu k_n^2 & -k_{n2}{}^{2} + \mu k_n^2 & -k_{n3}{}^{2} + \mu k_n^2 & -k_{n4}{}^{2} + \mu k_n^2 \\ -k_{n1}{}^{3}e_1 + (2-\mu)k_n^2 k_{n1} e_1 & -k_{n2}{}^{3}e_2 + (2-\mu)k_n^2 k_{n2} e_2 & -k_{n3}{}^{3}e_3 + (2-\mu)k_n^2 k_{n3} e_3 & -k_{n4}{}^{3}e_4 + (2-\mu)k_n^2 k_{n4} e_4 \\ k_{n1}{}^{2}e_1 - \mu k_n^2 e_1 & k_{n2}{}^{2}e_2 - \mu k_n^2 e_2 & k_{n3}{}^{2}e_3 - \mu k_n^2 e_3 & k_{n4}{}^{2}e_4 - \mu k_n^2 e_4 \end{bmatrix} \tag{2.39}$$

and $e_i = e^{k_{ni}L}$.

Combining (2.38) with (2.29) it is possible to eliminate $\mathbf{A}_n$

$$\mathbf{F}_{nf} = \mathbf{p}_{2n}\mathbf{A}_n = \mathbf{p}_{2n}\mathbf{p}_{1n}^{-1}\mathbf{u}_{nf} = \mathbf{K}_{nf}\mathbf{u}_{nf}, \tag{2.40}$$

where $\mathbf{K}_{nf}$ is the dynamic stiffness matrix for flexural vibrations of order n:

$$\mathbf{K}_{nf} = \mathbf{p}_{2n}\mathbf{p}_{1n}^{-1}, \tag{2.41}$$

2.2.2.2 In-plane motion

Equations (2.16) and (2.17) may similarly be used to derive a relationship between the in-plane displacements and forces at the ends of the plate, and thus the dynamic stiffness matrix of the plate for in-plane vibrations of order n.

Upon introducing the in-plane displacement vector

$$\mathbf{u}_{ni}^T = \{U_n(0) \quad V_n(0) \quad U_n(L) \quad V_n(L)\}, \tag{2.42}$$

then from equations (2.25) and (2.26),

$$\begin{aligned}
U_n(0) &= \lambda_{n1}C_{n1} + \lambda_{n2}C_{n2} + k_nC_{n3} + k_nC_{n4} \\
V_n(0) &= k_nC_{n1} + k_nC_{n2} + \lambda_{n3}C_{n3} + \lambda_{n4}C_{n4} \\
U_n(L) &= \lambda_{n1}e^{\lambda_{n1}L}C_{n1} + \lambda_{n2}e^{\lambda_{n2}L}C_{n2} + k_ne^{\lambda_{n3}L}C_{n3} + k_ne^{\lambda_{n4}L}C_{n4} \\
V_n(L) &= k_ne^{\lambda_{n1}L}C_{n1} + k_ne^{\lambda_{n2}L}C_{n2} + \lambda_{n3}e^{\lambda_{n3}L}C_{n3} + \lambda_{n4}e^{\lambda_{n4}L}C_{n4}
\end{aligned} \tag{2.43}$$

or in matrix form

$$\mathbf{u}_{ni} = \mathbf{r}_{1n}\mathbf{C}_n\,, \tag{2.44}$$

where $\mathbf{C}_n^T = \{C_{n1} \quad C_{n2} \quad C_{n3} \quad C_{n4}\}$ and

$$\mathbf{r}_{1n} = \begin{bmatrix} \lambda_{n1} & \lambda_{n2} & k_n & k_n \\ k_n & k_n & \lambda_{n3} & \lambda_{n4} \\ \lambda_{n1}e^{\lambda_{n1}L} & \lambda_{n2}e^{\lambda_{n2}L} & k_ne^{\lambda_{n3}L} & k_ne^{\lambda_{n4}L} \\ k_ne^{\lambda_{n1}L} & k_ne^{\lambda_{n2}L} & \lambda_{n3}e^{\lambda_{n3}L} & \lambda_{n4}e^{\lambda_{n4}L} \end{bmatrix}. \tag{2.45}$$

The in-plane longitudinal force $N(x)$ and transverse force $T(x)$ which correspond to the deflections, $U_n(x)$ and $V_n(x)$, may be written as [74, 76]

$$N = hB(1+\gamma)\left[\frac{\partial u}{\partial x} + \mu\frac{\partial v}{\partial y}\right], \tag{2.46}$$

$$T = hB\left[\frac{\partial u}{\partial y} + \frac{\partial v}{\partial x}\right]. \tag{2.47}$$

Then, introducing the restoring force vector

$$\mathbf{F}_{ni}^T = \{-N(0) \quad -T(0) \quad N(L) \quad T(L)\}, \tag{2.48}$$

i.e. then

$$\mathbf{F}_{ni} = \mathbf{r}_{2n}\mathbf{C}_n\,, \tag{2.49}$$

where

$$\mathbf{r}_{2n} = hB\begin{bmatrix} -(1+\gamma)(\lambda_{n1}^2 - \mu k_n^2) & -(1+\gamma)(\lambda_{n2}^2 - \mu k_n^2) & -(1+\gamma)k_n\lambda_{n3}(1-\mu) & -(1+\gamma)k_n\lambda_{n4}(1-\mu) \\ -2k_n\lambda_{n1} & -2k_n\lambda_{n2} & -(k_n^2 + \lambda_{n3}^2) & -(k_n^2 + \lambda_{n4}^2) \\ (1+\gamma)(\lambda_{n1}^2 - \mu k_n^2)e^{\lambda_{n1}L} & (1+\gamma)(\lambda_{n2}^2 - \mu k_n^2)e^{\lambda_{n2}L} & (1+\gamma)(1-\mu)k_n\lambda_{n3}e^{\lambda_{n3}L} & (1+\gamma)(1-\mu)k_n\lambda_{n4}e^{\lambda_{n4}L} \\ 2k_n\lambda_{n1}e^{\lambda_{n1}L} & 2k_n\lambda_{n2}e^{\lambda_{n2}L} & (k_n^2 + \lambda_{n3}^2)e^{\lambda_{n3}L} & (k_n^2 + \lambda_{n4}^2)e^{\lambda_{n4}L} \end{bmatrix} \tag{2.50}$$

Combining equation (2.44) with equation (2.49), the coefficients $\mathbf{C}_n$ can be eliminated, giving

$$\mathbf{F}_{ni} = \mathbf{r}_{2n}\mathbf{C}_n = \mathbf{r}_{2n}\mathbf{r}_{1n}^{-1}\mathbf{u}_{ni} = \mathbf{K}_{ni}\mathbf{u}_{ni}, \tag{2.51}$$

where $\mathbf{K}_{ni}$ is the dynamic stiffness matrix for in-plane vibrations of order n:

$$\mathbf{K}_{ni} = \mathbf{r}_{2n}\mathbf{r}_{1n}^{-1}, \tag{2.52}$$

2.2.2.3 Dynamic stiffness matrix for a single thin plate

Along each edge $x = 0$, $x = L$ it is assumed that the plate has four degrees of freedom, three translational degrees of freedom (u, v, w) and one rotational degree of freedom (ϕ), for each value of n. As the plate is thin, then the in-plane rotation is not significant. The dynamic stiffness matrices for flexure and in-plane motion may be combined in an 8×8 matrix

$$\mathbf{K}_n = \begin{bmatrix} \mathbf{K}_{nf} & 0 \\ 0 & \mathbf{K}_{ni} \end{bmatrix}, \tag{2.53}$$

where $\mathbf{K}_{nf}$ is the dynamic stiffness matrix for flexure and $\mathbf{K}_{ni}$ is the dynamic stiffness matrix for in-plane motion as given by equations (2.41) and (2.52). This represents the dynamic properties of a single plate. The components of $\mathbf{K}_{n}$ can also be reordered so that all deflections at $x = 0$ appear first, followed by all deflections at $x = L$.

2.2.2.4 The removal of a near-singularity from the matrix

If the length of the plate L is large compared with the wavelength, the matrices $\mathbf{p}_{1n}$, $\mathbf{p}_{2n}$, $\mathbf{r}_{1n}$ or $\mathbf{r}_{2n}$ may be nearly singular due to numerical rounding errors. This is caused by large differences in the relative values of the elements of the matrix. It can be overcome by multiplying by a diagonal scaling matrix $\mathbf{H}$.

For flexural vibration, write

$$\mathbf{p}_{1n}\mathbf{H}_f = \mathbf{p}'_{1n}, \quad \mathbf{p}_{2n}\mathbf{H}_f = \mathbf{p}'_{2n}, \tag{2.54}$$

$$\mathbf{K}_{nf} = \mathbf{p}_{2n}\mathbf{p}_{1n}^{-1} = \left(\mathbf{p}'_{2n}\mathbf{H}_f^{-1}\right)\left(\mathbf{p}'_{1n}\mathbf{H}_f^{-1}\right)^{-1} = \left(\mathbf{p}'_{2n}\mathbf{H}_f^{-1}\right)\left(\mathbf{H}_f\,\mathbf{p}'^{-1}_{1n}\right), \tag{2.55}$$

$$\mathbf{K}_{nf} = \mathbf{p}'_{2n}\,\mathbf{p}'^{-1}_{1n}, \tag{2.56}$$

where $\mathbf{H}_f$ is a diagonal scaling matrix. This is chosen to be

$$\mathbf{H}_f = \begin{bmatrix} e^{-k_{n1}L} & 0 & 0 & 0 \\ 0 & 1 & 0 & 0 \\ 0 & 0 & e^{-k_{n3}L} & 0 \\ 0 & 0 & 0 & 1 \end{bmatrix}, \tag{2.57}$$

where $\mathrm{Re}(k_{n1}) \geq 0$ and $\mathrm{Re}(k_{n3}) \geq 0$.

Similarly for in-plane vibration,

$$\mathbf{r}_{1n}\mathbf{H}_t = \mathbf{r}'_{1n}, \quad \mathbf{r}_{2n}\mathbf{H}_t = \mathbf{r}'_{2n}, \tag{2.58}$$

$$\mathbf{K}_{nt} = \mathbf{r}_{2n}\mathbf{r}_{1n}^{-1} = \left(\mathbf{r}'_{2n}\mathbf{H}_t^{-1}\right)\left(\mathbf{r}'_{1n}\mathbf{H}_t^{-1}\right)^{-1} = \left(\mathbf{r}'_{2n}\mathbf{H}_t^{-1}\right)\left(\mathbf{H}_t\,\mathbf{r}'^{-1}_{1n}\right), \tag{2.59}$$

$$\mathbf{K}_{nt} = \mathbf{r}'_{2n}\,\mathbf{r}'^{-1}_{1n}. \tag{2.60}$$

where $\mathbf{H}_t = \begin{bmatrix} e^{-\lambda_{n1}L} & 0 & 0 & 0 \\ 0 & 1 & 0 & 0 \\ 0 & 0 & e^{-\lambda_{n3}L} & 0 \\ 0 & 0 & 0 & 1 \end{bmatrix}$ is a different scaling matrix.

This effectively changes the coefficients to scaled coefficients in the description of the wave amplitudes in the plate.

2.2.3 Inclusion of damping

For an elastic structure the stress σ_x and the strain ε_x in the longitudinal direction are related by Hooke's law, *i.e.* when $\sigma_y = \sigma_z = 0$,

$$\sigma_x = E\varepsilon_x. \tag{2.61}$$

For hysteretic damping, the stress-strain relationship of a viscoelastic material excited harmonically is given by [27]

$$\sigma_x = E\left(\varepsilon_x + \frac{\eta}{\omega}\frac{\partial \varepsilon_x}{\partial t}\right) \qquad (2.62)$$

in which η is the loss factor, or hysteretic damping constant, and ω is the excitation frequency. For the steady-state response to harmonic excitation, all physical quantities can be represented in complex notation with a time dependence $e^{j\omega t}$. Thus

$$\partial\varepsilon_x/\partial t = j\omega\,\varepsilon_x \text{ and } \sigma_x = E\left(1+j\eta\right)\varepsilon_x . \qquad (2.63), (2.64)$$

Similar expressions can be used for other types of motion. The loss factor η may be introduced to represent the material damping. In the dynamic stiffness matrices, the Young's modulus E and the flexural rigidity D are replaced by $E(1+j\eta)$ and $D(1+j\eta)$. Table 2.1 summarises the application to material properties and wavenumbers for a hysteretically damped system, from [27].

Table 2.1. Assumed relationships applying for hysteretic damping models.

Property	Undamped	Damped	Lightly damped Approximation
Young's modulus	E	$E(1+j\eta)$	$E(1+j\eta)$
Shear modulus	G	$G(1+j\eta)$	$G(1+j\eta)$
Flexural wavenumber	k_f	$k_f(1+j\eta)^{-1/4}$	$k_f(1-j\eta/4)$
Longitudinal wavenumber	k_L	$k_L(1+j\eta)^{-1/2}$	$k_L(1-j\eta/2)$
Transverse wavenumber	k_T	$k_T(1+j\eta)^{-1/2}$	$k_T(1-j\eta/2)$

2.2.4 Point force

Previously the equation of motion of the plate has been solved by expanding the response into a series of half-sine orders across the plate width. If the excitation is a point force at position y_0, this needs to be expressed as a Fourier representation in the various orders. If a force is defined by $F(y) = F_0\,\delta(y - y_0)$ and assumed odd and periodic in (*-b*, *b*), then $F(y)$ can be expressed by a half-range Fourier series expansion [78], that is

$$F(y) = \frac{a_0}{2} + \sum_{n=1}^{\infty}\left(a_n \cos\frac{n\pi y}{b} + b_n \sin\frac{n\pi y}{b}\right) \tag{2.65}$$

where $a_0 = 0,\ a_n = 0,\ b_n = \frac{2}{b}\int_0^b F(y)\sin\frac{n\pi y}{b}dy = \frac{2F_0}{b}\sin\frac{n\pi y_0}{b}$ for n = 1, 2, 3, …

Hence, the force can be represented spatially by the series

$$F(y) = \frac{2F_0}{b}\sum_{n=1}^{\infty}\sin\frac{n\pi y_0}{b}\sin\frac{n\pi y}{b}. \tag{2.66}$$

If the point force is applied at the mid-point of the edge, $y_0 = b/2$, then

$$F(y) = \frac{2F_0}{b}\sum_{\substack{n=1\\ n,odd}}^{\infty}(-1)^{(n-1)/2}\sin\frac{n\pi y}{b} \tag{2.67}$$

or

$$F(y) = \frac{2F_0}{b}\sum_{n=1}^{\infty}(-1)^{n+1}\sin\frac{(2n-1)\pi y}{b}\ . \tag{2.68}$$

Figure 2.2 shows a reconstruction of a point force at $y_0 = b/2$ using Fourier components up to n = 5, 11 and 21. As more Fourier components are included, the force representation is closer to a point force of increasing amplitude as it converges to a Dirac delta function.

2.2.5 Energies and power

2.2.5.1 Strain energy for flexure and in-plane motion

The strain energy for flexural vibration is given by [27]

$$E_{strain,f} = \frac{D}{2}\int_0^b\int_0^L\left[\left(\frac{\partial^2 w}{\partial x^2}\right)^2 + \left(\frac{\partial^2 w}{\partial y^2}\right)^2 + 2\mu\frac{\partial^2 w}{\partial x^2}\frac{\partial^2 w}{\partial y^2} + 2(1-\mu)\left(\frac{\partial^2 w}{\partial x\partial y}\right)^2\right]dxdy. \tag{2.69}$$

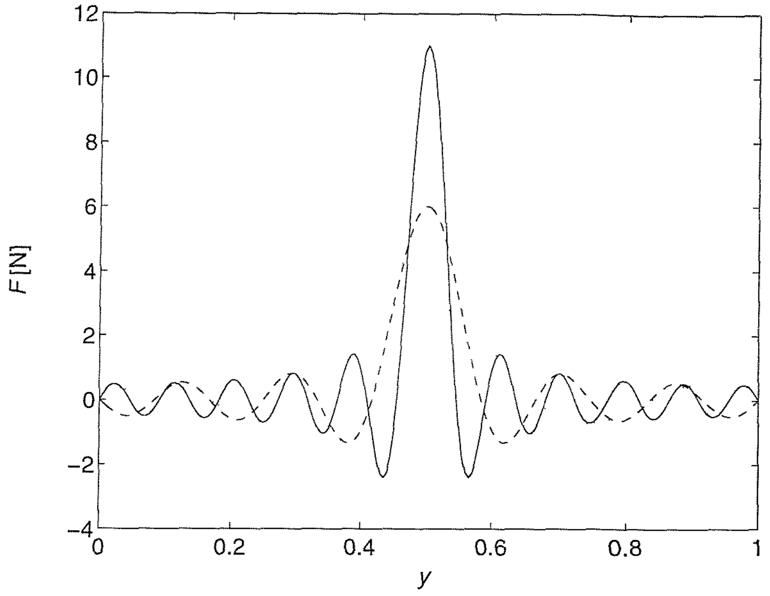

Figure 2.2. A point force at the middle of an edge of a plate represented by the Fourier components, n = 1-5, 1-11 and 1-21 (n odd). ; n = 1-5; ---, n = 1-11; —, n = 1-21.

The strain energy for in-plane vibration is given by [27]

$$E_{strain,i}=\frac{Eh}{2(1-\mu^2)}\int_0^b\int_0^L\left[\left(\frac{\partial u}{\partial x}\right)^2+\left(\frac{\partial v}{\partial y}\right)^2+2\mu\frac{\partial u}{\partial x}\frac{\partial v}{\partial y}+\frac{(1-\mu)}{2}\left(\frac{\partial u}{\partial y}+\frac{\partial v}{\partial x}\right)^2\right]dxdy. \quad (2.70)$$

2.2.5.2 Kinetic energy for flexure and in-plane motion

The kinetic energy for flexural and in-plane vibrations is also given by [27]

$$E_{kin}=\frac{\rho h}{2}\int_0^b\int_0^L\left[\left(\frac{\partial u}{\partial t}\right)^2+\left(\frac{\partial v}{\partial t}\right)^2+\left(\frac{\partial w}{\partial t}\right)^2\right]dxdy. \quad (2.71)$$

In practice, the integration of equations (2.69 - 71) may be performed numerically by summing over the step lengths Δx and Δy along the length and width of the plate. The discrete summation is an approximation to the continuous integral. It can also be integrated analytically to give an accurate measure of its energy (see Appendix A for the analytical integration of strain energy). Throughout this study the latter approach has been adopted.

2.2.5.3 Power

The time-averaged power input P_{in} produced by a harmonic force $Fe^{j\omega t}$ is given by [39]

$$P_{in} = \frac{1}{2}\mathrm{Re}(Y)\,|F|^2 = \frac{1}{2}\mathrm{Re}(Z)\,|v|^2 = \frac{1}{2}\mathrm{Re}\left(F^* v\right) \quad \text{[Watt (W) or Nm/s]} \qquad (2.72)$$

where Y is the input mobility, Z is the input impedance, v is the velocity amplitude at the excitation point and F^* is the complex conjugate of the applied force amplitude F.

The power balance equation for an isolated subsystem is given by [33, 79],

$$P_{in} = P_{diss} = 2\pi f \eta E_{strain} \qquad (2.73)$$

where, P_{in} is the input power, P_{diss} is the dissipated power, and E_{strain} is the maximum strain energy in a cycle of the dynamic response in the subsystem at frequency f (Hz). If the kinetic energy is used in this calculation, the 'dissipated power' does not agree well with the input power. This point will be discussed further in the simulation results section below. Thus the dissipated power P_{diss} can be calculated using the total strain energy of the system obtained from equations (2.69) and (2.70).

2.2.6 Simulations for a single plate

2.2.6.1 Model

A model was selected to compare the results with previously published data [80]. It is shown in Figure 2.3 and comprises of a square aluminium plate, simply supported along two edges, free along the other edges. For this model, only the flexural vibration is considered.

2.2.6.2 Natural frequencies

For free vibration problems $\mathbf{F}_n$ is zero and the natural frequencies for flexural vibration are determined from the equation

$$\det\,(\mathbf{K}_{nf}) = 0 \qquad (2.74)$$

where $\mathbf{K}_{nf}$ is the dynamic stiffness matrix for flexure, reduced as appropriate according to the boundary conditions at $x = 0$ and $x = L$. Equivalently the resonances correspond to peaks in $\left(\det\left(\mathbf{K}_{nf}\right)\right)^{-1}$.

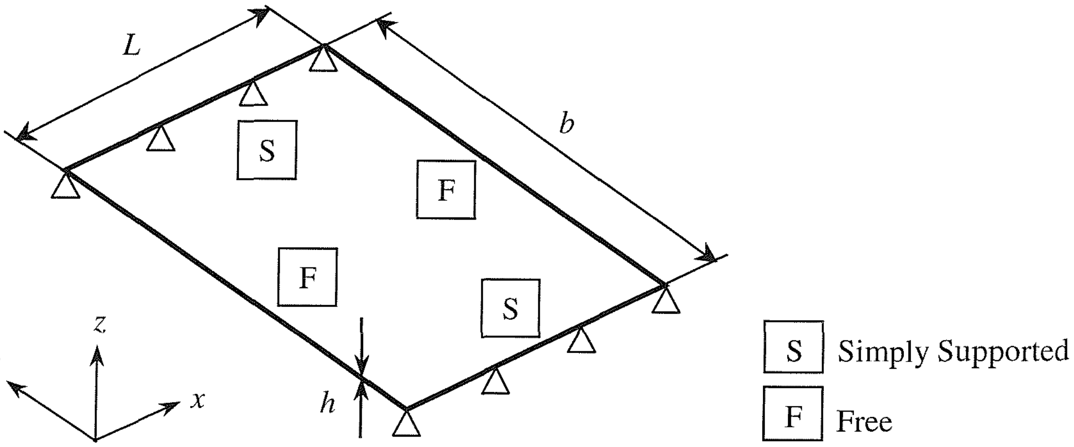

Figure 2.3. A single plate: width $b = 254$ mm, length $L = 254$ mm, thickness $h = 3.18$ mm, material: aluminium (Young's modulus $E = 7.24\times10^{10}$ N/m^2, Poisson's ratio $\mu = 0.333$, material density $\rho = 2.794\times10^3$ kg/m^3).

The natural frequencies of a single plate were obtained by a formula [80], as listed in Table 2.2. Figure 2.4 shows the flexural 'frequency functions', that is $\left(\det\left(\mathbf{K}_{nf}\right)\right)^{-1}$, for a single plate according to the number of half-sine waves along the y-direction, n. The natural frequencies for the first mode of each n, extracted from the frequency functions in Figure 2.4, agree well with previously published data [80], as listed in Table 2.3. The results obtained from the dynamic stiffness method are exact but the natural frequencies in Table 2.3 are subject to digitisation errors in reading values from the frequency functions.

Table 2.2. The natural frequencies in Hz for a single plate obtained from published data [80].

$$f=\frac{\lambda^2}{2\pi L^2}\sqrt{\frac{D}{\rho h}} \quad \left(b=254\,\text{mm},\ L=254\,\text{mm},\ h=3.18\,\text{mm}\right)$$

m / n	1		2		3		4	
	λ^2	f (Hz)	λ^2	f (Hz)	λ^2	f (Hz)	λ^2	f (Hz)
1	9.568	115.9	15.88	192.4	36.42	441.2	133.5	908.8
2	38.79	469.9	46.33	561.2	70.16	849.9	168.9	1337
3	87.74	1063	95.48	1157	121.3	1469	223.8	1984
4	156.4	1895	164.1	1988	191.0	2314	296.9	2849

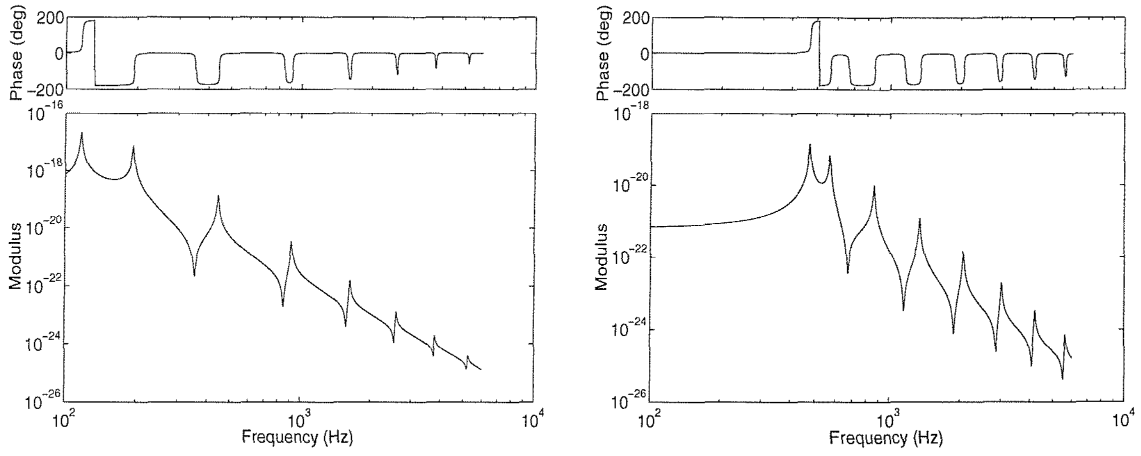

(a) $n=1$ (b) $n=2$

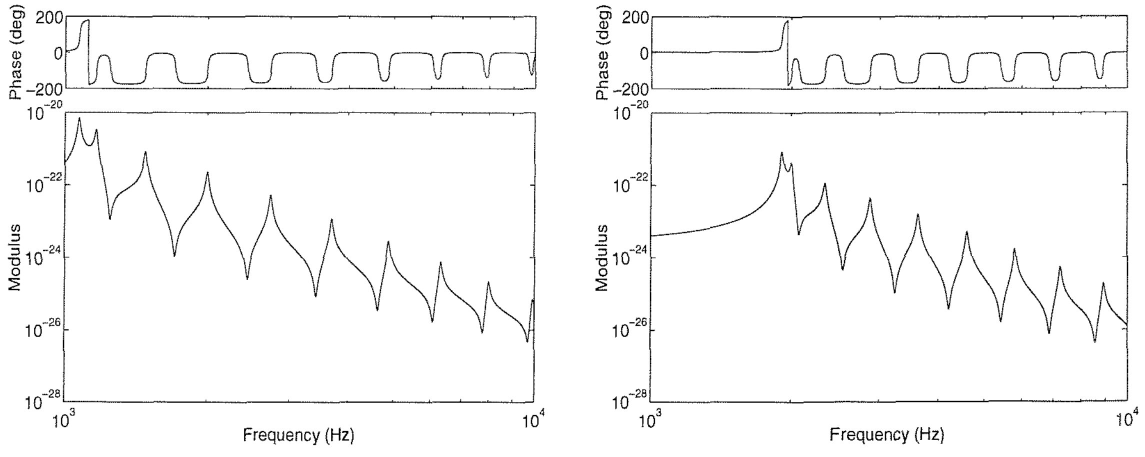

(c) $n=3$ (d) $n=4$

Figure 2.4. The flexural 'frequency functions' (*i.e.* $\left(\det\left(\mathbf{K}_{nf}\right)\right)^{-1}$) for a single plate for 4 different half-sine wave orders. $\eta = 0.01$.

Table 2.3. Comparison of the natural frequencies in Hz for the first mode ($m = 1$) of each n.

n	Gorman [80]	Dynamic Stiffness Method	Difference
1	115.9	115.9	0.0
2	469.9	470.1	0.2
3	1063	1063	0.0
4	1895	1895	0.0

2.2.6.3 Dispersion relationships for flexural vibration in a rectangular plate, simply supported on two parallel sides

Figure 2.5 shows the dispersion curves, the relationship between wavenumber and frequency, and also the wavespeed, for a single plate for the first half-sine order across the plate ($n = 1$). These show the wavenumbers and wavespeeds in the x direction.

There are four complex roots from equation (2.11) for each n. For two roots, k_{n1} and k_{n2}, the real parts of the wavenumbers, that is the evanescent components, are greater than the imaginary parts and these waves are not propagating but decaying along the plate. For the other two roots, k_{n3} and k_{n4}, on the other hand, the imaginary parts are greater than the real parts when $k > k_n$. The frequency at which $k = k_n$ is referred to as the 'cut-on' frequency and is given by

$$f_{\text{cut-on}} = \frac{\pi}{2}\left(\frac{n}{b}\right)^2\left(\frac{D}{\rho h}\right)^{1/2}. \qquad (2.75)$$

For $n = 1$ this is 120.5 Hz in the present example, or $\omega_{\text{cut-on}} = 756.7$ rad/s.

These two waves are propagating in the negative and positive directions, respectively, and each of them transmits energy along the plate. The wavespeed of a propagating wave k_{n3} changes rapidly around the cut-on frequency, which corresponds to the first mode of an infinitely long plate and converges to the free flexural wavespeed as frequency increases. In the absence of damping the wavespeed would tend to infinity at the cut-on frequency.

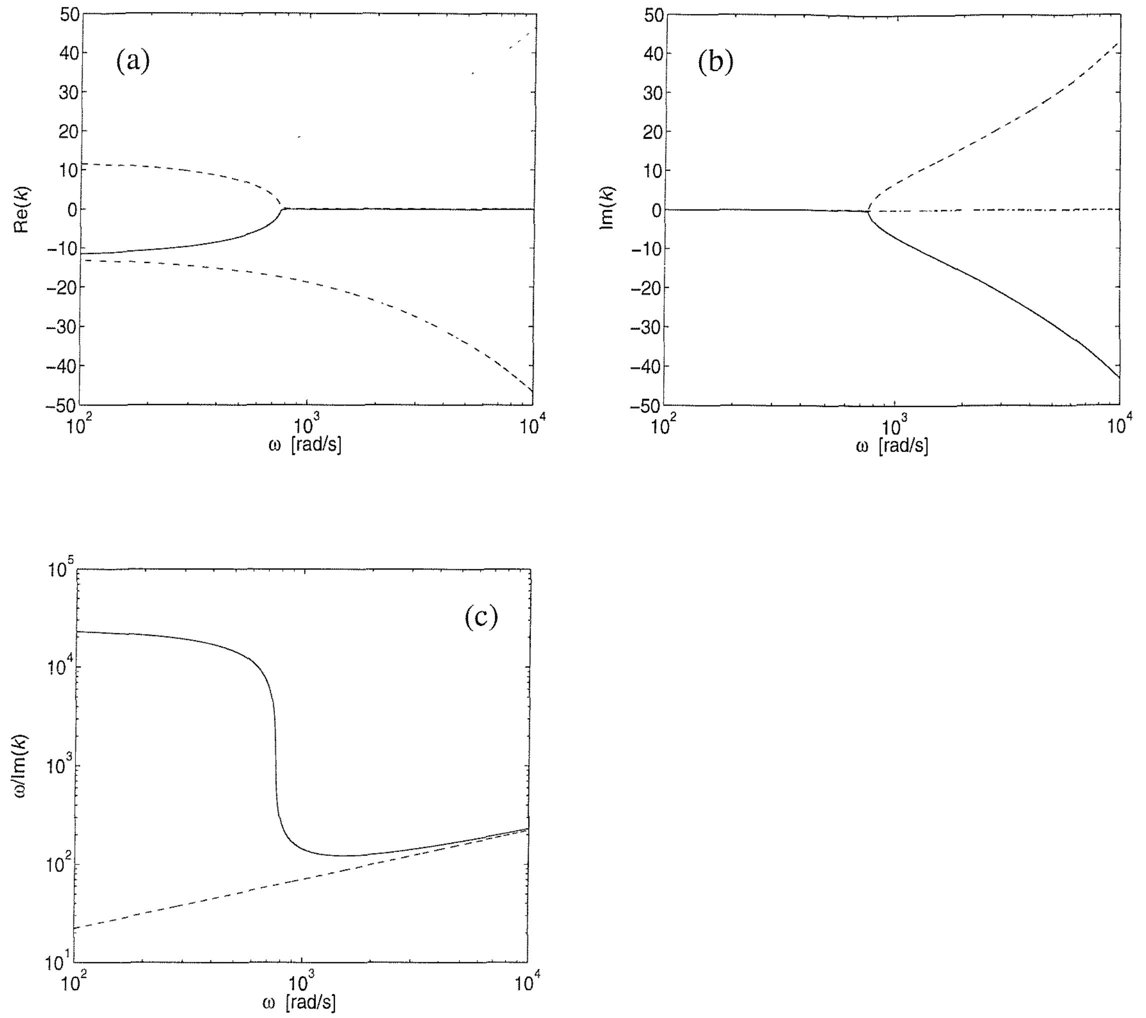

Figure 2.5. The dispersion curves and wavespeeds for the rectangular plate of Figure 2.3 (n = 1, $\eta = 0.01$); (a) real wavenumber components of k against ω, (b) imaginary wavenumber components of k against ω; ·····, k_{n1}; -·-, k_{n2}; ---, k_{n3}; —, k_{n4}, and (c) wavespeed $\omega/\mathrm{Im}(k)$ against ω; ---, free flexural wavespeed; —, propagating wavespeed of k_{n3}.

2.2.6.4 Validation of the input power calculation for a finite plate

The input power, when a point force is applied at the mid-point of the left-hand edge, *i.e.* $x = 0$, $y = b/2$, was calculated by equation (2.72) and compared with that for a semi-infinite plate excited on its edge. For a harmonic force of amplitude F, the time-averaged input power for the semi-infinite plate is given by

$$P_{in\infty} = \frac{1}{2}|F|^2 \operatorname{Re}\left\{\frac{1}{Z_\infty}\right\} \tag{2.76}$$

where Re denotes the real part and Z_∞ is the impedance of the semi-infinite plate [48, 81], corrected by [82]

$$Z_\infty \cong 2.165\sqrt{\rho h D}\,. \tag{2.77}$$

Note that Z_∞, and hence $P_{in\,\infty}$, is independent of frequency. The calculated input power for the single plate converges, as expected [59], to that for the semi-infinite plate at high frequencies, as shown in Figure 2.6.

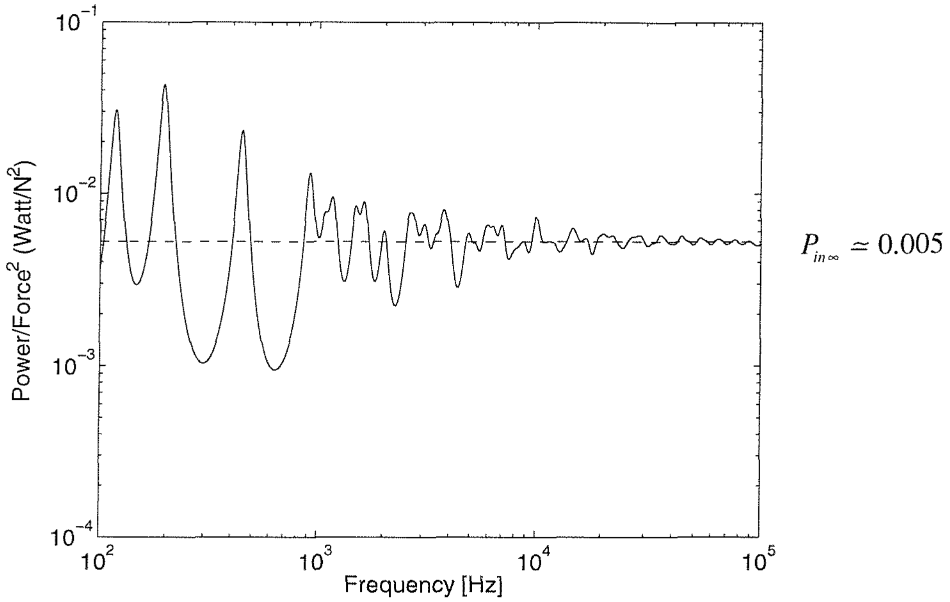

Figure 2.6. Comparison between the input power for the single plate of Figure 2.3 (DLF $\eta = 0.1$, $n_{max} = 29$) and that for the semi-infinite plate when a point force is applied at the mid-point of the left-hand edge. —, finite plate; ---, semi-infinite plate.

2.2.6.5 The number of Fourier components

Since the point force excites components of vibration with different values of n, a study has been performed to establish how many components should be included to achieve convergence of the solution. The force acts at the mid-point of the edge so only odd values of n need to be included. The total input power has been calculated using $n = 1$ to 11 and these powers were evaluated at frequencies spaced equally on a logarithmic scale such that the frequency spacing Δf is smaller than a half of the half-power bandwidth, $\eta f/2$. The results are then converted to one-third octave bands. The same calculation has been performed for a truncated series using $n = 1$ to n_{max} for different values of n_{max}. These results have then been normalised by the result for $n_{max} = 11$ in each band. Figure 2.7 shows these normalised input powers. As frequency increases the number of components that must be included, n_{max}, increases. Thus below 800 Hz $n_{max} = 1$ is sufficient whereas at 10 kHz $n_{max} = 9$ is required. These results are also listed in Table 2.4.

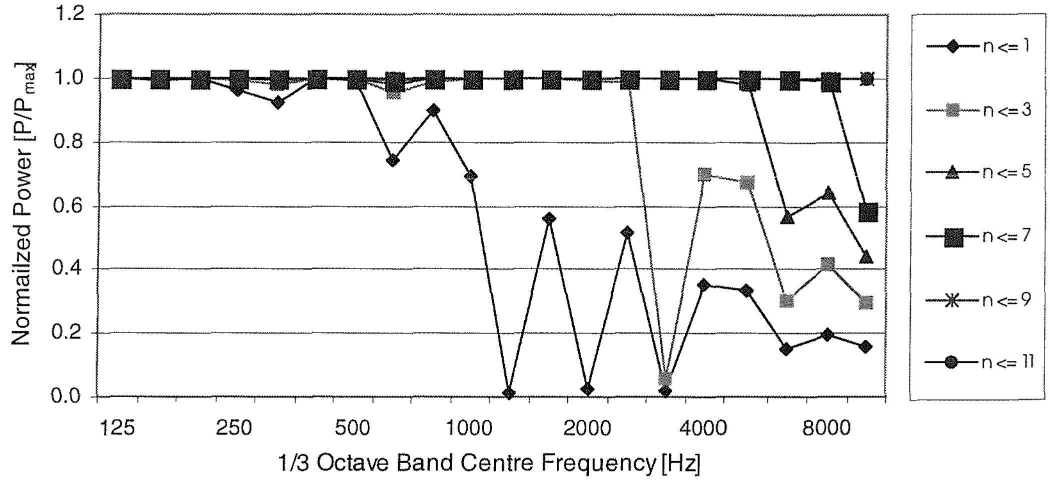

Figure 2.7. The convergence of the input power according to the number of Fourier components for the plate of Figure 2.3.

The choice of n_{max} should ideally be made beforehand, for example from a knowledge of the cut-on frequency, equation (2.75), for each n. Below the appropriate cut-on frequency the contribution of a given n is likely to be small. In the table, the shaded values correspond to n_{max} based on including only components with cut-on frequencies below the upper frequency of the current one-third octave band. This results in some inaccuracy especially in the 630 Hz band which corresponds to an anti-resonance, see Figure 2.6. However, for all higher orders of n, selecting n_{max} to include only those orders which have cut on in the frequency band of interest gives good results.

Table 2.4. The input power normalised with respect to the maximum input power of each 1/3 octave frequency band for each n_{max}, for the plate of Figure 2.3.

n_{max}	1	3	5	7	9	11
$f_{\text{cut-on}}$ f_c	120.5	1084	3012	5903	9758	14580
125	1.000	1.000	1.000	1.000	1.000	1.000
160	0.992	0.998	0.999	1.000	1.000	1.000
200	1.000	1.000	1.000	1.000	1.000	1.000
250	0.963	0.991	0.997	0.999	0.999	1.000
315	0.923	0.981	0.993	0.997	0.999	1.000
400	0.999	1.000	1.000	1.000	1.000	1.000
500	0.995	0.999	1.000	1.000	1.000	1.000
630	0.739	0.955	0.983	0.993	0.997	1.000
800	0.901	0.989	0.996	0.998	0.999	1.000
1000	0.692	0.999	1.000	1.000	1.000	1.000
1250	0.015	0.998	0.999	1.000	1.000	1.000
1600	0.557	0.998	0.999	1.000	1.000	1.000
2000	0.025	0.992	0.998	0.999	1.000	1.000
2500	0.515	0.984	0.999	0.999	1.000	1.000
3150	0.017	0.056	0.998	0.999	1.000	1.000
4000	0.354	0.697	0.996	0.999	1.000	1.000
5000	0.335	0.672	0.981	0.998	0.999	1.000
6300	0.148	0.303	0.566	0.998	1.000	1.000
8000	0.194	0.415	0.639	0.991	0.999	1.000
10000	0.155	0.298	0.441	0.583	0.998	1.000

Note. n_{max} = the maximum number of Fourier component
f_c = one-third octave band centre frequency
$f_{\text{cut-on}}$ = cut-on frequency

2.2.6.6 Estimates of dissipated power based on strain and kinetic energy

If losses are from material damping, the maximum strain energy in a cycle should be used in evaluating the dissipated power described in equation (2.73), from the definition of the loss factor given by [48]

$$\eta = \frac{\text{energy lost per cycle}}{2\pi\,(\text{reversible mechanical energy})} = \frac{P_{diss}}{\omega E_{strain}}. \qquad (2.78)$$

Often, especially in experimental SEA, the maximum kinetic energy in a cycle is used to estimate the dissipated power,

$$P_{diss} \cong \eta\omega E_{kin} \tag{2.79}$$

as it is a quantity more amenable to measurement. This relies on the equality [39]

$$E_{kin} \cong E_{strain} \cong \overline{E} \tag{2.80}$$

where $\overline{E}$ is the time-averaged total energy. This is satisfied in a broad-band sense, but not necessarily at single frequencies except at the natural frequencies.

In a steady state, the power balance between the predicted input power and the predicted dissipated power should be satisfied. To investigate whether this is the case, the single plate (Figure 2.3) was considered with a point force applied at the mid-point of the left-hand edge. Figure 2.8 compares the input power with the dissipated power. The right-hand figures show the error in each case, and are plotted against frequency. The dissipated power was calculated from either the strain or kinetic energy, integrated analytically. This shows that if the kinetic energy is used to calculate the dissipated power, the error in regions of low frequency is very large, whilst the error decreases as the frequency increases. On the other hand, the error produced when using the strain energy is extremely small and these powers coincide very well. The integration of energy was performed numerically in reference [86] by summing over the step lengths along the length and width of the plate. A step size was chosen between sampled points equal to 1/6 of the bending wavelength at the maximum frequency. It is noted that the result of the numerical integration [86] is subject to greater errors than the analytical result used here.

Thus, it is clear that the strain energy and the analytical integration should be used when the dissipated power is evaluated in the low and mid frequency range, whereas the kinetic energy is widely used in practice because of simplicity, both experimentally and analytically.

It should be noted that the current simulations use a damping model in which losses are introduced by making the Young's modulus complex. In practical structures other damping mechanisms may be present, such as friction at joints, which may be more related to kinetic energy rather than strain energy.

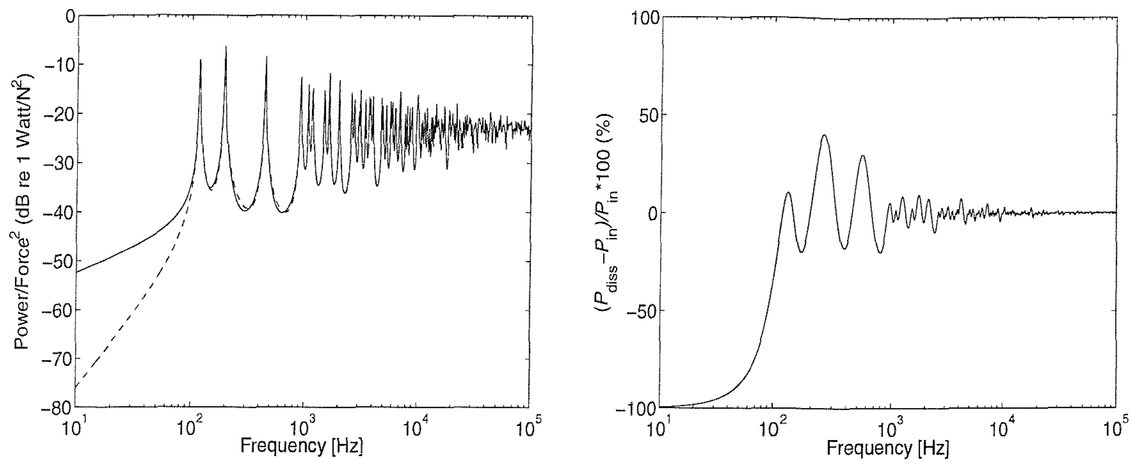

(a) Power obtained from kinetic energy and its error

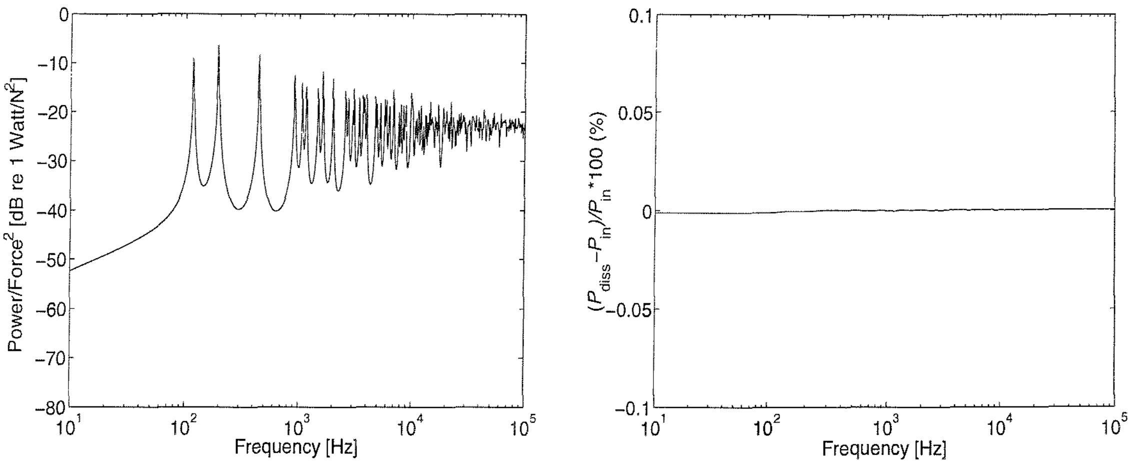

(b) Power obtained from strain energy and its error

Figure 2.8. Comparison of the predicted input power with the dissipated power and the corresponding error calculated from (a) kinetic energy and (b) strain energy for a single plate model (DLF $\eta = 0.01$, $n_{max} = 29$). —, the input power; ---, the dissipated power.

2.3 Coupled plate investigations using DSM

2.3.1 Dynamic stiffness matrix

Assuming a harmonic point force is applied at a transverse edge, a coupled plate system may be analysed by the assembled dynamic stiffness matrix for the system, as shown in Figure 2.9. The plates are assumed to have a common width, to be simply supported along opposite edges and connected along the other edges. The dynamic stiffness matrix of a coupled plate system is derived by assembling the dynamic stiffness matrix of each plate and applying the compatibility and equilibrium conditions at the joint. As for the single plate, the system is analysed for each half-sine order and each frequency separately.

The dynamic stiffness matrix of a coupled plate system, joined at an arbitrary angle, is given by (Appendix B.1),

$$\mathbf{K}_p = \mathbf{T}_p^{\ T}\ \mathbf{K}_{(p1+p2)}\ \mathbf{T}_P, \tag{2.81}$$

where $\mathbf{K}_p$ is a 12 × 12 matrix for the coupled plate system, $\mathbf{K}_{(p1+p2)}$ is a 16 × 16 assembled matrix for the two plates, $p1$ and $p2$, and $\mathbf{T}_p$ is a transformation matrix for plates defined in Appendix B.2, which allows for any angle between the plates and relates the displacements at edge 3 to those at edge 2 (see Figure 2.9).

The forced response is determined by premultiplying $\mathbf{K}_p^{\ -1}$ to the equation $\mathbf{F}_p = \mathbf{K}_p \mathbf{u}_p$, giving

$$\mathbf{u}_p = \mathbf{K}_p^{\ -1}\mathbf{F}_p, \tag{2.82}$$

where the force vector: $\mathbf{F}_p = \mathbf{T}_p^{\ T}\mathbf{F}_{(p1+p2)}$

$$\mathbf{F}_p^{\ T} = \{-S_1, M_1,\ -N_1,\ -T_1, S_2,\ -M_2, N_2, T_2, S_4,\ -M_4, N_4,\ T_4\}, \tag{2.83}$$

and the displacement vector: $\mathbf{u}_p = \mathbf{T}_p^{\ T}\ \mathbf{u}_{(p1+p2)}$

$$\mathbf{u}_p^{\ T} = \{w_1,\ \phi_1,\ u_1,\ v_1,\ w_2,\ \phi_2,\ u_2,\ v_2,\ w_4,\ \phi_4,\ u_4,\ v_4\}. \tag{2.84}$$

The subscript, 1, 2, 3, or 4, corresponds to the transverse edges of the system, as shown in Figure 2.9.

2.3.2 Simulations for two coplanar plates with flexural vibration only

2.3.2.1 Model

The system studied in this section consists of two plates joined at 0 degrees as shown in Figure 2.9. The model is selected to compare the natural frequencies and forced response between a single plate system and a coupled plate system, which have the same width and overall length. For this model, only the flexural vibration is considered.

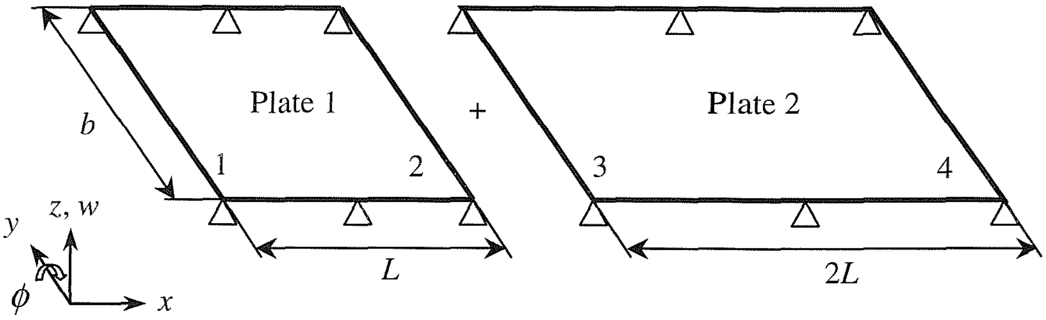

Figure 2.9. Two coplanar plates: width $b = 1.0$ m, length $L = 0.5$ m, thickness $h = 2$ mm, material: aluminium (Young's modulus $E = 7.24\times10^{10}$ N/m^2, Poisson's ratio $\mu = 0.333$, material density $\rho = 2.794\times10^3$ kg/m^3), DLF $\eta = 0.01$.

2.3.2.2 Natural frequencies

The flexural 'frequency functions' (that is $\left(\det\left(\mathbf{K}_{nf}\right)\right)^{-1}$) for a coupled plate system of total length $3L = 1.5$ m and a single plate which has the same dimension, are shown in Figure 2.10. These have been compared to check the accuracy of the analysis and the numerical implementation. In the plot, n presents the number of half-sine waves, from $y = 0$ to $y = b$, in the direction across the plate.

In Figure 2.10 the natural frequencies of a coupled plate system of total length $3L$ show good agreement with those of a single plate of the same overall length, although the magnitudes and shapes of the frequency functions are quite different. The resonances are easier to identify for the single plate system.

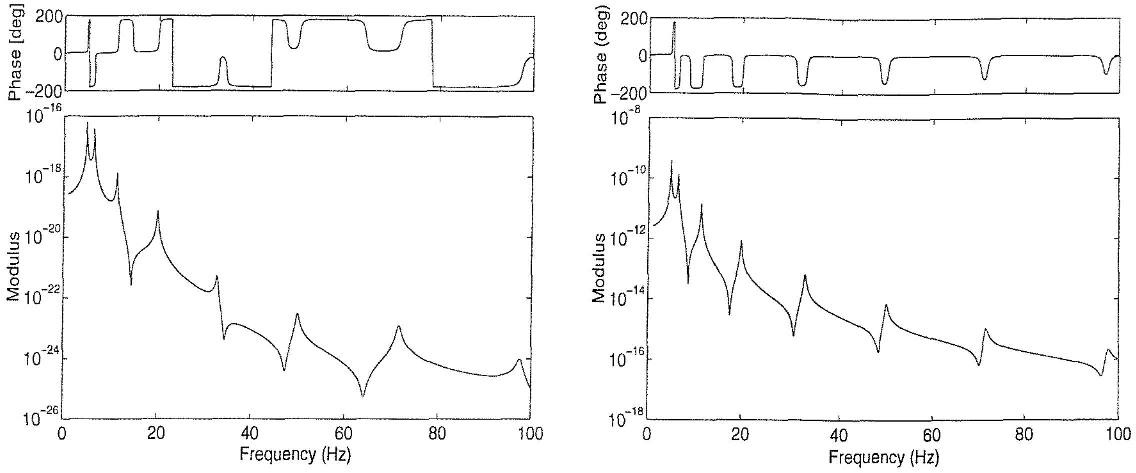

(a) Two plates ($n = 1$)

(b) Single plate ($n = 1$)

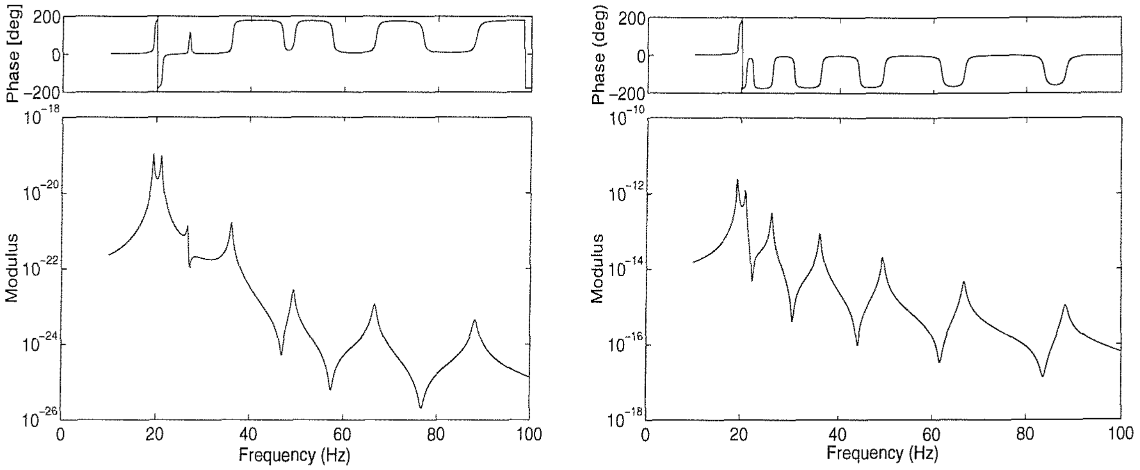

(c) Two plates ($n = 2$)

(d) Single plate ($n = 2$)

Figure 2.10 (a)-(d). The frequency functions (*i.e.* $\left(\det\left(\mathbf{K}_{nf}\right)\right)^{-1}$) of a coupled plate system and a single plate of identical overall dimensions.

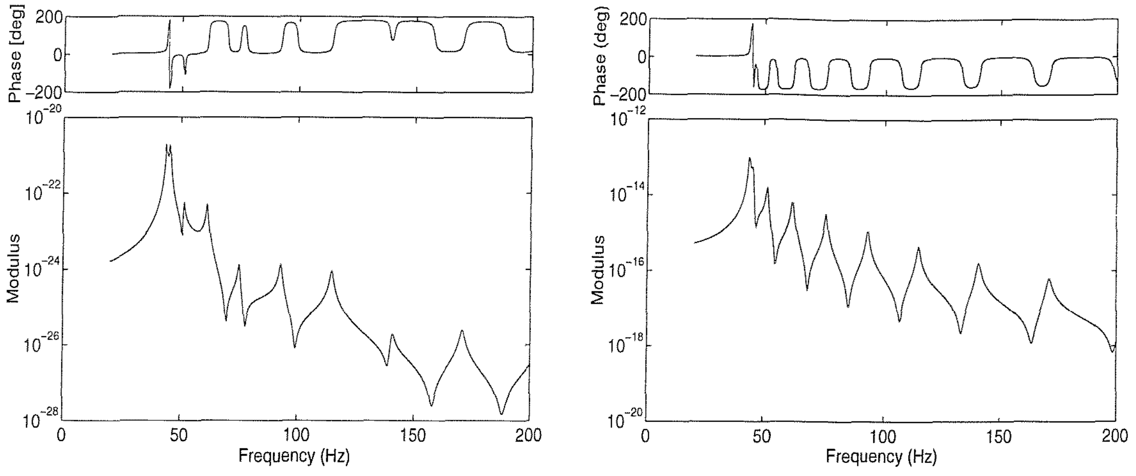

(e) Two plates (n = 3)

(f) Single plate (n = 3)

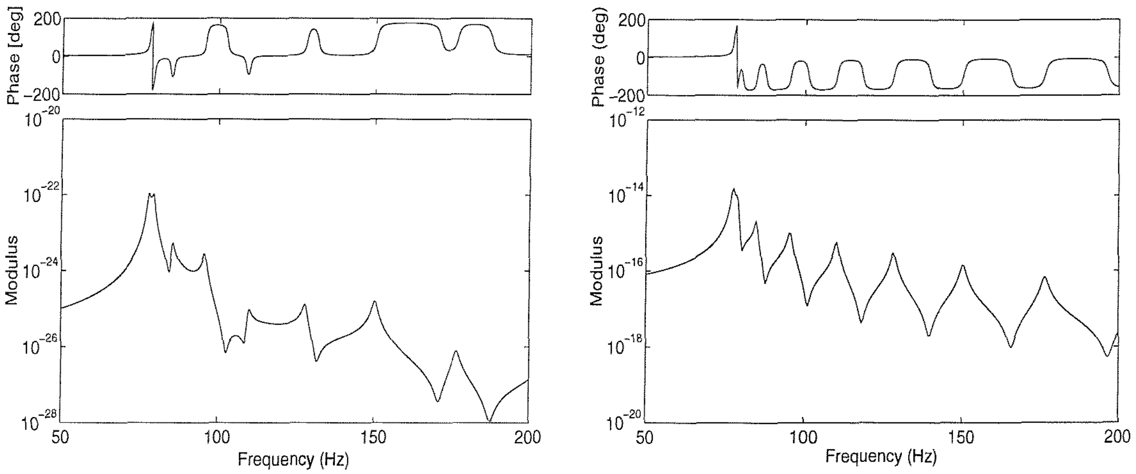

(g) Two plates (n = 4)

(h) Single plate (n = 4)

Figure 2.10 (e)-(h). The frequency functions (*i.e.* $\left(\det\left(\mathbf{K}_{nf}\right)\right)^{-1}$) of a coupled plate system and a single plate of identical overall dimensions.

2.3.2.3 Forced response

Figure 2.11 shows the forced response at the left-hand end, $x = 0$, when a unit amplitude distributed force with a half-sine wave spatial variation is applied at the right-hand edge, $x = 3L$. As expected, the result shows exact agreement between a single plate and a coupled plate system.

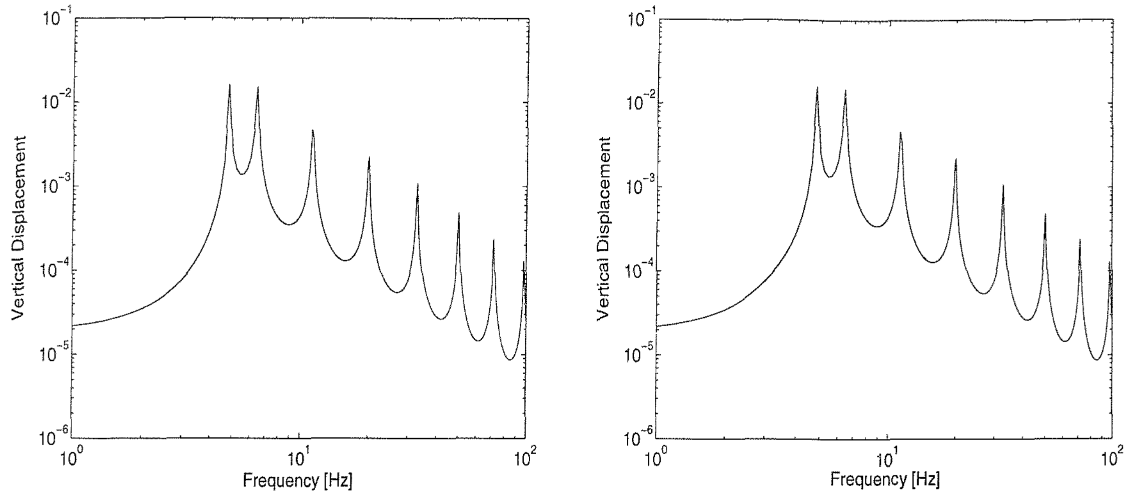

(a) Vertical displacement for two plates (b) Vertical displacement for a single plate

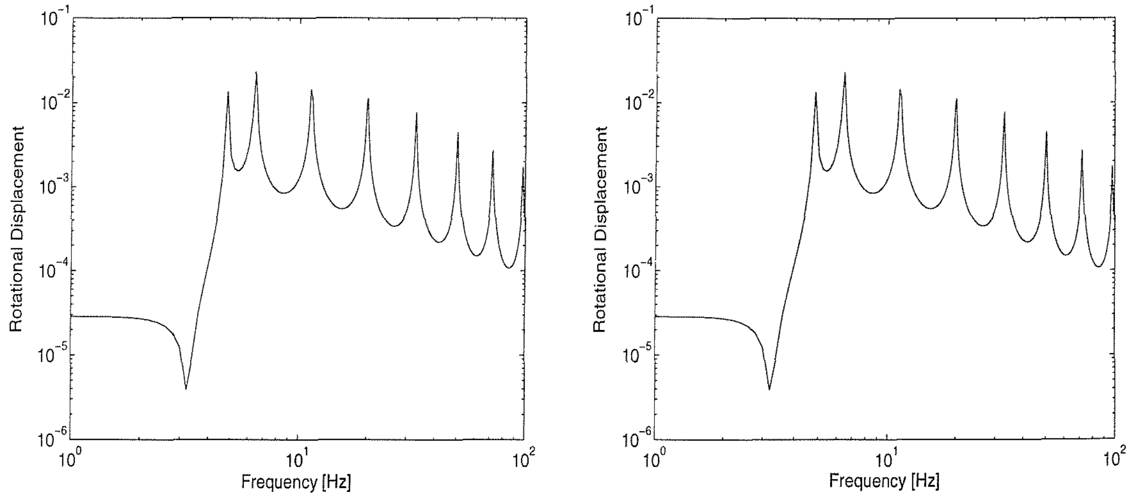

(c) Rotational displacement for two plates (d) Rotational displacement for a single plate

Figure 2.11. Forced response at the left-hand free edge due to a unit amplitude distributed force (n = 1) applied at the right-hand free edge: comparison of two coupled plates and a single plate of the same overall length.

The forced response for a coupled plate system has also been calculated when a unit amplitude force in each half-sine order is applied at the intermediate edge, *i.e.* $x = L$, where plate 1 is connected with plate 2. The vertical displacement is presented in Figure 2.12 and the rotational displacement in Figure 2.13. In this case it is not possible to predict the result using the single plate model.

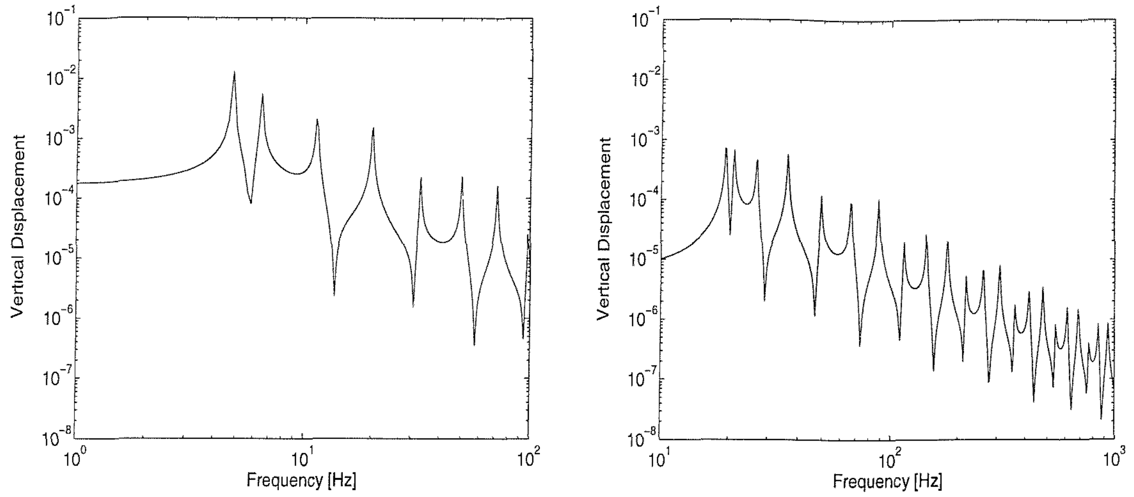

(a) $n = 1$

(b) $n = 2$

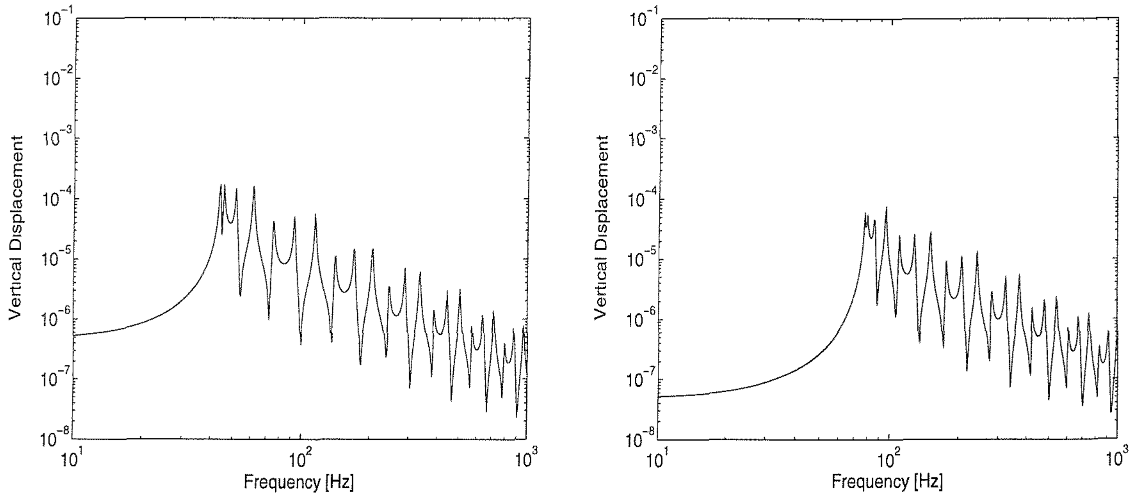

(c) $n = 3$

(d) $n = 4$

Figure 2.12. The vertical displacement for a coupled plate system at the left-hand edge due to a unit amplitude distributed force applied at the intermediate edge.

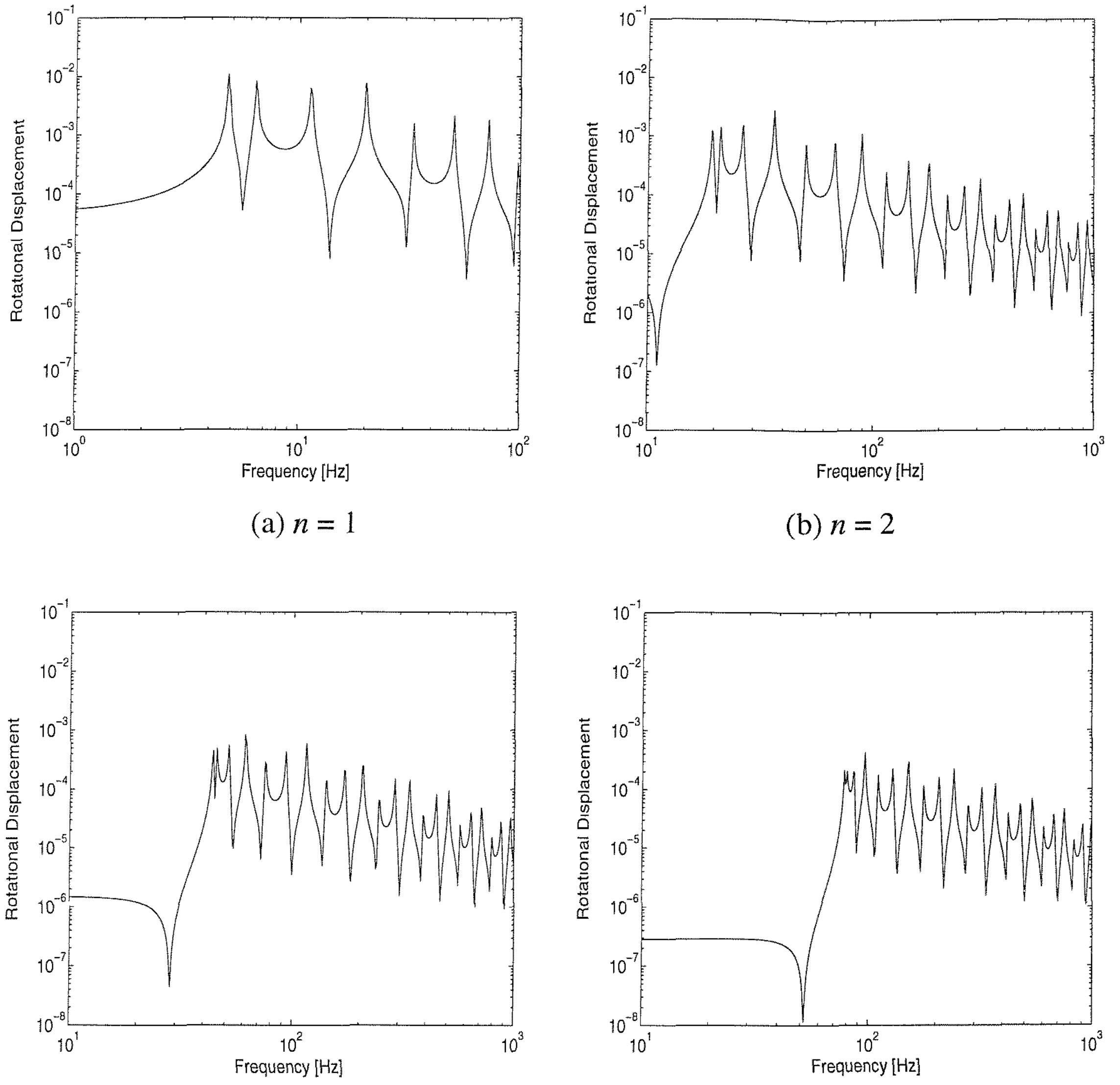

(a) $n = 1$ (b) $n = 2$

(c) $n = 3$ (d) $n = 4$

Figure 2.13. The rotational displacement for a coupled plate system at the left-hand edge due to a unit amplitude distributed force applied at the intermediate edge.

2.3.3 Simulations for two perpendicular plates considering in-plane vibrations

2.3.3.1 Model

The system studied in this section consists of two perpendicular plates, as shown in Figure 2.14, which allow both flexural and in-plane vibrations. It is assumed that the two opposite edges along the longitudinal direction, $y = 0$ and $y = b$, are simply supported and the other edges are free. The model is used to compare the input power due to the excitation with the total dissipated power for the two plates. A point force of amplitude F was applied first at the mid-point of the free edge of plate 1, $x_1 = 0$ and $y = b/2$, and then at the mid-point of the free edge of plate 2, $x_2 = L_2$ and $y = b/2$, in each case perpendicular to the plate surface.

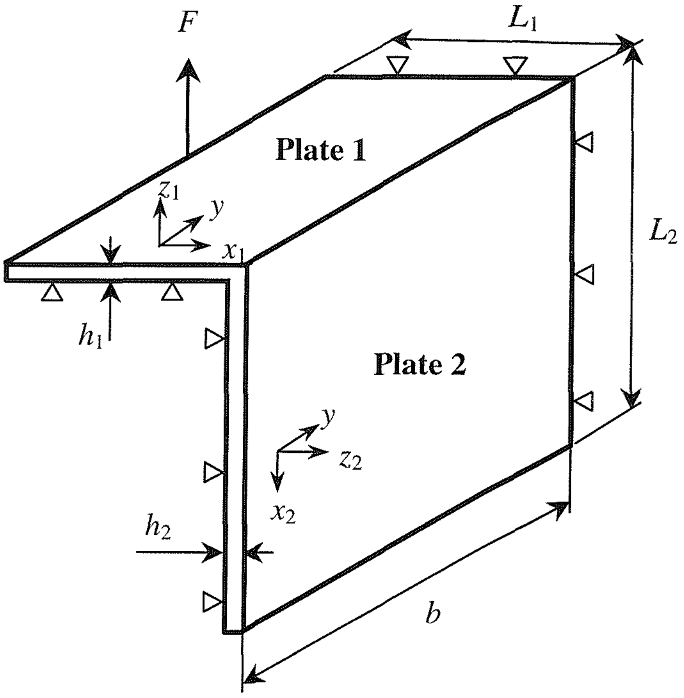

Figure 2.14. Two perpendicular plates: width $b = 200$ mm, length $L_1 = 100$ mm, $L_2 = 200$ mm, thickness $h_1 = h_2 = 3.0$ mm, DLF $\eta = 0.01$, material: aluminium (Young's modulus $E = 7.24\times10^{10}$ N/m^2, Poisson's ratio $\mu = 0.333$, material density $\rho = 2.794\times10^{3}$ kg/m^3).

2.3.3.2 The dissipated power for the receiver plate and the coupling power

The power transmitted from the source plate to the receiver plate, P_{12}, is obtained using modal orthogonality directly from,

$$P_{12} = \frac{1}{2}\mathrm{Re}\left[\sum_{n}\int_{0}^{b} j\omega\left\{F_n^*(y)w_n(y) + M_n^*(y)\phi_n(y) + N_n^*(y)u_n(y) + T_n^*(y)v_n(y)\right\}dy\right] \qquad (2.85)$$

where F_n^*, M_n^*, N_n^* and T_n^* are the complex conjugates of the internal force or moment amplitudes at the interface extracted from the elements of the dynamic stiffness matrix and w_n, ϕ_n, u_n and v_n are the displacement amplitudes at the interface, calculated for each

Fourier component n which includes $\sin(k_n y)$ or $\cos(k_n y)$. The products are integrated along the interface length, and then summed. This coupling power should be equal to the power dissipated in the receiver plate, as the coupling is conservative. The predicted power dissipated by the receiver plate and the coupling power are presented in Figure 2.15. The coupling power for each location of the applied force, on plate 1 or on plate 2, coincides well with the power dissipated by the respective receiver plate. As in Section 2.2.6.6, the error is very small in the range considered.

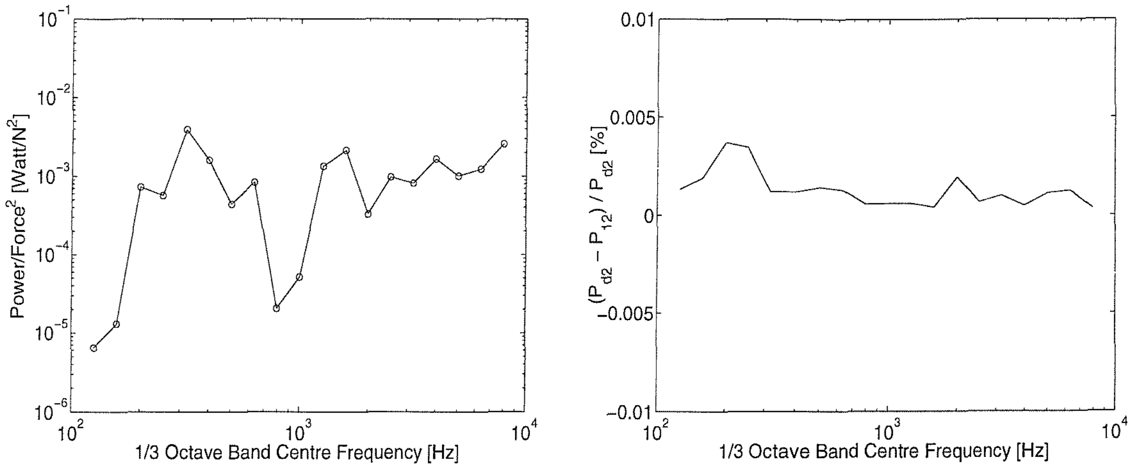

(a) The dissipated power for plate 2 for excitation on plate 1; —, P_{d2}, and the coupling power; -o-, P_{12}, and the error between them.

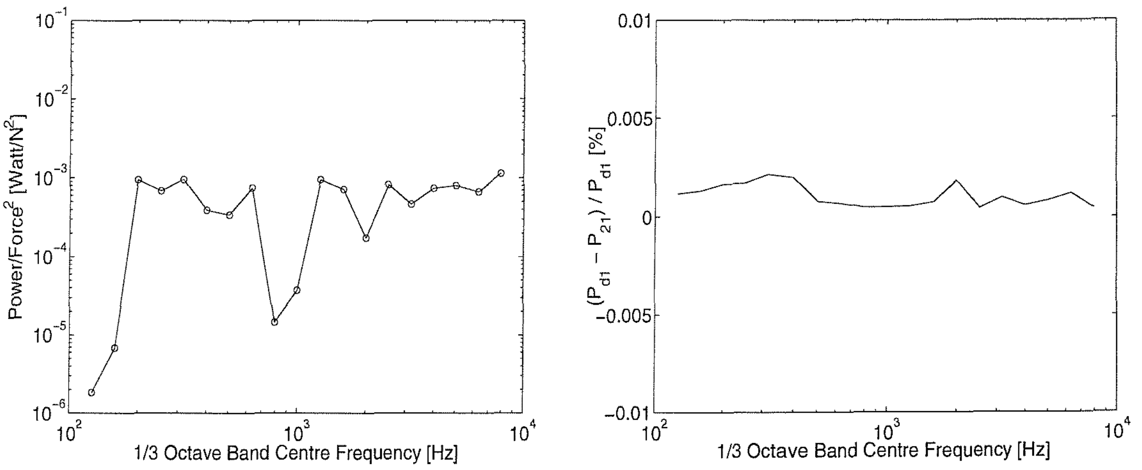

(b) The dissipated power for plate 1 for excitation on plate 2; —, P_{d1}, and the coupling power; -o-, P_{21}, and the error between them.

Figure 2.15. The dissipated power for the receiver plate and the coupling power between two plates.

2.3.3.3 The effect of in-plane vibration

This section describes the results obtained when in-plane motion is included in the full formulation of the dynamic stiffness matrix. For the two perpendicular plates (Figure 2.14), a harmonic force was again applied at the mid-point of the left-hand edge of plate 1 or the right-hand edge of plate 2, in each case in a direction perpendicular to the plate surface. Figure 2.16 shows the ratio of the time-averaged strain energies in the two plates, with and without in-plane motion. From this it can be seen that the inclusion of in-plane motion has only a small effect for the present case. In fact, it is negligible up to the cut-on frequencies of the shear wave propagation for both plates, which are found to be 1970 Hz for plate 1 and 3410 Hz for plate 2 (see equation (2.24); when $k_T > k_n$, λ_{n3} and λ_{n4} correspond to propagating waves). Above these frequencies, a small amount of flexural energy from the source plate is transmitted into in-plane energy in the receiver plate, through their common edge. Although the effect of in-plane vibrations on the two coupled plates considered here is small, it may be important for large structures or multi-plate structures, as investigated by Lyon [83] and Bercin [84].

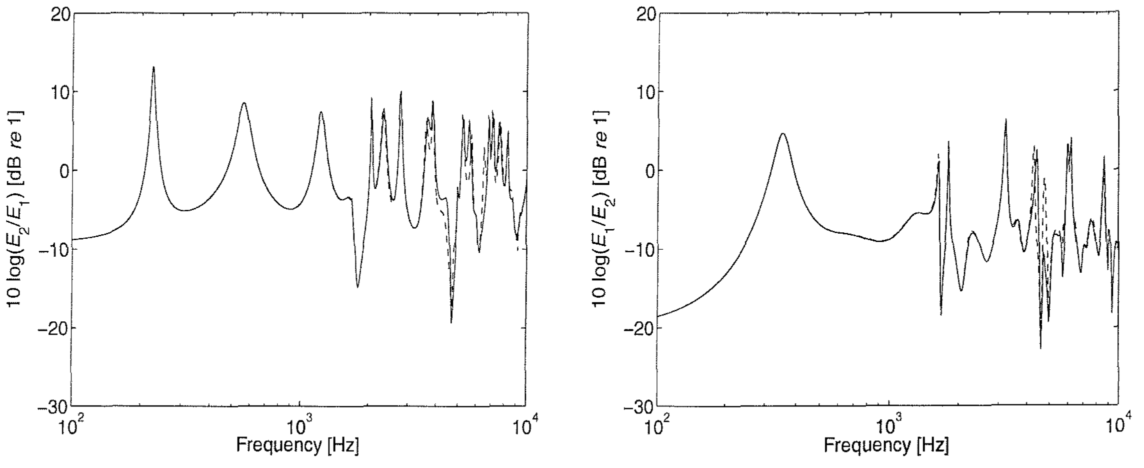

(a) $E_{\text{plate2}} / E_{\text{plate1}}$ (b) $E_{\text{plate1}} / E_{\text{plate2}}$

Figure 2.16. The effect of in-plane motion on the time-averaged strain energy ratio for the perpendicular plates when a harmonic force is applied (a) at the mid-point of the left-hand edge, $x_1 = 0$, of plate 1 and (b) at the mid-point of the right-hand edge, $x_2 = L_2$, of plate 2; —, flexure only; ---; with in-plane.

2.4 Discussion

The dynamic stiffness method provides a means of determining exactly the high frequency behaviour of idealised plate structures. In this chapter, the dynamic stiffness matrices of plates have been derived including flexural and in-plane motion and examples have been presented of single and coupled plates. Natural frequencies have been predicted and compared with analytical results to provide validation of the results of the simulation. Comparisons have been made in terms of natural frequencies and the forced responses between a system comprising a single element and the same system divided into two elements, as validation of the analysis and numerical implementation for the coupled case.

The objective in using the method in this research is to study the power flow in a system of plates. The input power due to excitation by a force has been obtained and the dissipated power has been determined using the strain energy. This provides the tools for a study of coupling between plates in terms of their coupling loss factors which is the next stage of the research. It has been found that significant errors occur in the dissipated power calculation if kinetic energy is used instead of strain energy, particularly at low frequencies.

CHAPTER 3

STATISTICAL ENERGY ANALYSIS FRAMEWORK

3.1 Introduction

This chapter describes the SEA framework and some of the methods used to obtain the CLF. The power flow between two subsystems is discussed and the concept of an 'effective' CLF for a particular realisation of the system is introduced. The effective CLF for a two-plate system is compared with the CLF derived from two semi-infinite plates and the ensemble average result [50]. The influence of damping on the ensemble average CLF is discussed. A theoretical upper and lower bound is presented for the effective CLF from [44], that can be used to evaluate the variability of the CLF.

3.2 Power flow between subsystems

In the SEA approach, a system is modelled in terms of the power which is input, dissipated and transmitted between subsystems. The power balance equations for two conservatively coupled subsystems 1 and 2, excited one at a time, as illustrated in Figure 3.1, can be expressed by [33]

$$\overline{P}^1_{1,\,\mathrm{in}} = \overline{P}^1_{1,\,\mathrm{diss}} + \overline{P}^1_{12} = \omega\left(\eta_1 \overline{E}^1_1 + \eta^1_{12} \overline{E}^1_1 - \eta^1_{21} \overline{E}^1_2\right), \tag{3.1}$$

$$0 = \overline{P}^1_{2,\,\mathrm{diss}} + \overline{P}^1_{21} = \omega\left(\eta_2 \overline{E}^1_2 + \eta^1_{21} \overline{E}^1_2 - \eta^1_{12} \overline{E}^1_1\right), \tag{3.2}$$

$$\overline{P}^2_{2,\,\mathrm{in}} = \overline{P}^2_{2,\,\mathrm{diss}} + \overline{P}^2_{21} = \omega\left(\eta_2 \overline{E}^2_2 + \eta^2_{21} \overline{E}^2_2 - \eta^2_{12} \overline{E}^2_1\right), \tag{3.3}$$

$$0 = \overline{P}^2_{1,\,\mathrm{diss}} + \overline{P}^2_{12} = \omega\left(\eta_1 \overline{E}^2_1 + \eta^2_{12} \overline{E}^2_1 - \eta^2_{21} \overline{E}^2_2\right), \tag{3.4}$$

where P_{in} and P_{diss} are the time-averaged input and dissipated powers, P_{12} ($= -P_{21}$) is the net power transmitted from subsystem 1 to 2, η_1 and η_2 are the DLFs, E_1 and E_2 are the total time-averaged energies, and η_{12} and η_{21} are the coupling loss factors. The superscript, 1 or 2, means the excitation is applied to subsystem 1 or 2 and ' ¯ ' denotes an ensemble-averaged quantity. The 'actual' CLFs are defined in terms of this ensemble average. The equations (3.1)-(3.4) also hold for individual realisations, however, in which case the CLFs are replaced by $\hat{\eta}_{ij}$, the 'effective' CLF.

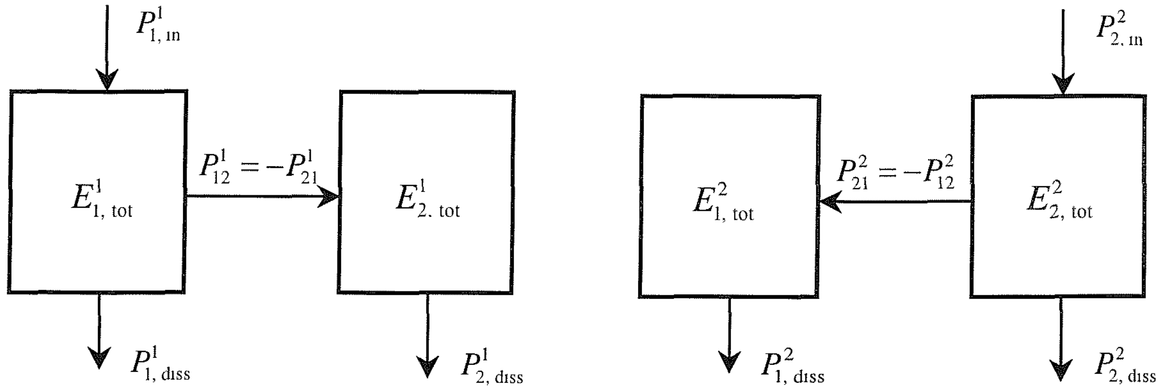

(a) Power input to subsystem 1 (b) Power input to subsystem 2

Figure 3.1. Two subsystem model.

Equations (3.1)-(3.2) and (3.3)-(3.4) can be rearranged to give,

$$\overline{P}^1_{1,in}=\overline{P}^1_{1,diss}+\overline{P}^1_{2,diss}, \tag{3.5}$$

$$\overline{P}^2_{2,in}=\overline{P}^2_{1,diss}+\overline{P}^2_{2,diss}. \tag{3.6}$$

Whereas equations (3.1)-(3.4) assume that power flow between subsystems is proportional to the difference in average modal energy, equations (3.5) and (3.6) are always correct and do not assume any relationships between the transmitted power and the average subsystem energies. Accordingly, the input power for each subsystem is equal to the sum of the dissipated powers for the two subsystems. As power is input to only one subsystem at a time, the net coupling powers are equal to the dissipated powers of the receiver subsystems.

$$\overline{P}^1_{12}=\overline{P}^1_{2,diss}, \tag{3.7}$$

$$\overline{P}^2_{21}=\overline{P}^2_{1,diss}. \tag{3.8}$$

Equations (3.1)-(3.4) can be used to obtain the CLFs if the input powers and subsystem energies are known. In general $\eta^1_{ij}\neq\eta^2_{ij}$. It might be expected that the four equations would allow solution for these four unknowns (if η_1 and η_2 are known). However equations (3.1)-

(3.4) are not linearly independent in η_{ij}^{i}. It has therefore been necessary to make the usual SEA assumption that $\eta_{ij}^{1} = \eta_{ij}^{2}$. Moreover it is usually assumed that the CLFs are related to one another by the consistency relation

$$n_1\,\eta_{12} = n_2\,\eta_{21} \tag{3.9}$$

where n_1 and n_2 are the asymptotic modal densities of the subsystems. This is derived from a fundamental assumption in SEA, that the coupling power is proportional to the difference in average modal energy, *i.e.* $P_{12} \propto \omega(E_1/n_1 - E_2/n_2)$, the constant of proportionality being $n_1\,\eta_{12}$ [85]. However, in the present work equation (3.9) will not usually be assumed to hold.

3.3 The effective CLF

If the time-averaged input power, the time-averaged energy and the DLF for both subsystems are known for a particular realisation, the 'effective' CLF $\hat{\eta}_{ij}$ may be evaluated by using the power balance equations (3.1) and (3.3) (assuming $\hat{\eta}_{ij}^{1} = \hat{\eta}_{ij}^{2}$)

$$\begin{Bmatrix} \hat{\eta}_{12} \\ \hat{\eta}_{21} \end{Bmatrix} = \frac{1}{\omega} \begin{bmatrix} E_1^1 & -E_2^1 \\ -E_1^2 & E_2^2 \end{bmatrix}^{-1} \begin{Bmatrix} P_{1,\mathrm{in}}^1 - \omega\eta_1 E_1^1 \\ P_{2,\mathrm{in}}^2 - \omega\eta_2 E_2^2 \end{Bmatrix}. \tag{3.10}$$

From equations (3.5)-(3.8), the right-hand terms of equation (3.10) are equivalent to

$$P_{1,\mathrm{in}}^1 - \omega\eta_1 E_1^1 = P_{1,\mathrm{in}}^1 - P_{1,\mathrm{diss}}^1 = P_{12}^1 = P_{2,\mathrm{diss}}^1 \tag{3.11}$$

and

$$P_{2,\mathrm{in}}^2 - \omega\eta_2 E_2^2 = P_{2,\mathrm{in}}^2 - P_{2,\mathrm{diss}}^2 = P_{21}^2 = P_{1,\mathrm{diss}}^2\,. \tag{3.12}$$

Therefore the 'effective' CLF for a particular realisation of the system is given by

$$\begin{Bmatrix} \hat{\eta}_{12} \\ \hat{\eta}_{21} \end{Bmatrix} = \frac{1}{\omega} \begin{bmatrix} E_1^1 & -E_2^1 \\ -E_1^2 & E_2^2 \end{bmatrix}^{-1} \begin{Bmatrix} \omega\eta_2 E_2^1 \\ \omega\eta_1 E_1^2 \end{Bmatrix}. \tag{3.13}$$

This is the same concept as performing 'experimental' SEA based on the power injection method [57]. Alternatively, exciting only one subsystem and using the consistency relation (3.9), the CLF can be obtained from

$$\hat{\eta}_{12}=\frac{P_{12}}{\omega\left\{E_1-\frac{N_1}{N_2}E_2\right\}} \text{ or } \hat{\eta}_{12}=\frac{P_{12}}{\omega\left\{E_1-\frac{n_1(\omega)}{n_2(\omega)}E_2\right\}} \qquad (3.14), (3.15)$$

where N_1 and N_2 are the actual numbers of modes in a given frequency band and $n_1(\omega)$ and $n_2(\omega)$ are the asymptotic modal densities. For example, the modal density of a simply supported uniform isotropic plate can be approximated as [48]

$$n(\omega)=\left(\frac{S}{4\pi}\right)\left(\frac{\rho h}{D}\right)^{1/2} \qquad (3.16)$$

where S is the area of plate, ρ is the material density, h is the thickness of plate and $D\left(=Eh^3/12(1-\mu^2)\right)$ is the flexural rigidity. It can be expected that equations (3.13)-(3.15) will give different estimates of $\hat{\eta}_{ij}$. Equation (3.13) is the more general but involves a greater amount of calculation. This is considered in Chapter 4, where numerical simulations are presented.

3.4 Analytical CLF estimates from semi-infinite structures

The CLF in SEA is traditionally obtained by the travelling wave approach from semi-infinite structures. It is assumed that the source subsystem is reverberant, the transmission efficiency is much smaller than unity, and the incident fields are diffuse. For two-dimensional subsystems coupled along a line, the CLF can be estimated from analytical results for the transmission efficiency, or power transmission coefficient, $\tau_{ij,\,d}$, which is the ratio of transmitted power to incident power at the boundary [48]

$$\eta_{ij\infty}=\frac{c_{gi}b\tau_{ij,d}}{\pi\omega S_i} \qquad (3.17)$$

where c_{gi} is the group velocity of the source subsystem i, b is the junction length, and S_i is the surface area of the source subsystem. If the incident wave is a bending wave on a homogeneous thin plate then the group velocity $c_g = 2c_b$, where c_b is the phase velocity of the bending wave. Equation (3.17) can be derived from the definition of the transmitted power and the power flow between two semi-infinite plates [86]. This CLF may be corrected by multiplying it by a factor of $2/(2-\tau)$, as investigated in [86, 87]. This is to allow for the difference between the incident and reflected amplitudes on a semi-infinite plate when τ is large. An example is presented in Section 4.2.4. It was discussed in [87] that there are a number of different expressions for the relationship between the transmission efficiency and the CLF, and the relation remains uncertain.

The transmission efficiency $\tau_{ij,\,d}$ in equation (3.17) is the angular averaged value. In SEA it is usually assumed that a diffuse field is present in each subsystem, so the energy is equally likely to be incident on the boundary at any angle. Then the incident power is given by

$$P_{inc\;d} = \int_0^{\pi/2} \cos\theta P_{inc}(\theta)d\theta = P_{inc}(\theta)\int_0^{\pi/2} \cos\theta d\theta = P_{inc}(\theta) \tag{3.18}$$

where $P_{inc}(\theta)$ is the power incident from angle θ, which is a constant independent of θ. Similarly the transmitted power is given by

$$P_{ij,d} = \int_0^{\pi/2} \tau_{ij}(\theta)\cos\theta\, P_{inc}(\theta)\,d\theta = P_{inc}(\theta)\int_0^{\pi/2} \tau_{ij}(\theta)\cos\theta\, d\theta \tag{3.19}$$

where $\tau_{ij}(\theta)$ is the transmission efficiency for angle θ. Hence

$$\tau_{ij,d} = \int_0^{\pi/2} \tau_{ij}(\theta)\cos\theta\, d\theta \tag{3.20}$$

where θ is the angle of incidence. The transmission efficiency $\tau_{ij}(\theta)$ for two plates joined at right angles, neglecting in-plane motion, is given by [48]

$$\tau_{ij}(\theta) = \frac{2\psi\sqrt{\chi^2 - s^2}\sqrt{1-s^2}}{\psi^2 + \psi\left(\sqrt{\chi^2 + s^2}\sqrt{1+s^2} + \sqrt{\chi^2 - s^2}\sqrt{1-s^2}\right) + \chi^2} \tag{3.21}$$

where $s = \sin\theta$ and, if the plates have identical material properties, $\chi = \sqrt{h_1/h_2}$ and $\psi = (h_2/h_1)^2$. Numerical integration of this expression yields $\tau_{ij,\,d}$. Reference [49] gives an approximate formula for the angular averaged transmission efficiency $\tau_{ij,\,d}$ expressed in terms of the transmission loss, $R_{ij} = -10\log_{10}(\tau_{ij\;d})$:

$$R_{12} \simeq 20\log_{10}\left(\sqrt{\frac{\chi}{\psi}} + \sqrt{\frac{\psi}{\chi}}\right) + C_1 + \frac{C_2}{\chi} + C_3\log_{10}\left(1 + \frac{1}{\chi^4}\right) \quad \text{for } \chi \geq 1 \tag{3.22a}$$

$$R_{21} \simeq 20\log_{10}\left(\sqrt{\frac{\chi}{\psi}}+\sqrt{\frac{\psi}{\chi}}\right)+C_1+C_2\chi+C_3\log_{10}\left(1+\chi^4\right) \quad \text{for } \chi \le 1 \qquad (3.22b)$$

where $C_1 = -2.0053$, $C_2 = 0.2535$ and $C_3 = 1.56$. For $\chi \le 1$, the angular averaged transmission efficiency $\tau_{12,d}$ is obtained from equation (3.22b) and $\tau_{12,d} = \chi\tau_{21,d}$ [86]. According to [49], the approximate transmission efficiency agrees with the integral (3.20) of equation (3.21) to within 0.03 dB for $0.01 \le \chi \le 100$.

3.5 Ensemble average CLF

The CLF estimates $\eta_{ij\infty}$ determined from the transmission efficiency for semi-infinite subsystems, are usually taken as representative of ensemble averages of the CLF for finite subsystems. However, this is only valid where the subsystems are weakly coupled and exhibit a diffuse field. It has been shown that, when the average modal overlap is smaller than unity, the predicted CLFs fall below the semi-infinite results [42]. The modal overlap factor, a parameter generally used in SEA, is given by

$$M = \eta\omega n(\omega) \qquad (3.23)$$

where $n(\omega)$ is the modal density of the subsystem. The modal overlap factor is sometimes used as a measure of whether the response may be considered diffuse. The 'coupling strength', on the other hand, is normally defined by the ratio of the CLF to the DLF of the source subsystem [88].

The ensemble average CLF can be obtained from the traditional SEA formulations in equation (3.15), as the coupling power and energies are defined in terms of the ensemble average quantities. The ensemble average coupling and input powers for a system comprising two simply supported, rectangular, edge-coupled plates, was expressed by Wester and Mace by using the wave approach [50]. The analysis results of energy flow using the wave approach can be exact, except for the neglect of the nearfield effects. The total response of the plates was expressed as the sum of wave components, for which the system may be regarded as a dynamically 'one-dimensional' system [45]. The following assumptions were made concerning the ensemble [50]; (i) variations over the ensemble in the properties of the plates, the coupling and the excitation are taken to be statistically independent, (ii) the energies and powers of interest are taken to be constant over the ensemble, and (iii) the lengths of the plates are large compared with the bending wavelengths.

By this analysis Wester and Mace [50] derived a more general expression for the ensemble average CLF of two connected rectangular plates,

$$\eta_{ij,ens}=\eta_{ij\infty}\Bigg/\left[\left(\frac{1}{k_i}\int_0^{\min(k_i,k_j)}\frac{\tau_{ij}(k_s)/\tau_{ij\,d}}{\sqrt{1+\gamma^2(k_s)}\sqrt{1+\delta^2(k_s)}}dk_s\right)^{-1}-\frac{\tau_{ij,d}}{\pi\mu_{i0}}\left(1+\frac{k_i\mu_{i0}}{k_j\mu_{j0}}\right)\right] \tag{3.24}$$

where k_i and k_j are the free wavenumbers of plates i and j, $\mu_{i0}=k_iL_i\eta_i/2$ and $\mu_{j0}=k_jL_j\eta_j/2$ are the limiting subsystem 'reflectances' for small trace wavenumber k_s. $\tau_{ij}(k_s)$ corresponds to $\tau_{ij}(\theta)$ in equation (3.21) for $\sin\theta=k_s/k_i$. Two coupling parameters, γ and δ, are defined in [50]

$$\gamma^2=\frac{\tau(k_s)\cosh^2(\mu_d)}{\sinh(\mu_i)\sinh(\mu_j)}\ \text{and}\ \delta^2=\frac{\tau(k_s)\sinh^2(\mu_d)}{\sinh(\mu_i)\sinh(\mu_j)} \tag{3.25}$$

where $\mu_i\approx\mu_{i0}/\sqrt{1-(k_s/k_i)^2}$, $\mu_j\approx\mu_{j0}/\sqrt{1-(k_s/k_j)^2}$ and $\mu_d=(\mu_i-\mu_j)/2$.

The ensemble average CLF was obtained from equation (3.24), irrespective of the coupling strength. The qualitative features of the strength of coupling were examined by evaluating equation (3.24) for the weak and strong coupling limits of the CLF. For weakly coupled plates ($\gamma\ll1$ and $\delta\ll1$), equation (3.24) approximates to

$$\eta_{ij,ens}\approx\eta_{ij\infty}\Bigg/\left[1-\frac{\tau_{ij\,d}}{\pi\mu_{i0}}\left(1+\frac{k_i\mu_{i0}}{k_j\mu_{j0}}\right)\right]. \tag{3.26}$$

In the weak coupling limit, $\tau_{ij\,d}/\mu_{i0}$ approach zero, so that $\eta_{ij,ens}\approx\eta_{ij\infty}$. It was shown using a numerical example, comprising plates of nominally identical material and thickness, that $\eta_{ij,ens}\approx\eta_{ij\infty}$ for large reflectances for which the plates are weakly coupled. For smaller reflectances it was shown that, $\eta_{ij,ens}\ll\eta_{ij\infty}$. The subsystem base reflectance μ_{i0}, was suggested [50] as a more relevant parameter for describing coupling strength and indicating the accuracy of the CLF estimate $\eta_{ij\infty}$, rather than the modal overlap factor, for plate systems assumed to be wide.

As an example, a two-plate system is considered here with thicknesses $h_1 = 3$ mm and $h_2 = 2$ mm, lengths $L_1 = 0.5$ m and $L_2 = 1$ m, width $b = 1$ m, damping $\eta_1 = \eta_2 = 0.1$ and material properties of aluminium. The ensemble average CLF $\eta_{ij,\,ens}$, the CLF for two semi-infinite plates $\eta_{ij\infty}$ and the effective CLF $\hat{\eta}_{ij}$ calculated using DSM for this two-plate system, which is presented in Chapter 4, are compared in Figure 3.2. Two arrows in Figure 3.2 indicate frequencies at which the modal overlap factors of the two individual plates equal 1.

At low frequencies, the ensemble average CLFs are lower than the semi-infinite results $\eta_{ij\infty}$ since the coupling is strong [41]. The effective CLFs fluctuate considerably relative to the ensemble average CLF $\eta_{ij,\,ens}$. These CLFs all coincide closely at high frequencies, where the modal overlap is high.

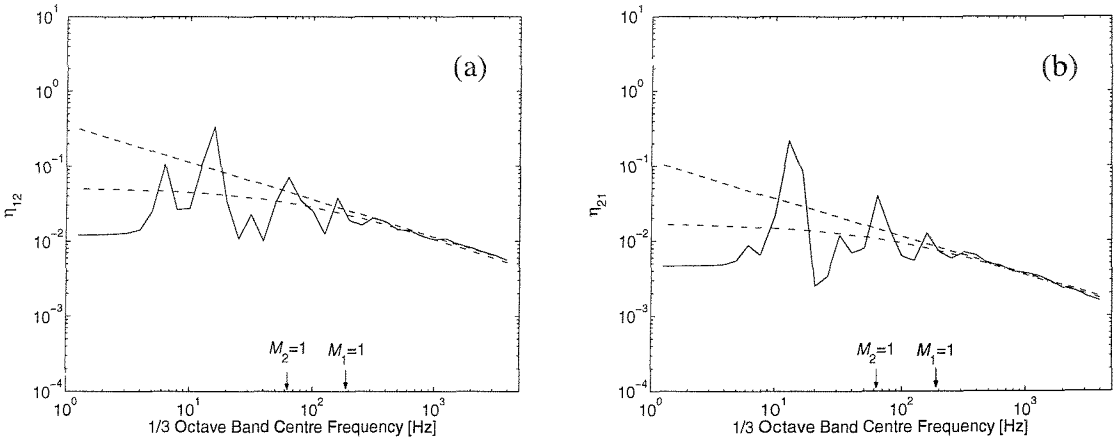

Figure 3.2. Various estimates of CLF, (a) η_{12} and (b) η_{21}, for a two-plate system ($h_1 = 3$ mm, $L_1 = 0.5$ m, $h_2 = 2$ mm, $L_2 = 1$ m, $b = 1$ m, $\eta_1 = \eta_2 = 0.1$, material: aluminium). ---, from equation (3.17) for semi-infinite plates $\eta_{ij\infty}$; -·-, ensemble average $\eta_{ij,\,ens}$; —, 'effective' CLF $\hat{\eta}_{ij}$. Two arrows indicate frequencies at which the modal overlap factors of the two plates equal 1.

Figure 3.3 shows the influence of damping on the ensemble average CLF. Here the damping of the source plate, the receiver or both plates is varied. The values considered for the DLFs are 0.001, 0.01 and 0.1. As the damping of the source plate or the receiver increases, the ensemble average CLF increases in the low frequency region. The spread of results at low frequency indicates that approximately $\eta_{ij,\,ens} \propto \sqrt{\eta_{source}}$, and $\eta_{ij,\,ens} \propto \sqrt{\eta_{receiver}}$. A change by a factor of 100 in the individual loss factors leads to a factor of about 10 in $\eta_{ij,\,ens}$. Comparing the upper and middle graphs of Figure 3.3 it can be seen that $\eta_{receiver}$ has slightly more effect than η_{source}. When both DLFs are changed simultaneously, this causes a proportional change in $\eta_{ij,\,ens}$ at low frequency, as shown in the lower figures.

3.6 Previously published upper and lower limits for CLF

As seen above, for a finite structure, η_{ij} will differ from $\eta_{ij\infty}$ and, for a particular realisation of a structure, $\hat{\eta}_{ij}$ will differ from η_{ij}, particularly at low modal overlap. Craik *et al.* [44] observed that the fluctuations with frequency at low modal overlap in the energy level difference, which is related to the CLF, closely match the fluctuations in the spatially-averaged point mobility relative to the predicted mobility for an infinite subsystem. An empirical expression for the fluctuations in the CLF at any frequency is given in [44] without derivation as

$$\frac{\hat{\eta}_{12}}{\eta_{12\infty}} = \frac{\mathrm{Re}(Y_2)}{\mathrm{Re}(Y_{2\infty})}, \tag{3.27}$$

where $\eta_{12\infty}$ is the CLF derived from semi-infinite structures, Y_2 is the spatially-averaged point mobility of the receiver subsystem and $Y_{2\infty}$ is the point mobility of the equivalent infinite system.

The modal density can be expressed by [33]

$$n(\omega) = 2m\,\mathrm{Re}(Y_\infty)/\pi \tag{3.28}$$

where m is the total mass. The consistency relationship (3.9) can thus be written as

$$\eta_{12}\,\mathrm{Re}\left(Y_{1\infty}\right)m_1 = \eta_{21}\,\mathrm{Re}\left(Y_{2\infty}\right)m_2. \tag{3.29}$$

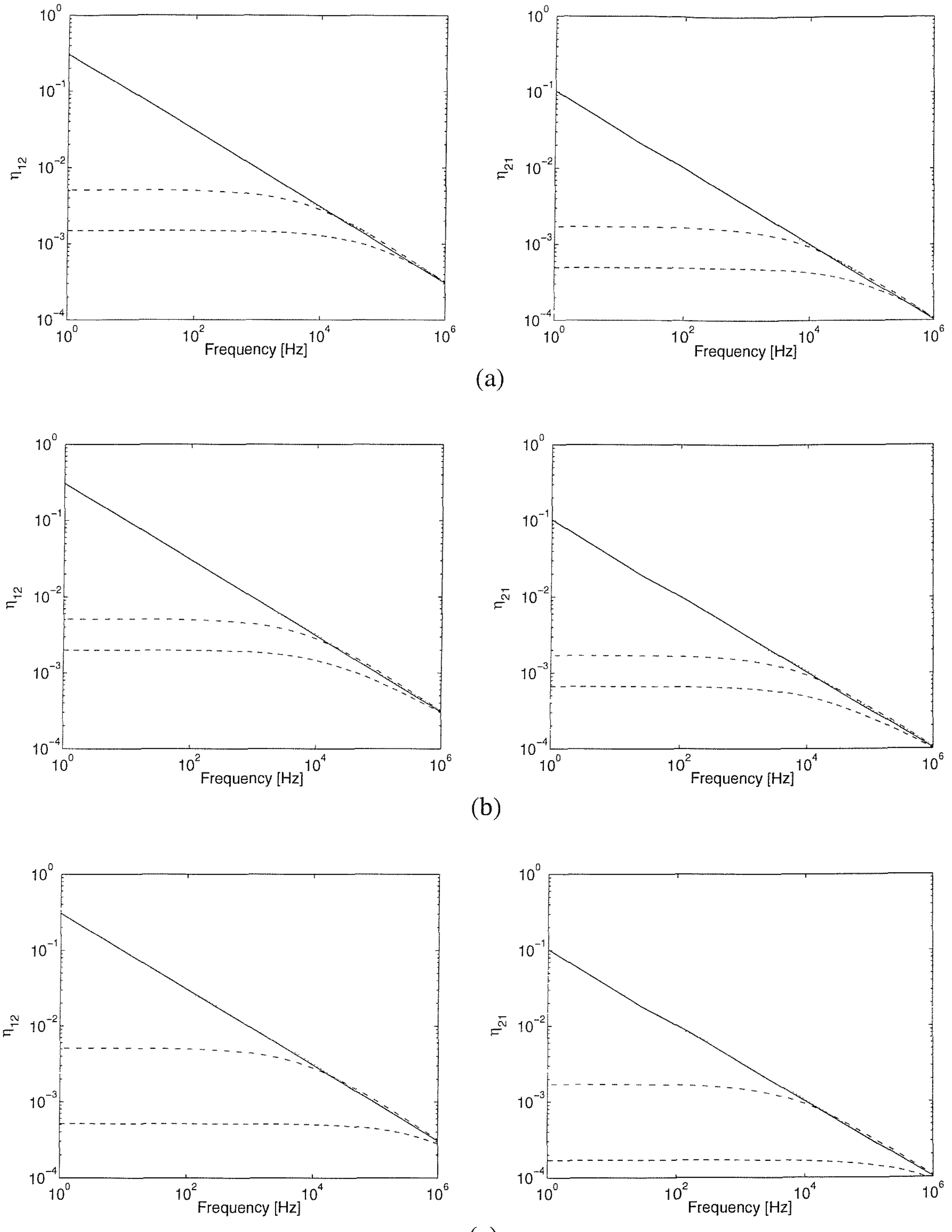

(a)

(b)

(c)

Figure 3.3. The influence of damping on the ensemble average CLF $\eta_{ij,ens}$ for the two-plate system described in Figure 3.2: (a) η_{source} is fixed as 0.01 and η_{receiver} is varied (---, 0.001; -·-, 0.01; ·····, 0.1), (b) η_{receiver} is fixed as 0.01 and η_{source} is varied (---,0.001; -·-, 0.01; ·····, 0.1) and (c) $\eta_{\text{source}} = \eta_{\text{receiver}}$ are varied (---, 0.001; -·-, 0.01; ·····, 0.1); —, semi-infinite plate result $\eta_{ij\infty}$.

The real part of the spatially-averaged point mobility can be found by summing the contribution from all modes given as [33, 48]

$$\operatorname{Re}(Y(\omega))=\sum_{i}\left[\omega_i\eta m\left\{1+\left(\frac{\omega_i}{\omega}-\frac{\omega}{\omega_i}\right)^2\frac{1}{\eta^2}\right\}\right]^{-1} \tag{3.30}$$

where ω_i is the resonance frequency of the ith mode and use is made of the fact that the modal masses for a plate are all equal. If the response is dominated by a single mode, the peak mobility $\hat{Y}$, where ω equals ω_i, is given by

$$\hat{Y}=\frac{1}{\omega_i\eta m} \tag{3.31}$$

which is a real quantity.

Thus the ratio of the peak mobility for a finite system $\hat{Y}$ to the real part of the mobility for the equivalent infinite system Y_∞ is obtained from equations (3.28) and (3.31)

$$\frac{\hat{Y}}{\operatorname{Re}(Y_\infty)}=\frac{2}{\pi\omega_i\eta n(\omega)}=\frac{2}{\pi M} \tag{3.32}$$

where M is the modal overlap factor as defined in equation (3.23). This expression gives the height of the resonance maxima above the characteristic mobility (defined as the geometric mean between the resonance peaks and the anti-resonance minima) as given by [59, 89].

For a frequency band, the maximum value of the frequency averaged mobility $<\hat{Y}>$ can be approximated by [48]

$$\left\langle\hat{Y}\right\rangle=\frac{1}{m\Delta\omega}\tan^{-1}\left(\frac{\Delta\omega}{\eta\omega_i}\right) \tag{3.33}$$

where $\Delta\omega$ is the width of the frequency band. When $\Delta\omega/\eta\omega_i$ is very small (high damping, low frequency, or a narrow frequency band for the analysis), then $<\hat{Y}>/\operatorname{Re}(Y_\infty)$ is the same as equation (3.32). However, if $\Delta\omega/\eta\omega_i$ is large (such as for a one-third octave band containing many modes), $\tan^{-1}(\Delta\omega/\eta\omega_i)$ is approximately $\pi/2$, and then

$$\frac{\langle \hat{Y} \rangle}{\mathrm{Re}(Y_\infty)} = \frac{1}{n\Delta\omega} = \frac{1}{N} \tag{3.34}$$

where N is the number of modes in a specific frequency band.

The minimum value for the mobility has been given by [39, 59], considering the contributions of all mode pairs,

$$\frac{\breve{Y}}{\mathrm{Re}(Y_\infty)} = \frac{1}{\beta} \tag{3.35}$$

where

$$\beta = \frac{2}{\pi\eta\omega}\frac{d\omega}{dN} = \frac{2}{\pi M}. \tag{3.36}$$

If we consider a two-mode approximation, this anti-resonance mobility becomes

$$\breve{Y} = \frac{\mathrm{Re}(Y_\infty)}{\beta}\frac{8}{\pi^2} = \mathrm{Re}(Y_\infty)\frac{4M}{\pi}. \tag{3.37}$$

From equations (3.27), (3.34) and (3.37), therefore, Craik *et al.* [44] estimate the upper and lower limits for the ratio of the actual CLF to the semi-infinite result as

$$\frac{(\hat{\eta}_{ij})_{\max}}{\eta_{ij\infty}} = \frac{1}{N}, \tag{3.38}$$

and

$$\frac{(\hat{\eta}_{ij})_{\min}}{\eta_{ij\infty}} = \frac{4M}{\pi}. \tag{3.39}$$

These estimates for the upper and lower limits are compared in Chapter 5 with the effective CLFs for simulations on a two-plate system. In Chapter 6 two previously published models by Mohammed [43] and Lyon and DeJong [33], as described in Section 1.2.1.3, are also compared with the variability of the effective CLFs obtained from simulations for the two rectangular plates.

CHAPTER 4

ANALYTICAL MODELS FOR COUPLING BETWEEN TWO PLATES

4.1 Introduction

In the previous chapters, the dynamic response of a single plate and two coupled plates were theoretically predicted using the DSM, and various methods to evaluate the CLF, which is used in SEA to define the transmission of energy from one subsystem to another, were described.

The use of SEA to predict the response of vibro-acoustic systems relies on good estimates of the DLFs of subsystems and the CLFs between them. Damping is usually estimated from measurement data, whilst the CLFs are normally the parameters that are difficult to evaluate either analytically, numerically or experimentally. The 'actual' CLF is defined in terms of an ensemble average and as such it is not uncertain once this ensemble of systems is defined. Usually theoretical estimates of the CLF, based on the wave transmission between infinite subsystems, are used (see Section 3.4). The CLF estimates determined from the wave transmission are taken as representative of ensemble averages of finite subsystems. However, the CLF obtained from the wave approach generally overestimates the actual transmission of energy at low frequencies or low modal overlap (see Figure 3.2). Significant fluctuations with frequency are also observed in this low frequency region. These fluctuations are in part due to the particular realisation of the subsystems within the notional ensemble. Underlying the fluctuations are the modal properties of the subsystems, which can be described in terms of both modal density and modal overlap.

This chapter describes the use of various analytical models to evaluate the CLFs and to investigate the influence of the modal behaviour of the source or receiver plate or both. The models considered are (i) two finite rectangular plates coupled along a line, (ii) a semi-infinite source plate coupled to a finite receiver, and (iii) a finite source plate coupled to a semi-infinite receiver. The effect of damping on the fluctuations of the effective CLFs is also examined. A model of two semi-infinite plates of finite width is also introduced to investigate the effect of the finite width compared with the results for coupled semi-infinite plates of infinite width.

4.2 Coupling between two finite plates of the same width

Two finite rectangular plates of the same width coupled along a common edge can be modelled using the DSM as discussed in Chapter 2. To model a harmonic point force applied inside one plate, the source plate is separated into two parts at the longitudinal position of the applied force, as shown in Figure 4.1. Actually one considers this system as consisting of three plates, two directly excited plates and one receiver plate.

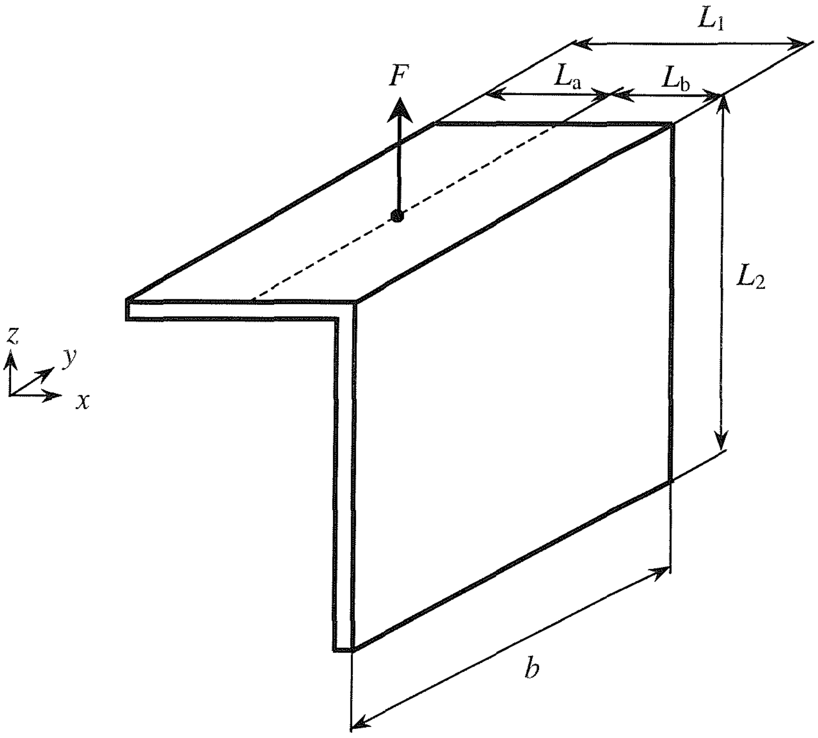

Figure 4.1. Two perpendicular plates with a point force F applied inside one plate: width $b = 1.0$ m, length $L_1 = 0.5$ m, $L_2 = 1.0$ m, thickness $h_1 = 3.0$ mm, $h_2 = 2.0$ mm, DLF $\eta_1 = \eta_2 = 0.1$, material: aluminium (Young's modulus $E = 7.24\times10^{10}$ N/m^2, Poisson's ratio $\mu = 0.333$, material density $\rho = 2794$ kg/m^3).

The global dynamic stiffness matrix of this system can be assembled as described in Chapter 2. This model has been used to evaluate the effective CLF and the confidence intervals and to perform various parameter studies. In these calculations the point force is located at a range of different positions to simulate 'rain-on-the-roof' excitation. For each forcing point the source plate has to be subdivided at the corresponding lengthwise x coordinate.

4.2.1 The sensitivity to number and location of forcing points

In SEA it is usually assumed that the forcing of each subsystem is of the ‘rain-on-the-roof’ or ‘delta-correlated’ form. To simulate this, a total of 400 point forces have been used, applied individually first on plate 1, then on plate 2. For numerical convenience, these were chosen at 20 random y co-ordinates, the same for each of 20 random x co-ordinate positions. All points are chosen to exclude an area at the edge of the plate within 1/4 of the smallest bending wavelength, in order to avoid nearfield effects, although these are inevitable at low frequencies. These forces are all uncorrelated, and are assumed to have an identical broad-band spectrum.

An investigation has been performed into the variability in the results obtained for different numbers of forcing points. As the number increases, the solution should converge. This investigation was performed for the two plate system of Figure 4.1. Results were obtained, for 400 forcing points as shown in Figure 4.2.

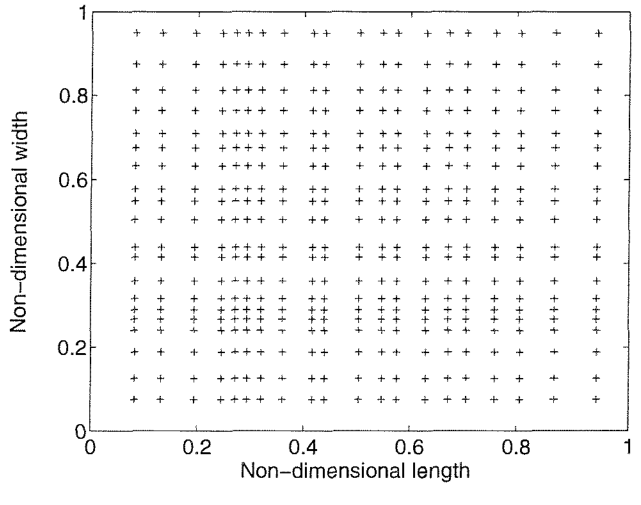

Figure 4.2. Forcing points applied in plate 1.

These were then grouped into sets of different sizes and the CLFs were determined from equation (3.13) using the energies and the dissipated powers due to each set of forcing points. For example, using 50 sets of 8 forcing points gave 50 estimates of CLF which were each calculated from the results for 8 forcing points, randomly selected from the 400 available. These CLF estimates were then used to determine confidence intervals. In order to avoid bias in the results, no overlapping sets were taken. Results were calculated for 400 sets of 1 forcing point, 100 sets of 4 forcing points, 50 sets of 8 forcing points, 20 sets of 20 forcing points, 10 sets of 40 forcing points and 8 sets of 50 forcing points.

The confidence intervals were examined for these 6 different sized sets of forcing points. Figure 4.3 shows the mean values and 90% confidence intervals for these different sets. The 90% confidence intervals are determined by taking the values of each set between 5% and 95%, *i.e.* 90% of data is between the limits. Since the numbers of results for 10 sets of 40 forcing points and 8 sets of 50 forcing points are not enough to get the numbers for the 5% and 95% limits, the confidence interval is approximated by interpolation. It can be seen that the confidence intervals are large for small numbers of forcing points and reduce as more points are taken. They are not strongly dependent on frequency. It should be noted that the first natural frequencies of the two uncoupled plates are 6 and 12 Hz. For frequencies below about 12 Hz, therefore, it is inappropriate to apply SEA due to the lack of modes.

Figure 4.4 shows the logarithmic ratio of the 95% and 67% confidence limits to the 5% and 33% confidence limits, $10\log_{10}\left(\left(\hat{\eta}_{ij}\right)_{95\%}/\left(\hat{\eta}_{ij}\right)_{5\%}\right)$ and $10\log_{10}\left(\left(\hat{\eta}_{ij}\right)_{67\%}/\left(\hat{\eta}_{ij}\right)_{33\%}\right)$, for three particular frequency bands (100, 500 Hz and 1 kHz). This shows, for example, that using a single excitation point (set size of 1) can be expected to introduce an uncertainty of up to 10 dB (*i.e.* ±5 dB) in the CLF. As the number of forcing points increases, the CLF estimates become more reliable, so that for a 90% confidence interval of 3 dB (±1.5 dB) at least 10 points should be taken. For 400 forcing points by extrapolation it can be expected that the 90% confidence interval will be reduced to ±0.25 dB. The approximate 90% confidence intervals are listed for the number of forcing points (1, 3, 10, 100 and 400) in Table 4.1.

Figure 4.5 shows the variation of the mean values of the effective CLFs for these 6 different set sizes. The mean value of the effective CLF for 400 sets of 1 is systematically higher at low frequencies, but the differences become small as the set size increases and as frequency increases.

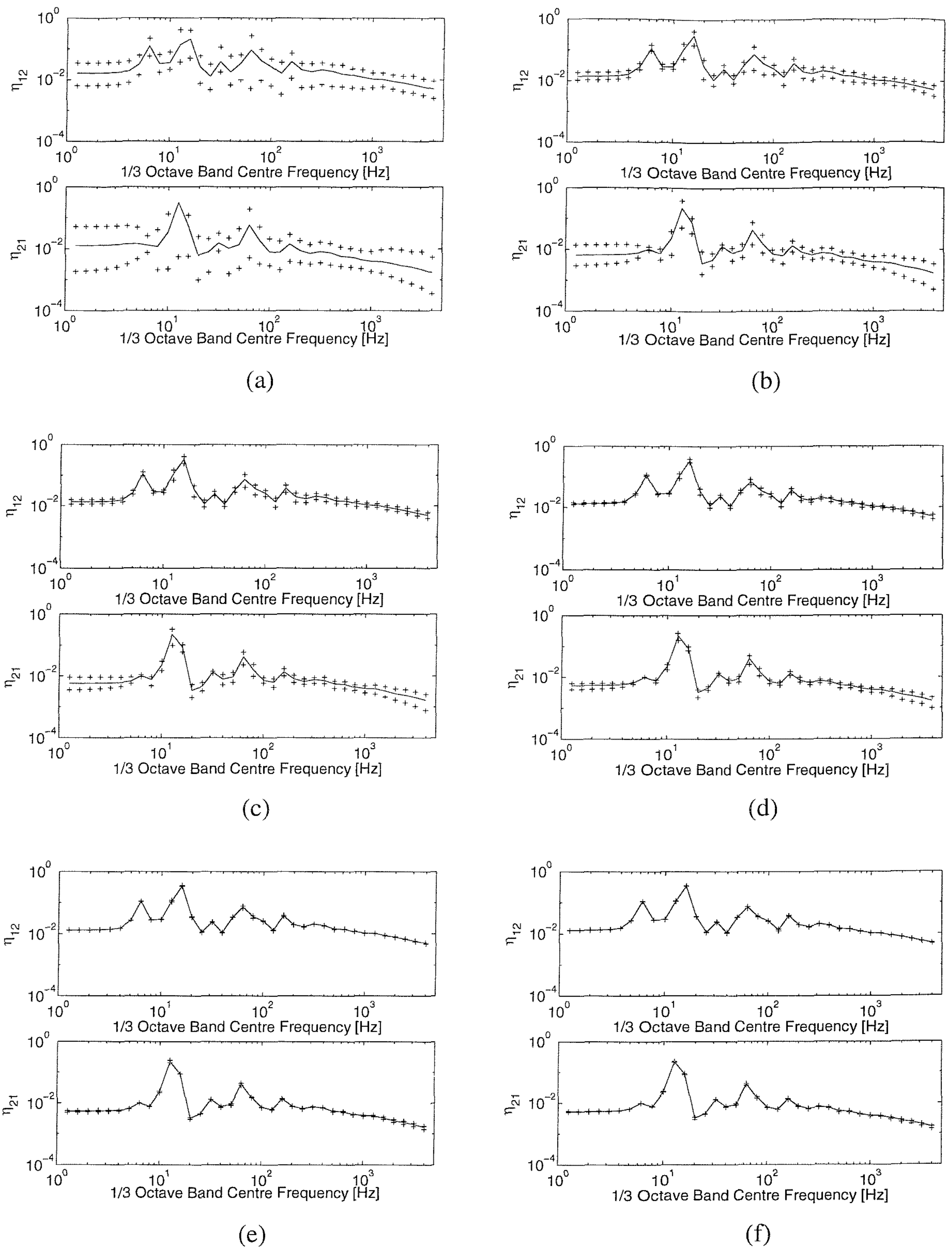

(a) (b) (c) (d) (e) (f)

Figure 4.3. The mean values and 90% confidence intervals for the effective CLFs; (a) 400 sets of 1, (b) 100 sets of 4, (c) 50 sets of 8, (d) 20 sets of 20, (e) 10 sets of 40 and (f) 8 sets of 50. —, mean CLF; +, 90% confidence interval.

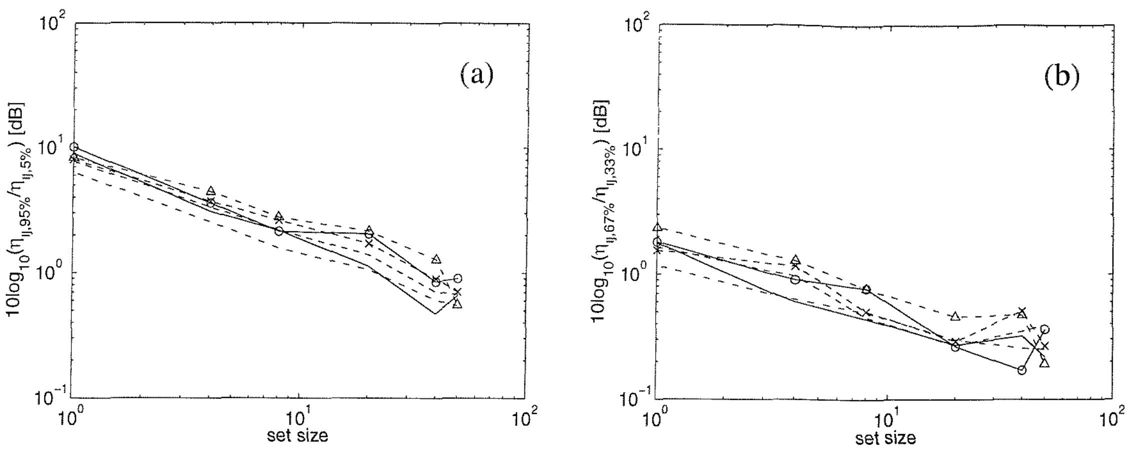

Figure 4.4. The logarithmic ratio of the 95% and 67% confidence limits to the 5% and 33% confidence limits, (a) $10\log_{10}\left(\left(\hat{\eta}_{ij}\right)_{95\%}/\left(\hat{\eta}_{ij}\right)_{5\%}\right)$ and (b) $10\log_{10}\left(\left(\hat{\eta}_{ij}\right)_{67\%}/\left(\hat{\eta}_{ij}\right)_{33\%}\right)$, for different numbers of forcing points, 400 sets of 1, 100 sets of 4, 50 sets of 8, 20 sets 20, 10 sets of 40 and 8 sets of 50 at three different frequencies. —, $\hat{\eta}_{12}$ at 100 Hz; ---, $\hat{\eta}_{12}$ at 500 Hz; -·-, $\hat{\eta}_{12}$ at 1 kHz; -o-, $\hat{\eta}_{21}$ at 100 Hz; -x-, $\hat{\eta}_{21}$ at 500 Hz; -Δ-, $\hat{\eta}_{21}$ at 1 kHz.

Table 4.1. The approximate 90% confidence intervals for the number of forcing points.

Forcing points	1	3	10	100	400
90% Confidence Interval	±5 dB	±3.0 dB	±1.5 dB	±0.45 dB	±0.25 dB

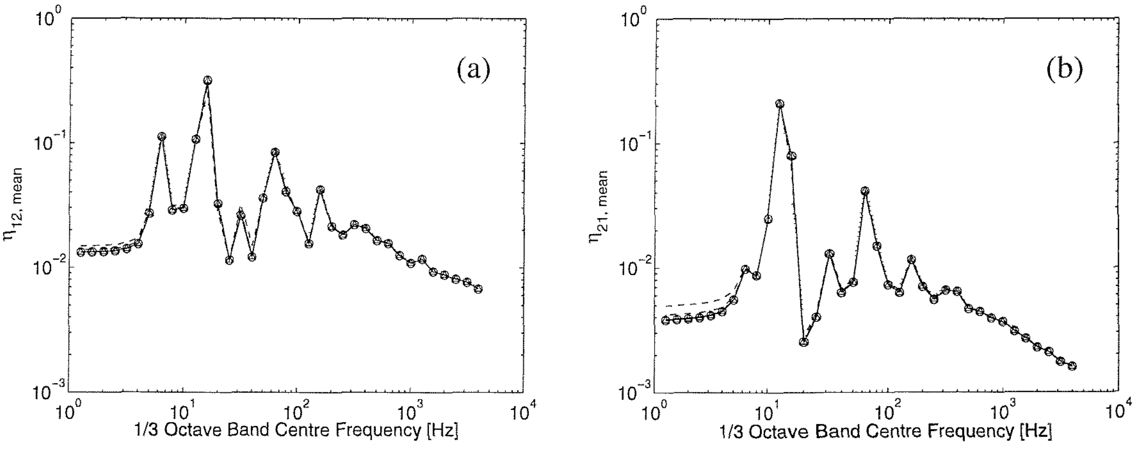

Figure 4.5. The mean values of the CLF estimates, (a) $\hat{\eta}_{12,\text{mean}}$ and (b) $\hat{\eta}_{21,\text{mean}}$, for different numbers of forcing points. ·····, 400 sets of 1; ---, 100 sets of 4; -·-, 50 sets of 8; —, 20 sets 20; -Δ-, 10 sets of 40; -o-, 8 sets of 50.

4.2.2 The evaluation of CLFs using different methods

As described in Section 3.3, there are a number of methods that can be used to evaluate the CLF; these are compared here. By exciting one plate and taking into account the actual number of modes in each frequency band, or using the asymptotic modal densities of the plates, the CLF can be calculated by using equation (3.14) or (3.15) respectively.

The actual number of modes in each frequency band has been obtained by plotting the determinant of the inverse of the dynamic stiffness matrix of each individual uncoupled plate for the various Fourier components *n*. A simply supported boundary condition is imposed at the edge usually joined to the other plate. The number of modes in each 1/3 octave band for the two uncoupled plates is presented in Figure 4.6. These are also listed in Tables 4.2 and 4.3. It can be seen that the number of modes corresponds to that evaluated from the asymptotic modal density at high frequencies but that at low frequencies there are large differences with some bands containing no modes at all.

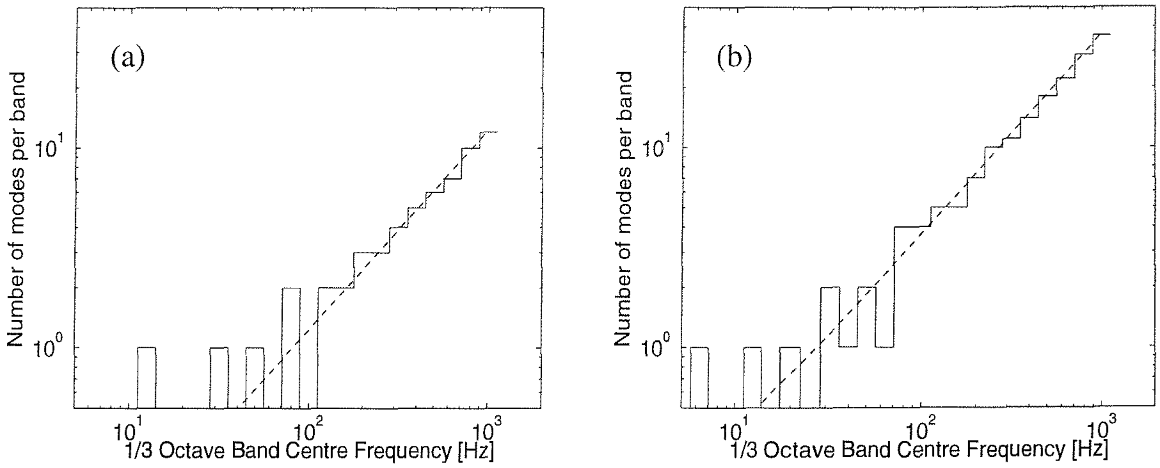

Figure 4.6. The number of modes in each 1/3 octave band for two uncoupled plates; (a) plate 1 and (b) plate 2. —, the number of modes counted from the ‘frequency function’ (*i.e.* det (**K**) = 0); ---, asymptotic value obtained from modal density given by equation (3.16).

Table 4.2. The number of modes in each 1/3 octave frequency band for plate 1 (L_1 = 0.5 m, h_1 = 3 mm, b = 1.0 m) with 3 simply supported edges and one free edge from n = 1 to 12, where n is the widthwise mode order, f_l = lower frequency, f_c = centre frequency, f_u = upper frequency of band.

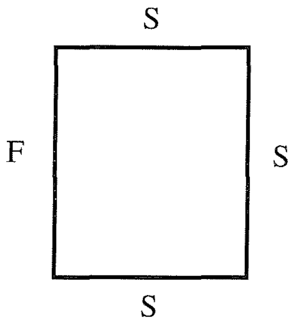

S : simply supported edge

F : free edge

f_l	f_c	f_u	1	2	3	4	5	6	7	8	9	10	11	12	sum
5.62	6.3	7.08													
7.08	8	8.91													
8.91	10	11.2													
11.2	12.5	14.1	1												1
14.1	16	17.8													
17.8	20	22.4													
22.4	25	28.2													
28.2	31.5	35.5		1											1
35.5	40	44.7													
44.7	50	56.2	1												1
56.2	63	70.8													
70.8	80	89.1		1	1										2
89.1	100	112													
112	125	141			1	1									2
141	160	178	1			1									2
178	200	224		1	1		1								3
224	250	282				1	1	1							3
282	315	355	1	1			1	1							4
355	400	447			1	1		1	2						5
447	500	562	1	1			1		1	2					6
562	630	708			1	1		1	1	1	2				7
708	800	891	1	1	1		1	1		1	1	2	1		10
891	1000	1120				1	1	1	1	1	1	2	2	2	12

Table 4.3. The number of modes in each 1/3 octave frequency band for plate 2 ($L_2 = 1.0$ m, $h_2 = 2$ mm, $b = 1.0$ m) with 3 simply supported edges and one free edge from $n = 1$ to 15, where n is the widthwise mode order, f_l = lower frequency, f_c = centre frequency, f_u = upper frequency of band.

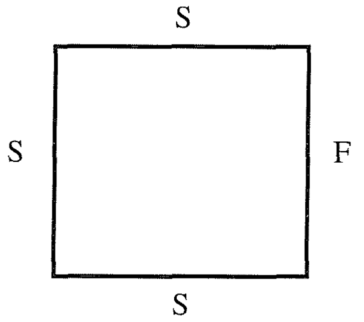

S : simply supported edge
F : free edge

f_l	f_c	f_u	1	2	3	4	5	6	7	8	9	10	11	12	13	14	15	sum
4.47	5	5.62																
5.62	6.3	7.08	1															1
7.08	8	8.91																
8.91	10	11.2																
11.2	12.5	14.1	1															1
14.1	16	17.8																
17.8	20	22.4		1														1
22.4	25	28.2																
28.2	31.5	35.5	1	1														2
35.5	40	44.7			1													1
44.7	50	56.2		1	1													2
56.2	63	70.8	1															1
70.8	80	89.1		1	1	2												4
89.1	100	112	1	1	1	1												4
112	125	141	1		1	1	2											5
141	160	178		1		1	2	1										5
178	200	224	1	1	1	1	1	2										7
224	250	282	1	1	1	1	1	2	3									10
282	315	355	1	1	1	1	1	1	2	3								11
355	400	447	1	1	1	1	1	2	2	2	3							14
447	500	562	1	1	2	1	2	1	1	2	3	4						18
562	630	708	1	1	1	2	1	2	2	2	2	3	4	1				22
708	800	891	2	2	1	1	2	1	2	2	2	2	3	5	4			29
891	100	1120	1	1	2	2	2	2	2	2	2	2	3	3	4	6	2	36

Alternatively, the CLF can be directly evaluated by using equation (3.13), in which case each plate has to be excited in turn. The strain energies have been calculated for each of 400 randomly selected forcing points on each plate, which was explained in Section 4.2.1. The power input by the force, the power transmitted to the receiver plate, and the power dissipated in each plate were also calculated. Results were calculated at discrete frequencies (three per 1/3 octave band) and averaged into 1/3 octave bands before applying equations (3.13) - (3.15). The results of these three methods are compared in Figure 4.7 with the conventional CLF estimate obtained from the wave transmission approach based on semi-infinite plates, $\eta_{ij\infty}$, given by equation (3.17).

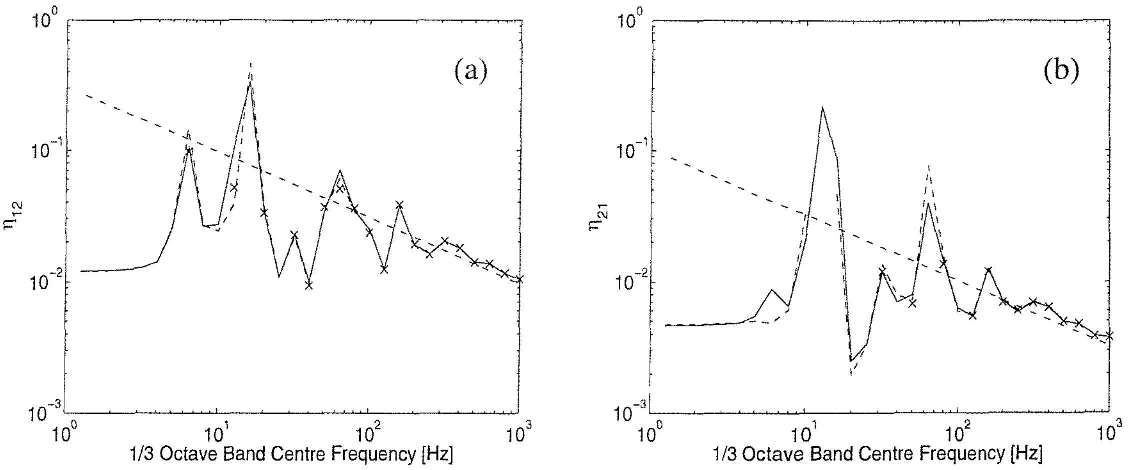

Figure 4.7. Comparison of CLFs (a) $\hat{\eta}_{12}$ (b) $\hat{\eta}_{21}$ obtained from several methods. ×, from equation (3.14) using mode count: ---, from equation (3.15) using modal density; —, 'numerical experiment' (equation (3.13)); -·-, semi-infinite plates (equation (3.17)).

The calculated CLFs agree well with the semi-infinite result $\eta_{ij\infty}$ in the high frequency region. At low frequencies, the predicted CLFs fluctuate considerably relative to $\eta_{ij\infty}$. The results based on the mode count and the modal density coincide closely, although there are some negative or non-available values omitted from the graph. These occur due to numerical problems in some frequency bands where no resonant modes of either plate exist (see Figure 4.6). Negative CLFs, mentioned and investigated by Fredo [53], and Bies and Hamid [57], may be attributed to the non-resonant response. This means that the energy of the receiver plate, at a particular frequency, can be greater than that of the source plate so that E_2 / E_1 rises above 0 dB. Accordingly, the 'numerical experiment' result, from equation (3.13), turns out to be a more reliable method than the others and does not usually produce negative values. The remaining results in this thesis are based on this latter method.

4.2.3 The CLF and its relationship to the energy ratio and the modal characteristics of plates

This section illustrates the relationships between the effective CLF and the energy ratio of two subsystems and the effect of the modal characteristics of the receiver plate, which, according to Craik *et al.* [44], is the reason for the occurrence of fluctuations in the coupling of two subsystems. The energy in each plate and the ratio between the energy of the receiver plate and that of the source plate are shown in Figure 4.8. The left-hand figures show results when plate 1 is excited while the right-hand figures correspond to excitation of plate 2. In each case the average from 400 forcing points is used. Over nearly all 1/3 octave bands, the receiver plate has a lower energy level than the source plate, see Figures 4.8 (a) and (b).

The energy results are related to the modal characteristics of the receiver plate, especially the peaks in the energy ratio occurring at low frequencies (see Figure 4.8 (c) and (d)). When the source plate is excited by a harmonic force with a particular frequency, which corresponds to a resonant mode of the receiver plate but not that of the source plate, the propagating wave produced by that force is partly transmitted to the receiver plate at the joint and the remainder is dissipated in the source plate by its damping. The transmitted wave excites a resonant mode of the receiver plate at that frequency and the energy of the receiver plate becomes large. If the energy of the receiver plate is greater than that of the source, or not much less, then a peak is found in the respective energy ratio. In particular the first and second peaks in Figure 4.8 (c) and the first peak in Figure 4.8 (d) can be seen to correspond to peaks in the corresponding effective CLF in Figure 4.7.

Conversely, when a harmonic force excites a resonant mode of the source plate at a particular frequency, the energy of the source plate is larger than that of the receiver plate (see for example the first peak in Figure 4.8 (b)). Since there is no resonant mode in the receiver plate, the energy of the receiver plate remains relatively small although the propagating wave produced by that force is partly transmitted to the receiver plate at the joint. Most of the energy is dissipated in the source plate by its damping. In this case, the ratio between the energy of the receiver plate and that of the source is small and there are no peaks in the energy ratio, although peaks occur in the energy results of both plates (see the peaks at 12 Hz in Figure 4.8 (a) and at 6 Hz in Figure 4.8 (b)).

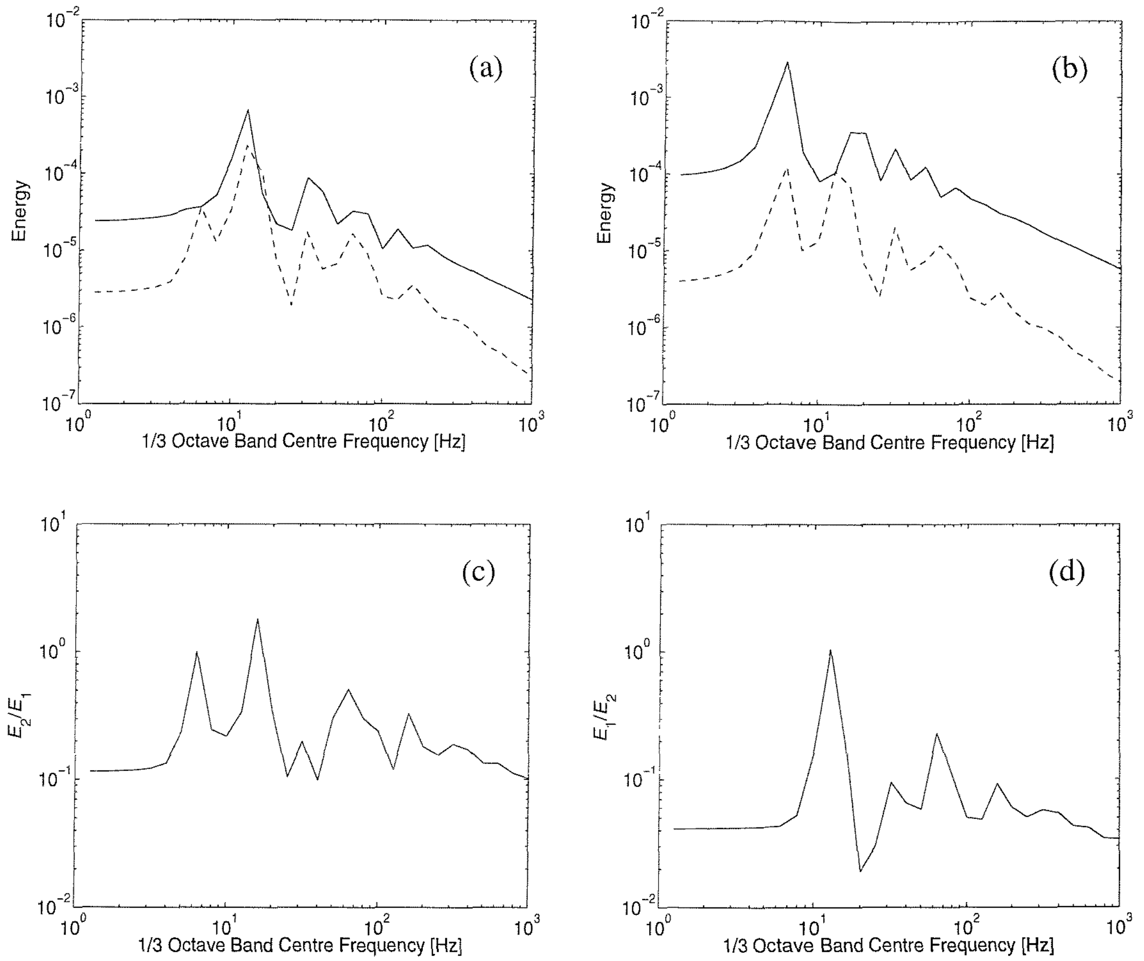

Figure 4.8. The energy of each plate, (a) and (b): —, the energy of the source plate; ---, the energy of the receiver plate, and the ratio between the energy of the receiver plate and that of the source plate, (c) and (d). (a) and (c); plate 1 is the source plate and plate 2 is the receiver plate, (b) and (d); plate 2 is the source plate and plate 1 is the receiver plate.

Figure 4.9 shows the flexural frequency functions (that is $\left(\det\left(\mathbf{K}_f\right)\right)^{-1}$) plotted against frequency, (a) for the two-plate system and (b and c) the uncoupled plates with each plate simply supported at the joint. In each case results are shown for motion with $n = 1$. In Figure 4.9 (a), the first and third peaks at approximately 6 Hz and 14 Hz correspond to peaks in the energy ratio when plate 1 is excited (see Figure 4.8 (c)) and also to peaks in $\hat{\eta}_{12}$ (see Figure 4.7 (a)). These peaks correspond to the first two resonances of the uncoupled plate 2 (see Figure 4.9 (c)). The second peak in Figure 4.9 (a), at approximately 12 Hz, corresponds to a peak in the energy ratio when plate 2 is excited (see Figure 4.8 (d)) and to a peak in $\hat{\eta}_{21}$ (see Figure 4.7 (b)). This 12 Hz peak corresponds to the first resonance of plate 1 (see Figure 4.9 (b)). Thus the peaks in the effective CLF estimates at low frequencies, which correspond to the first few modes, can be attributed to the uncoupled modes of the receiver plate. It is also possible that resonances of the source plate may affect the effective CLF. This is investigated further in Sections 4.4.3 and 4.5.4.

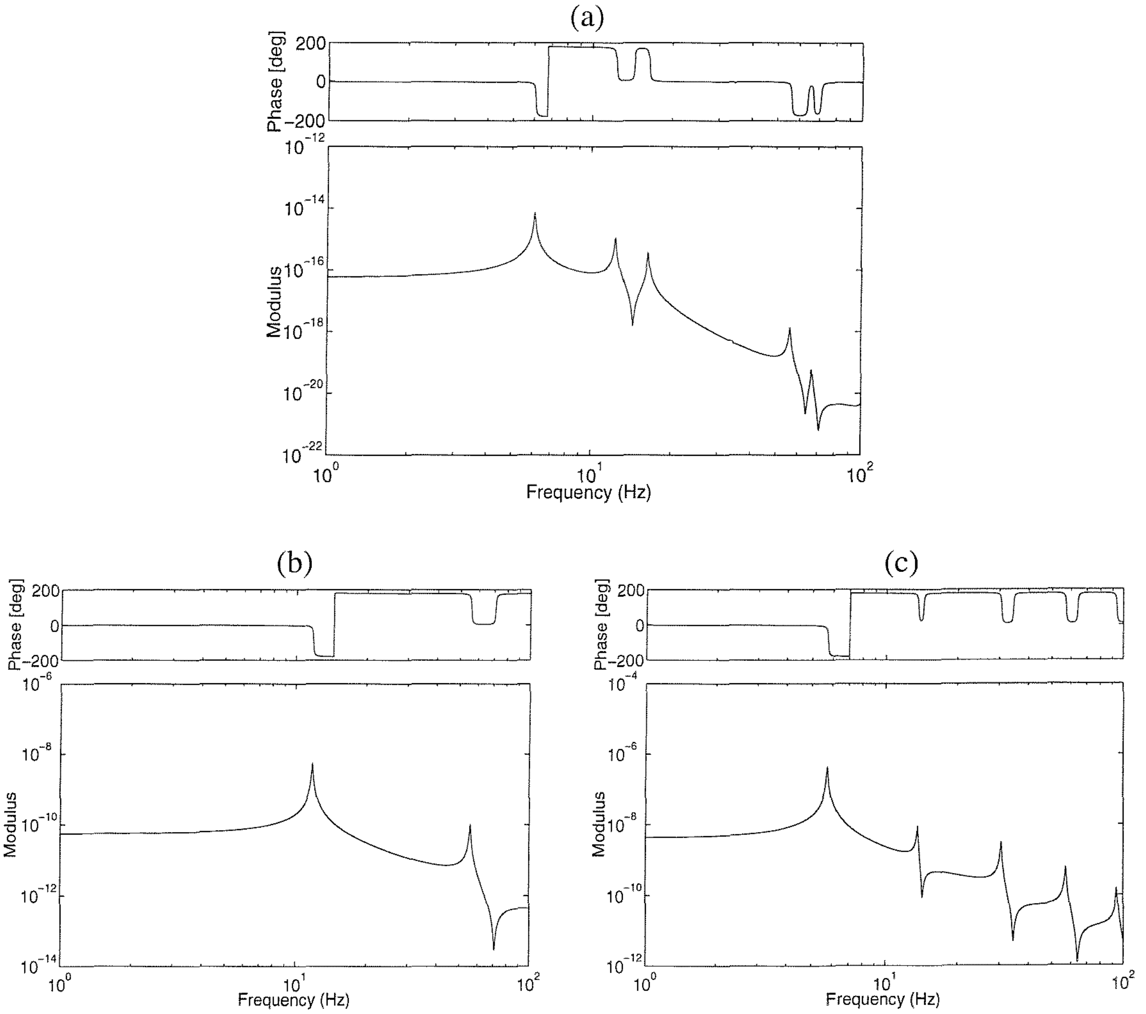

Figure 4.9. Frequency functions (that is (*i.e.* $\left(\det\left(\mathbf{K}_{nf}\right)\right)^{-1}$) plotted against frequency, for the two plate system (a) and the uncoupled plate with 3 simply supported edges and one free edge ((b) plate 1 and (c) plate 2), for the Fourier component $n = 1$. Peaks correspond to modes.

4.2.4 Effect of plate thickness on high frequency asymptotic behaviour

In Section 4.2.2 the results obtained for two finite plates were compared with equivalent results obtained for two semi-infinite plates, and it was shown that the results converged at high frequencies (see Figure 4.7). Nevertheless some discrepancies remained. In this section the results are compared at high frequencies for a range of plate thicknesses. Plate 1 is fixed at $h_1 = 3$ mm and plate 2 is varied between $h_2 = 0.949$ and $h_2 = 9.49$ mm. The DLFs of the two plates are equal and 0.1, $\eta_1 = \eta_2 = 0.1$.

In order to compare these results for finite and infinite plates more readily it is more convenient to express them in terms of a transmission efficiency τ_{ij} rather than a coupling loss factor η_{ij}. The reason for this choice is that τ_{ij} is independent of frequency and also of plate dimensions (other than thickness). The equivalence between the two parameters is given by equation (3.17) for the infinite plate case. Here equation (3.17) is used in reverse to infer an equivalent transmission efficiency τ for the finite plates. The finite plate results are expressed as the average over the frequency range 400 - 4000 Hz, to give an approximation to the high frequency asymptotic behaviour. The finite plate simulations are based on two square plates with width $b = 1$ m and length $L = 1$ m, joined at right angles. In-plane motion is not included in this section in order to facilitate comparison with the semi-infinite results. The infinite plate results are the angular averaged transmission efficiency for a right angle joint from equations (3.20) and (3.21) (see [48, 86]). Figure 4.10 compares the results. Although good agreement is found for dissimilar thicknesses, there is a discrepancy when $h_1 \approx h_2$.

If the angular averaged transmission efficiency for the infinite plate, τ, is corrected by a factor of $2/(2-\tau)$ (see [86, 87]), it coincides well with that obtained for the finite plates, as presented in Figure 4.11. This correction is one which needs to be applied to the transmission efficiency for infinite plates in determining coupling loss factors. It allows for the fact that, when τ is large, the average energy of the source plate depends on τ as a large proportion of the power incident on the boundary is transmitted, whereas if τ is small the reflected and incident energies are approximately equal.

The remaining discrepancy seen previously in Figure 4.7 (and later for parametric variations in Chapter 5) can be attributed to the influence of in-plane motion in the finite plate results and its neglect in $\eta_{ij\infty}$. This is discussed further in Chapter 5.

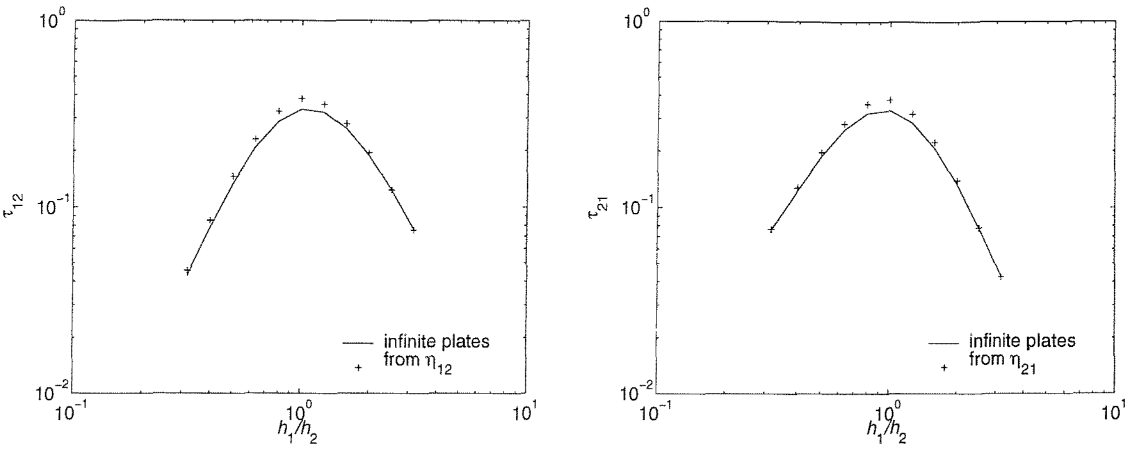

Figure 4.10. Comparison of the transmission efficiencies for finite plates with the angular averaged transmission efficiency defined by equation (3.20). —, angular averaged transmission efficiency; +, transmission efficiency obtained for finite plates averaged over 400 – 4000 Hz.

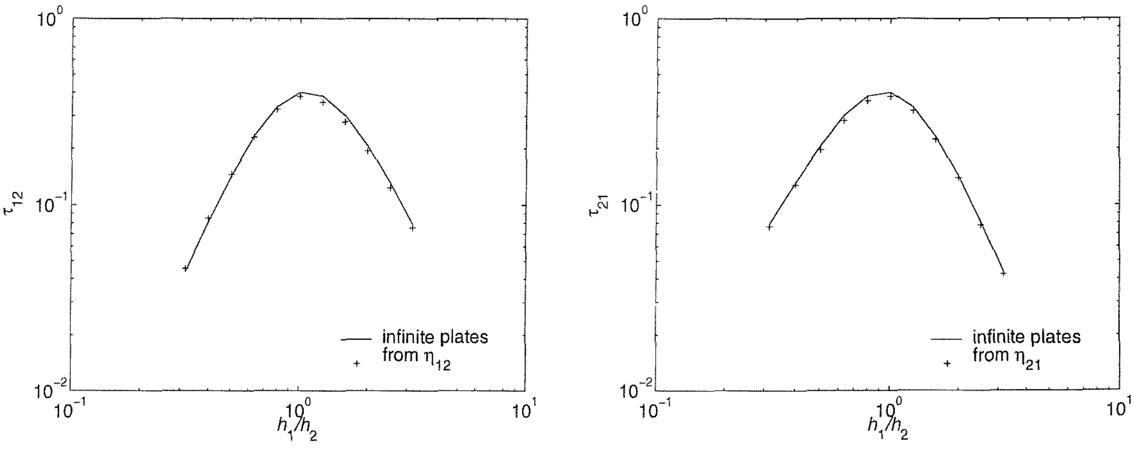

Figure 4.11. Comparison of the transmission efficiencies for finite plates with the corrected angular averaged transmission efficiency [86, 87]. —, corrected angular averaged transmission efficiency $2\tau/(2-\tau)$; +, transmission efficiency obtained for finite plates averaged over 400 – 4000 Hz.

4.2.5 Consistency relationship

The consistency relationship, described in equation (3.9), is not assumed in the 'numerical experiment' method of equation (3.13). The difference between $n_1\hat{\eta}_{12}$ and $n_2\hat{\eta}_{21}$ has been examined for the two plates of Figure 4.1 and the result is presented in Figure 4.12. The ratio $n_2\hat{\eta}_{21} / n_1\hat{\eta}_{12}$ for the two coupled finite plates fluctuates at low frequencies and converges approximately to 1, as expected, as frequency increases.

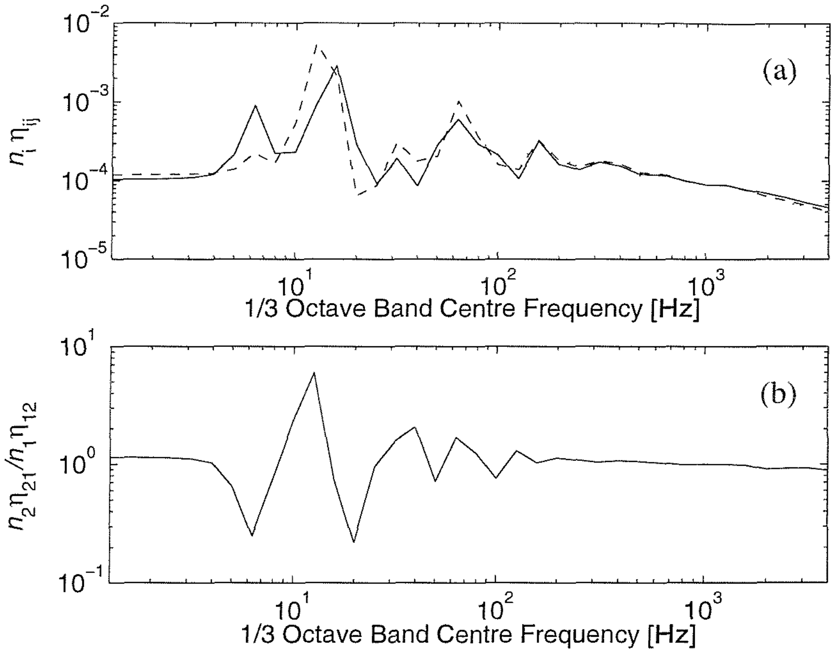

Figure 4.12. (a) Comparison of the $n_1\hat{\eta}_{12}$ and $n_2\hat{\eta}_{21}$ for two coupled plates obtained from numerical experiment with those for semi-infinite plates. —, $n_1\hat{\eta}_{12}$; ---, $n_2\hat{\eta}_{21}$; ·····, $n_1\eta_{12\infty}$ and $n_2\eta_{21\infty}$. n_1 and n_2 are the asymptotic modal densities of plate 1 and plate 2 obtained from equation (3.16). (b) Ratio $n_2\hat{\eta}_{21}/n_1\hat{\eta}_{12}$.

4.3 Two semi-infinite plates of finite width

In this section, the restriction imposed by a finite width is studied. Consider two semi-infinite plates, which are simply supported along the longitudinal edges, $y = 0$ and $y = b$, and joined at the interface $x = 0$, as shown in Figure 4.13. At $x = 0$ a simple support is assumed, which could also represent a right-angled joint in the absence of in-plane motion. In this model, it is assumed that there is no damping in the two semi-infinite plates.

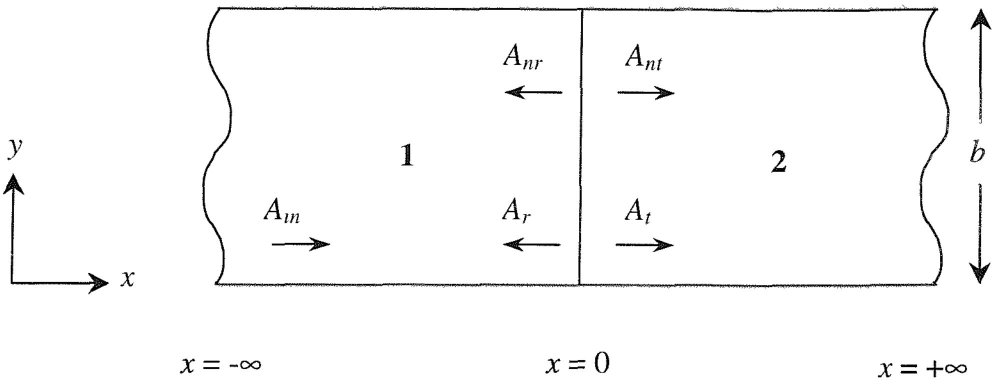

Figure 4.13. Two semi-infinite aluminium plates of finite width b joined at a line.

Allowable wave solutions have a trace wavenumber in the y direction $k_n = n\pi/b$ for integer values of n. Considering only flexural waves, the motion of plate 1 of order n has the form

$$w_1(x, y) = (A_{in}e^{-k_{11}x} + A_r e^{k_{11}x} + A_{nr}e^{k_{21}x})\ \sin(k_n y) \tag{4.1}$$

where A_{in}, A_r and A_{nr} are the complex amplitudes of the propagating incident and reflected and non-propagating nearfield waves at the interface, and k_{11} and k_{21} are the respective propagating and nearfield wavenumbers of plate 1. These wavenumbers are the roots obtained from the wave equation for plate 1, *i.e.*

$$k_{11} = (k_n^2 - k_{f1}^2)^{1/2} \tag{4.2}$$

$$k_{21} = (k_n^2 + k_{f1}^2)^{1/2} \tag{4.3}$$

where k_{f1} $(=(\rho_1 h_1 \omega^2/D_1)^{1/4})$ is the free bending wavenumber of plate 1.

The effective angle of incidence θ at the interface $x = 0$ can be obtained from

$$\theta = \tan^{-1}\left|\frac{k_n}{k_{11}}\right| \tag{4.4}$$

where $\theta = 0$ corresponds to normal incidence.

Similarly for plate 2,

$$w_2(x, y) = (A_t e^{-k_{12}x} + A_{nt} e^{-k_{22}x}) \sin(k_n y) \tag{4.5}$$

where A_t and A_{nt} are the complex amplitudes of the propagating transmitted and non-propagating nearfield waves at the interface, and k_{12} and k_{22} are the respective wavenumbers of plate 2. These wavenumbers are the roots obtained from the wave equation for plate 2,

$$k_{12} = (k_n^2 - k_{f2}^2)^{1/2} \tag{4.6}$$

$$k_{22} = (k_n^2 + k_{f2}^2)^{1/2} \tag{4.7}$$

where k_{f2} $(=(\rho_2 h_2 \omega^2 / D_2)^{1/4})$ is the free bending wavenumber of plate 2.

Constraining the displacement along the joint, only rotational motion is allowed. Applying the equilibrium and continuity conditions at the joint, one can determine the amplitude of each wave: *i.e.*

(1) displacements at the joint

$$w_1(0, y) = 0 \tag{4.8}$$

$$w_2(0, y) = 0 \tag{4.9}$$

(2) rotations at the joint

$$\frac{\partial w_1(0, y)}{\partial x} = \frac{\partial w_2(0, y)}{\partial x} \tag{4.10}$$

(3) bending moments at the joint

$$M_{xx,1}(0, y) = D_1 \left\{ \frac{\partial^2 w_1}{\partial x^2} \right\}_{x=0} = M_{xx,2}(0, y) = D_2 \left\{ \frac{\partial^2 w_2}{\partial x^2} \right\}_{x=0} \tag{4.11}$$

Substituting equations (4.1) and (4.5) into these boundary conditions (4.8) - (4.11), the four unknown amplitudes can be determined in terms of the amplitude of the incident wave A_{in}, as follows;

$$A_t + A_{nt} + A_{in} = 0\,, \tag{4.12}$$

$$A_t + A_{nt} = 0\,, \tag{4.13}$$

$$k_{11}A_r + k_{21}A_{nr} - k_{11}A_{in} = -k_{12}A_t - k_{22}A_{nt}, \tag{4.14}$$

and

$$D_1\left(k_{11}{}^2A_r + k_{21}{}^2A_{nr} + k_{11}{}^2A_{in}\right) = D_2\left(k_{12}{}^2A_t + k_{22}{}^2A_{nt}\right). \tag{4.15}$$

Equations (4.12) - (4.15) can be written in matrix form,

$$\mathbf{B}_1\mathbf{A}_1 = \mathbf{C}_1 \tag{4.16}$$

where

$$\mathbf{B}_1 = \begin{bmatrix} 1 & 1 & 0 & 0 \\ 0 & 0 & 1 & 1 \\ k_{11} & k_{21} & k_{12} & k_{22} \\ D_1k_{11}^2 & D_1k_{21}^2 & -D_2k_{12}^2 & -D_2k_{22}^2 \end{bmatrix}, \tag{4.17}$$

$$\mathbf{A}_1 = \begin{bmatrix} \frac{A_r}{A_{in}} & \frac{A_{nr}}{A_{in}} & \frac{A_t}{A_{in}} & \frac{A_{nt}}{A_{in}} \end{bmatrix}^T, \tag{4.18}$$

and

$$\mathbf{C}_1 = \begin{bmatrix} -1 & 0 & k_{11} & -D_1k_{11}^2 \end{bmatrix}^T. \tag{4.19}$$

Above the cut-on frequency for order n, power is transmitted by the propagating waves. The near-field waves do not transmit energy at any frequency. In general, the transmitted powers are proportional to the propagating wave amplitude squared, but also depend on the plate properties. The incident and reflected waves exist in the same plate so the transmission efficiency τ can be obtained most easily from

$$\tau = 1 - \left|\frac{A_r}{A_{in}}\right|^2. \tag{4.20}$$

Figure 4.14 shows example results for a source plate of thickness 3 mm and a receiver plate of thickness 2 mm, both of aluminium with no damping. The transmission efficiency only exists above the cut-on frequency for any particular value of n of plate 1. Below the cut-on frequency of plate 1, no propagating incident wave will occur and it is meaningless to calculate the transmission efficiency. When the cut-on frequency in the source plate is lower than that in the receiver plate, no energy will be transmitted into pure propagating waves in the receiver plate below its cut-on frequency and the transmission efficiency is zero. Thus the transmission efficiencies are zero up to the higher of the two cut-on frequencies, which in this case is for plate 1. Then they rise gradually and at high frequencies they tend to the result for normal incidence for semi-infinite plates. This can be explained by consideration of the angle of incidence, equation (4.4). At cut-on, $k_n = k_f$ and wave propagation occurs in a direction parallel to the joint, *i.e.* $k_{11} = 0$, whereas at high frequencies $k_n/k_{11} \to 0$ and $\theta \to 0$. Note that the cut-on frequency for transverse order n is $n^2 f_{\text{cut-on},\,1}$; *i.e.* $f_{\text{cut-on},\,2} = 4 f_{\text{cut-on},\,1}$, $f_{\text{cut-on},\,3} = 9 f_{\text{cut-on},\,1}$, etc., as expressed in equation (2.75).

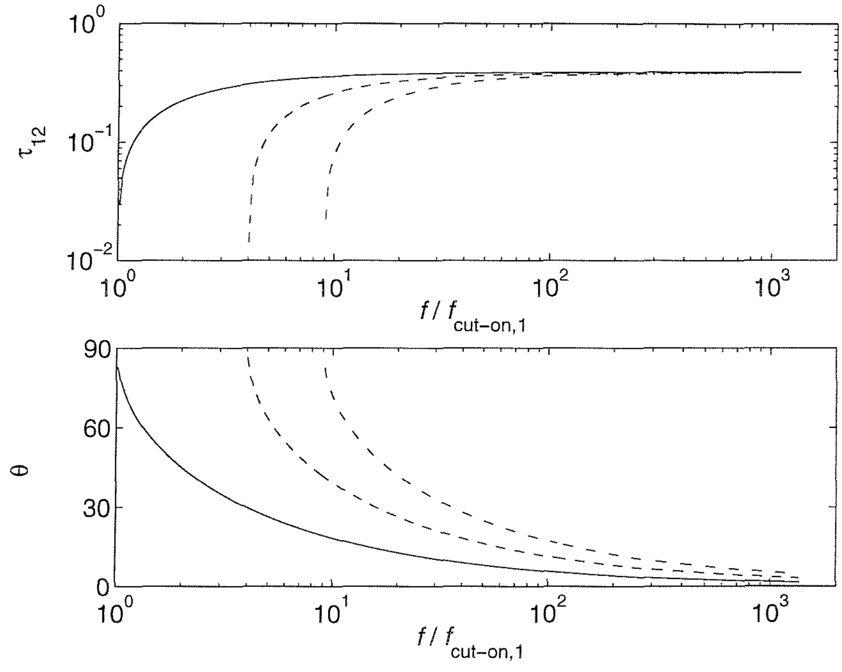

Figure 4.14. Transmission efficiencies and the angle of incidence predicted for two semi-infinite aluminium plates of width b = 1m, thickness of the source plate h_1 = 3mm, and the thickness of the receiver plate h_2 = 2mm. Four curves represent the results for different transverse orders, n: —, $n = 1$; ---, $n = 2$; -·-, $n = 3$; ····, $n = 4$. The x-axis is a non-dimensional frequency, $f\,/\,f_{\text{cut-on},\,1}$, where $f_{\text{cut-on},\,1}$ is the cut-on frequency of the source plate for $n = 1$ ($f_{\text{cut-on},\,1}$ = 7.34 Hz).

For two semi-infinite plates, the transmission efficiency for oblique incidence is also obtained from equation (3.21). For the case of grazing incidence $\theta = \pm\pi/2$, τ_{12} is zero [86].

As the frequency increases, the direction of propagation gradually approaches normal, $\theta \rightarrow 0$ and τ_{12}, for a given n, tends to $\tau_{12}(0) = 0.39$. As more orders across the plate width, n, cut on and are included in the incident field, this approximates more closely to a diffuse field, with the incident energy not primarily being at a single angle of incidence. Thus the sum over all such n will tend to the diffuse field value of $\tau_{12,d}$ found for infinite plates.

The CLF is only defined for finite plates. The transmission efficiency, τ, for two semi-infinite plates can be used to estimate the CLF of an equivalent finite plate by using equation (3.17). The CLF results, using these semi-infinite plate transmission efficiencies for particular transverse orders, are shown in Figure 4.15 for a source plate of area 0.5 m^2. Individual CLFs for particular orders converge to the normal incidence result, which are individually greater than the infinite plate diffuse result $\eta_{12\infty}$.

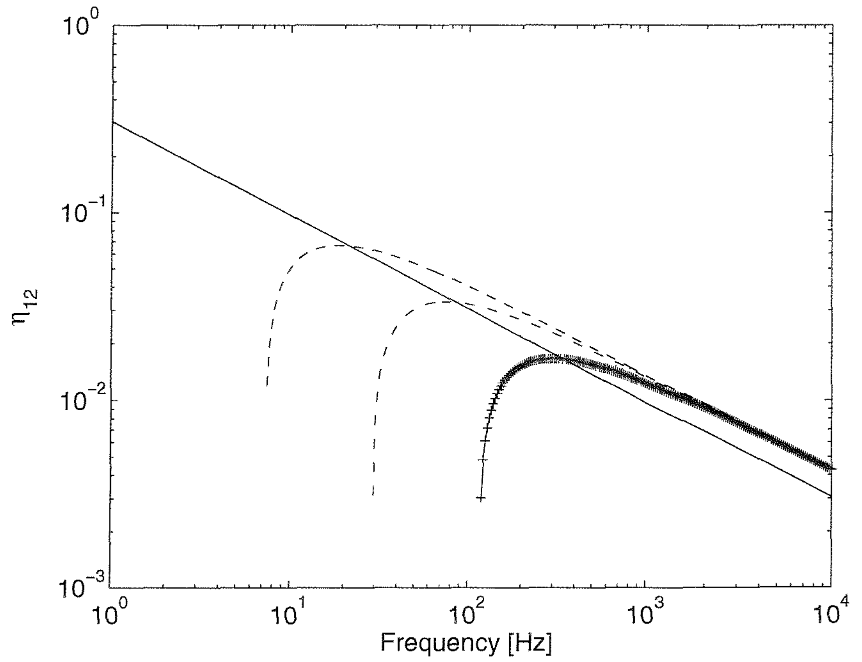

Figure 4.15. Coupling loss factors derived from models of two infinite plates and of two semi-infinite plates of finite width: —, $\eta_{12\infty}$; ---, n = 1; -·-, n = 2; ····, n = 3; -+-, n = 4.

4.4 Semi-infinite source plate of finite width coupled to a finite receiver plate

4.4.1 Model

In this section, a model is considered in which a semi-infinite source plate is connected to a finite receiver plate of length L_2, as shown in Figure 4.16. The right-hand edge of plate 2 $x = L_2$ is assumed to be free and at the interface $x = 0$ a simple support is assumed. This model is used to investigate the influence of the modal behaviour of the receiver plate on the energy transmission. An incident wave A_{in} is introduced in the semi-infinite source plate, as in the previous section. The transmission efficiencies are evaluated for different thickness ratios of the source plate to the receiver plate and the results are then considered in terms of the modal behaviour of the finite receiver plate.

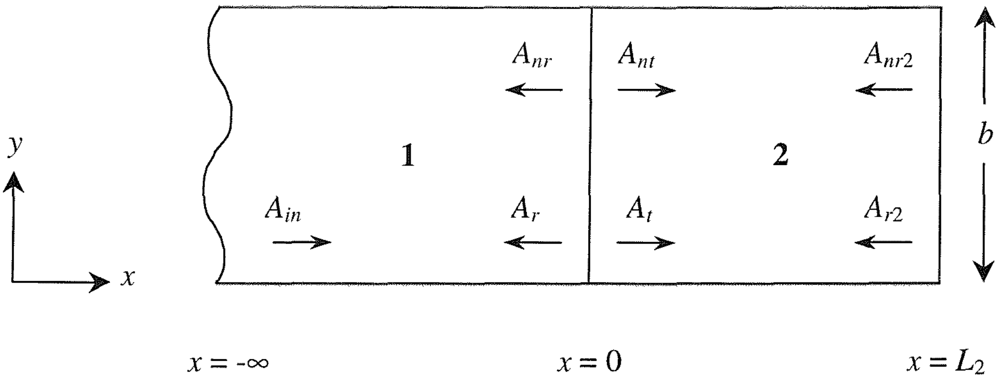

Figure 4.16. Semi-infinite (source) plate of finite width b connected to a finite (receiver) plate.

The out-of-plane displacement of plate 2, given in equation (4.5), must be extended to include a second reflected wave and a second nearfield wave.

$$w_2(x, y) = (A_t e^{-k_{12}x} + A_{nt} e^{-k_{22}x} + A_{r2} e^{k_{12}x} + A_{nr2} e^{k_{22}x}) \sin(k_n y) \qquad (4.21)$$

where A_{r2} and A_{nr2} are the complex amplitudes of the propagating reflected and non-propagating nearfield waves at the right-hand edge of plate 2. Applying the equilibrium and continuity conditions at the joint and boundary conditions at the right-hand free edge of plate 2 to this equation and equation (4.1), the six unknown amplitudes can be solved in terms of A_{in}. Equations (4.13)-(4.15) can be modified to

$$A_t + A_{nt} + A_{r2} + A_{nr2} = 0 \tag{4.22}$$

$$k_{11}A_r + k_{21}A_{nr} - k_{11}A_{in} = -k_{12}A_t - k_{22}A_{nt} + k_{12}A_{r2} + k_{22}A_{nr2} \tag{4.23}$$

$$D_1\left(k_{11}{}^2A_r + k_{21}{}^2A_{nr} + k_{11}{}^2A_{in}\right) = D_2\left(k_{12}{}^2A_t + k_{22}{}^2A_{nt} + k_{12}{}^2A_{r2} + k_{22}{}^2A_{nr2}\right). \tag{4.24}$$

In addition to equations (4.8)-(4.10), two further boundary conditions at the right-hand free edge of plate 2 are included.

(1) bending moment at the right-hand edge of plate 2:

$$M_{x2}(L_2, y) = D_2\left\{\frac{\partial^2 w_2}{\partial x^2} + \mu_2\frac{\partial^2 w_2}{\partial y^2}\right\}_{x=L_2} = 0. \tag{4.25}$$

(2) shear force at the right-hand edge of plate 2:

$$F_2(L_2, y) = -D_2\left\{\frac{\partial^3 w_2}{\partial x^3} - (2-\mu_2)k_n^2\frac{\partial w_2}{\partial x}\right\}_{x=L_2} = 0. \tag{4.26}$$

Substituting equation (4.21) into equations (4.25) and (4.26), then

$$\begin{aligned}&(k_{12}^2 - \mu_2k_n^2)e^{-k_{12}L_2}A_t + (k_{22}^2 - \mu_2k_n^2)e^{-k_{22}L_2}A_{nt} + \\ &(k_{12}^2 - \mu_2k_n^2)e^{k_{12}L_2}A_{r2} + (k_{22}^2 - \mu_2k_n^2)e^{k_{22}L_2}A_{nr2} = 0\end{aligned}, \tag{4.27}$$

$$\begin{aligned}&k_{12}\left\{-k_{12}^2 + (2-\mu_2)k_n^2\right\}e^{-k_{12}L_2}A_t + k_{22}\left\{-k_{22}^2 + (2-\mu_2)k_n^2\right\}e^{-k_{22}L_2}A_{nt} + \\ &k_{12}\left\{k_{12}^2 - (2-\mu_2)k_n^2\right\}e^{k_{12}L_2}A_{r2} + k_{22}\left\{k_{22}^2 - (2-\mu_2)k_n^2\right\}e^{k_{22}L_2}A_{nr2} = 0.\end{aligned} \tag{4.28}$$

Equations (4.12), (4.22)-(4.24) and (4.27)-(4.28) can be written in matrix form,

$$\mathbf{B}_2\mathbf{A}_2 = \mathbf{C}_2, \tag{4.29}$$

where

$$\mathbf{B}_2 = \begin{bmatrix} 1 & 1 & 0 & 0 & 0 & 0 \\ 0 & 0 & 1 & 1 & 1 & 1 \\ k_{11} & k_{21} & k_{12} & k_{22} & -k_{12} & -k_{22} \\ D_1k_{11}^2 & D_1k_{21}^2 & -D_2k_{12}^2 & -D_2k_{22}^2 & -D_2k_{12}^2 & -D_2k_{22}^2 \\ 0 & 0 & b_{12}e_{12}^- & b_{22}e_{22}^- & b_{12}e_{12}^+ & b_{22}e_{22}^+ \\ 0 & 0 & c_{12}e_{12}^- & c_{22}e_{22}^- & -c_{12}e_{12}^+ & -c_{22}e_{22}^+ \end{bmatrix}, \tag{4.30}$$

$$b_{ij} = k_{ij}^{\ 2} - \mu_j k_n^{\ 2},\ c_{ij} = k_{ij}\left\{-k_{ij}^{\ 2} + \left(2-\mu_j\right)k_n^{\ 2}\right\},\ e_{ij}^{+} = e^{k_{ij}L_j},\ e_{ij}^{-} = e^{-k_{ij}L_j}, \tag{4.31}$$

$$\mathbf{A}_2 = \begin{bmatrix} \frac{A_r}{A_{in}} & \frac{A_{nr}}{A_{in}} & \frac{A_t}{A_{in}} & \frac{A_{nt}}{A_{in}} & \frac{A_{r2}}{A_{in}} & \frac{A_{nr2}}{A_{in}} \end{bmatrix}^T, \tag{4.32}$$

and

$$\mathbf{C}_2 = \begin{bmatrix} -1 & 0 & -k_{11} & -D_1k_{11}^2 & 0 & 0 \end{bmatrix}^T. \tag{4.33}$$

The reflection efficiency r and the transmission efficiency τ of the joint between the two plates can be obtained from

$$r = \left|\frac{A_r}{A_{in}}\right|^2 \tag{4.34}$$

and

$$\tau = 1 - r. \tag{4.35}$$

Figure 4.17 (a) shows results for an example case, a semi-infinite source plate (thickness 3 mm, finite width 1 m) coupled to a finite receiver plate (thickness 2 mm, length 1 m) for $n = 1$. At low frequencies, the transmission efficiency oscillates considerably around that for two semi-infinite plates, whereas it converges to that for two semi-infinite plates ($\tau_{12} = 0.42$) as frequency increases. It is noted that the transmission efficiency for two semi-infinite plates differs slightly from that shown in Figure 4.14, $\tau_{12}(0) = 0.39$. In this model, it is assumed that there is no damping in the semi-infinite source plate ($\eta_1 = 0$), as before, whereas the receiver plate is damped with a loss factor ($\eta_2 = 0.1$). This loss factor makes the bending wavenumber complex and affects the transmission efficiency. Since the finite receiver plate is damped with a loss factor η, the transmitted wave at the joint is propagated to the far edge of the receiver plate and then reflected back towards the joint. The influence of damping of the receiver plate is investigated in the following section. The peaks and troughs in the transmission efficiency for the finite receiver plate are related to the modal behaviour of the receiver plate. This issue is discussed further in Section 4.4.3.

Figure 4.17 (b) shows the CLF results for a transverse order $n = 1$ estimated by equations (4.35) and (3.17), and the infinite plate diffuse result $\eta_{12\infty}$, when the length of the source plate is taken as 0.5 m. The CLF for the finite receiver plate for $n = 1$ converges to the normal incidence result as frequency increases and these CLFs are greater than the infinite plate diffuse result $\eta_{12\infty}$. When the transmission efficiencies are averaged for all possible transverse orders n, the CLF for the finite receiver plate converges to $\eta_{12\infty}$, as shown in Figure 4.17 (c).

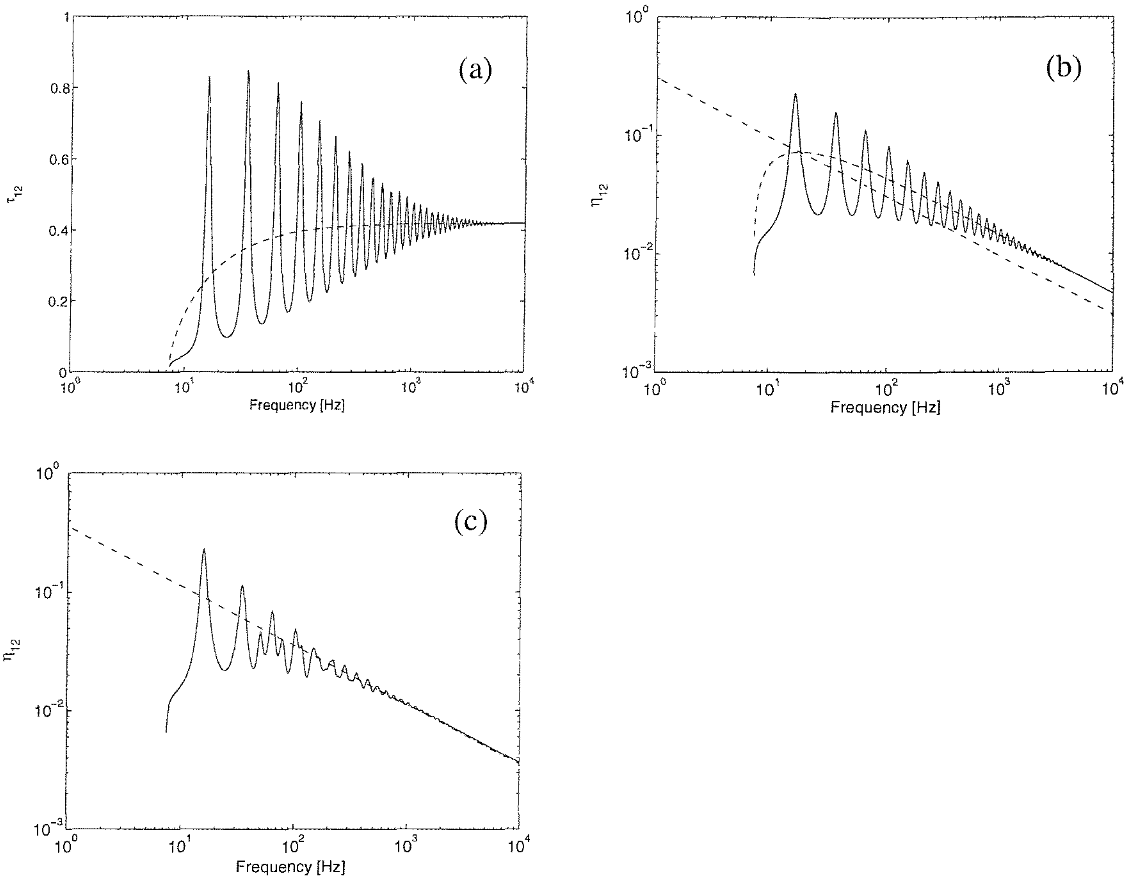

Figure 4.17. Transmission efficiency and CLFs for a semi-infinite plate ($h_1 = 3$ mm, $\eta_1 = 0$) of finite width ($b = 1$ m) coupled to a finite plate ($h_2 = 2$ mm, $L_2 = 1$ m, $\eta_2 = 0.1$); (a) transmission efficiency τ_{12} for $n = 1$: —, semi-infinite to finite plates; ---, two semi-infinite plates of finite width, (b) CLFs obtained from τ_{12} for source plate of length 0.5 m for $n = 1$, and (c) CLF obtained from τ_{12} averaged for all possible transverse orders n: —, semi-infinite to finite plates; ---, two semi-infinite plates of finite width; -·-, two semi-infinite plates (diffuse incidence).

4.4.2 The influence of damping of the receiver plate

The influence of damping of the receiver plate was investigated by performing calculations for three damping values, $\eta_2 = 0.03$, 0.1 and 0.3. The transmission efficiencies are shown in Figure 4.18. As the damping of the receiver plate increases, more energy is absorbed by the receiver plate and less energy is reflected back towards the joint. As a result of this, the transmission efficiency τ_{12} oscillates less and converges more quickly to that for two semi-infinite plates with the receiver damping. At high frequencies the transmission efficiency for the damped semi-infinite receiver plate is greater than that for the undamped semi-infinite receiver plate, $\tau_{12} = 0.39$, as described in the previous section. The transmission efficiencies converge to that for the undamped semi-infinite receiver plate, as the damping of the receiver plate decreases, *i.e.* $\tau_{12} = 0.48$, 0.42 and 0.40 for $\eta_2 = 0.3$, 0.1 and 0.03 respectively.

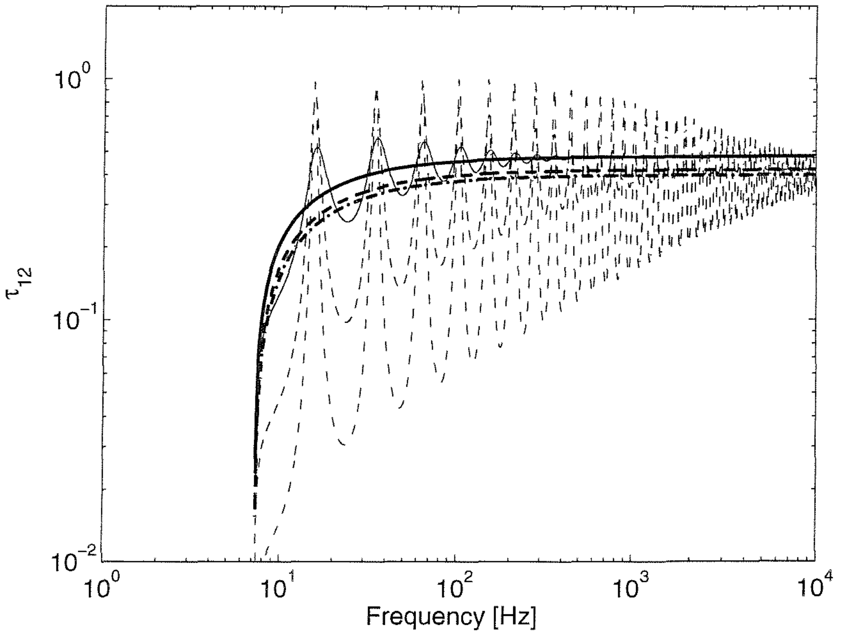

Figure 4.18. The influence of receiver damping on the transmission efficiency for a semi-infinite plate (thickness $h_1 = 3$ mm) of finite width ($b = 1$ m) coupled to a finite plate (thickness $h_2 = 2$ mm, length $L_2 = 1$ m) for $n = 1$: —, $\eta_2 = 0.3$; ---, $\eta_2 = 0.1$; -·-, $\eta_2 = 0.03$. Thick lines present the results for the two-semi infinite plates with the receiver damping.

4.4.3 The influence of the modal behaviour of the finite receiver plate

The transmission efficiencies vary with the ratio of the thicknesses of the source and receiver plates. First, the thickness of the source plate is varied between 3 and 1/3 times the thickness of the finite receiver plate, which is fixed as 2 mm. Next, the thickness of the receiver plate is varied in the same range relative to the thickness of the semi-infinite source plate, which is fixed as 3 mm. There is no damping in the source plate and the receiver plate is damped with $\eta_2 = 0.1$.

Figure 4.19 shows the transmission efficiencies for these thickness ratios. The high frequency asymptote of the transmission efficiency has a maximum value when the thicknesses of the two plates are equal and this asymptote reduces when the ratio is large or small. At high frequencies, the transmission efficiency for this model (the semi-infinite plate coupled to the finite plate) converges to that for two semi-infinite plates with damping in the receiver plate $\eta_2 = 0.1$, as seen in Figure 4.17 (a). The finite receiver plates are damped and hence the transmission efficiencies are greater than the normal incidence results, as discussed in Section 4.4.2.

The frequencies of the peaks in Figure 4.19 (a) (varying the thicknesses of the infinite source plate) remain essentially invariant as the thickness ratio varies, whereas the peaks in Figure 4.19 (b) (varying the thicknesses of the finite receiver plate) are shifted according to the modal behaviour of the receiver plate. In order to compare these results with the modal behaviour, the natural frequencies of the uncoupled receiver plate are summarised in Table 4.4. Results are given for two sets of boundary conditions on the edge that is usually coupled to the infinite plate (simply supported or clamped).

The peaks in the transmission efficiency are found to occur between the natural frequencies of the uncoupled receiver finite plate with either simply supported or clamped boundary condition at the interface, *i.e.* F-S-S-S or F-S-C-S, as shown in Figure 4.20. At resonances of the finite plate, the wave impedance of the receiver plate is low, producing a maximum in the transmitted energy, and hence in the power dissipated in the receiver plate. At anti-resonances of the receiver plate, the transmission efficiency has a minimum.

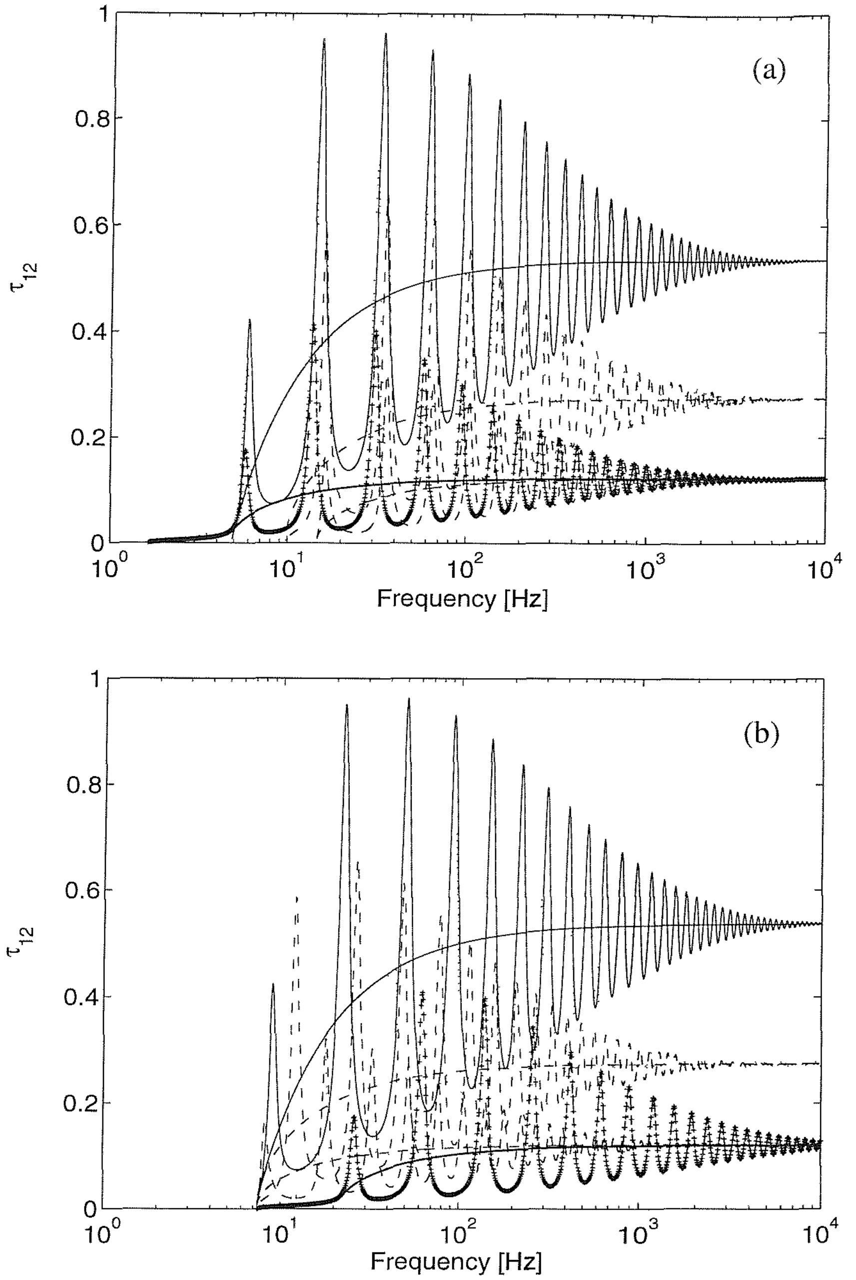

Figure 4.19. Transmission efficiencies for a semi-infinite source plate connected to a finite plate (width $b = 1$ m, length $L_2 = 1$ m, DLF $\eta_2 = 0.1$) for different values of h_1/h_2 (a) h_2 fixed as 2 mm and (b) h_1 is fixed as 3 mm: ---, $h_1/h_2 = 3$; – –, $h_1/h_2 = 2$; —, $h_1/h_2 = 1$; , $h_1/h_2 = 1/2$; -+-, $h_1/h_2 = 1/3$. Also shown are the corresponding results for two semi-infinite plates of finite width, which are the asymptotes for the former results.

Table 4.4. The natural frequencies of the uncoupled receiver plate (width b = 1 m, length L_2 = 1 m, n = 1) with 3 simply supported edges and one free edge [F-S-S-S] and with 2 simply supported edges, one clamped edge and one free edge [F-S-C-S].

Thickness h_2 (mm)	F-S-S-S (Hz)	F-S-C-S (Hz)
2	5.74, 13.7, 30.4, 57.0, 93.5	6.20, 16.3, 35.6, 65.3, 104
1	2.87, 6.83, 15.2, 28.6, 47.0	3.11, 8.17, 17.8, 32.5, 51.8
1.5	4.28, 10.3, 22.8, 42.8, 69.8	4.66, 12.2, 26.7, 48.7, 78.1
3	8.64, 20.4, 45.8, 85.4, 140	9.32, 24.4, 53.3, 97.8, 155
6	17.2, 41.2, 91.4, 171, 281	18.7, 48.7, 107, 195, 311
9	25.8, 61.3, 137, 257, 421	28.1, 73.0, 160, 291, 469

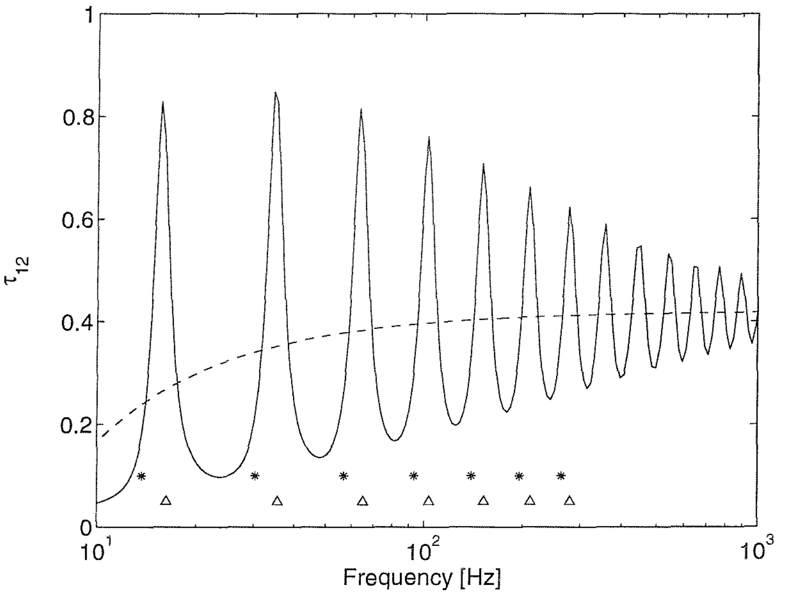

Figure 4.20. The transmission efficiency for an infinite source plate (width b = 1 m, h_1 = 3 mm) coupled to a finite receiver plate (width b = 1 m, L_2 = 1 m, h_2 = 2 mm) and two semi-infinite plates for n = 1; —, semi-infinite to finite; ---, semi-infinite to semi-infinite: natural frequencies of finite plate; *, F-S-S-S; Δ, F-S-C-S.

Figure 4.21 shows the results for various thicknesses of infinite source with the thickness of the finite receiver plate fixed as $h_2 = 2$ mm. These are again compared with the plate natural frequencies. When the thickness ratio h_1/h_2 is large, the infinite plate constrains the finite plate and the peaks tend towards the natural frequencies for a clamped edge [F-S-C-S]; when the ratio h_1/h_2 is small, the peaks tend towards those for a simply supported edge [F-S-S-S].

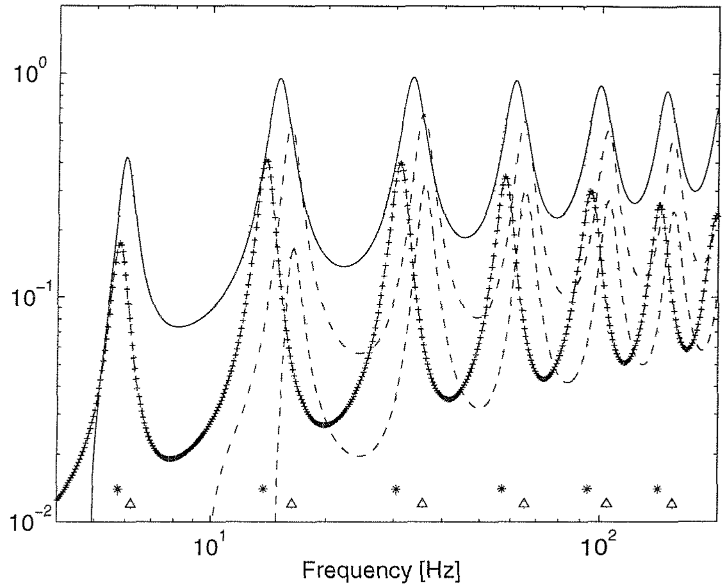

Figure 4.21. The transmission efficiencies for an infinite source plate coupled to a finite receiver plate with $b = 1$ m, $L_2 = 1$ m, $n = 1$, $h_2 = 2$ mm, for different values of h_1/h_2; ---, $h_1/h_2 = 3$; --, $h_1/h_2 = 2$; —, $h_1/h_2 = 1$;   , $h_1/h_2 = 1/2$; -+-, $h_1/h_2 = 1/3$: natural frequencies of finite plate; ∗, F-S-S-S; Δ, F-S-C-S. The vertical dotted lines correspond to the natural frequency of each mode.

4.5 Finite source plate coupled to a semi-infinite receiver plate of finite width

4.5.1 Model

In order to evaluate the influence of the modal behaviour of the source plate on the coupling loss factor, one can consider a finite source plate connected to a semi-infinite receiver plate, as shown in Figure 4.22. At the interface $x = L_1$, a simple support is assumed.

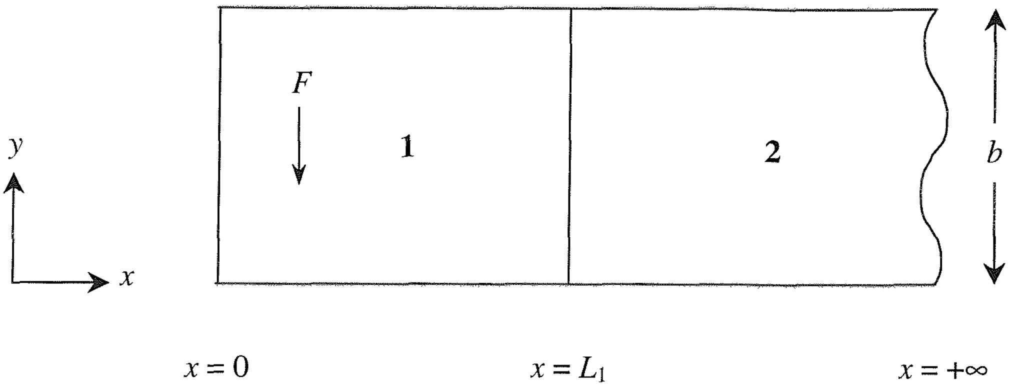

Figure 4.22. Finite (source) plate connected to a semi-infinite (receiver) plate of finite width b.

For this system, it is more appropriate to simulate a 'rain-on-the-roof' type excitation rather than a propagating source wave as in the previous sections. In the investigation of two finite plates in Section 4.2, it has been shown that if 400 excitation points are used in the finite source plate, reliable results are obtained, independent of the forcing points. Single point excitation is therefore applied here at 400 randomly chosen points, avoiding edges. For each point force, this excites vibration in many different transverse orders, n, across the plate width. For a given frequency, all such components have been included whose cut-on frequency is below the frequency under consideration.

The equations of motion are solved using a dynamic stiffness approach, as described in Chapter 2. A harmonic point force is applied inside one plate. Thus the source plate is separated into two dynamic stiffness elements at the longitudinal position of the applied force. The dynamic stiffness matrices for the source plate, $\mathbf{K}_1$ and $\mathbf{K}_2$, are as given in Chapter 2. For the semi-infinite receiver plate, a dynamic stiffness matrix $\mathbf{K}_{inf}$ (see Appendix C) can be defined in terms of the positive-going propagating and nearfield waves at the interface. The global dynamic stiffness matrix of the total system can be derived by assembling the dynamic stiffness matrices of the two finite plates and the semi-infinite plate and applying the continuity and equilibrium conditions at the interface including the simple support. This global dynamic stiffness matrix $\mathbf{K}_{\mathrm{tot}}$ can be reduced using a transformation matrix as before. The reduced dynamic stiffness matrix $\mathbf{K}$, for flexural motion only, is a 5×5 frequency-dependent matrix (the 5 dof are the displacement and rotation at $x = 0$, the displacement and rotation at the forcing point and the rotation at $x = L_1$). The response can be obtained from $\mathbf{K}^{-1}\mathbf{F}$ for each frequency, where $\mathbf{F}$ is the applied force vector.

4.5.2 CLF

The CLF can be determined from the power balance equation (3.1) in this case for a particular plate. As in the previous sections, no damping is included in the semi-infinite plate. Due to the infinite nature of plate 2, energy is only transmitted away from the joint and the term $\omega\eta_{21}E_2^{\,1}$ representing power transmitted from plate 2 back to plate 1, is zero. Since $P_{1,diss}^{\;1} = \omega\eta_1 E_1^{\,1}$, the effective CLF for a particular finite source plate is obtained from

$$\hat{\eta}_{12} = \frac{P_{12}}{\omega E_1} = \eta_1 \frac{P_{12}}{P_{1,diss}} \tag{4.36}$$

where the superscript 1 is omitted for clarity.

To evaluate the effective CLF, one needs to calculate the strain energy of the source plate E_1 and the power transmitted at the joint P_{12}. The response of the source plate is integrated analytically to give an accurate measure of its strain energy (see Appendix A). The power transmitted at the interface P_{12} is obtained directly from equation (2.86). In the present case, since the in-plane motion is not considered ($u_n = 0$ and $v_n = 0$) and the interface is assumed to be a simple support ($w_n = 0$), so only the moment at the interface transmits power. These are calculated for each transverse order n, integrated along the interface length b analytically, and then summed.

The power dissipated and power transmitted for this system fluctuate as functions of frequency due to the modal behaviour of the finite source plate, as shown in Figure 4.23. However the peaks in the two curves tend to coincide. The power transmitted becomes significantly lower than the power dissipated as frequency increases.

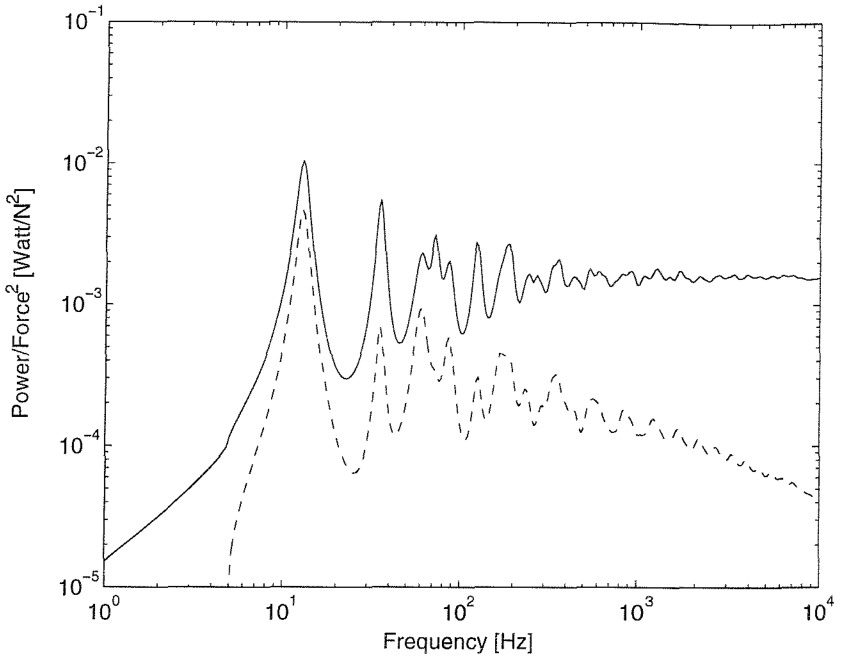

Figure 4.23. The power dissipated $P_{1,diss}$ and power transmitted P_{12} for a finite source plate ($h_1 = 3$ mm, $L_1 = 0.5$ m, $\eta_1 = 0.1$) coupled to a semi-infinite receiver plate ($h_2 = 2$ mm, $\eta_2 = 0$) of finite width ($b = 1$ m): —, $P_{1,diss}$; ---, P_{12}.

The effective CLF for a finite plate coupled to a semi-infinite plate of finite width ($b = 1$ m), obtained from equation (4.36), is plotted in Figure 4.24 (a) for transverse orders $n = 1$ up to 4. In each case these are based on the averages over 400 forcing points. Also shown is the result for $n = 1$ to $n_{\max}$, which includes all 46 transverse orders for all frequencies. This result is shown again in Figure 4.24(b) in one-third octave bands. At low frequencies, the effective CLF fluctuates relative to that obtained from two semi-infinite plates. As the number of transverse orders n increases and the sum over $n_{\max}$ is taken, the effective CLF converges to the CLF for two semi-infinite plates. However, it may be observed that the effective CLF for a given n is relatively smooth compared to the fluctuations in the CLF for a semi-infinite source plate coupled to a finite receiver plate (see Figure 4.17 (b)).

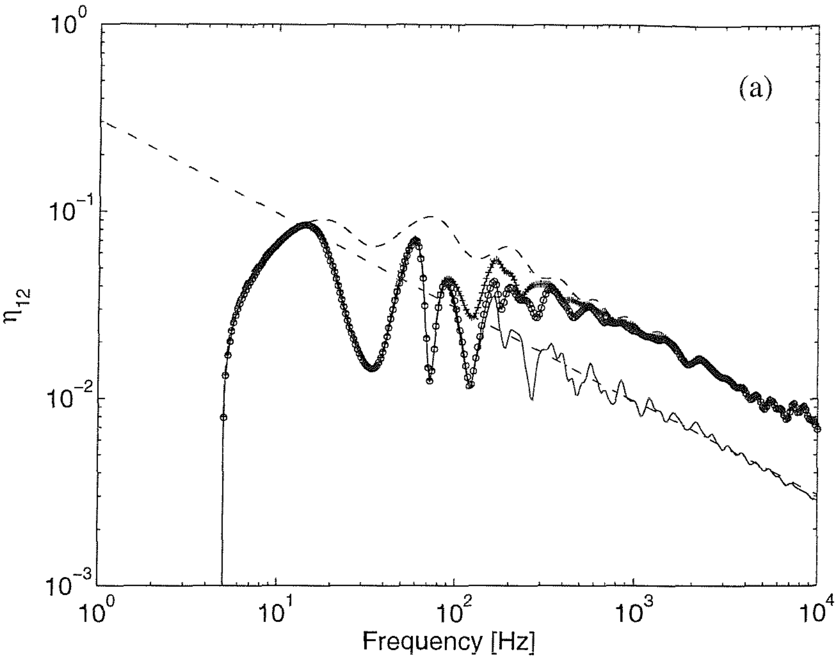

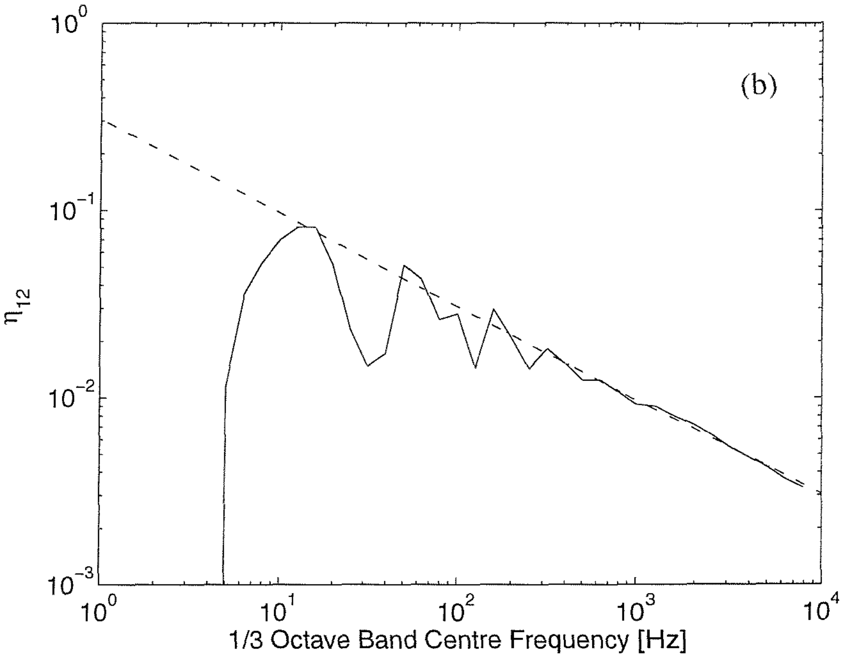

Figure 4.24. Effective CLF for finite source plate ($h_1 = 3$ mm, $L_1 = 0.5$ m, $\eta_1 = 0.1$) coupled to a semi-infinite receiver plate ($h_2 = 2$ mm, $\eta_2 = 0$) of finite width ($b = 1$ m); (a) η_{12} versus frequency and (b) η_{12} versus 1/3 octave frequency band: ---, $n = 1$; ····, $n = 1+2$; -+-, $n = 1+2+3$; -o-, $n = 1+2+3+4$; —, $n = 1$ up to 46; --, $\eta_{12\infty}$.

4.5.3 The influence of damping of the finite source plate

As the damping of the source plate increases, the level of the peaks in the energy E_1 and the power transmitted P_{12} decreases, as shown in Figure 4.25. However damping has only a small effect on the effective CLF, as shown in Figure 4.26, as similar proportional reductions occur in both the energy in the source plate and the transmitted power.

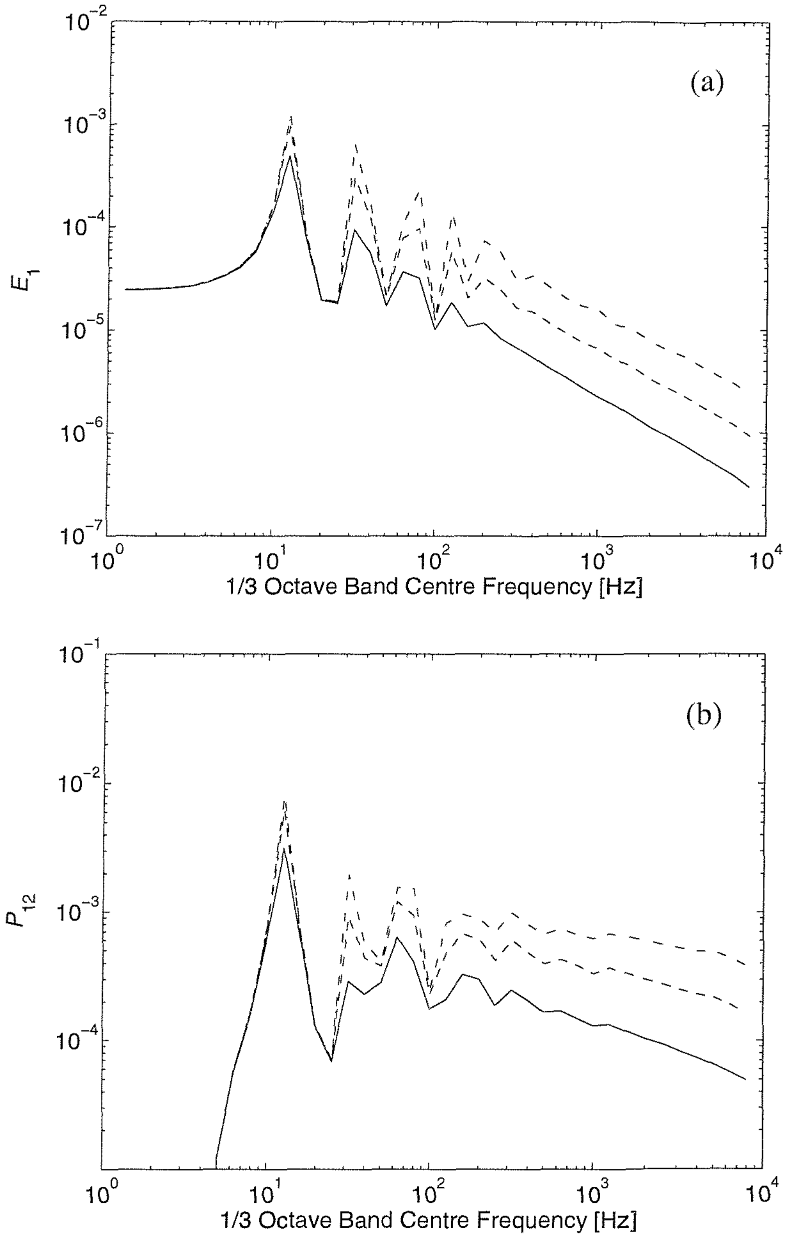

Figure 4.25. The influence of damping of the source plate on: (a) the strain energy of the source plate E_1 for different DLFs and (b) the transmitted power P_{12}: —, $\eta_1 = 0.1$; ---, $\eta_1 = 0.03$; -·-, $\eta_1 = 0.01$. The dimensions of the source and receiver plates are the same as in Figure 4.24.

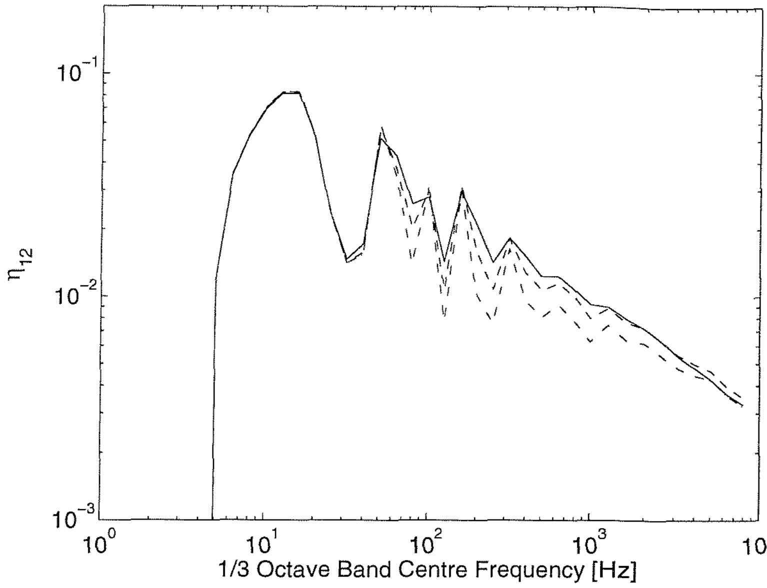

Figure 4.26. The influence of damping on the effective CLF for a finite source plate ($h_1 = 3$ mm, $L_1 = 0.5$ m, $\eta_1 = 0.1$) coupled to a semi-infinite receiver plate ($h_2 = 2$ mm, $\eta_2 = 0$) of finite width ($b = 1$ m): —, $\eta_1 = 0.1$; ---, $\eta_1 = 0.03$; -·-, $\eta_1 = 0.01$.

4.5.4 The influence of the modal behaviour of the finite source plate

This section investigates the influence of the modal behaviour of the finite source plate on the energy transmission in terms of the effective CLF. A parameter study is performed in which the ratio of the thicknesses of the two plates is varied and the modal behaviour of the finite source plate is examined.

First, the thickness of the finite source plate is varied between 3 and 1/3 times the thickness of the semi-infinite receiver plate, which is fixed as 2 mm. The influence of the thickness of the source plate is shown in Figure 4.27 (a). The peaks and troughs can be related to the modal behaviour of the source plate. The natural frequencies for the uncoupled source plate are summarised in Table 4.5. This will be considered in more detail below. Energy transmission starts at the cut-on frequency of the receiver plate the thickness of which is kept the same, as indicated above, even if the cut-on frequency for the source plate is greater. The maximum energy transmission occurs when the two plates have the same thicknesses (see also Figure 4.11 and Figure 4.19).

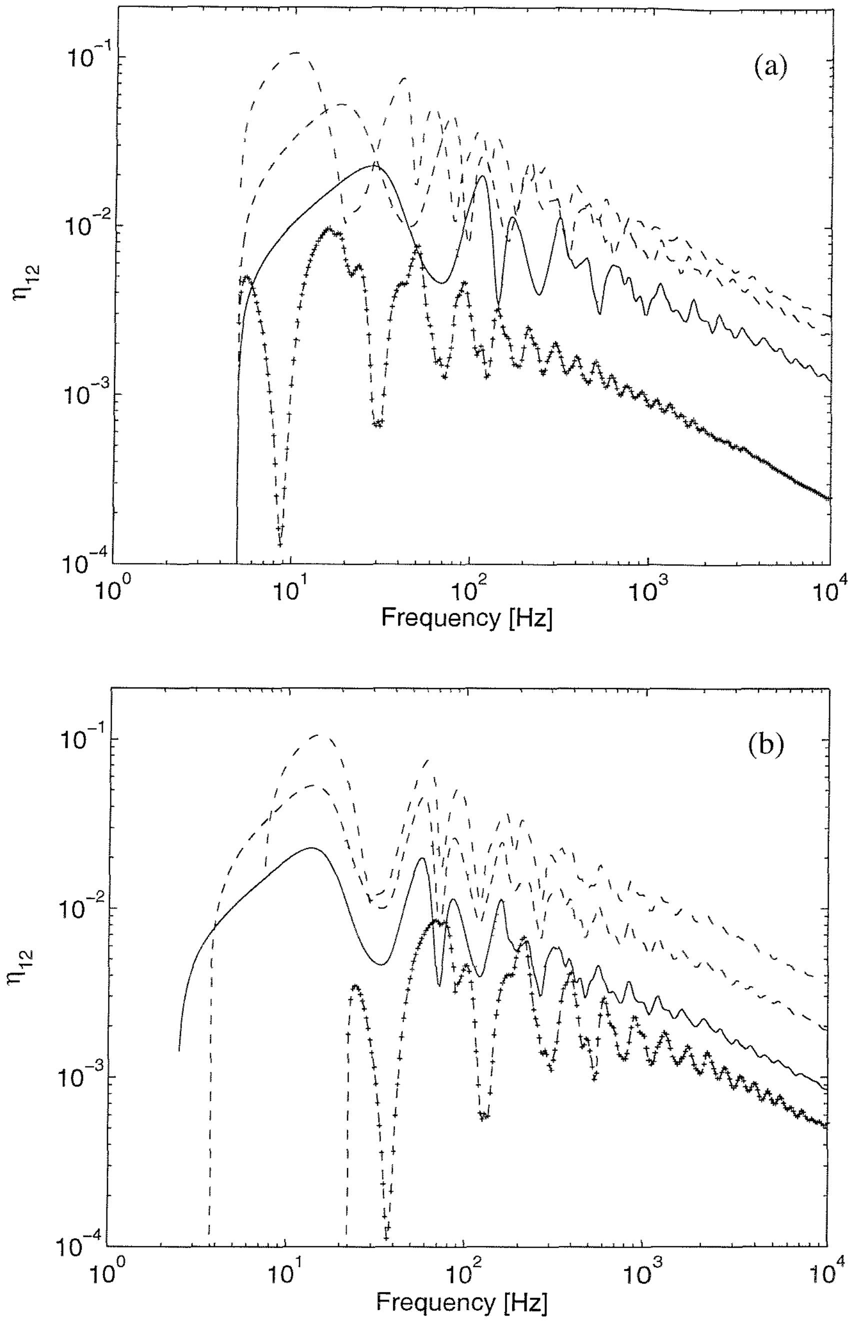

Figure 4.27. The effective CLFs for transmission from a finite source plate (width b = 1 m, length L_1 = 0.5 m) to an infinite receiver plate for different values of h_1/h_2; (a) h_2 is fixed as 2 mm and (b) h_1 is fixed as 3 mm: —, $h_1/h_2 = 3$; ---, $h_1/h_2 = 2$; -·-, $h_1/h_2 = 1$; ····, $h_1/h_2 = 1/2$; -+-, $h_1/h_2 = 1/3$.

To investigate the influence of the modal behaviour of the semi-infinite receiver plate, next the thickness of the receiver plate is varied in the same range relative to the thickness of the finite source plate, which is fixed as 3 mm: the thickness of the semi-infinite receiver plate is varied between 1/3 and 3 times the thickness of the finite source plate. The effective CLFs are shown in Figure 4.27 (b).

As before the energy transmission starts at the cut-on frequency of the semi-infinite receiver plate. The energy transmission varies, as the thickness of the receiver plate is changed. The effective CLF fluctuates at low frequencies and converges to the result of the corresponding infinite plate as shown in Figure 4.24. The peaks and troughs occur at similar frequencies as the thickness of the semi-infinite receiver plate varies. These peaks can therefore be seen to depend on the modal behaviour of the finite source plate, as the thickness of that plate is fixed. Table 4.6 presents the natural frequencies of an uncoupled source plate for different transverse orders, n and two different boundary conditions along the edge usually joined to plate 2.

Table 4.5. The natural frequencies of the uncoupled source plate (width $b = 1$ m, length $L_1 = 0.5$ m, $n = 1$) with 3 simply supported edges and one free edge [F-S-S-S] and with 2 simply supported edges, one clamped edge and one free edge [F-S-C-S].

Thickness h_1 (mm)	F-S-S-S (Hz)	F-S-C-S (Hz)
6	23.6, 111, 314, 636, 1070	33.4, 148, 381, 728, 1200
4	15.8, 74.3, 210, 423, 714	22.3, 98.3, 254, 490, 799
2	7.88, 37.1, 105, 211, 358	11.1, 49.0, 127, 243, 399
1	3.95, 18.6, 39.5, 186, 524	5.58, 24.6, 63.6, 122, 200
0.7	2.61, 12.3, 35.0, 70.4, 119	3.72, 16.4, 42.5, 81.2, 134
3	11.8, 55.8, 157, 318, 536	16.8, 73.8, 191, 367, 602

Table 4.6. The natural frequencies of the uncoupled source plate (thickness $h_1 = 3.0$ mm, length $L_1 = 0.5$ m, width $b = 1$ m) with 3 simply supported edges and one free edge [F-S-S-S] and with 2 simply supported edges, one clamped edge and one free edge [F-S-C-S].

n	F-S-S-S (Hz)	F-S-C-S (Hz)
1	11.8, 55.8, 157, 318, 536, 812	16.8, 73.8, 191, 367, 602, 894
2	34.6, 82.2, 182, 342, 561, 840	37.3, 97.5, 215, 390, 624, 917
3	71.2, 122, 224, 384, 600, 876	72.8, 135, 253, 428, 662, 953
4	122, 175, 279, 439, 658, 930	123, 187, 306, 482, 716
5	188, 242, 348, 510, 730	189, 252, 372, 548, 783
6	267, 323, 431, 597, 812	269, 332, 453, 631, 864

Figure 4.28 compares these natural frequencies for the two different boundary conditions with the ratio between the effective CLFs for a finite source plate ($h_1 = 3$ mm, length $L_1 = 0.5$ m) coupled to a semi-infinite plate of finite width ($b = 1$ m) and the semi-infinite results, $\hat{\eta}_{12}/\eta_{12\infty}$. These natural frequencies are shown for each value of n. When $h_2 \gg h_1$, the semi-infinite receiver plate constrains the finite source plate and the peaks tend towards the natural frequencies for a clamped edge [F-S-C-S]; when $h_2 \ll h_1$, the peaks tend towards those for a simply supported edge [F-S-S-S] as described in Section 4.4.3. However, it is also found that the first resonance corresponds to a peak in the effective CLF, the second to a dip, the third to a peak and so on.

In Figure 4.29, the effective CLF for a finite source plate and semi-infinite receiver plate is compared with the CLF for two semi-infinite plates, for a diffuse field and for 4 transverse orders. Two sets of results are given corresponding to $h_1 = 3$ mm, $L_1 = 0.5$ m, $b = 1.0$ m, $h_2 = 2$ mm and $h_1 = 2$ mm, $L_1 = 1.0$ m, $b = 1.0$ m, $h_2 = 3$ mm. Corresponding modes of the uncoupled source plate are shown, in the first case for F-S-S-S and in the second case for F-S-C-S. The troughs in the effective CLF correspond to the first resonance for a given n (> 1) which in turn correspond approximately to the cut-on frequency of the source plate for $n > 1$.

These results can be understood as follows. At a resonance of the finite plate, the effective angle of incidence is dominated by that corresponding to the mode. Consequently the effective CLF follows closely that for the semi-infinite plates with the corresponding order n. The fluctuations in the effective CLF in this case are therefore due to the predominance of particular angles of incidence, not due to the direct influence of the modal behaviour of the source plate. This explains, also, the relatively small influence of the source plate DLF (Figure 4.25).

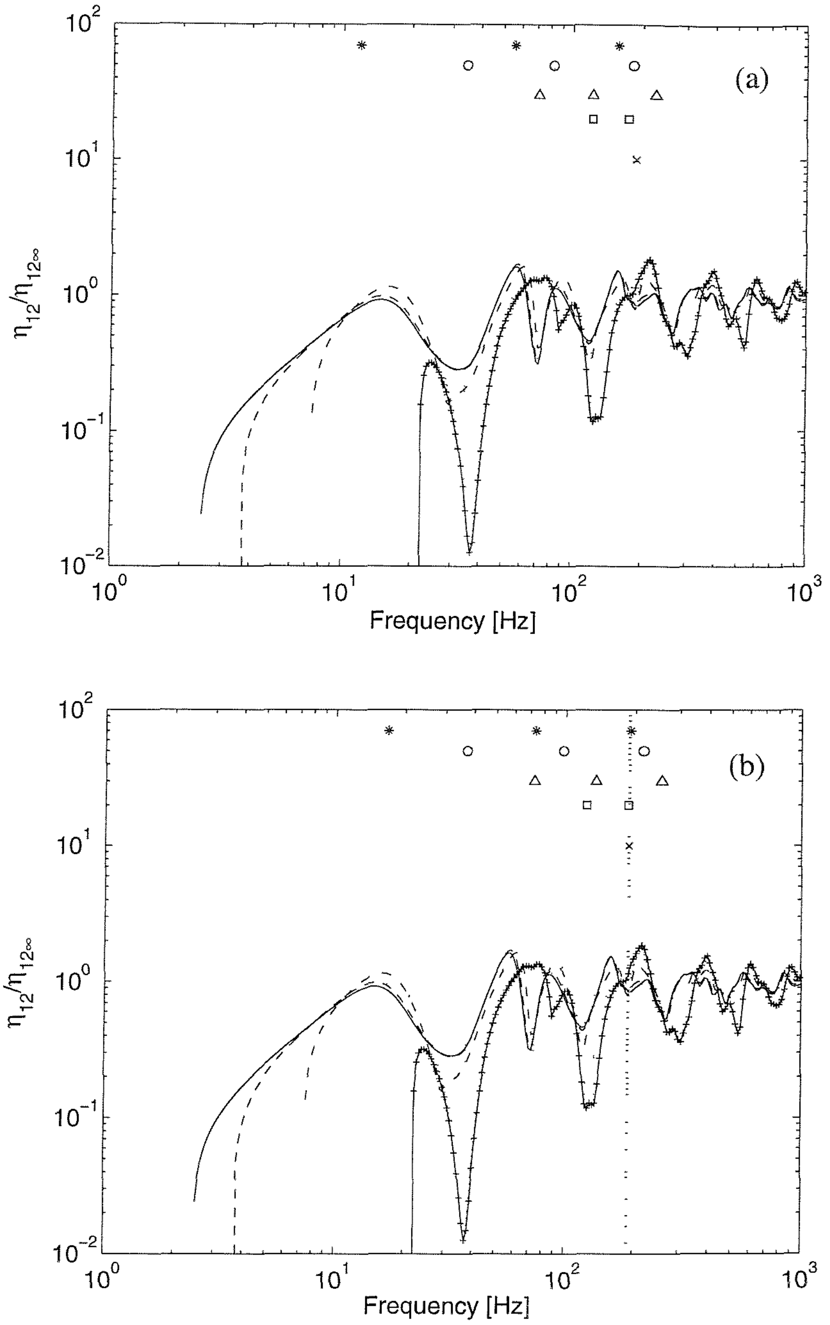

Figure 4.28. The ratio between the effective CLFs for a finite plate ($L_1 = 0.5$ m, $h_1 = 3$ mm) coupled to a semi-infinite plate of finite width ($b = 1$ m) and the semi-infinite results, $\hat{\eta}_{12}/\eta_{12\infty}$: —, $h_2 = 1$ mm; ---, $h_2 = 1.5$ mm; -·-, $h_2 = 3$ mm; ·····, $h_2 = 6$ mm; -+-, $h_2 = 9$ mm. The symbols denote natural frequencies of finite source plate for different boundary conditions along the edge, (a) F-S-S-S and (b) F-S-C-S, and different transverse orders n: *, $n = 1$; o, $n = 2$; △, $n = 3$; □, $n = 4$; ×, $n = 5$. The vertical dotted lines show the natural frequency of each mode.

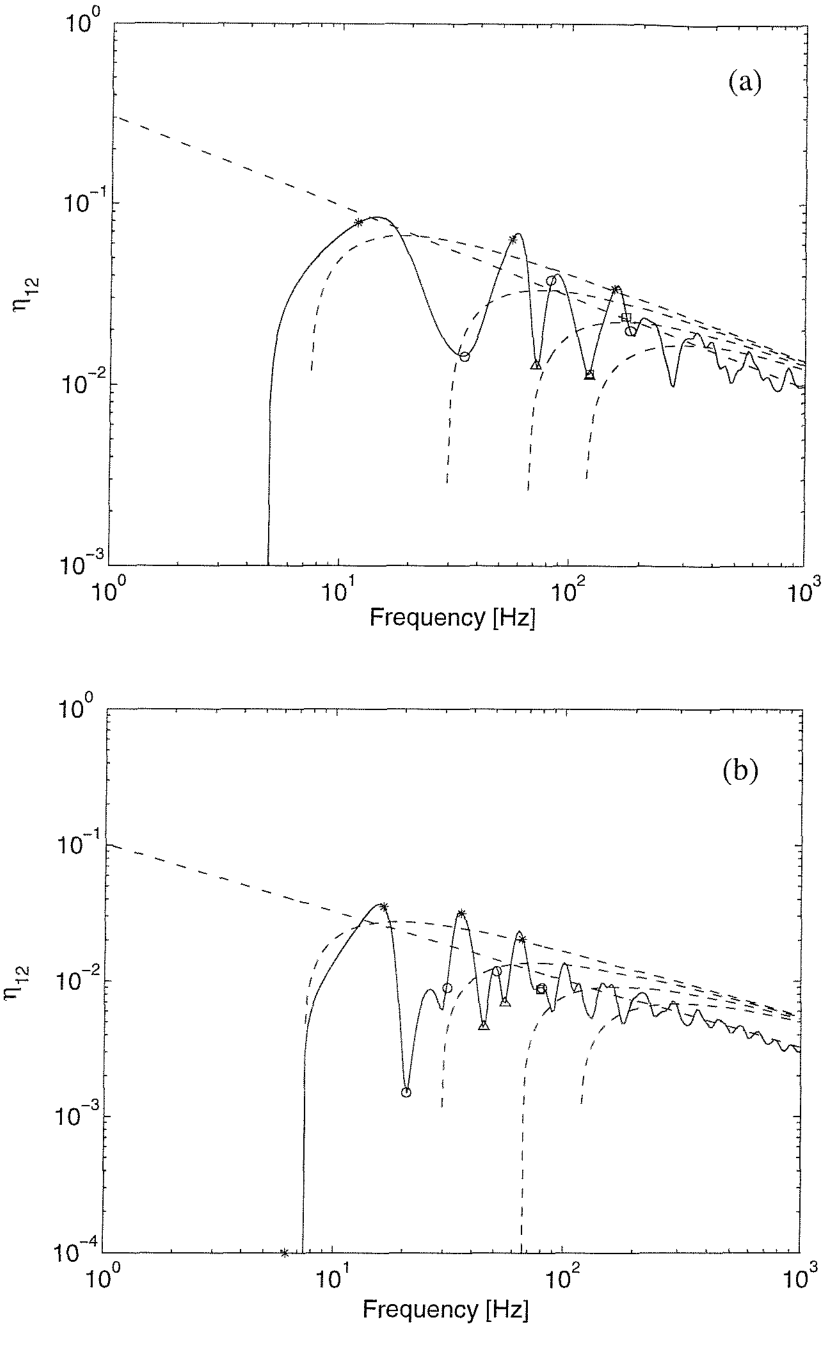

Figure 4.29. Comparison of the CLFs for a finite plate coupled to a semi-infinite plate of finite width, (a) $h_1 = 3$ mm, $h_2 = 2$ mm, $L_1 = 0.5$ m, and (b) $h_1 = 2$ mm, $h_2 = 3$ mm, $L_1 = 1.0$ m: -·-, the CLF for two semi-infinite plates; —, the effective CLF for a finite plate coupled to a semi-infinite plate of finite width ($b = 1$ m); ---, the effective CLFs obtained from equation (3.17) for two semi-infinite plates of finite width ($n = 1$, 2, 3 and 4). The symbols denote natural frequencies of finite source plate for different boundary conditions along the edge, (a) F-S-S-S and (b) F-S-C-S, and different transverse orders n: $*$, $n = 1$; o, $n = 2$; △, $n = 3$; □, $n = 4$.

4.6 Discussion

From the results of a two-plate system, some of the uncertainties in CLF estimates have been examined and quantified. The variability due to modal behaviour in the effective CLF or transmission efficiency has been examined using a systematic investigation involving finite width semi-infinite plates and finite plates.

The effective CLF for a finite two-plate system has been directly evaluated using the DSM. The effective CLF for finite plates fluctuates at low frequencies (low modal overlap) and converges to that for semi-infinite plates at high frequencies, as expected. It has been shown that the consistency relationship is satisfied by the predicted CLF at high frequencies, although at low frequencies considerable variation is found.

The spatial location and the number of forcing points used also affect the confidence intervals of the effective CLF. As the number of forcing points increases, the effective CLF estimates become more reliable. For 400 forcing points it can be expected that the uncertainty will be reduced to ±0.25 dB. In order to obtain a 90% confidence interval of ±1.5 dB at least 10 forcing points should be taken.

Examination of the effective CLF has shown that its fluctuations can be related to the ratio between the energy of the source plate and that of the receiver plate, and the modal behaviour of the source or receiver plate or both. At low frequencies, in the region of the first few modes, the effective CLF estimates and the energy ratio contain peaks which correspond to the uncoupled modes of the receiver plate. If the energy of the source plate is much larger than that of the receiver plate, the energy ratio is small and there are no peaks in the energy ratio, although peaks occur in the energy results.

The variability in the effective coupling loss factor, or the transmission efficiency, due to the modal behaviour of the finite coupled subsystems, has been examined using a systematic investigation involving both finite width semi-infinite and finite plates.

It was shown that the modal behaviour of both the source and receiver plates affects the energy transmission between two subsystems. Large variability in the energy transmission was found to be due to the modal behaviour of the receiver plate, with peaks occurring in the transmission efficiency at resonances of the receiver. The damping of the receiver plate controls the magnitude of these variations. However, variations in the energy transmission can also be attributed to the source subsystem characteristics, as seen for the finite source plate coupled to a semi-infinite receiver plate. This variation is due to the predominance of particular angles of incidence at a given frequency. Both peaks and troughs in the effective CLF correspond to natural frequencies of the uncoupled source plate. The damping of the source plate has only a small influence. Figure 4.30 summarises these trends by comparing the CLFs found for a finite receiver or a finite source plate, taken from Figures 4.17 (b) and 4.24 (a).

The next two chapters aim to quantify the limits of the variability in the effective CLF using a wide range of parameter investigations which will incorporate both variations in modal density and modal overlap, either together or separately, in finite plate simulations.

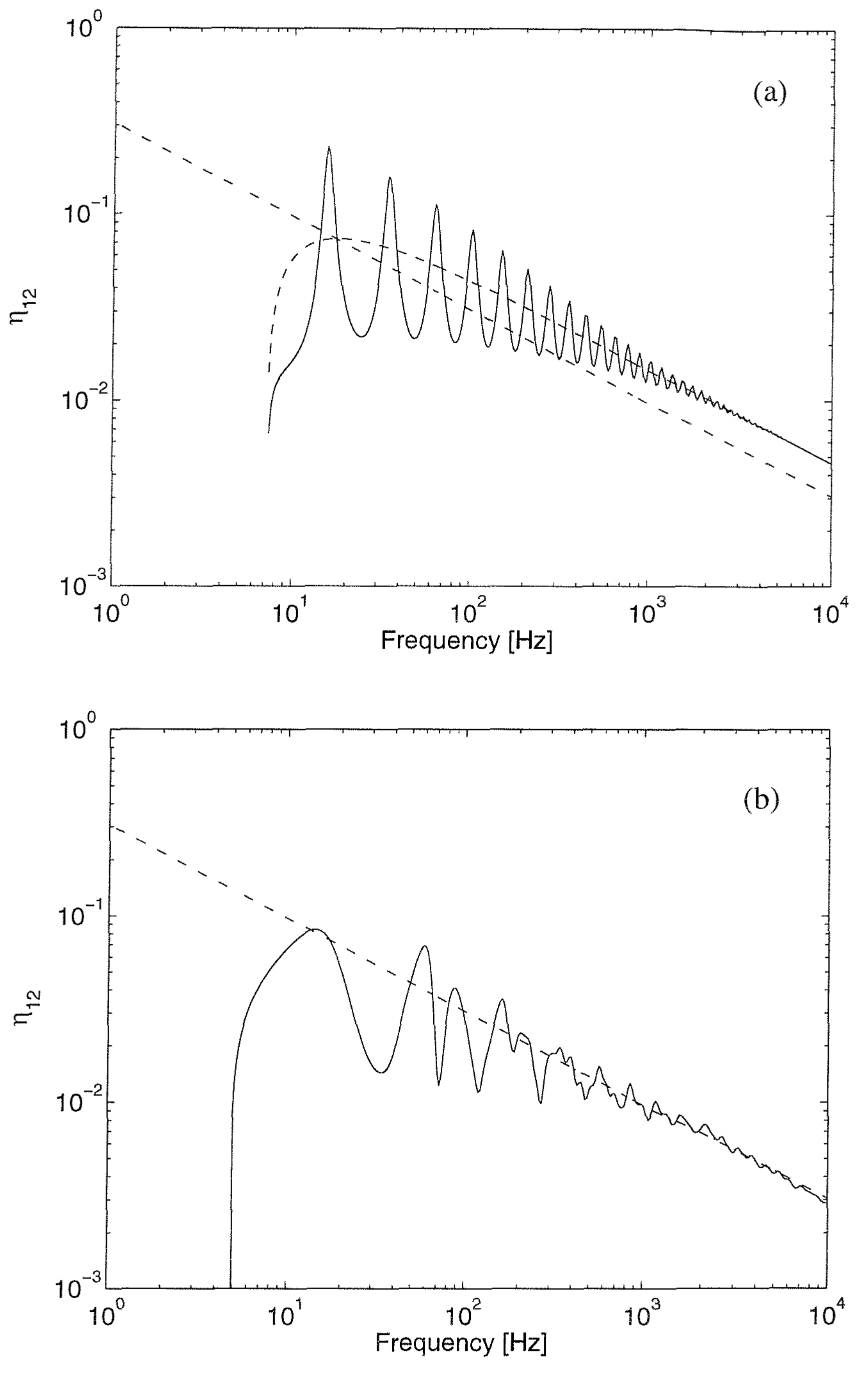

Figure 4.30. Comparison of the CLFs predicted using two different models ($h_1 = 3$ mm, $h_2 = 2$ mm, $L_1 = 0.5$ m, $L_2 = 1.0$ m, $b = 1$ m); (a) semi-infinite source plate ($\eta_1 = 0$) coupled to a finite receiver plate ($n = 1$, $\eta_2 = 0.1$), and (b) finite source plate ($\eta_1 = 0.1$) coupled to a semi-infinite receiver plate ($n = 1$ up to 46, $\eta_2 = 0$): —, the effective CLF for model (a) or (b); -·-, the CLF for two semi-infinite plates; ---, the effective CLF obtained from equation (3.17) for two semi-infinite plates of finite width ($n = 1$).

CHAPTER 5

INITIAL PARAMETRIC INVESTIGATION

5.1 Introduction

This chapter describes an initial parametric investigation into the variability of the effective CLF. One objective is to identify the most appropriate parameter, *e.g.* modal overlap, against which to plot the results and the other is to evaluate Craik's bounds [44] described in Section 3.6.

A sensitivity analysis has been performed using the DSM model for two finite plates described in Chapter 4 to evaluate the influence of the following parameters: (i) the plate thickness ratio, h_1/h_2, (ii) the length ratio, L_1/L_2, (iii) the length-to-width ratio of the two plates L_1/b and (iv) the DLFs which are assumed equal, $\eta_1 = \eta_2$. The two plates are both simply supported along two opposite edges, connected at right angles and free at their outer edges. In-plane vibration is included in the model as well as flexure. The widths of the two plates are the same, $b_1 = b_2$ for all cases, as required by the DSM. As in previous chapters the material properties of aluminium are used.

In the calculations for the parameter variations of (i) and (ii), the dimensions of plate 1 ($L_1 = 0.5$ m, $b = 1.0$ m, $h_1 = 3$ mm) are kept fixed and the relevant dimensions of plate 2 are given by 11 logarithmically spaced values between 0.316 and 3.16 times that for plate 1. For (iii), the widths of the two plates are given by 11 logarithmically spaced values between 0.316 L_1 and 3.16 L_1. The DLFs considered for (iv) are $\eta_1 = \eta_2 = 0.03$, 0.1 and 0.3. In all the other cases, the same values of the DLF are used, $\eta_1 = \eta_2 = 0.1$.

The effective CLFs $\hat{\eta}_{ij}$ for the finite plates and the corresponding semi-infinite plate results $\eta_{ij\infty}$ are determined for these parameter variations. The results are plotted in terms of the CLF ratio in dB between the effective CLFs for the finite plates and the semi-infinite results, $10\log_{10}\left(\hat{\eta}_{ij}/\eta_{ij\infty}\right)$, in each case as a function of frequency. The results are also plotted against the modal overlap factor given by equation (3.23), which depends on the modal density, damping and frequency.

Craik *et al.* [44] proposed that the fluctuations in the coupling are related to the fluctuations in the point mobility of the receiving subsystems. However, it was found in Chapter 4 that the modal behaviour of both the source and receiver subsystems affects the energy transmission for two subsystems. In order to investigate which parameter is most appropriate to represent the variability of the CLFs, the results are plotted against the modal overlap factor for the source plate M_1, that for the receiver plate M_2, and the geometric mean modal overlap factor M_{12} as used by Mohammed [43], $M_{12} = (M_1 M_2)^{1/2}$. Also shown, at low modal overlap, are estimates of the upper and lower bounds, equations (3.38) and (3.39), as given by [44]. These are based on the appropriate value of modal overlap factor, M_1, M_2 or M_{12}.

5.2 Thickness ratio

The thickness of plate 1 ($h_1 = 3$ mm) was kept fixed and the thicknesses of plate 2 were given by 11 logarithmically spaced values between 3.16 and 0.316 times that for plate 1. The parameters used in this set of calculations are summarised in Table 5.1. The damping values of the two plates were constant at all frequencies, $\eta_1 = \eta_2 = 0.1$ so that, as a result, modal overlap factors obtained from equation (3.23) increase with frequency (the modal density of each plate $n(\omega)$ is constant from equation (3.16), η is constant so $M \propto \omega$). The cut-on frequency, where wave propagation begins, was calculated by using equation (2.76) and is listed in Table 5.1.

The effective CLFs were evaluated using the DSM and the semi-infinite plate results were obtained from equation (3.17). The ratio (in dB) between the effective CLF and the semi-infinite result, $10\log_{10}\left(\hat{\eta}_{ij} / \eta_{ij\infty}\right)$, obtained for different values of the thickness ratio is plotted against frequency in Figure 5.1. The results below the lower of the first cut-on frequencies have been excluded, as SEA assumptions would not be valid and it is inappropriate to use an SEA approach. At low frequencies, the variability of the effective CLFs is particularly large, while it generally reduces as frequency increases. The case of $h_2 = 9.49$ mm, however, shows large variation at high frequencies due to the influence of in-plane motion (see Figure 5.2).

Table 5.1. Variants studied to show the effect of varying the plate thickness ratio h_1/h_2.

h_1/h_2	h_1 (mm)	h_2 (mm)	L_1 (m)	L_2 (m)	b (m)	$n_1(\omega)$	$n_2(\omega)$	$f_{\text{cut-on, 1}}$	$f_{\text{cut-on, 2}}$
0.316	3.00	9.49	0.50	1.00	1.00	0.0085	0.0054	7.34	23.2
0.398	3.00	7.54	0.50	1.00	1.00	0.0085	0.0068	7.34	18.5
0.501	3.00	5.99	0.50	1.00	1.00	0.0085	0.0085	7.34	14.7
0.631	3.00	4.75	0.50	1.00	1.00	0.0085	0.011	7.34	11.6
0.793	3.00	3.78	0.50	1.00	1.00	0.0085	0.014	7.34	9.25
1.00	3.00	3.00	0.50	1.00	1.00	0.0085	0.017	7.34	7.34
1.26	3.00	2.38	0.50	1.00	1.00	0.0085	0.022	7.34	5.83
1.58	3.00	1.89	0.50	1.00	1.00	0.0085	0.027	7.34	4.63
2.00	3.00	1.50	0.50	1.00	1.00	0.0085	0.034	7.34	3.67
2.51	3.00	1.19	0.50	1.00	1.00	0.0085	0.043	7.34	2.91
3.16	3.00	0.949	0.50	1.00	1.00	0.0085	0.054	7.34	2.32

The first resonances for the two uncoupled plates, with either simply supported (F-S-S-S) or clamped boundary condition (F-S-C-S) at the interface for the 11 variants (for transverse order $n = 1$) were obtained from the frequency functions (*i.e.* $\left(\det(\mathbf{K})\right)^{-1}$) of the DSM models. The first resonance frequencies for the two uncoupled plates and the first peak frequencies in $\hat{\eta}_{12}/\eta_{12\infty}$ and $\hat{\eta}_{21}/\eta_{21\infty}$ are listed in Table 5.2.

The first peaks in the CLF ratio correspond to the resonances of either the uncoupled receiver or source plate, as discussed in Chapter 4. The first peaks of $10\log_{10}\left(\hat{\eta}_{12}/\eta_{12\infty}\right)$ correspond to the first resonances of the uncoupled receiver plate (plate 2) with either simply supported (F-S-S-S) or clamped boundary condition (F-S-C-S) at the interface, listed in Table 5.2. Thus the first peaks apparently move to the left as the thickness of plate 2 decreases, as seen in Figure 5.1 (a). The first peaks of $10\log_{10}\left(\hat{\eta}_{21}/\eta_{21\infty}\right)$ are found to occur between the first cut-on frequency of the receiver plate (plate 1), 7.34 Hz, and the first resonance frequencies of the receiver plate with either F-S-S-S or F-S-C-S, listed in Table 5.2.

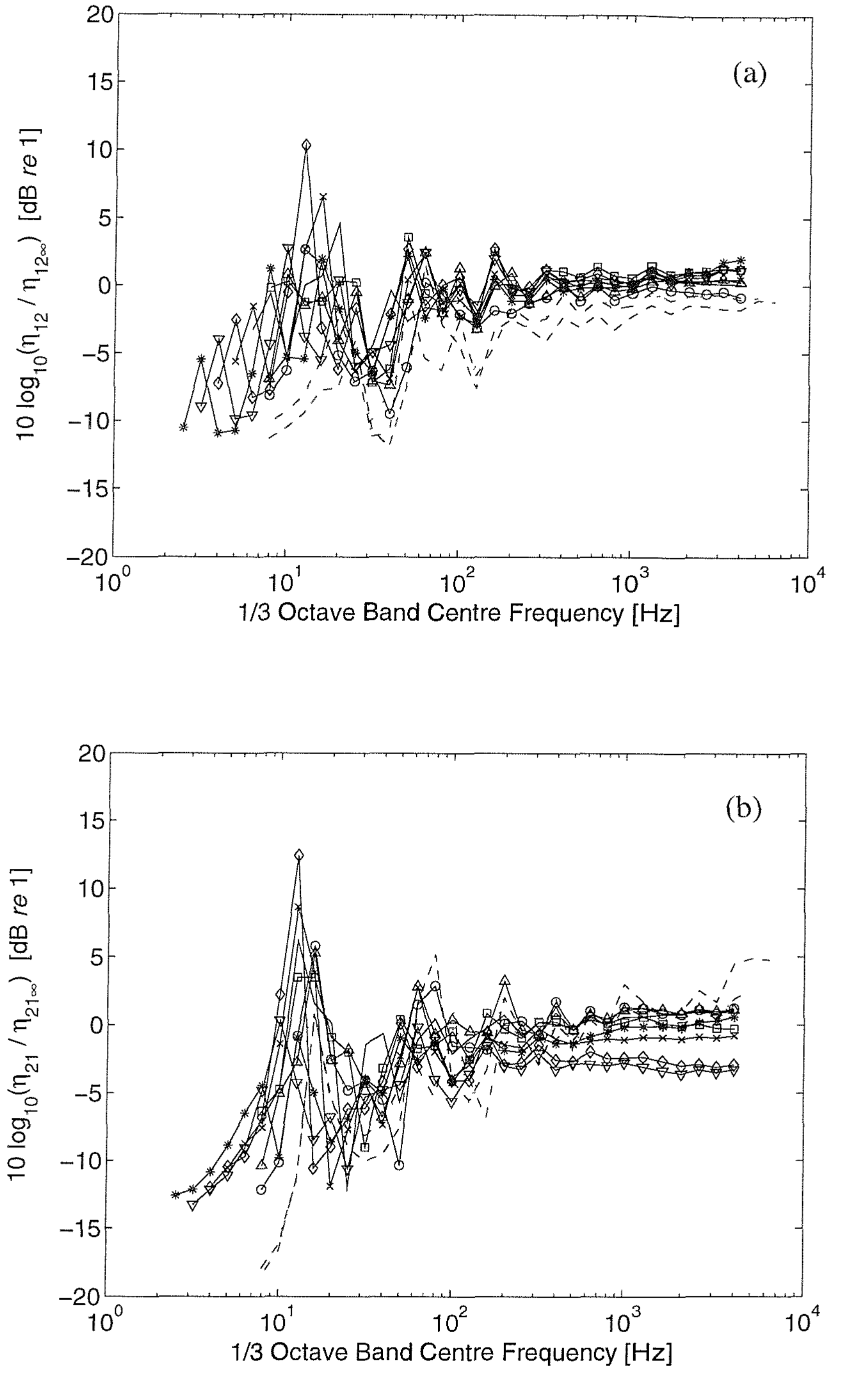

Figure 5.1. CLF ratio, (a) $10\log_{10}\left(\hat{\eta}_{12}/\eta_{12\infty}\right)$ and (b) $10\log_{10}\left(\hat{\eta}_{21}/\eta_{21\infty}\right)$, for different values of the thickness ratio (h_1/h_2) plotted against frequency; the thickness of plate 1 is fixed (3 mm) and the thickness of plate 2 (in millimetres) varies from 9.49 to 0.949: ---, 9.49; -·-, 7.54; ·····, 5.99; -o-, 4.75; -△-, 3.78; -□-, 3.00; —, 2.38; -x-, 1.89; -◇-, 1.50; -▽-,1.19; -*-, 0.949.

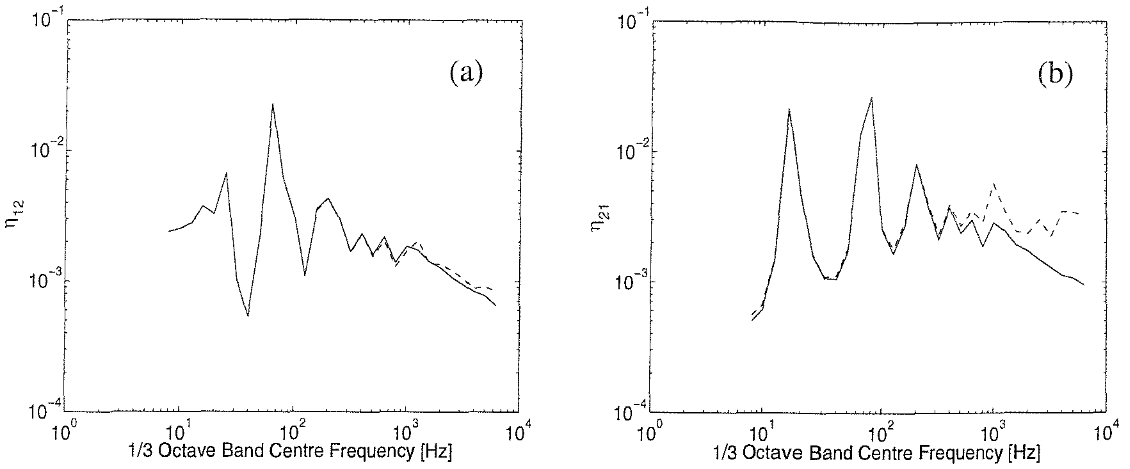

Figure 5.2. The effective CLF, (a) $\hat{\eta}_{12}$ and (b) $\hat{\eta}_{21}$, for $h_1/h_2 = 0.316$ (the thickness of plate 1 is 3 mm and the thickness of plate 2 is 9.49mm) plotted against frequency: —, flexural motion only; ---, inclusion of in-plane motion.

Table 5.2. The first resonance frequencies obtained from the frequency functions (*i.e.* $(\det(\mathbf{K}))^{-1}$), for the two uncoupled plates of the 11 variants of h_1/h_2 (for transverse order $n = 1$) and the first peak frequencies in $\hat{\eta}_{12}/\eta_{12\infty}$ and $\hat{\eta}_{21}/\eta_{21\infty}$.

h_1/h_2	Plate 1		Plate 2		$\hat{\eta}_{12}/\eta_{12\infty}$	$\hat{\eta}_{21}/\eta_{21\infty}$
	F-S-S-S	F-S-C-S	F-S-S-S	F-S-C-S		
0.316	11.8	16.8	27.2	29.6	25	16
0.398	11.8	16.8	21.7	23.6	20	16
0.501	11.8	16.8	17.2	18.6	16	16
0.631	11.8	16.8	13.7	14.9	12.5	16
0.793	11.8	16.8	10.9	11.7	10	16
1.00	11.8	16.8	8.62	9.35	8.8	14
1.26	11.8	16.8	6.85	7.42	8.0	12.5
1.58	11.8	16.8	5.44	5.89	6.3	12.5
2.00	11.8	16.8	4.32	4.68	5.0	12.5
2.51	11.8	16.8	3.42	3.71	4.0	10
3.16	11.8	16.8	2.73	2.96	3.15	8.0

Figure 5.3 shows the same results as Figure 5.1, but plotted now against three different modal overlap factors. Also shown are estimates of the upper and lower bounds as given by Craik *et al.* [44]. These bounds are only shown for low modal overlap ($M < 0.4$), where the upper bound is positive and the lower is negative.

The upper plots show the results plotted against the modal overlap factor of the source plate. As the thickness of plate 2 decreases, the first resonance frequencies of the uncoupled receiver plate decrease, and the first peak moves to the left when plotted against M_1 (see Table 5.2 and Figure 5.3 (a) $10\log_{10}\left(\hat{\eta}_{12}/\eta_{12\infty}\right)$). For $10\log_{10}\left(\hat{\eta}_{21}/\eta_{21\infty}\right)$, the first peak moves to the right, since the modal density of the source plate ($n_2(\omega)$) is inversely proportional to the thickness of this plate whereas the first resonance of plate 1 is kept fixed (see Table 5.2 and Figure 5.3 (a) $10\log_{10}\left(\hat{\eta}_{21}/\eta_{21\infty}\right)$). Conversely, when plotted against the modal overlap factor for the receiver plate, the peaks stay roughly fixed even though the thickness of plate 2 varies (see Figure 5.3 (b)). This can also be identified from the cut-on frequency ($f_{\text{cut-on}}$) of the receiver plate and its modal density, *i.e.* $f_{\text{cut-on}} \propto h$ and $n(\omega) \propto 1/h$; thus the cut-on frequency corresponds to a value of M that is independent of h. The lower plots show the results plotted against the geometric average M_{12}.

At low modal overlap the CLF ratio, $10\log_{10}\left(\hat{\eta}_{ij}/\eta_{ij\infty}\right)$, fluctuates considerably and most results are seen to fall between estimates of the upper and lower bounds. The percentage of values of $10\log_{10}\left(\hat{\eta}_{ij}/\eta_{ij\infty}\right)$ falling between estimates of the upper and lower bounds are discussed in the last section of this chapter.

Figure 5.4 shows the results in the form of the ratio (in dB) between the effective CLF and the *ensemble* average result $\eta_{ij,ens}$, $10\log_{10}\left(\hat{\eta}_{ij}/\eta_{ij,ens}\right)$. These results are shifted up at low frequencies compared to the previous results since the ensemble average CLFs are smaller than the semi-infinite results, as shown in Figure 3.2.

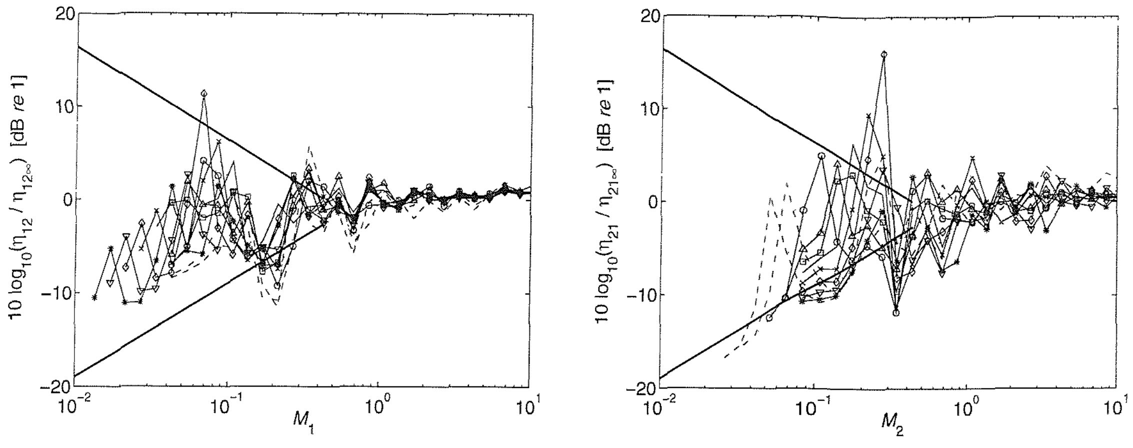

(a) CLF ratio plotted against the modal overlap factor for the source plate.

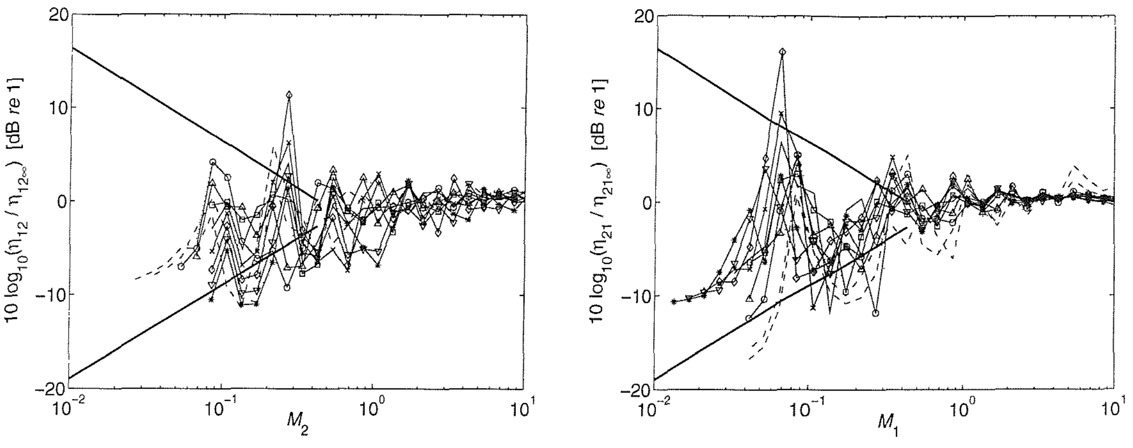

(b) CLF ratio plotted against the modal overlap factor for the receiver plate.

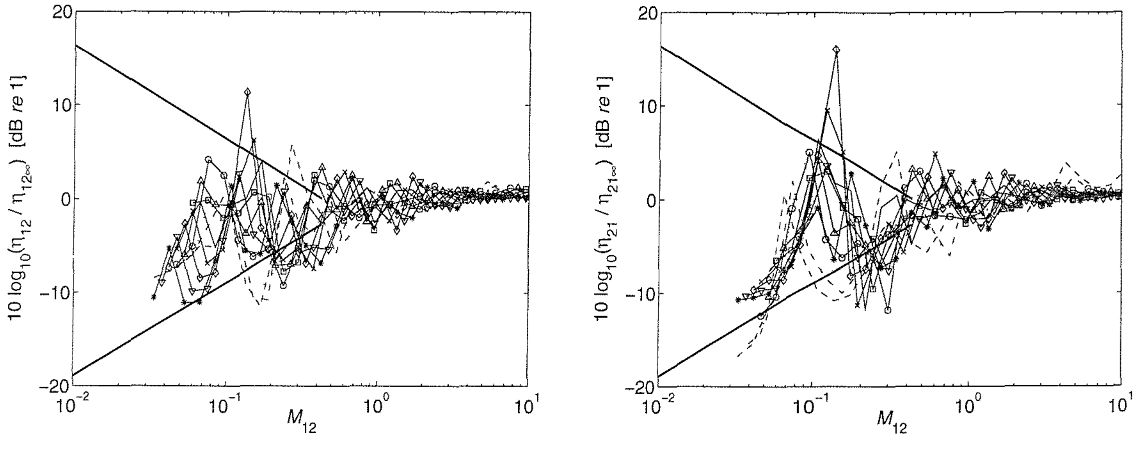

(c) CLF ratio plotted against the geometric mean modal overlap factor [M_{12}].

Figure 5.3. CLF ratio $10\log_{10}\left(\hat{\eta}_{ij}/\eta_{ij\infty}\right)$ for different values of the thickness ratio (h_1/h_2) plotted against the source, receiver and mean modal overlap factor; the thickness of plate 1 is fixed (3 mm) and the thickness of plate 2 (in millimetres) varies from 9.49 to 0.949: ---, 9.49; -·-, 7.54; ·····, 5.99; -o-, 4.75; -Δ-, 3.78; -□-, 3.00; —, 2.38; -x-, 1.89; -◇-, 1.50; -▽-,1.19; -*-, 0.949; —, estimates of the upper and lower bounds from equations (3.38) and (3.39).

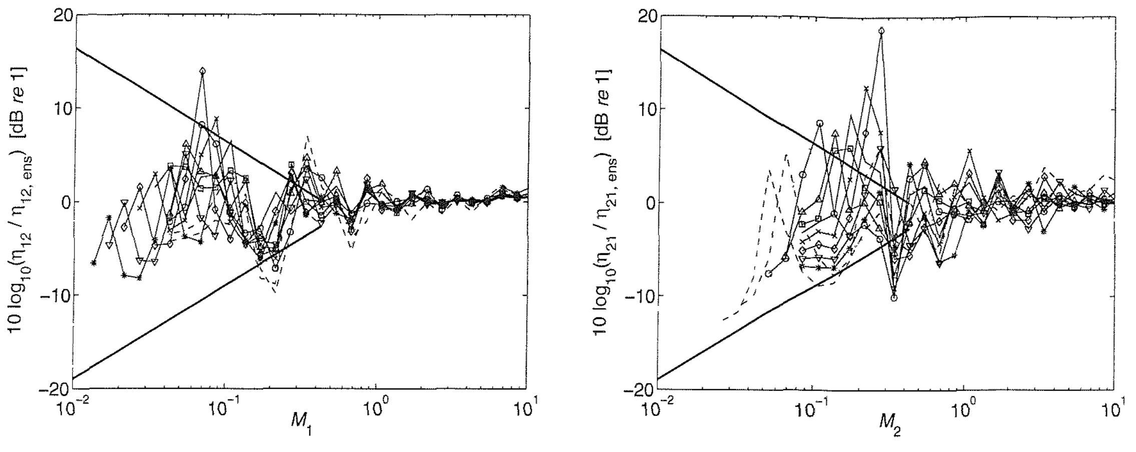

(a) CLF ratio plotted against the modal overlap factor for the source plate.

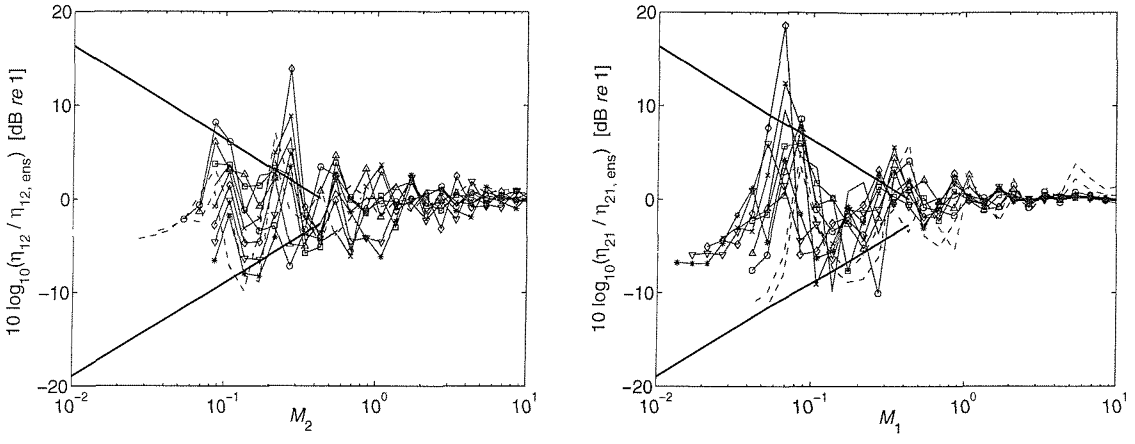

(b) CLF ratio plotted against the modal overlap factor for the receiver plate.

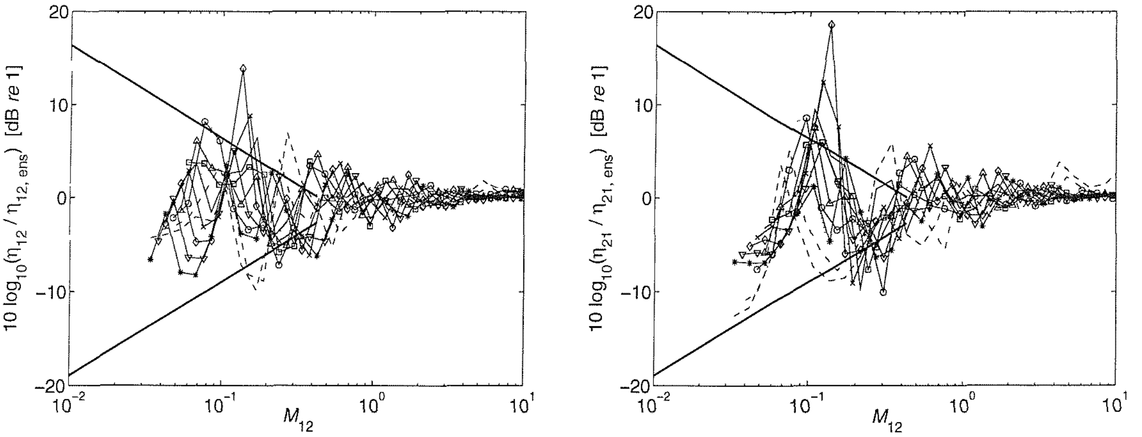

(c) CLF ratio plotted against the geometric mean modal overlap factor [M_{12}].

Figure 5.4. CLF ratio $10\log_{10}\left(\hat{\eta}_{ij} / \eta_{ij.ens}\right)$ for different values of the thickness ratio (h_1/h_2) plotted against the source, receiver and mean modal overlap factor; the thickness of plate 1 is fixed (3 mm) and the thickness of plate 2 (in millimetres) varies from 9.49 to 0.949: ---, 9.49; -·-, 7.54; ·····, 5.99; -o-, 4.75; -Δ-, 3.78; -□-, 3.00; —, 2.38; -x-, 1.89; -◇-, 1.50; -▽-,1.19; -*-, 0.949; —, estimates of the upper and lower bounds from equations (3.38) and (3.39).

5.3 Length ratio

The influence of the plate length ratio L_1/L_2 on the effective CLF was investigated by keeping the length of plate 1 fixed and giving the length of plate 2 each of 11 logarithmically spaced values between 3.16 and 0.316 times that for plate 1, as listed in Table 5.3. The damping values of the two plates were constant at all frequencies $\eta_1 = \eta_2 = 0.1$. As the thicknesses of the plates do not vary, the cut-on frequency for each case is the same, since it is independent of the length of the plate.

Table 5.3. Variants studied to show the effect of varying the plate length ratio L_1/L_2.

L_1/L_2	h_1 (mm)	h_2 (mm)	L_1 (m)	L_2 (m)	b (m)	$n_1(\omega)$	$n_2(\omega)$	$f_{\text{cut-on, 1}}$	$f_{\text{cut-on, 2}}$
0.316	3.00	2.00	0.50	1.58	1.00	0.0085	0.040	7.34	4.90
0.398	3.00	2.00	0.50	1.26	1.00	0.0085	0.032	7.34	4.90
0.501	3.00	2.00	0.50	1.00	1.00	0.0085	0.026	7.34	4.90
0.631	3.00	2.00	0.50	0.79	1.00	0.0085	0.020	7.34	4.90
0.793	3.00	2.00	0.50	0.63	1.00	0.0085	0.016	7.34	4.90
1.00	3.00	2.00	0.50	0.50	1.00	0.0085	0.013	7.34	4.90
1.26	3.00	2.00	0.50	0.40	1.00	0.0085	0.010	7.34	4.90
1.58	3.00	2.00	0.50	0.32	1.00	0.0085	0.0081	7.34	4.90
2.00	3.00	2.00	0.50	0.25	1.00	0.0085	0.0064	7.34	4.90
2.51	3.00	2.00	0.50	0.20	1.00	0.0085	0.0051	7.34	4.90
3.16	3.00	2.00	0.50	0.158	1.00	0.0085	0.0040	7.34	4.90

The ratio (in dB) between the effective CLF and the semi-infinite result, $10\log_{10}\left(\hat{\eta}_{ij} / \eta_{ij\infty}\right)$, is plotted against frequency in Figure 5.5 for these variants. The results are only shown for frequencies above the lower of the first cut-on frequencies, as described in Section 5.2. At low frequencies, the variability of the effective CLFs is again large and then it gradually reduces as frequency increases.

The first resonance frequencies for the two uncoupled plates of the 11 variants (for transverse order $n = 1$) were obtained from the frequency functions (*i.e.* $\left(\det(\mathbf{K})\right)^{-1}$) of the DSM models, as in the previous section. These resonance frequencies and the first peak frequencies in $\hat{\eta}_{12}/\eta_{12\infty}$ and $\hat{\eta}_{21}/\eta_{21\infty}$ are also listed in Table 5.4.

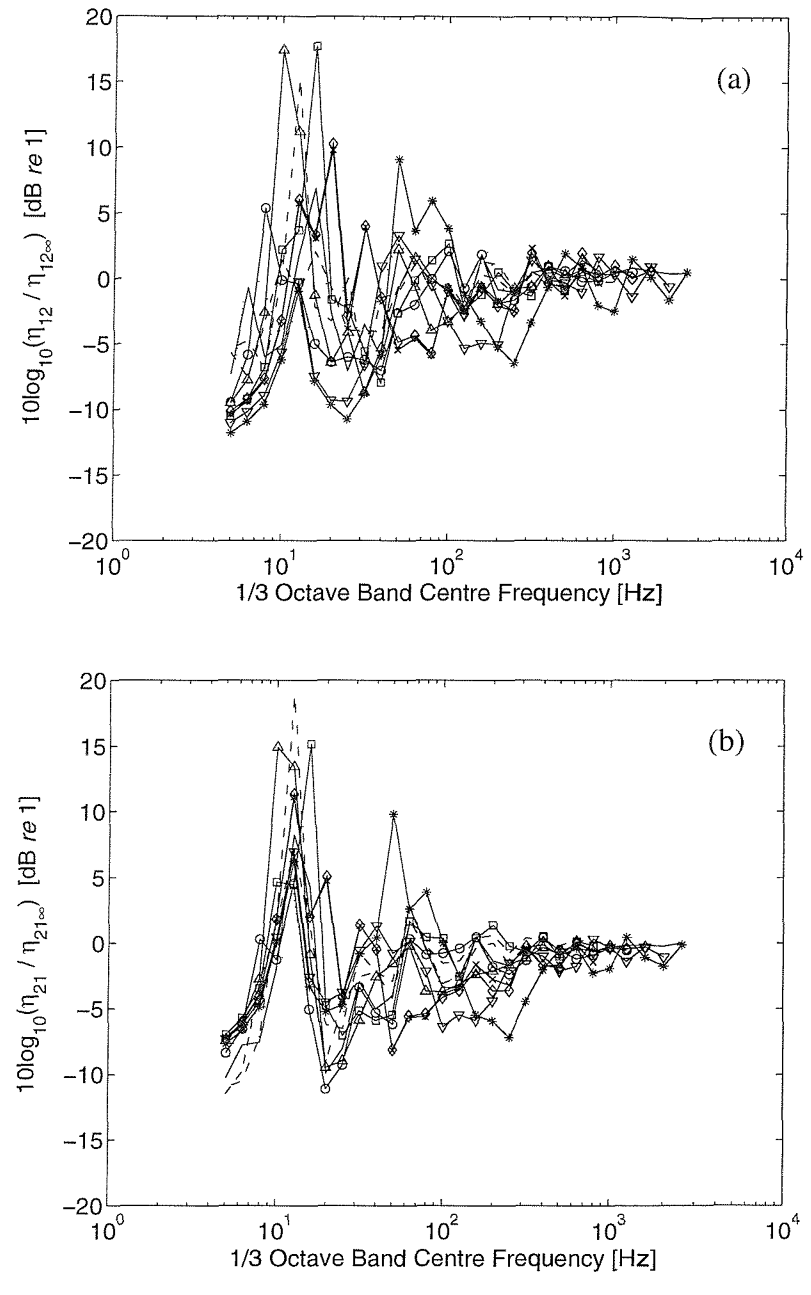

Figure 5.5. CLF ratio, (a) $10\log_{10}(\hat{\eta}_{12}/\eta_{12\infty})$ and (b) $10\log_{10}(\hat{\eta}_{21}/\eta_{21\infty})$, for different values of the length ratio (L_1/L_2) plotted against frequency; the length of plate 1 is fixed (0.5 m) and the length of plate 2 (in metres) varies from 1.58 to 0.158: ---, 1.58; -·-, 1.26; —, 1.0; ·····, 0.79; -o-, 0.63; -Δ-, 0.50; -□-, 0.40; -x-, 0.32; -◊-, 0.25; -v-,0.20; -*-, 0.158.

The first peaks in the CLF ratio correspond to the first resonances of the two uncoupled plates with either simply supported (F-S-S-S) or clamped boundary condition (F-S-C-S) at the interface, as listed in Table 5.4. The first resonance of the uncoupled receiver plate (plate 2) increases as the length of plate 2 decreases, whereas that of the source plate does not vary since the dimensions of plate 1 are kept fixed. The first peak in $10\log_{10}(\hat{\eta}_{12}/\eta_{12\infty})$ (Figure 5.5 (a)) moves to the right as the length of plate 2 decreases while the resonance frequency of the receiver plate is less than that of the source plate. However, for the last three cases in Table 5.4, the resonance frequency of the receiver plate is greater than that of the source plate, and it is the latter which determines the peak. For the result of $10\log_{10}(\hat{\eta}_{21}/\eta_{21\infty})$ in Figure 5.5 (b) the first peaks are roughly fixed at 12.5 Hz even though the length of plate 2 varies. When the length of plate 2 is much smaller than that of plate 1, the first peak frequencies in $10\log_{10}(\hat{\eta}_{12}/\eta_{12\infty})$ and $10\log_{10}(\hat{\eta}_{21}/\eta_{21\infty})$ are the same (see the italic values in Table 5.4).

Table 5.4. The first resonance frequencies obtained from the frequency functions (*i.e.* $(\det(\mathbf{K}))^{-1}$), for the two uncoupled plates of the 11 variants of L_1/L_2 (for transverse order $n = 1$) and the first peak frequencies in $\hat{\eta}_{12}/\eta_{12\infty}$ and $\hat{\eta}_{21}/\eta_{21\infty}$.

L_1/L_2	Plate 1		Plate 2		$\hat{\eta}_{12}/\eta_{12\infty}$	$\hat{\eta}_{21}/\eta_{21\infty}$
	F-S-S-S	F-S-C-S	F-S-S-S	F-S-C-S		
0.316	11.8	16.8	5.25	5.36	5.0	12.5
0.398	11.8	16.8	5.42	5.67	5.6	12.5
0.501	11.8	16.8	5.75	6.23	6.3	12.5
0.631	11.8	16.8	6.23	7.18	7.1	12.5
0.793	11.8	16.8	6.92	8.68	8.0	12.5
1.00	11.8	16.8	7.88	11.2	10	10
1.26	11.8	16.8	9.18	15.0	16	16
1.58	11.8	16.8	10.9	21.1	*12.5*	*12.5*
2.00	11.8	16.8	13.4	31.9	*12.5*	*12.5*
2.51	11.8	16.8	16.3	47.6	*12.5*	*12.5*
3.16	11.8	16.8	20.3	73.9	*12.5*	*12.5*

The CLF ratio in dB is plotted in Figure 5.6 against the three different modal overlap factors, M_1, M_2 and M_{12}. Estimates of the upper and lower bounds are again shown for low modal overlap ($M < 0.4$). The CLF ratios plotted against M_1, $10\log_{10}(\hat{\eta}_{12}/\eta_{12\infty})$ in Figure 5.6 (a) and $10\log_{10}(\hat{\eta}_{21}/\eta_{21\infty})$ in Figure 5.6 (b), are similar to the results plotted against frequency in Figure 5.5 since the modal density of plate 1 is kept constant and the frequency axis in Figure 5.5 is only replaced by M_1. The first peaks of the results plotted against M_2, $10\log_{10}(\hat{\eta}_{21}/\eta_{21\infty})$ plotted in Figure 5.6 (a) and $10\log_{10}(\hat{\eta}_{12}/\eta_{12\infty})$ in Figure 5.6 (b), move to the left as the length of plate 2 is decreased since the modal density of plate 2 is proportional to the length of plate 2. The lower plots show the results plotted against the geometric average M_{12}.

Note that the results of three of the 11 cases are outside bounds at the first or the second peak by up to 10 dB. These are two cases where the lengths of plate 2 ($L_2 = 0.63$ m and $L_2 = 0.50$ m) are similar to that of plate 1 ($L_1 = 0.50$ m) and the other case where the lengths are dissimilar ($L_2 = 1.26$ m and $L_1 = 0.50$ m). It was found that the first resonance frequencies of the two uncoupled plates are close to each other when the lengths of two plates are similar (see the shaded values in Table 5.4) and the peaks in both $10\log_{10}(\hat{\eta}_{12}/\eta_{12\infty})$ and $10\log_{10}(\hat{\eta}_{21}/\eta_{21\infty})$ are large at the same frequency (see △ and □ in Figure 5.5).

5.4 Length-to-width ratio

The influence of the plate length-to-width ratio L_1/b on the effective CLF was investigated by keeping the length of both plates fixed and giving the widths of both plates each of 11 logarithmically spaced values between 3.16 and 0.316 times the length of plate 1. The damping values of the two plates were again constant at all frequencies $\eta_1 = \eta_2 = 0.1$. Table 5.5 below summarises the configurations investigated. The cut-on frequencies for the two plates varied, as $f_{\text{cut-on}}$ is proportional to $1/b^2$.

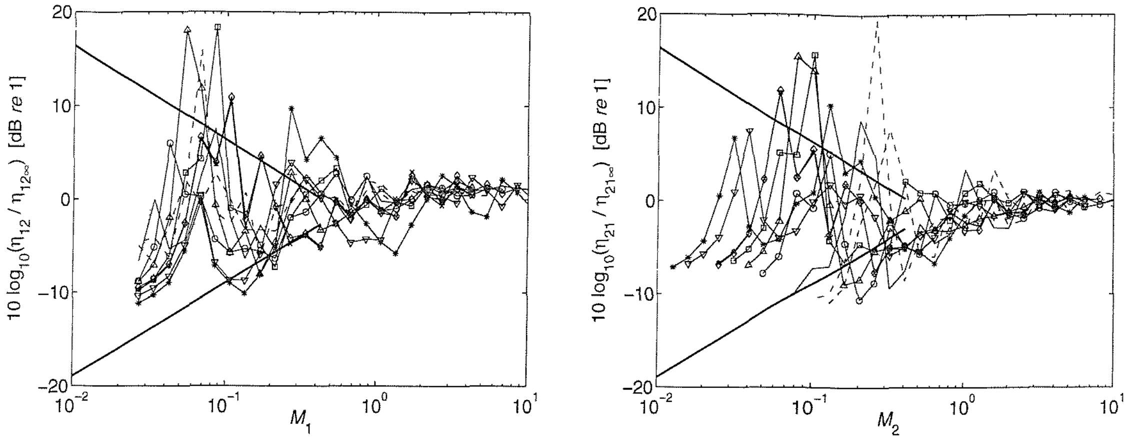

(a) CLF ratio plotted against the modal overlap factor for the source plate.

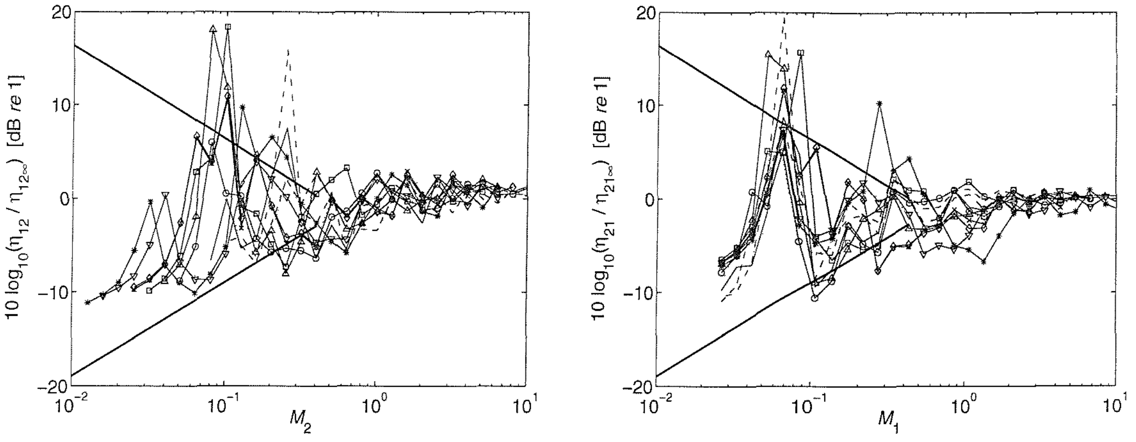

(b) CLF ratio plotted against the modal overlap factor for the receiver plate.

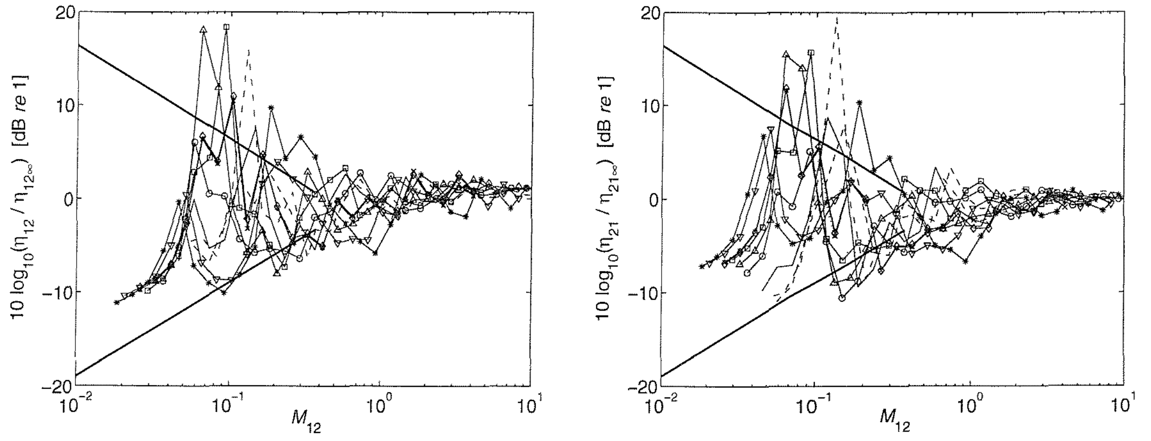

(c) CLF ratio plotted against the geometric mean modal overlap factor [M_{12}].

Figure 5.6. CLF ratio for different values of the length ratio (L_1/L_2) plotted against the modal overlap factor; the length of plate 1 is fixed (0.5 m) and the length of plate 2 (in metres) varies from 1.58 to 0.158: ---, 1.58; -·-, 1.26; —, 1.0; ·····, 0.79; -o-, 0.63; -Δ-, 0.50; -□-, 0.40; -x-, 0.32; -◊-, 0.25; -∇-,0.20; -*-, 0.158; —, estimates of the upper and lower bounds from equations (3.38) and (3.39).

Table 5.5. Variants studied to show the effect of the plate length-to-width ratio L_1/b.

L_1/b	h_1 (mm)	h_2 (mm)	L_1 (m)	L_2 (m)	b (m)	$n_1(\omega)$	$n_2(\omega)$	$f_{\text{cut-on, 1}}$	$f_{\text{cut-on, 2}}$
0.316	3.00	2.00	0.50	1.00	1.58	0.013	0.040	2.94	1.96
0.398	3.00	2.00	0.50	1.00	1.26	0.011	0.032	4.63	3.08
0.501	3.00	2.00	0.50	1.00	1.00	0.0085	0.026	7.34	4.90
0.631	3.00	2.00	0.50	1.00	0.79	0.0067	0.020	11.7	7.81
0.793	3.00	2.00	0.50	1.00	0.63	0.0054	0.016	18.5	12.3
1.00	3.00	2.00	0.50	1.00	0.50	0.0043	0.013	29.4	19.6
1.26	3.00	2.00	0.50	1.00	0.40	0.0034	0.010	46.6	31.1
1.58	3.00	2.00	0.50	1.00	0.32	0.0027	0.0081	73.6	49.0
2.00	3.00	2.00	0.50	1.00	0.25	0.0021	0.0064	117	77.7
2.51	3.00	2.00	0.50	1.00	0.20	0.0017	0.0051	185	124
3.16	3.00	2.00	0.50	1.00	0.158	0.0013	0.0040	294	196

Figures 5.7 and 5.8 show, respectively, the results plotted against frequency and against the various modal overlap factors, as in the previous sections. Estimates of the upper and lower bounds determined from equations (3.38) and (3.39) are shown for low modal overlap ($M < 0.4$).

As the width of the plate is varied, it affects the modal density, $n \propto S$ ($= L\,b$), as well as the cut-on frequency, $f_{\text{cut-on}} \propto 1/b^2$, of the source and receiver plate. Thus the peaks move to the right for every case in Figures 5.7 and 5.8 as the width of the plate b is reduced.

The first resonance frequencies for the two uncoupled plates of the 11 variants of L_1/b (for transverse order $n = 1$) were obtained from the frequency functions (*i.e.* $\left(\det(\mathbf{K})\right)^{-1}$) of the DSM models. The first resonance frequencies for the two uncoupled plates and the first peak frequencies in $\hat{\eta}_{12}/\eta_{12\infty}$ and $\hat{\eta}_{21}/\eta_{21\infty}$ are listed in Table 5.6.

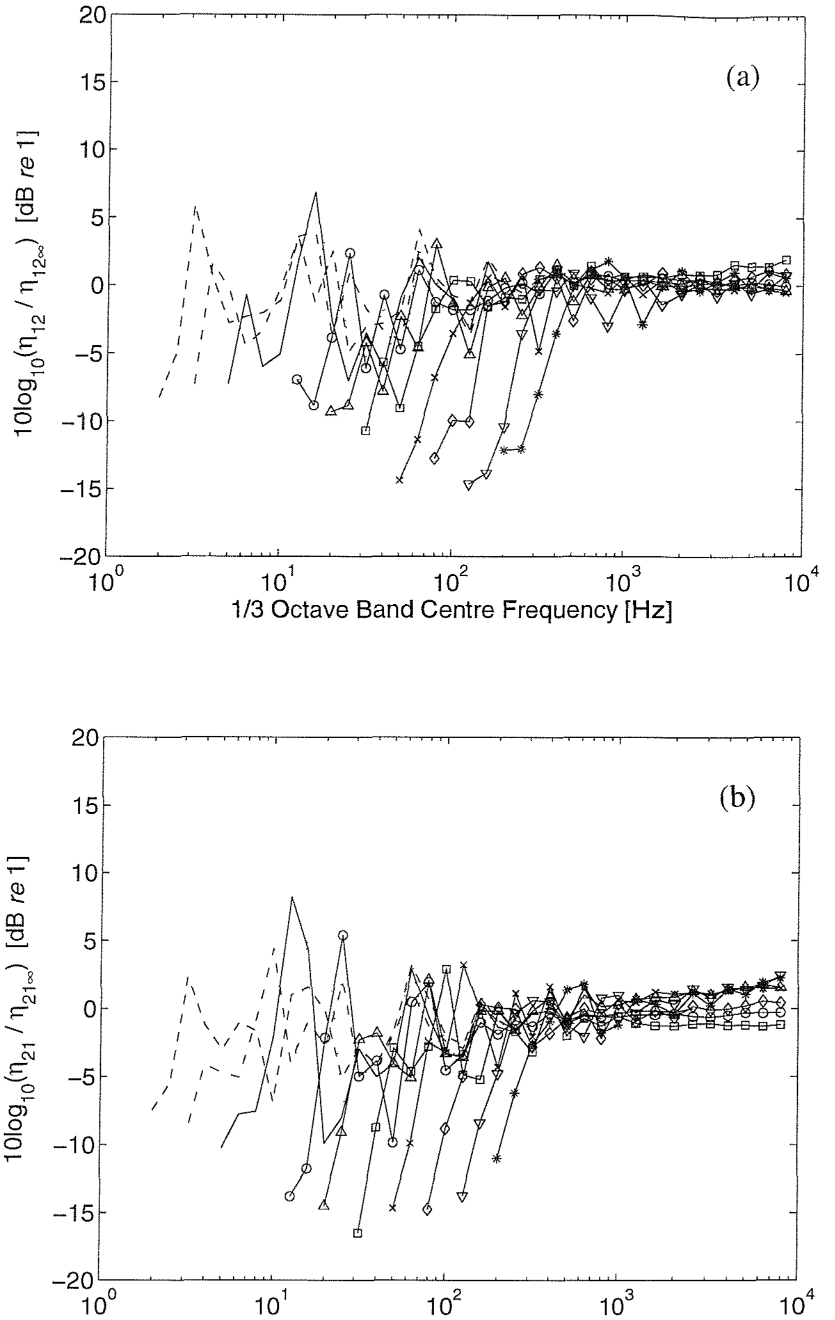

Figure 5.7. CLF ratio, (a) $10\log_{10}(\hat{\eta}_{12}/\eta_{12\infty})$ and (b) $10\log_{10}(\hat{\eta}_{21}/\eta_{21\infty})$, for different values of the length-to-width ratio (L_1/b) plotted against frequency; the length of plate 1 is fixed (0.5 m) also plate 2 (1.0 m) and the width of the two plates (in metres) varies from 1.58 to 0.158: ---, 1.58; -·-, 1.26; —, 1.0; ·····, 0.79; -o-, 0.63; -Δ-, 0.50; -□-, 0.40; -x-, 0.32; -◇-, 0.25; -∇-,0.20; -*-, 0.158.

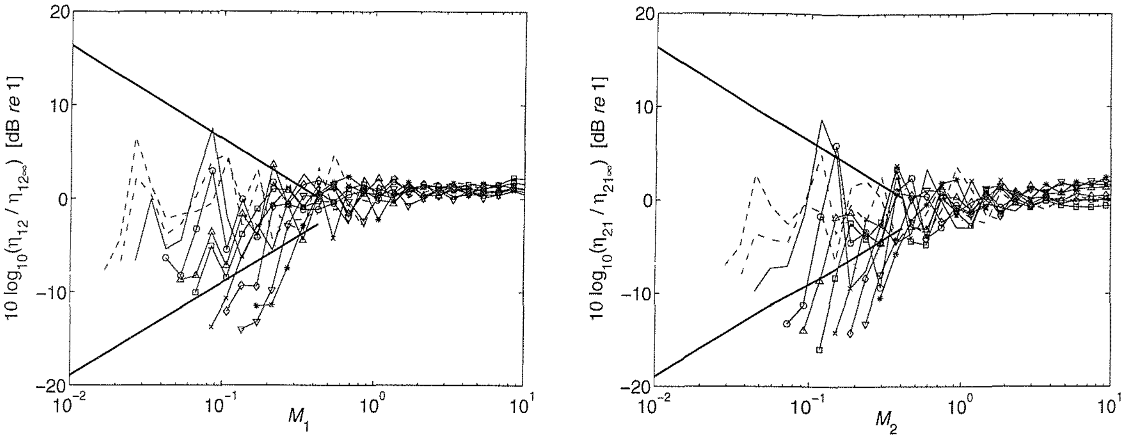

(a) CLF ratio plotted against the modal overlap factor for the source plate

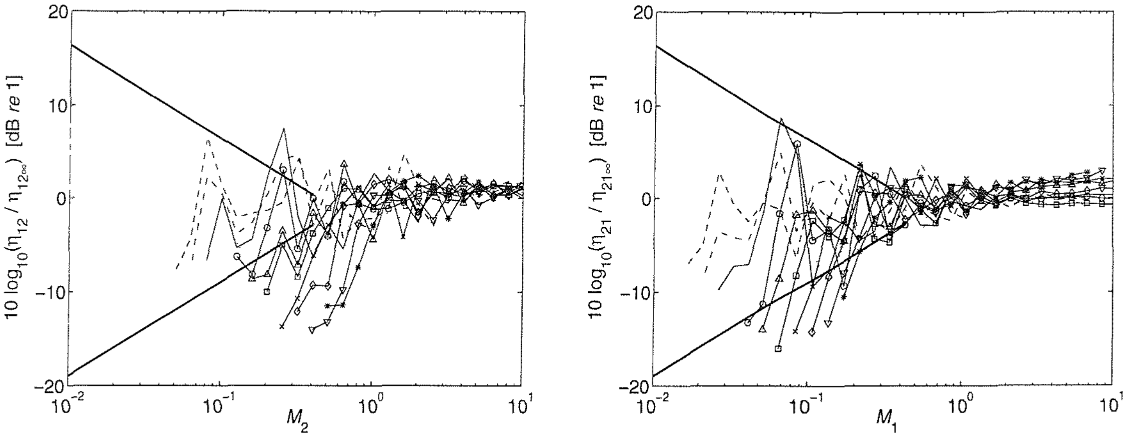

(b) CLF ratio plotted against the modal overlap factor for the receiver plate

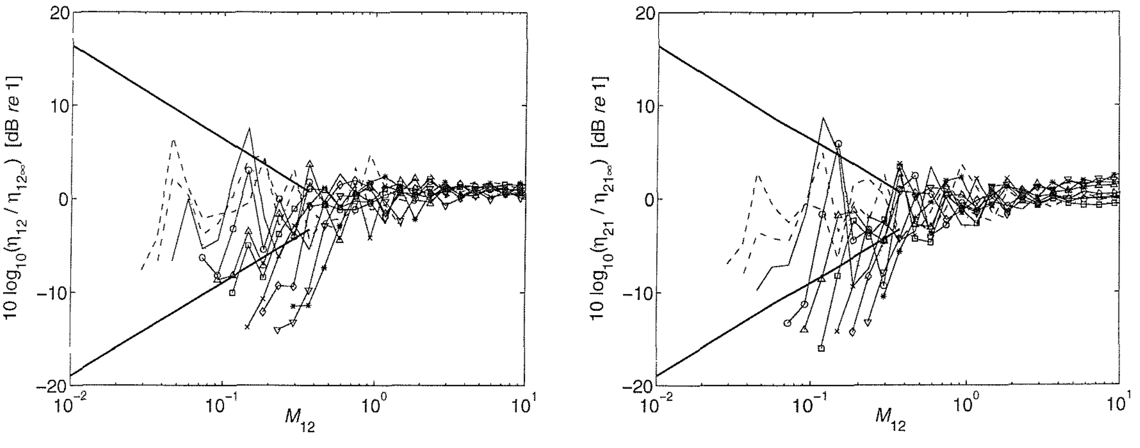

(c) CLF ratio plotted against the geometric mean modal overlap factor [M_{12}]

Figure 5.8. CLF ratio for different values of the length-to-width ratio (L_1/b) plotted against the modal overlap factor; the length of plate 1 is fixed (0.5 m) also plate 2 (1.0 m) and the width of the two plates (in metres) varies from 1.58 to 0.158: ---, 1.58; -·-, 1.26; —, 1.0; ·····, 0.79; -o-, 0.63; -Δ-, 0.50; -□-, 0.40; -x-, 0.32; -◇-, 0.25; -∇-,0.20; -*-, 0.16; —, estimates of the upper and lower bounds from equations (3.38) and (3.39).

Table 5.6. The first resonance frequencies obtained from the frequency functions (*i.e.* $\left(\det(\mathbf{K})\right)^{-1}$), for the two uncoupled plates of the 11 variants of L_1/b (for transverse order $n = 1$) and the first peak frequencies in $\hat{\eta}_{12}/\eta_{12\infty}$ and $\hat{\eta}_{21}/\eta_{21\infty}$.

L_1/b	Plate 1		Plate 2		$\hat{\eta}_{12}/\eta_{12\infty}$	$\hat{\eta}_{21}/\eta_{21\infty}$
	F-S-S-S	F-S-C-S	F-S-S-S	F-S-C-S		
0.316	6.59	12.9	2.76	3.46	3.15	3.15
0.398	8.69	14.3	3.92	4.51	4.0	4.0
0.501	11.8	16.8	5.75	6.23	6.3	12.5
0.631	16.5	20.7	8.69	9.06	8.0	16
0.793	23.5	27.1	13.1	13.5	12.5	25
1.00	34.5	37.3	20.4	20.6	20	31.5
1.26	51.0	53.3	31.3	31.5	40	50
1.58	76.7	78.6	48.4	48.5	50	80
2.00	123	123	78.8	79.0	100	160
2.51	188	189	122	123	125	250
3.16	298	299	196	196	200	315

5.5 Damping Loss Factor (DLF)

In the previous configurations only geometric factors were varied and so, to conclude, the effect of damping is considered. The dimensions of the two plates ($h_1 = 3$ mm, $L_1 = 0.5$ m, $h_2 = 2$ mm, $L_2 = 1.0$ m, $b = 1.0$ m) are kept fixed and three different levels of the DLFs, $\eta_1 = \eta_2 = 0.03$, 0.1 and 0.3 are considered here.

The ratio (in dB) between the effective CLF and the semi-infinite result, $10\log_{10}\left(\hat{\eta}_{ij}/\eta_{ij\infty}\right)$, is plotted against frequency in Figure 5.9 for these three different levels of the DLFs. As the DLFs of both plates increase, the variation in the effective CLF becomes small. Figure 5.10 shows the CLF ratios, (a) $10\log_{10}\left(\hat{\eta}_{12}/\eta_{12\infty}\right)$ and (b) $10\log_{10}\left(\hat{\eta}_{21}/\eta_{21\infty}\right)$, plotted against the geometric mean modal overlap factor, for the different DLFs. Estimates of the upper and lower bounds are obtained from equations (3.38) and (3.39) and are shown by thick solid lines. Since the modal overlap factor is proportional to the DLF, the lower bounds increase and the upper bounds are moved to the right as the DLFs increase.

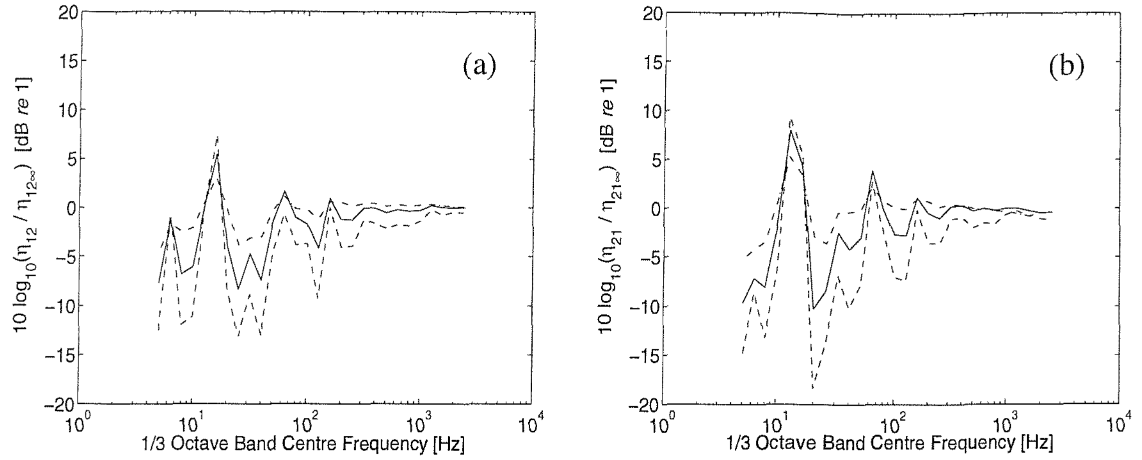

Figure 5.9. CLF ratio, (a) $10\log_{10}(\hat{\eta}_{12}/\eta_{12\infty})$ and (b) $10\log_{10}(\hat{\eta}_{21}/\eta_{21\infty})$, plotted against frequency for three different levels of the DLFs: ---, $\eta = 0.03$; —, $\eta = 0.1$; -·-, $\eta = 0.3$. The damping is the same in both plates.

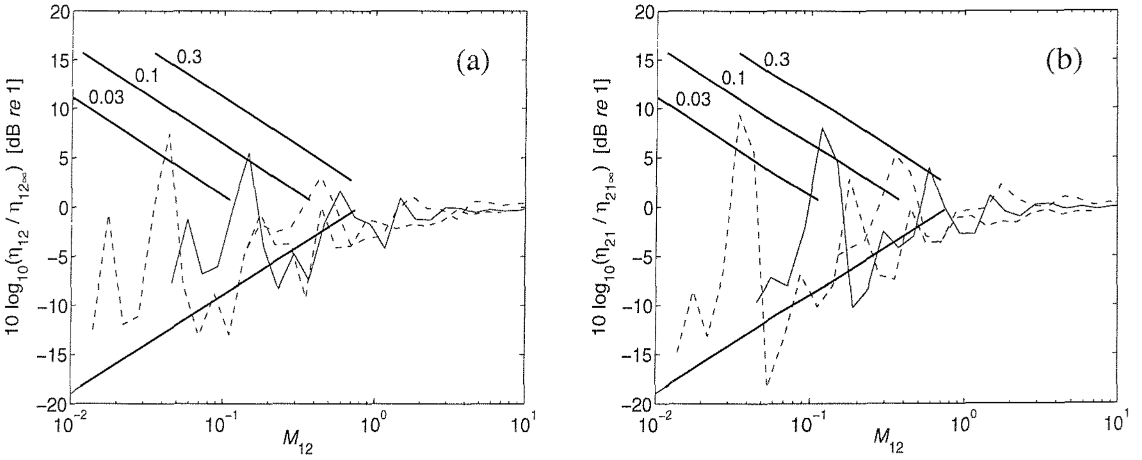

Figure 5.10. CLF ratio, (a) $10\log_{10}(\hat{\eta}_{12}/\eta_{12\infty})$ and (b) $10\log_{10}(\hat{\eta}_{21}/\eta_{21\infty})$, for different DLFs plotted against the geometric mean modal overlap factor M_{12}: ---, $\eta = 0.03$; —, $\eta = 0.1$; -·-, $\eta = 0.3$; —, estimates of the upper and lower bounds from equations (3.38) and (3.39). The damping is the same in both plates.

5.6 Discussion

In general, for modal overlap greater than 1, the variation in the effective CLF is small, although the effective CLF does not always converge to that for the semi-infinite plate, as the latter does not take into account the in-plane vibrations. At low modal overlap ($M < 0.4$) the results fluctuate considerably and most are found to fall within the bounds described in Section 3.6. Results at high modal overlap $M > 0.4$ are not covered by the bounds proposed by Craik *et al.* The results show that some fluctuations remain in this region also.

The percentage of the values falling within these bounds in Figures 5.3, 5.6, and 5.8 has been investigated for $M < 0.4$. The results below the first cut-on frequency of either plate have been discounted, as SEA assumptions would not be valid. The results are given in Table 5.7. When the CLF ratio is plotted against the geometric mean modal overlap factor M_{12}, this shows more consistent results (lower standard deviation) than when it is plotted against the modal overlap factor for the source or receiver plate. Virtually all of the results fall within the slightly wider range $\eta_{\min} / 3 < \hat{\eta}_{ij} < 3\eta_{\max}$ (estimates of the upper and lower bounds ± 5 dB), as listed in Table 5.8.

Table 5.7. The percentage of values of $10\log_{10}\left(\hat{\eta}_{ij} / \eta_{ij\infty}\right)$ falling between estimates of the upper and lower bounds of equations (3.38) and (3.39) when plotted against the modal overlap factor for the source plate M_s, that for the receiver plate M_r and the geometric mean value $(M_s M_r)^{1/2}$.

	Parameter	M_s	M_r	$(M_s M_r)^{1/2}$
$10\log_{10}\left(\hat{\eta}_{12} / \eta_{12\infty}\right)$	Thickness ratio	78	57	70
	Length ratio	76	81	77
	Length-to-width ratio	75	38	52
$10\log_{10}\left(\hat{\eta}_{21} / \eta_{21\infty}\right)$	Thickness ratio	49	70	60
	Length ratio	65	78	74
	Length-to-width ratio	32	68	52
Average		62.5	65.3	64.2
Standard deviation		18.4	15.8	11.0

(Unit: %)

Table 5.8. The percentage of values of $10\log_{10}\left(\hat{\eta}_{ij}/\eta_{ij\infty}\right)$ falling between estimates of the upper and lower bounds of equations (3.38) and (3.39) ± 5 dB when plotted against the modal overlap factor for the source plate M_s, that for the receiver plate M_r and the geometric mean value $(M_s M_r)^{1/2}$

	Parameter	M_s	M_r	$(M_s M_r)^{1/2}$
$10\log_{10}\left(\hat{\eta}_{12}/\eta_{12\infty}\right)$	Thickness ratio	98	98	98
	Length ratio	97	97	97
	Length-to-width ratio	93	71	74
$10\log_{10}\left(\hat{\eta}_{21}/\eta_{21\infty}\right)$	Thickness ratio	88	97	95
	Length ratio	92	97	96
	Length-to-width ratio	62	95	84
Average		88.3	92.5	90.7
Standard deviation		13.4	10.6	9.63

(Unit: %)

There are two things under investigation here; one is the validity of Craik's upper and lower bounds and the other is to determine whether the variability in the CLF depends on the modal properties of the source subsystem, the receiver subsystem, or both the source and receiver subsystems. It appears from the results presented that Craik's upper and lower bounds are a useful indication of the variability in the CLF, although the most consistent agreement occurs when the modal overlap of both subsystems is taken into account rather than that of the receiver as proposed by Craik.

Since the ensemble average CLFs are lower than the semi-infinite results at low frequencies, as shown in Figure 3.2, using the former instead of the latter may be more appropriate for investigating the variability of the CLF. In the next chapter, the ratio between the effective CLFs and the ensemble average results is examined in a further study of the variability of the CLF, from which a new empirical model will be obtained to quantify this variability.

5.7 Conclusions

The results of extensive DSM simulations allow confidence intervals, as well as the mean CLF, to be investigated. For modal overlap greater than 1, the variation in the effective CLF is small, whereas at low modal overlap most of the results fluctuate considerably.

Craik's upper and lower bounds are shown to be useful indications of the degree of variability, although better agreement occurs when the combined modal overlap of the two subsystems is taken into account, rather than that of the receiver as originally proposed by Craik. However these bounds did not account for remaining variability when the modal overlap is greater than about 0.4.

The variability in the effective CLF was found to depend not only on the modal properties of the receiver subsystems but also on those of the source subsystem, as discussed in Chapter 4.

The results of this chapter are dominated by variability caused by a very few low frequency modes. Moreover, the parameter variations introduced also affect the modal densities and modal overlap factors. In the next chapter therefore a modified strategy for parameter variations is introduced the aim of which is to separate the various effects as much as possible.

CHAPTER 6

DEVELOPMENT OF AN EMPIRICAL MODEL FOR THE VARIABILITY OF THE CLF

6.1 Introduction

The variability of the effective CLF was investigated in Chapter 5 by a preliminary set of parameter variations for a two-plate system. The properties of both the source and receiver plates were varied, but in each case, although the modal density was constant with frequency, the modal overlap factor increased with increasing frequency. Moreover, the use of one-third octave bands meant that the number of modes in a band also increased as frequency increased.

The effective CLF was found to depend not only on the geometric and material properties of the subsystems, such as thickness, length, width and damping, but also on frequency as the modal overlap factor increased with frequency. However, the frequency, the bandwidth, and the modal overlap factor were not varied independently. The results of Chapter 5 showed the degree of the variability in the CLF but were not sufficient to quantify this variability due to the complexities of those parameters.

In this chapter, the variability of the effective CLF is quantified by means of an in-depth systematic parameter study. Two parameters which affect the variability of the CLF, the average number of modes in a frequency band N and modal overlap factor M, are considered as independent control parameters. In this, the effects of frequency and modal overlap are separated by using frequency averages for a series of constant bandwidths rather than 1/3 octave band averages.

In order to provide a more consistent basis for comparisons, independent of frequency, the true ensemble average CLF $\eta_{ij,\,ens}$, discussed in Section 3.5, is introduced [50]. The effective CLF results are presented relative to this rather than the CLF derived from semi-infinite plates, $\eta_{ij\infty}$, which is biased for strongly coupled subsystems.

These results are used to derive an empirical formula for the confidence interval of the effective CLF in terms of the modal overlap factor and the number of modes in a frequency band. This should subsequently allow confidence intervals in the SEA predictions to be determined in an improved manner compared to the previously published estimates (Mohammed [43] and Lyon and DeJong [33]).

Finally, statistical investigations are performed in order to review the statistical distribution of the logarithmic ratio of the effective CLF to the ensemble average CLF and the interdependence of η_{12} and η_{21}.

6.2 Results for a baseline model

6.2.1 Constant loss factor

A model of two coupled aluminium plates (thickness $h_1 = 3$ mm and $h_2 = 2$ mm, length $L_1 = 0.5$ m and $L_2 = 1.0$ m, and width $b = 1.0$ m) was considered in the previous chapters as a baseline model. This model has a modal density that is constant with frequency but the modal overlap factor depended on frequency as the DLFs were kept constant ($\eta_1 = \eta_2 = 0.1$).

The effective CLF $\hat{\eta}_{ij}$ derived using DSM, the ensemble average CLF $\eta_{ij,\,ens}$ [50] and the CLF obtained using semi-infinite plates $\eta_{ij\infty}$ for this baseline model, have been shown in Figure 3.2. These results were based on 1/3 octave frequency bands. The effective CLFs fluctuated considerably relative to $\eta_{ij,\,ens}$ or $\eta_{ij\infty}$ at low frequencies and the various results all coincided more closely as frequency, consequently modal overlap, increased.

6.2.2 Constant modal overlap factor and frequency average CLF

In order to simulate a system with a constant modal density $n(\omega)$ and constant modal overlap factor $M = \eta\,\omega n(\omega)$, for all frequencies, the DLF was chosen to be inversely proportional to frequency, $\eta_1 = \eta_2 \propto 1/\omega$. In the baseline model, the DLF is characterised by $\eta = 1/f$ with f the frequency. This gives $\eta = 0.01$ at 100 Hz and 0.001 at 1 kHz. Below 3 Hz the DLF was limited to 0.3 to avoid it becoming too large. Above 3 Hz the corresponding modal overlap factors have the constant values, $M_1 = 0.053$ and $M_2 = 0.16$, for the baseline model. Other values of damping will be considered later.

The response of a dynamic system becomes much smoother when a frequency band average is taken. A one-third octave band average is typically used in acoustic analyses. In this section, the frequency averaging effects for different frequency bandwidths have been investigated. Firstly, narrow-band energies and powers were calculated for the two-plate system discussed above using a DSM model with 1 Hz spacing up to 1 kHz. In this model at least one frequency point lies within the half-power bandwidth ηf of each mode. The plate energies were then averaged in overlapping bands with constant frequency bandwidths (20, 40, 60, 100, 200 and 400 Hz) to provide a continuously varying curve.

The effective CLFs relating to these frequency bands $\left\langle \hat{\eta}_{ij} \right\rangle$ were obtained from these energies by a numerical experiment as defined in equation (3.13). $< >$ denotes a frequency averaged quantity. Rather than the semi-infinite plate results $\eta_{ij\infty}$, used as a reference in Chapter 5, the ensemble average CLF [50] is used as a basis for comparison of the effective CLFs obtained.

Figure 6.1 shows the effective CLFs calculated at 1 Hz spacing up to 1 kHz and the ensemble average CLF. Also shown, are estimates of the upper and lower bounds*, $2/\pi M$ and $\pi M/2$. These are obtained from the maxima and minima of the mobility (equations (3.32) and (3.35)) given by Skudrzyk [59], as used in the formulae (equations (3.38) and (3.39)) for CLF bounds given by Craik *et al.* [44, 52]. The bounds in Figure 6.1 were based on using the modal overlap factor for the source plate M_s, the receiver plate M_r, or the geometric mean values $\sqrt{M_s M_r}$. It can be seen that the variation in the CLF is considerably greater than that estimated from the bounds shown in this case. The consistency relationship, $n_1 \hat{\eta}_{12} = n_2 \hat{\eta}_{21}$, is not satisfied as also found in Section 4.2.5.

---

* [NB] These bounds are wider than Craik's

(a) at the peaks because they are based on single modes

(b) at the troughs because the full expression is used rather than the two-mode approximation.

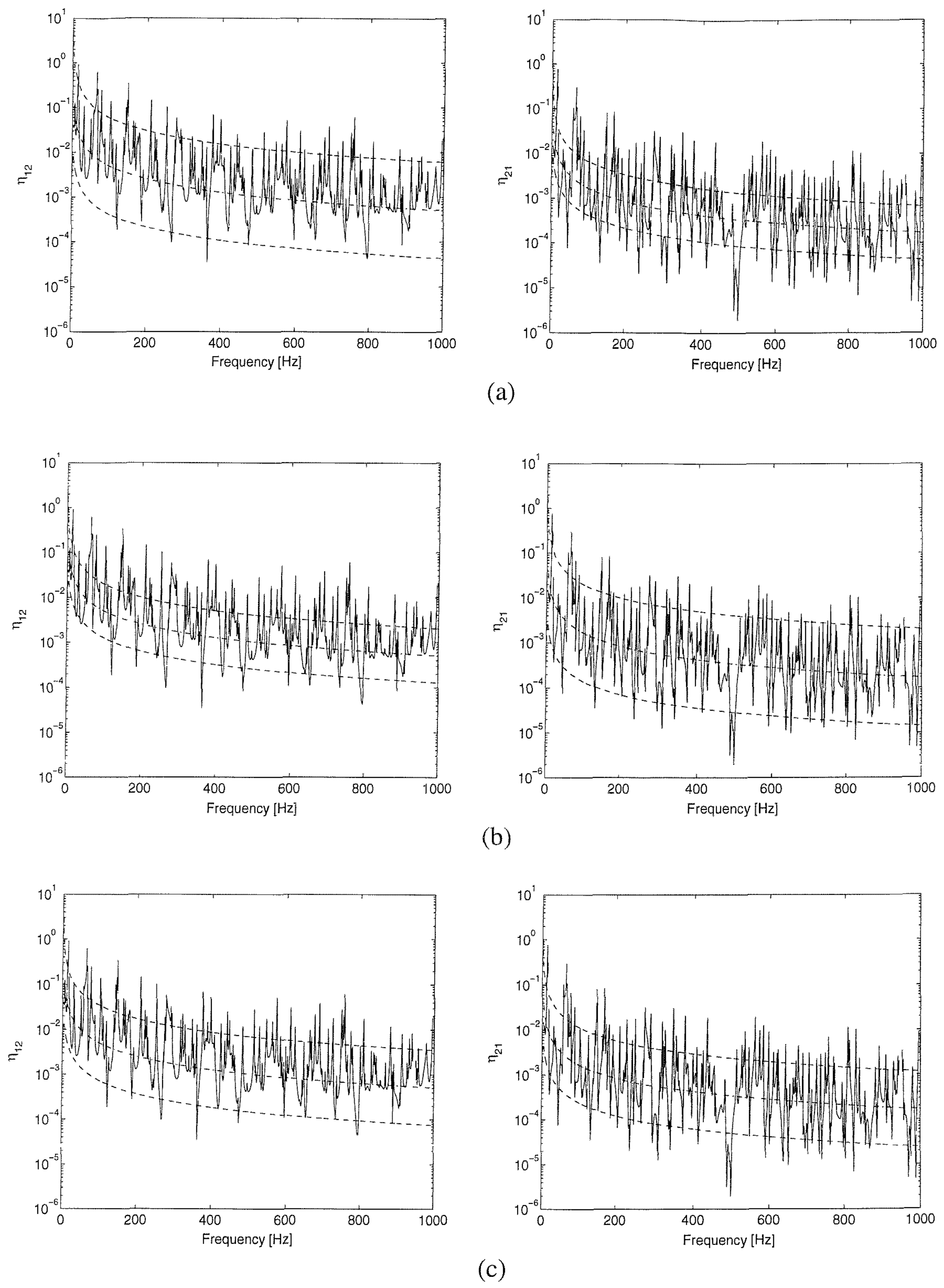

Figure 6.1. The effective CLFs $\hat{\eta}_{ij}$, the ensemble average CLF $\eta_{ij,\,ens}$, and estimates of the upper and lower bounds, for the baseline model ($\eta = \min(0.3,\ 1/f)$, $M_1 = 0.053$, $M_2 = 0.16$). —, the effective CLF; -·-, the ensemble average CLF; ---, upper and lower bounds estimated from Skudrzyk's bounds for mobility [59]: (a) M_s, (b) M_r and (c) $\sqrt{M_s M_r}$.

Next, the ratio of the frequency averaged effective CLF to the ensemble average CLF, $\langle \hat{\eta}_{ij} \rangle / \eta_{ij,\,ens}$, was determined. This is shown in decibel (dB) form in Figures 6.2 and 6.3 for η_{12} and η_{21} respectively. The mean over all centre frequencies, along with a range of ±2 standard deviations (σ) calculated in terms of the dB values, is also shown in each case. Clearly, as the bandwidth increases the range $\pm 2\sigma$ reduces, whereas the mean is close to 0 dB throughout. As the bandwidth increases, the average number of modes in a frequency band, N_1 or N_2 also increases. This can be obtained from the modal density $n(\omega)$ (equation (3.16)) multiplied by the bandwidth $\Delta\omega$. Figure 6.4 shows the values of 2σ from Figures 6.2 and 6.3 plotted against N_1, N_2, and N_{12} (as used by Mohammed [43]), where $N_{12} = \sqrt{N_1 N_2}$, *i.e.* the geometric mean value of N_1 and N_2. The results of 2σ for η_{12} and for η_{21} show similar levels for a given frequency bandwidth and are shifted horizontally by plotting against N_1, N_2 or N_{12}. The combined measure N_{12} therefore seems more appropriate as it accounts for both plates. This is further discussed in Section 6.5.1.

In the remainder of the results in this chapter, constant bandwidth frequency averaging is used and the frequency dependent DLF is used to make the modal overlap factor independent of frequency. The subsequent results of 2σ for η_{12} and for η_{21} are plotted against by the geometric mean value N_{12}.

6.3 Parameter variation using DSM model

In this chapter a wide range of parameter variations is considered. This section summarises the reasons for the cases considered. The parameters used in this chapter are summarised in Table 6.1. Some of the values of plate thickness or length are listed below the table. The values of the various parameters will be given in more detail in the following sections along with the results. The revised baseline considered in Section 6.2.2 corresponds to the case identified as 'light damping' in Table 6.1.

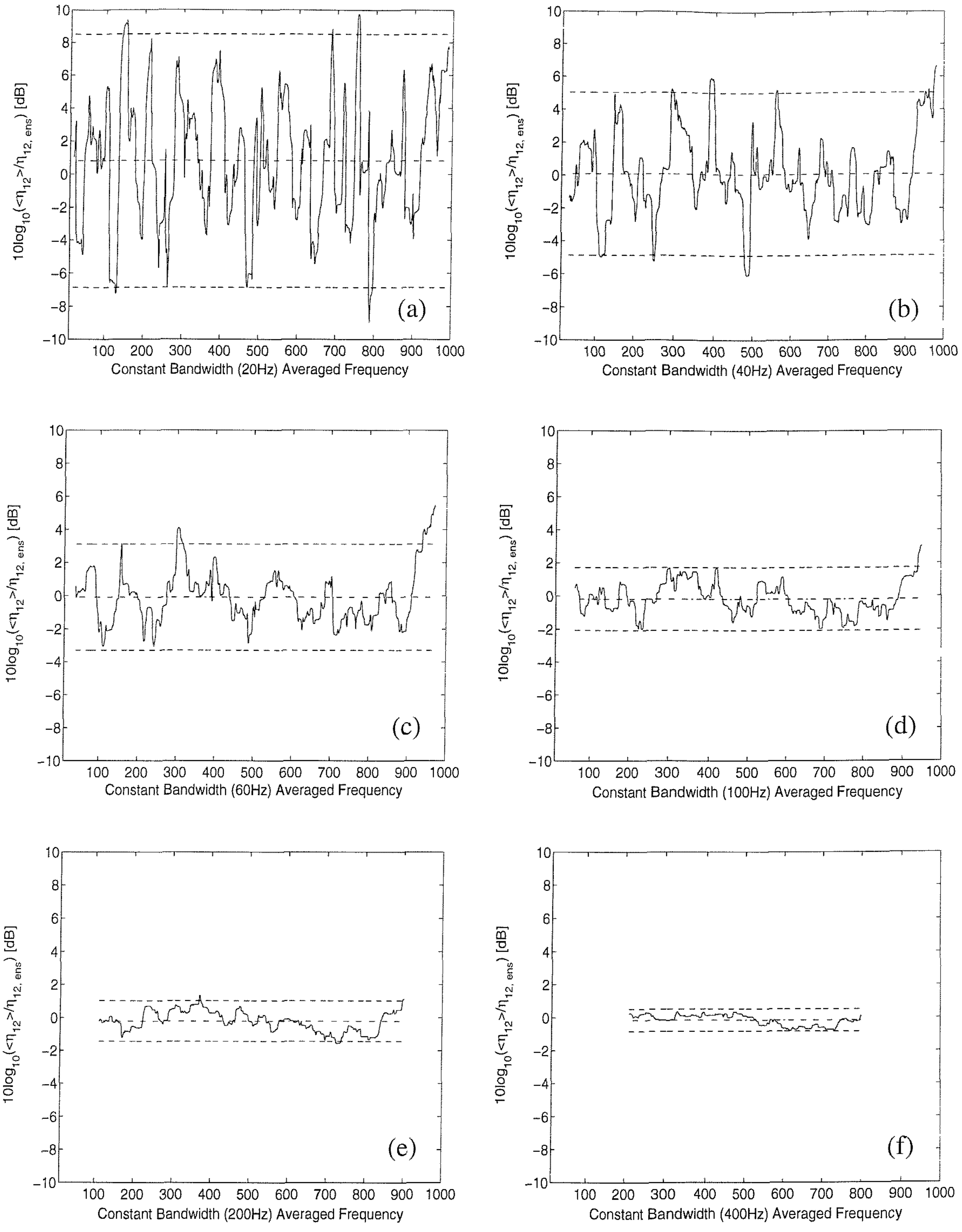

Figure 6.2. Bandwidth effect on the mean and ± two standard deviations (2σ) of the logarithmic ratio of the frequency averaged effective CLF $\langle\hat{\eta}_{12}\rangle$ to the ensemble average CLF $\eta_{12,ens}$ ($\eta = \min(0.3,\ 1/f)$, $M_1 = 0.053$, $M_2 = 0.16$). —, $10\log_{10}\left(\langle\hat{\eta}_{12}\rangle/\eta_{12,ens}\right)$; -·-, $10\log_{10}\left(\langle\hat{\eta}_{12}\rangle/\eta_{12,ens}\right)_{mean}$; ---, mean $\pm 2\sigma$ of $10\log_{10}\left(\langle\hat{\eta}_{12}\rangle/\eta_{12,ens}\right)$. (a) 20 Hz bandwidth, (b) 40 Hz bandwidth, (c) 60 Hz bandwidth, (d) 100 Hz bandwidth and, (e) 200 Hz bandwidth, and (f) 400 Hz bandwidth.

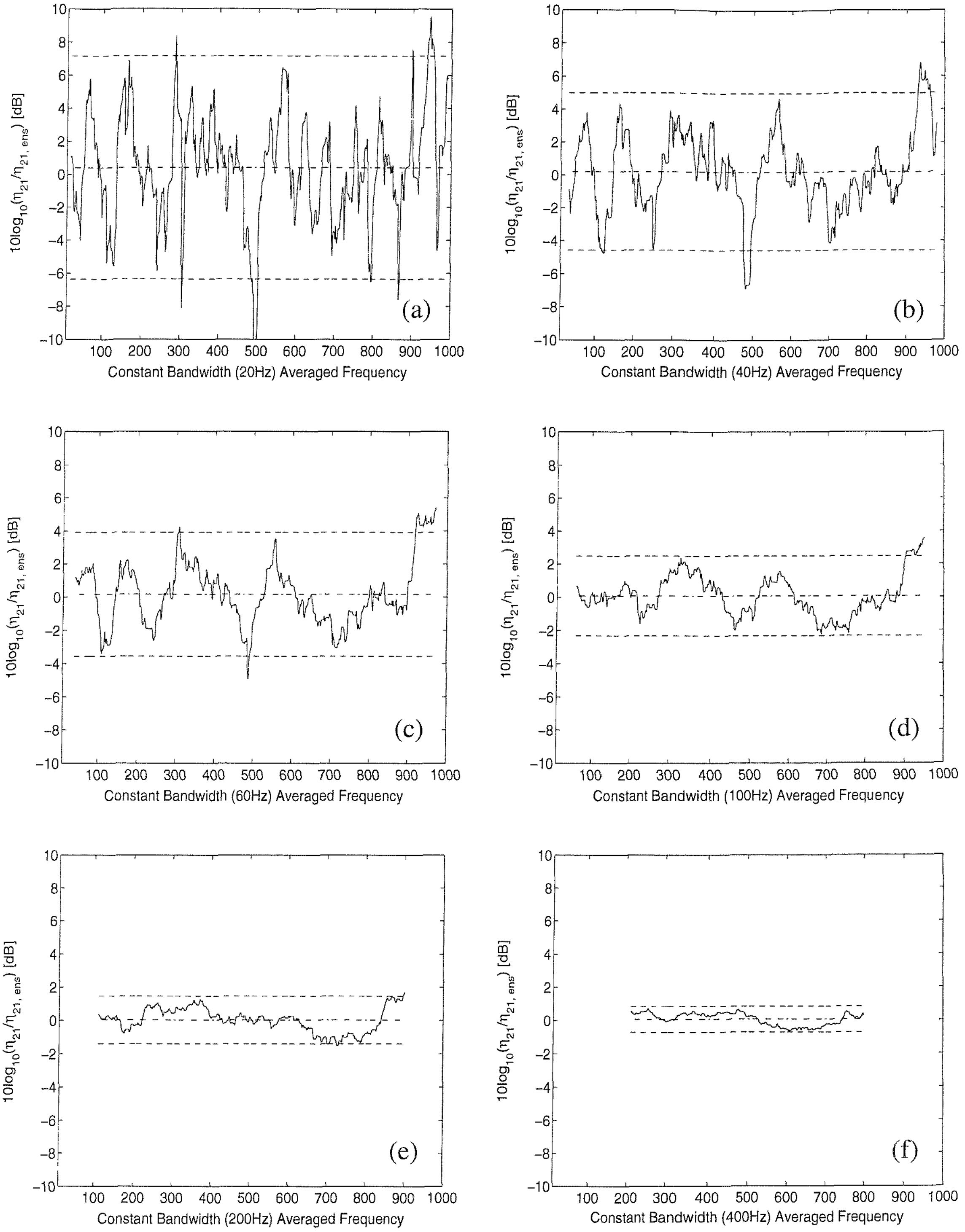

Figure 6.3. Bandwidth effect on the mean and ± two standard deviations (2σ) of the logarithmic ratio of the frequency averaged effective CLF $\langle\hat{\eta}_{21}\rangle$ to the ensemble average CLF $\eta_{21,ens}$ ($\eta = \min(0.3,\ 1/f)$, $M_1 = 0.053$, $M_2 = 0.16$). —, $10\log_{10}\left(\langle\hat{\eta}_{21}\rangle/\eta_{21,ens}\right)$; -·-, $10\log_{10}\left(\langle\hat{\eta}_{21}\rangle/\eta_{21,ens}\right)_{mean}$; ---, mean $\pm 2\sigma$ of $10\log_{10}\left(\langle\hat{\eta}_{21}\rangle/\eta_{21,ens}\right)$. (a) 20 Hz bandwidth, (b) 40 Hz bandwidth, (c) 60 Hz bandwidth, (d) 100 Hz bandwidth and, (e) 200 Hz bandwidth, and (f) 400 Hz bandwidth.

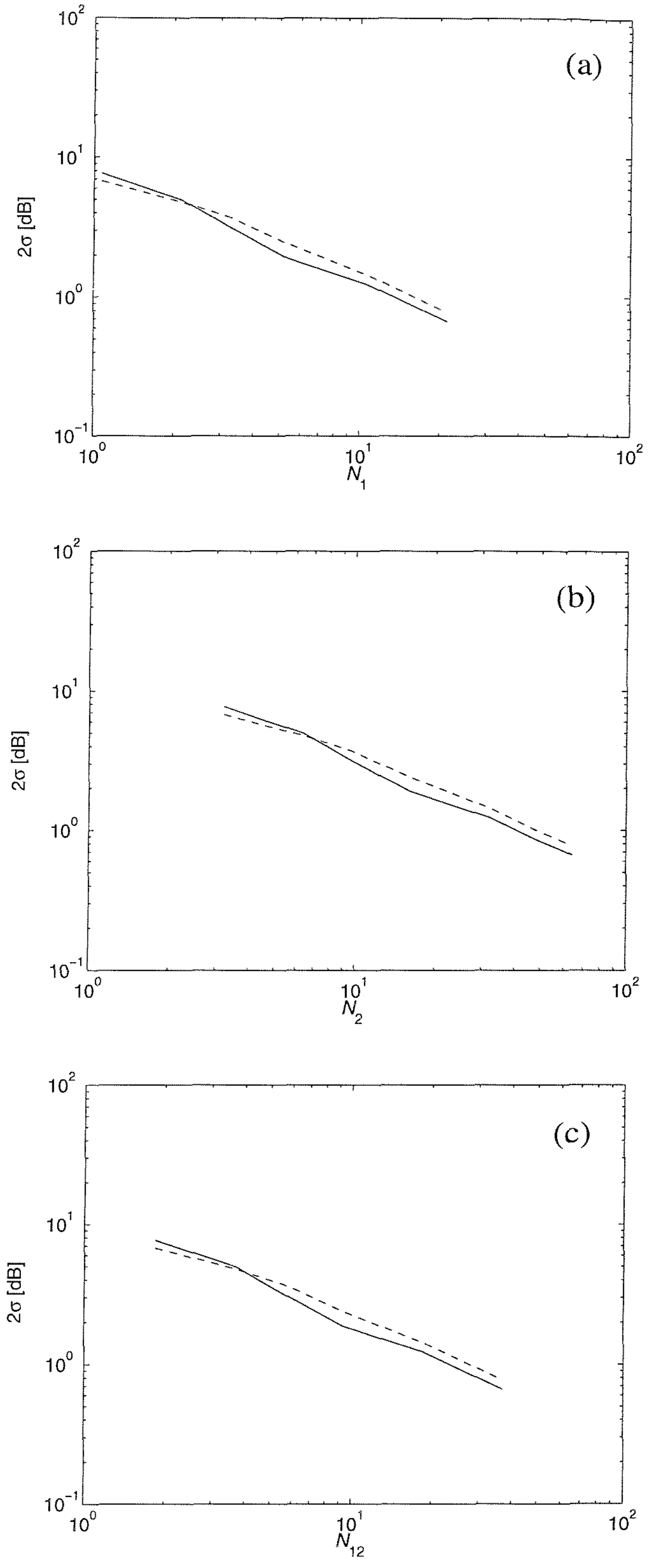

Figure 6.4. Two standard deviations (2σ) of $10\log_{10}\left(\left\langle\hat{\eta}_{ij}\right\rangle/\eta_{ij,\,ens}\right)$ for different frequency bandwidths plotted against (a) N_1, (b) N_2, and (c) N_{12}, the geometric mean of N_1 and N_2 ($h_1 = 3$ mm, $h_2 = 2$ mm, $\eta \propto 1/\omega$ ($\eta = \min(0.3, 1/f)$, $M_1 = 0.053$, $M_2 = 0.16$): —, 2σ for η_{12}; ---, 2σ for η_{21}.

Table 6.1. Summary of parameter variations for L-shaped coupled plates.

Parameter	Fixed	Varied		M_1	M_2	η_2/η_1
Baseline (h_1=3mm, h_2=2mm)	$L_1,L_2,h_1,h_2,b,\eta_1,\eta_2$, $n_1(\omega)$, $n_2(\omega)$	-	-	$\propto f$	$\propto f$	1.0
High damping	L_1,L_2,h_1,h_2,b	-	$\eta_1=\eta_2\propto 1/\omega$	0.53	1.6	1.0
Medium damping	L_1,L_2,h_1,h_2,b	-	$\eta_1=\eta_2\propto 1/\omega$	0.16	0.48	1.0
Light damping	L_1,L_2,h_1,h_2,b	-	$\eta_1=\eta_2\propto 1/\omega$	0.053	0.16	1.0
$\eta_1>\eta_2$	L_1,L_2,h_1,h_2,b	-	$\eta_1\neq\eta_2\propto 1/\omega$	0.53	0.48	0.30
$\eta_1>\eta_2$	L_1,L_2,h_1,h_2,b	-	$\eta_1\neq\eta_2\propto 1/\omega$	0.16	0.16	0.33
h_1/h_2(*1)	L_1,h_1,b	L_2,h_2	$\eta_1=\eta_2\propto 1/\omega$	0.53	1.6	1.0
L_1/L_2(*2)	L_1,h_1,h_2,b	L_2	$\eta_1=\eta_2\propto 1/\omega$	0.53	2.5~0.32	1.0
L_1/b(*3)	h_1,h_2	L_1,L_2,b	$\eta_1=\eta_2\propto 1/\omega$	0.53	1.6	1.0

(*1) h_1/h_2: the thickness of plate 1 (3 mm) is fixed and the thickness of plate 2 is varied from 9.49 mm to 0.949 mm (9.49, 7.54, 5.99, 4.75, 3.78, 3.00, 2.38, 1.89, 1.50, 1.19, 0.949 mm). The length L_2 is varied simultaneously to ensure constant N_2.

(*2) L_1/L_2: the length of plate 1 (0.5 m) is fixed and the length of plate 2 is varied from 1.58 m to 0.20 m (1.58, 1.26, 1.00, 0.79, 0.63, 0.50, 0.40, 0.32, 0.25, 0.20 m).

(*3) L_1/b: the widths of the two plates are varied from 1.58 m to 0.20 m (1.58, 1.26, 1.00, 0.79, 0.63, 0.50, 0.40, 0.32, 0.25, 0.20 m). The lengths of the plates are varied simultaneously to maintain the same areas and hence constant values of N_1 and N_2.

The variation of η_1 and η_2 subsequently produces constant values of M_1 and M_2.

The modal density and modal overlap factor are related to the geometric and material properties. The modal density of a simply supported uniform isotropic plate is approximated as in equation (3.16). If the material properties are assumed to be constant, the modal density is proportional to the *area* (*length* × *width*) / *thickness* of the plate and it is independent of frequency. Thus the modal overlap factor $\eta\omega n(\omega)$ is in general dependent on frequency as well as the geometric and material properties.

In the present chapter, in order to keep the modal overlap factors M_1 and M_2 constant for all frequencies, the DLF is chosen to vary with frequency *i.e.* $\eta\propto 1/\omega$. In most cases considered the DLFs of the two plates are assumed to be equal, and three different levels of DLF (high damping $\eta = 10/f$, medium damping $\eta = 3/f$ and light damping $\eta = 1/f$) are considered to investigate the effect of damping. In this case, as $\eta_1 = \eta_2$, $\eta_2 / \eta_1 = 1.0$. From the definition of M, the modal overlap factor, and N, the number of modes in a frequency band, η_2/η_1 is the same as $M_2 N_1 / M_1 N_2$. These results are intended to show the effective CLF and its variability due to frequency bandwidth and different levels of damping.

To investigate the effect of different damping levels for the two plates, whilst keeping the modal overlap factors constant, calculations are also performed with the two plates chosen to have different levels of damping whilst retaining $\eta \propto 1/\omega$. These were from high to medium damping ($\eta_2/\eta_1 = 0.3$) and from medium to low ($\eta_2/\eta_1 = 0.33$). The CLF η_{21} corresponds to the opposite cases, so these are not considered separately.

Next, a series of systematic numerical simulations are performed covering extensive parameter variations similar to those described in Chapter 5. The influence of these parameters on the variability of the CLF is investigated by keeping the dimensions of plate 1 fixed and giving the appropriate dimensions of plate 2 logarithmically spaced values. However, when the thickness h_2 is varied, the length L_2 is also varied in order to retain the same value of modal density. Similarly when the width is varied, the length is adjusted to retain a constant area and hence constant modal density. The damping values of the two plates are frequency dependent $\eta \propto 1/\omega$, in order to keep the modal overlap factors constant, as before. The other parameters are the same as the baseline model.

6.4 Variability of the effective CLF

6.4.1 Two plates with same loss factors

Three levels of damping (characterised by $\eta = 10/f$, $3/f$ and $1/f$ with f the frequency) were considered to investigate the influence of the modal overlap factor on the CLF. Since $\eta_1 = \eta_2$, the ratio $M_2 N_1 / M_1 N_2$, was fixed as 1 for the three levels of damping. The maximum damping was again limited to 0.3 at low frequencies as described in Section 6.2.2.

Energies were calculated using the DSM model at 1Hz spacing. The effective CLFs were determined using these energies averaged over frequency bands with bandwidths of 2, 4, 6, 10, 20, 40, 60, 100, 200 and 400 Hz in overlapping bands, as described in Section 6.2. Then the logarithmic ratio of the effective CLF to the ensemble average, $10\log_{10}\left(\langle\hat{\eta}_{ij}\rangle/\eta_{ij,ens}\right)$, was determined as already shown in Figures 6.2 and 6.3.

The range of two standard deviations (2σ) was obtained over the whole frequency region to express the variability of the effective CLF compared to the ensemble average, as shown in Figures 6.2 and 6.3 for one level of damping. Figure 6.5 shows the values of 2σ for the three levels of damping, plotted against N_{12}. The uncertainty (2σ) increases as the average number of modes in a frequency band reduces to about 1. Below this it reaches a value that is independent of any further change in the frequency bandwidth or the number of modes in a band. The value of 2σ at low values of N_{12} increases as the damping reduces (*i.e.* as M_1 and M_2 reduce). Interestingly, the results for η_{12} and η_{21} are similar, despite the values of M differing by a factor of 3. This justifies the use of the average modal overlap M_{12} considered below.

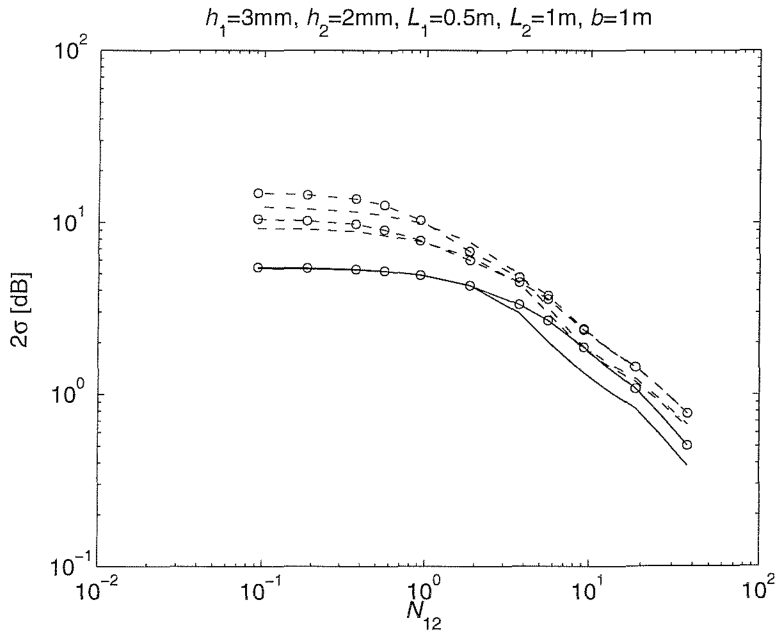

Figure 6.5. Variability of the CLF (2σ) for three levels of damping ($\eta_1 = \eta_2$) as a function of N_{12} as bandwidth is altered. —, high damping ($M_1 = 0.53$, $M_2 = 1.6$); ---, medium damping ($M_1 = 0.16$, $M_2 = 0.48$); -·-, light damping ($M_1 = 0.05$, $M_2 = 0.16$). Circles denote results for η_{21}, other results are for η_{12}.

6.4.2 Two plates with different loss factors

Using different damping values for the two plates whilst keeping the modal overlap factors constant with frequency, the ratio $M_2 N_1 / M_1 N_2$ takes values other than 1. Three damping values (high damping $\eta = 10/f$, medium damping $\eta = 3/f$ and low damping $\eta = 1/f$), were used in combination to give different damping values for the two plates: high to medium and medium to low. Figure 6.6 shows the variability (2σ) of $10\log_{10}\left(\langle\hat{\eta}_{ij}\rangle/\eta_{ij,ens}\right)$ as a function of N_{12} for these cases. Similar trends are found to those in Figure 6.5. Again the results for η_{12} and η_{21} are similar in each case despite differences in the damping of the two plates.

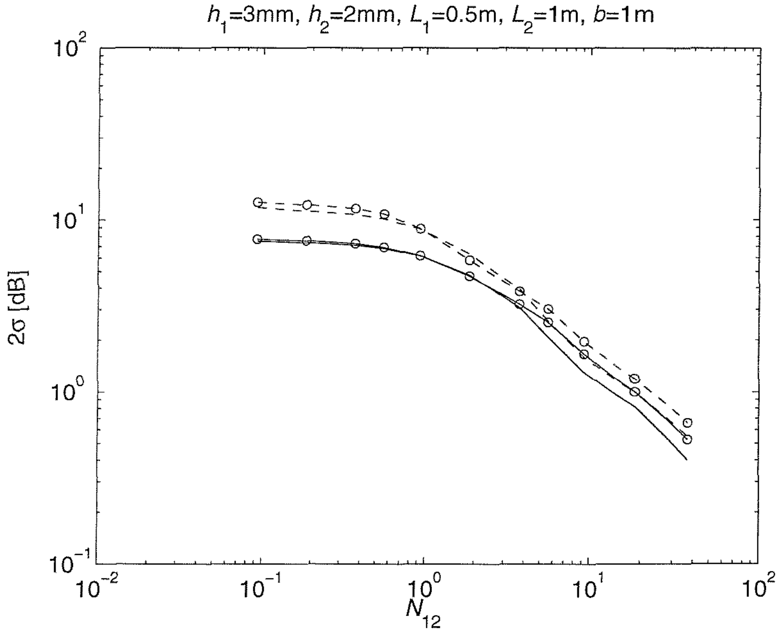

Figure 6.6. Variability of the CLF (2σ) as a function of N_{12} as bandwidth is altered. Modal overlap factor constant for all frequencies, $\eta_1 \neq \eta_2$. —, $\eta_1 = 10/f$, $\eta_2 = 3/f$; ---, $\eta_1 = 3/f$, $\eta_2 = 1/f$. Circles denote results for η_{21}, other results are for η_{12}.

6.4.3 Variation of thickness ratio (h_1/h_2) without varying modal density

To investigate the influence of the plate thickness ratio h_1/h_2 on the variability of the CLF, the thickness of plate 1 was kept fixed and the thickness of plate 2 was given 11 logarithmically spaced values 3.16 between and 0.316 times that for plate 1, as listed in Table 6.2. In order to maintain the same value for the modal density of plate 2, its length was varied to compensate for the thickness, see equation (3.16). The damping values of the two plates were varied with frequency in order to give constant values of the modal overlap factor, as before. The highest of the three levels of damping was used here. The other parameters were the same as for the baseline model.

The effective CLF and the ensemble average CLF for the 11 cases were calculated and their logarithmic ratio, $10\log_{10}\left(\hat{\eta}_{ij}/\eta_{ij,ens}\right)$, in dB is shown in Figure 6.7 derived from results at 1 Hz spacing up to 1 kHz. The results below 1.25 times the lower of the cut-on frequencies of the two plates were excluded, as SEA assumptions would not be valid and it is inappropriate to use an SEA approach. All of the results fall within ±10 dB.

Table 6.2. Parameter values used for 11 variants with different values of the plate thickness ratio h_1/h_2.

h_1/h_2	h_1 (mm)	h_2 (mm)	L_1 (m)	L_2 (m)	b (m)	$n_1(\omega)$	$n_2(\omega)$	M_1	M_2
0.316	3.00	9.49	0.50	4.74	1.00	0.0085	0.026	0.53	1.60
0.398	3.00	7.54	0.50	3.77	1.00	0.0085	0.026	0.53	1.60
0.501	3.00	5.99	0.50	2.99	1.00	0.0085	0.026	0.53	1.60
0.631	3.00	4.75	0.50	2.37	1.00	0.0085	0.026	0.53	1.60
0.793	3.00	3.78	0.50	1.89	1.00	0.0085	0.026	0.53	1.60
1.00	3.00	3.00	0.50	1.50	1.00	0.0085	0.026	0.53	1.60
1.26	3.00	2.38	0.50	1.19	1.00	0.0085	0.026	0.53	1.60
1.58	3.00	1.89	0.50	0.944	1.00	0.0085	0.026	0.53	1.60
2.00	3.00	1.50	0.50	0.749	1.00	0.0085	0.026	0.53	1.60
2.51	3.00	1.19	0.50	0.594	1.00	0.0085	0.026	0.53	1.60
3.16	3.00	0.949	0.50	0.474	1.00	0.0085	0.026	0.53	1.60

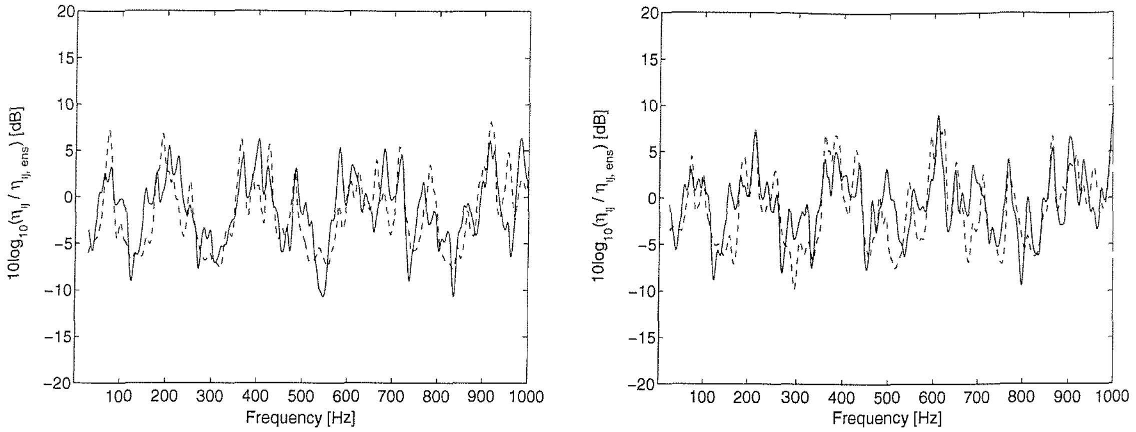

(a) $h_2 = 9.49$ mm, $L_2 = 4.74$ m

(b) $h_2 = 7.54$ mm, $L_2 = 3.77$ m

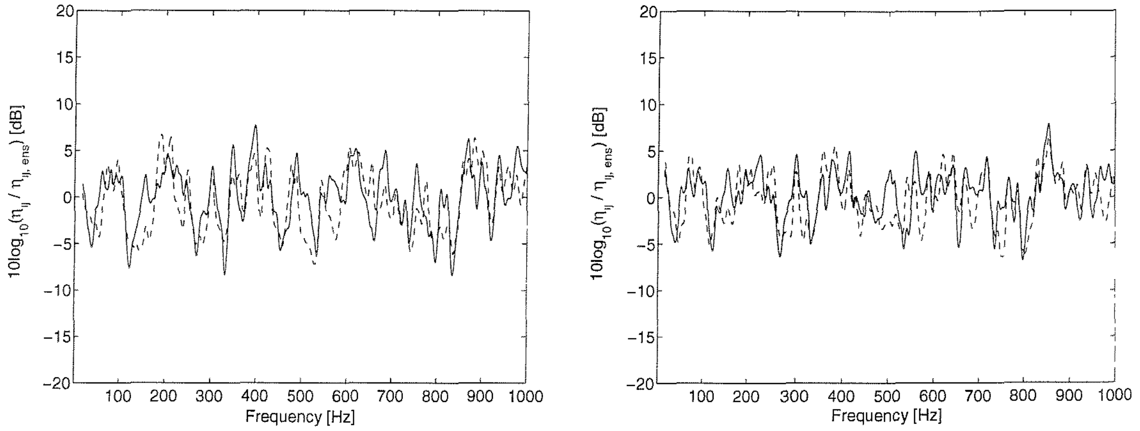

(c) $h_2 = 5.99$ mm, $L_2 = 2.99$ m

(d) $h_2 = 4.75$ mm, $L_2 = 2.37$ m

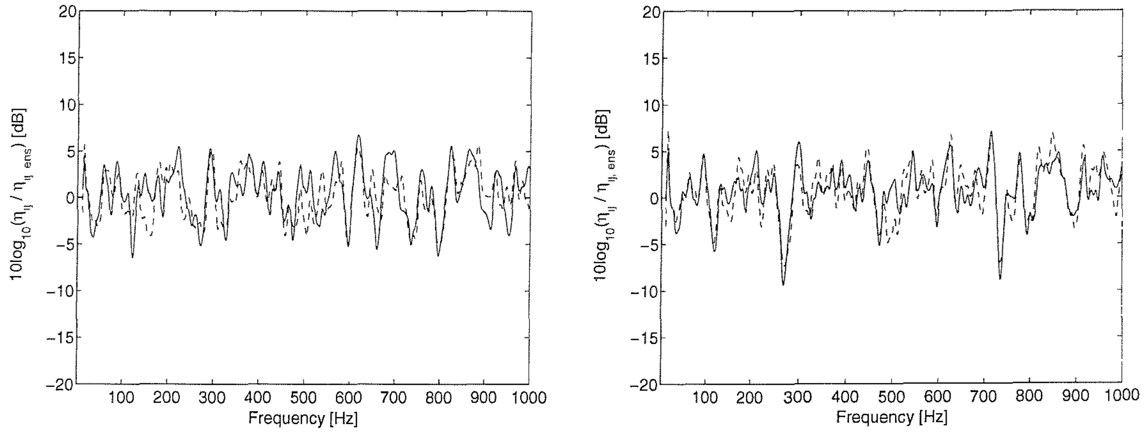

(e) $h_2 = 3.78$ mm, $L_2 = 1.89$ m

(f) $h_2 = 3.00$ mm, $L_2 = 1.50$ m

Figure 6.7 (a)-(f). The logarithmic CLF ratio $10\log_{10}\left(\hat{\eta}_{ij}/\eta_{ij,\,ens}\right)$ for different values of h_1/h_2 with constant modal overlap factors, $M_1 = 0.53$ and $M_2 = 1.6$ (h_2 and L_2 are varied, η depends on frequency). —, $10\log_{10}\left(\hat{\eta}_{12}/\eta_{12,\,ens}\right)$; ---, $10\log_{10}\left(\hat{\eta}_{21}/\eta_{21,\,ens}\right)$.

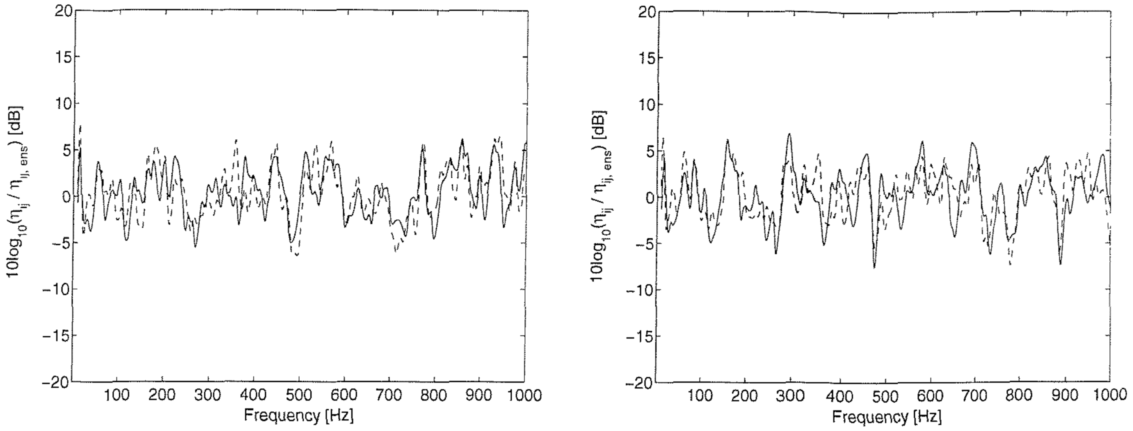

(g) $h_2 = 2.38$ mm, $L_2 = 1.19$ m

(h) $h_2 = 1.89$ mm, $L_2 = 0.94$ m

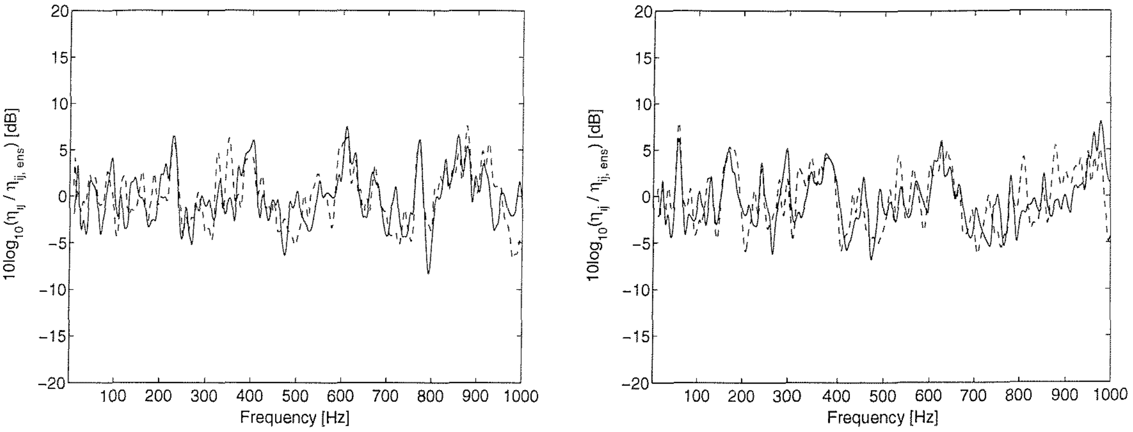

(i) $h_2 = 1.50$ mm, $L_2 = 0.75$ m

(j) $h_2 = 1.19$ mm, $L_2 = 0.59$ m

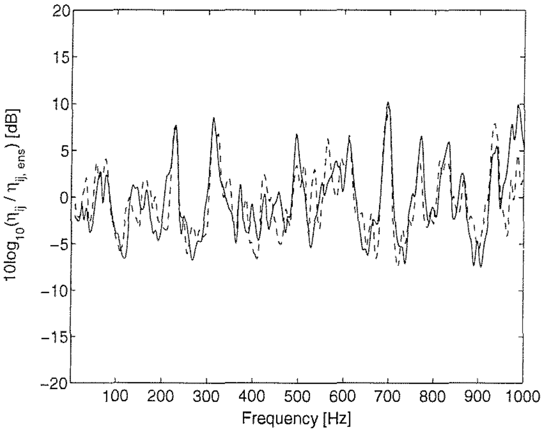

(k) $h_2 = 0.95$ mm, $L_2 = 0.47$ m

Figure 6.7 (g)-(k). The logarithmic CLF ratio $10\log_{10}\left(\hat{\eta}_{ij}/\eta_{ij,\,ens}\right)$ for different values of h_1/h_2 with constant modal overlap factors, $M_1 = 0.53$ and $M_2 = 1.6$ (h_2 and L_2 are varied, η depends on frequency). —, $10\log_{10}\left(\hat{\eta}_{12}/\eta_{12,\,ens}\right)$; ---, $10\log_{10}\left(\hat{\eta}_{21}/\eta_{21,\,ens}\right)$.

The results were also determined using energies averaged over frequency bands (2, 4, 6, 10, 20, 40, 60, 100, 200, and 400 Hz) in overlapping bands. The two standard deviation range (2σ) of $10\log_{10}\left(\langle\hat{\eta}_{ij}\rangle/\eta_{ij,\,ens}\right)$ was calculated in each case and a graph of 2σ against N_{12} is shown in Figure 6.8. The variability of the effective CLF is affected slightly by the plate thickness ratio h_1/h_2 but much more by the frequency bandwidth. The dependence on the average number of modes in the band N_{12} has a similar form to those shown in Figures 6.5 and 6.6. The results seem to be highest for either large or small values of the thickness ratio h_1/h_2; the results are lowest for $h_1/h_2 \cong 1$.

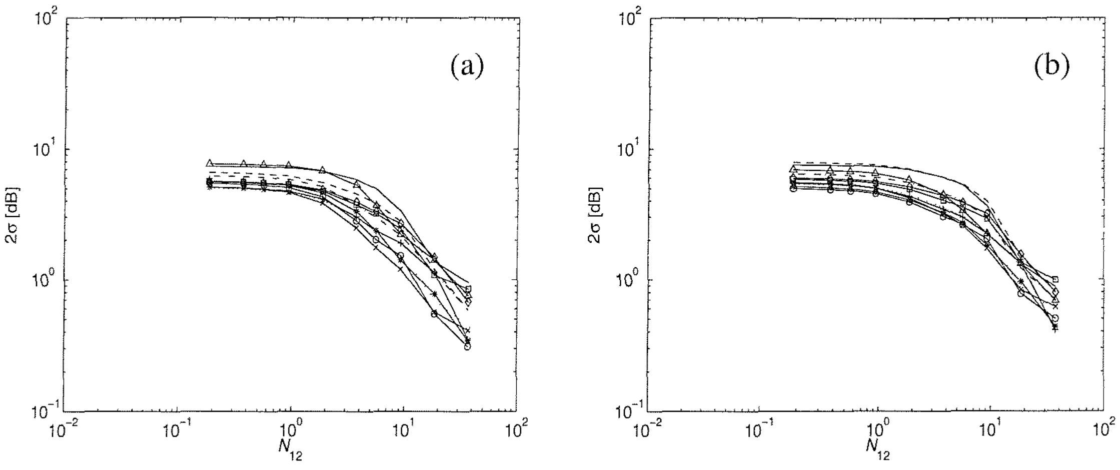

Figure 6.8. Variability of the CLF (2σ), (a) for η_{12} and (b) for η_{21}, for different values of h_1/h_2 with constant modal overlap factors, $M_1 = 0.53$ and $M_2 = 1.6$ (h_2 and L_2 are varied, η depends on frequency). —, 9.49; ---, 7.54; -·-, 5.99; ····, 4.75; -o-, 3.78; -x-, 3.00; -+-, 2.38; -*-, 1.89; -□-, 1.50; -◇-,1.19; -△-, 0.95 (h_2 in millimetres).

6.4.4 Variation of length ratio (L_1/L_2) with varying modal overlap factor ratio

The influence of the plate length ratio L_1/L_2 on the variability of the CLF was investigated by keeping the length of plate 1 fixed and giving the length of plate 2 each of 10 logarithmically spaced values between 3.16 and 0.4 times that for plate 1, as listed in Table 6.3. The damping was again chosen to be inversely proportional to frequency so that the modal overlap factor for each plate was constant. Again the highest damping value was used. The modal overlap factor for plate 2 was constant for each calculation, but was proportional to its length. The other parameters were the same as the baseline model.

Table 6.3. Parameter values used for 10 variants with different values of the plate length ratio L_1/L_2.

L_1/L_2	h_1 (mm)	h_2 (mm)	L_1 (m)	L_2 (m)	b (m)	$n_1(\omega)$	$n_2(\omega)$	M_1	M_2
0.316	3.00	2.00	0.50	1.58	1.00	0.0085	0.040	0.53	2.53
0.398	3.00	2.00	0.50	1.26	1.00	0.0085	0.032	0.53	2.02
0.501	3.00	2.00	0.50	1.00	1.00	0.0085	0.026	0.53	1.60
0.631	3.00	2.00	0.50	0.79	1.00	0.0085	0.020	0.53	1.26
0.793	3.00	2.00	0.50	0.63	1.00	0.0085	0.016	0.53	1.01
1.00	3.00	2.00	0.50	0.50	1.00	0.0085	0.013	0.53	0.80
1.26	3.00	2.00	0.50	0.40	1.00	0.0085	0.010	0.53	0.64
1.58	3.00	2.00	0.50	0.32	1.00	0.0085	0.0081	0.53	0.51
2.00	3.00	2.00	0.50	0.25	1.00	0.0085	0.0064	0.53	0.40
2.51	3.00	2.00	0.50	0.20	1.00	0.0085	0.0051	0.53	0.32

The effective CLF and the ensemble average CLF for the 10 cases were calculated and their logarithmic ratio $10\log_{10}\left(\hat{\eta}_{ij}/\eta_{ij,\,ens}\right)$ in dB is shown in Figure 6.9, for results calculated at 1Hz spacing up to 1kHz. The results below 1.25 times the lower of the first cut-on frequencies of the two plates were excluded, as in the previous section. All of the results fall within ±10 dB except for $L_2 = 0.4$ m where a single peak of 30 dB is seen.

The results were next determined using energies averaged over frequency bands (2, 4, 6, 10, 20, 40, 60, 100, 200, and 400 Hz) in overlapping bands. The two standard deviation range (2σ) of $10\log_{10}\left(\left\langle\hat{\eta}_{ij}\right\rangle/\eta_{ij,\,ens}\right)$ was calculated and is shown plotted against N_{12} in Figure 6.10. These results show that the variability of the effective CLFs depends somewhat on the ratio of M_1 to M_2, introduced here by varying the plate length ratio L_1/L_2. The constant value of 2σ for low N_{12} is greatest when $M_1/M_2 \cong 1$ (× in Figure 6.10) and lowest when M_1 and M_2 are most dissimilar. The result for $L_2 = 0.4$ m does not show up as unusual when averaged over the whole frequency range.

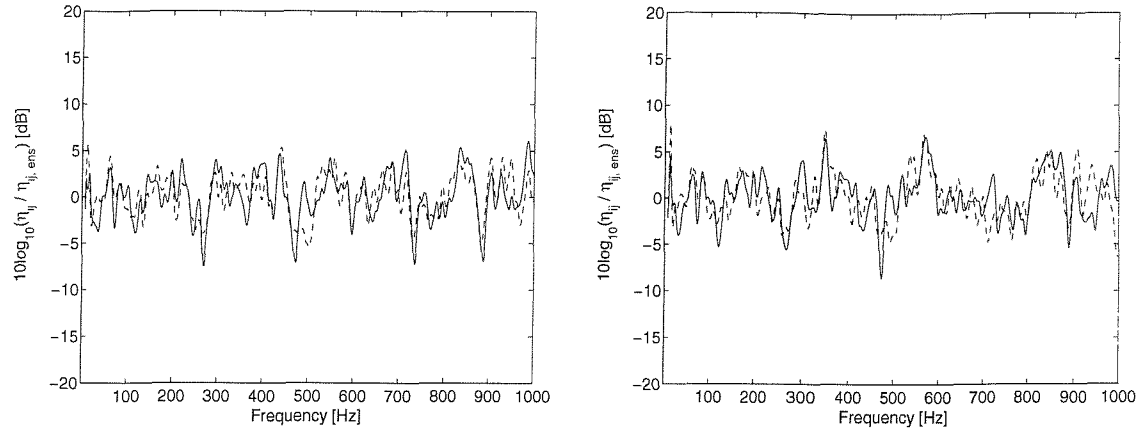

(a) $L_2 = 1.58$ m, $M_1/M_2 = 0.21$

(b) $L_2 = 1.26$ m, $M_1/M_2 = 0.26$

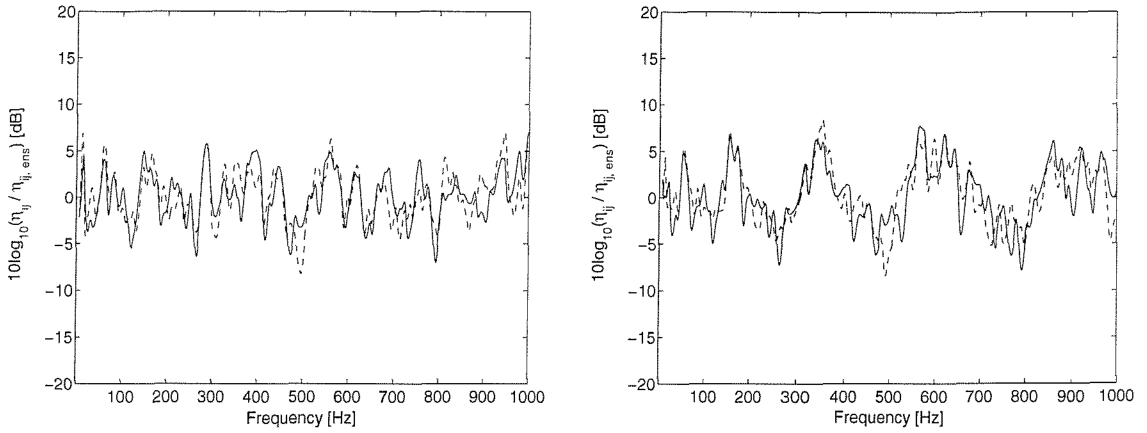

(c) $L_2 = 1.00$ m, $M_1/M_2 = 0.33$

(d) $L_2 = 0.79$ m, $M_1/M_2 = 0.42$

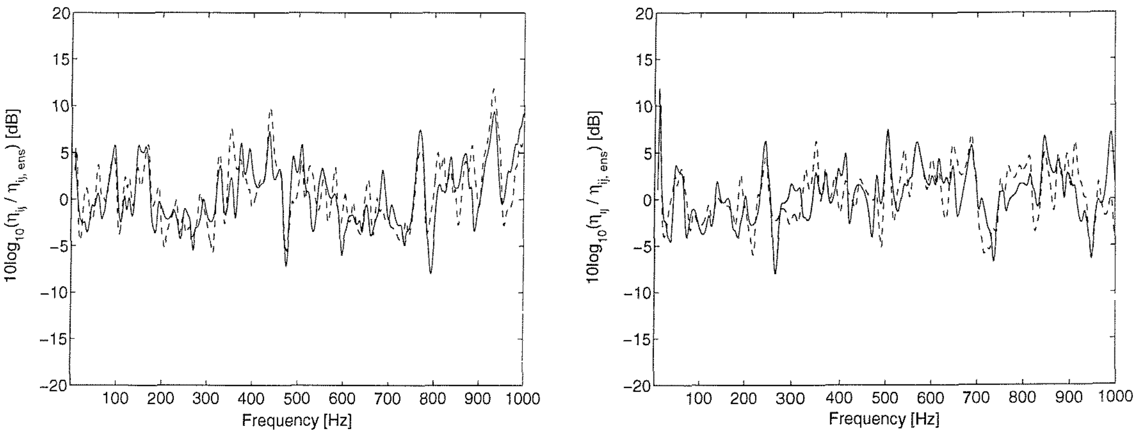

(e) $L_2 = 0.63$ m, $M_1/M_2 = 0.53$

(f) $L_2 = 0.50$ m, $M_1/M_2 = 0.67$

Figure 6.9 (a)-(f). The logarithmic CLF ratio $10\log_{10}\left(\hat{\eta}_{ij}/\eta_{ij,\,ens}\right)$ for different values of L_1/L_2. The modal overlap factor ratio M_1/M_2 varies between 0.21 and 1.66 ($M_1 = 0.53$ is fixed, L_2 and M_2 ($= 2.53 \sim 0.32$) varying). —, $10\log_{10}\left(\hat{\eta}_{12}/\eta_{12,\,ens}\right)$; ---, $10\log_{10}\left(\hat{\eta}_{21}/\eta_{21,\,ens}\right)$.

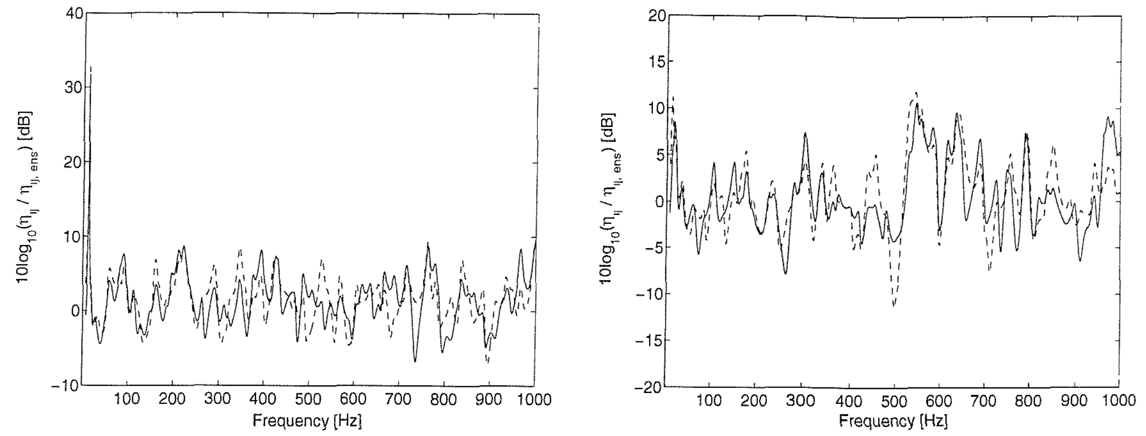

(g) $L_2 = 0.40$ m, $M_1/M_2 = 0.83$ (h) $L_2 = 0.32$ m, $M_1/M_2 = 1.04$

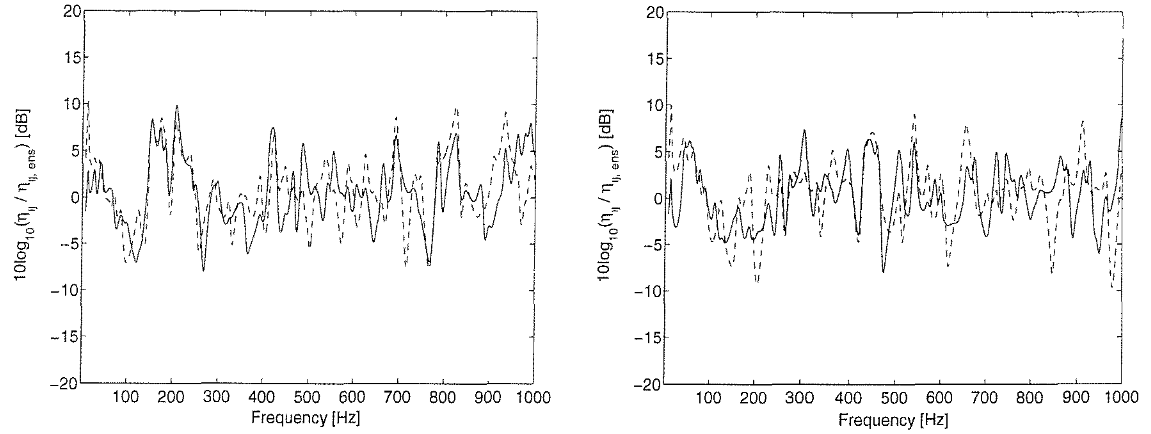

(i) $L_2 = 0.25$ m, $M_1/M_2 = 1.33$ (j) $L_2 = 0.20$ m, $M_1/M_2 = 1.67$

Figure 6.9 (g)-(j). The logarithmic CLF ratio $10\log_{10}\left(\hat{\eta}_{ij}/\eta_{ij,\,ens}\right)$ for different values of L_1/L_2. The modal overlap factor ratio M_1/M_2 varies between 0.21 and 1.66 ($M_1 = 0.53$ is fixed, L_2 and M_2 ($= 2.53 \sim 0.32$) varying). —, $10\log_{10}\left(\hat{\eta}_{12}/\eta_{12,\,ens}\right)$; ---, $10\log_{10}\left(\hat{\eta}_{21}/\eta_{21,\,ens}\right)$.

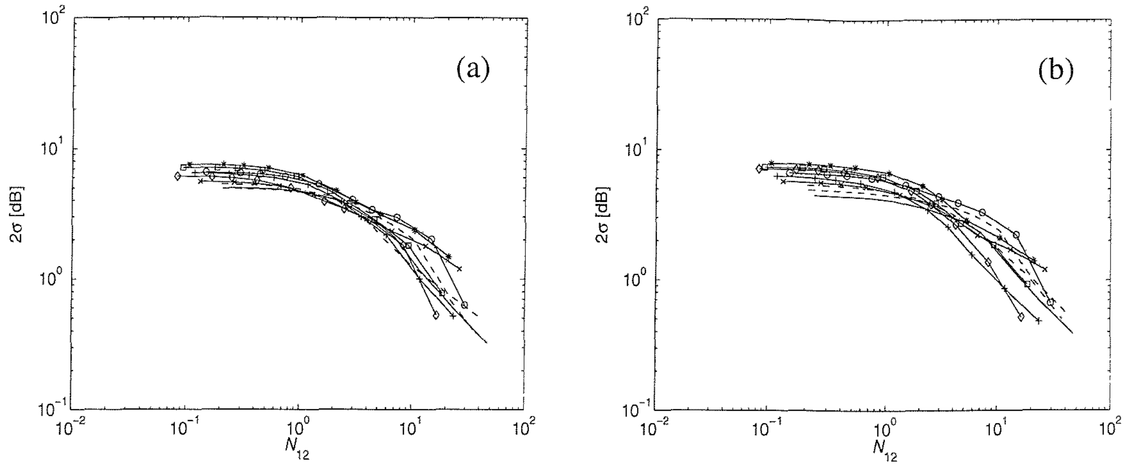

Figure 6.10. Variability of CLF (2σ), (a) for η_{12} and (b) for η_{21}, for various values of L_2. —, 1.58; ---, 1.26; -·-, 1.00; ····, 0.79; -o-, 0.63; -x-, 0.50; -+-, 0.40; -*-, 0.32; -□-, 0.25; -◇-, 0.20 (L_2 in metres).

6.4.5 Variation of length-to-width ratio (L_1/b) without varying modal density

The influence of the plate length-to-width ratio L_1/b on the variability of the CLF was investigated by setting the widths of the two plates to 10 logarithmically spaced values between 3.16 and 0.4 times the baseline length of plate 1 (L_1 = 0.5 m), see Table 5.5. The lengths of the plates are varied simultaneously to maintain the same areas, $S_1 = 0.5$ m^2 and $S_2 = 1.0$ m^2, and hence constant values of N_1 and N_2. The parameter values used for 10 variants are listed in Table 6.4.

The modal densities for the two plates were kept constant, by varying their lengths in order to keep the area and hence the modal density fixed. The damping values of the two plates were also made frequency dependent as before, in order to give constant modal overlap factors. Again the highest damping value was used. The other parameters were the same as the baseline model.

The effective CLF and the ensemble average CLF for these 10 cases were calculated and their logarithmic ratio, $10\log_{10}\left(\hat{\eta}_{ij}/\eta_{ij.ens}\right)$, in dB is shown in Figure 6.11, for results calculated at 1 Hz spacing up to 1 kHz. The results below 1.25 times the lower of the first cut-on frequencies of the two plates were also excluded, as before. Most of the CLF ratios fluctuated within ±10 dB.

Table 6.4. Parameter values for 10 variants with different values of the plate length-to-width ratio L_1/b.

L_1/b	h_1 (mm)	h_2 (mm)	L_1 (m)	L_2 (m)	b (m)	$n_1(\omega)$	$n_2(\omega)$	M_1	M_2
0.203	3.00	2.00	0.32	0.63	1.58	0.0085	0.026	0.53	1.60
0.318	3.00	2.00	0.40	0.79	1.26	0.0085	0.026	0.53	1.60
0.500	3.00	2.00	0.50	1.00	1.00	0.0085	0.026	0.53	1.60
0.798	3.00	2.00	0.63	1.27	0.79	0.0085	0.026	0.53	1.60
1.25	3.00	2.00	0.79	1.59	0.63	0.0085	0.026	0.53	1.60
2.00	3.00	2.00	1.00	2.00	0.50	0.0085	0.026	0.53	1.60
3.13	3.00	2.00	1.25	2.50	0.40	0.0085	0.026	0.53	1.60
4.88	3.00	2.00	1.56	3.13	0.32	0.0085	0.026	0.53	1.60
8.00	3.00	2.00	2.00	4.00	0.25	0.0085	0.026	0.53	1.60
12.5	3.00	2.00	2.50	5.00	0.20	0.0085	0.026	0.53	1.60

The results were again determined using energies averaged over frequency bands (2, 4, 6, 10, 20, 40, 60, 100, 200, and 400 Hz) in overlapping bands. The two standard deviation range (2σ) of $10\log_{10}\left(\left\langle\hat{\eta}_{ij}\right\rangle/\eta_{ij,ens}\right)$ was calculated in each case and 2σ is shown plotted against N_{12} in Figure 6.12. These results show that while the results are largely independent of width b at low values of N_{12}, as the bandwidth is increased considerable variations occur. Especially, if the plates are narrow and long (□, ◊ in Figure 6.12), the variability of the CLF is significant even for large values of N_{12}. This can be seen in Figure 6.11 (i) and (j) as systematic variations in the CLF ratio, especially below the second cut-on frequency of plate 1 (470 Hz and 734 Hz).

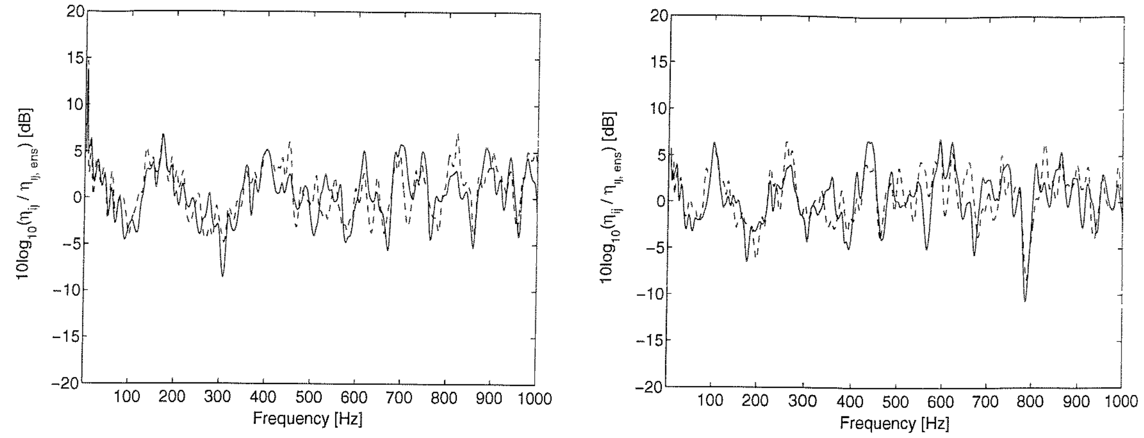

(a) $b = 1.58$ m

(b) $b = 1.26$ m

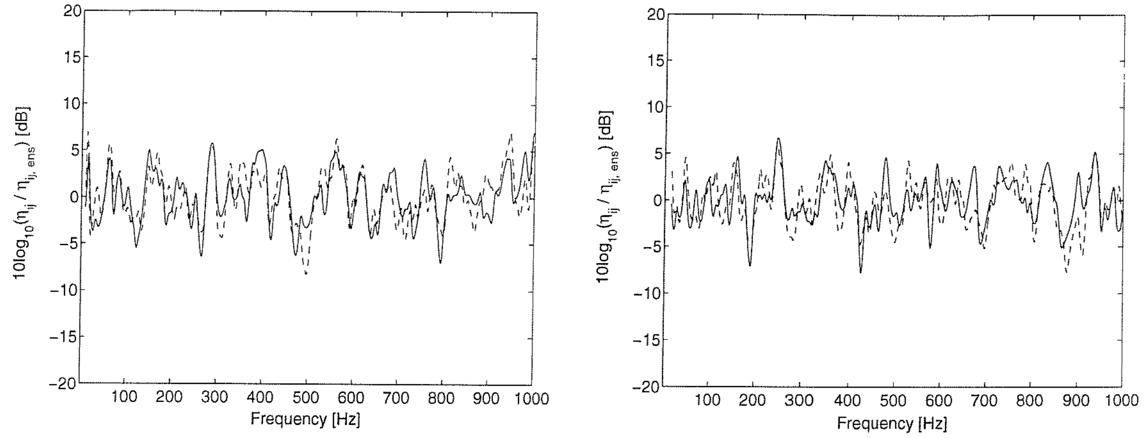

(c) $b = 1.00$ m

(d) $b = 0.79$ m

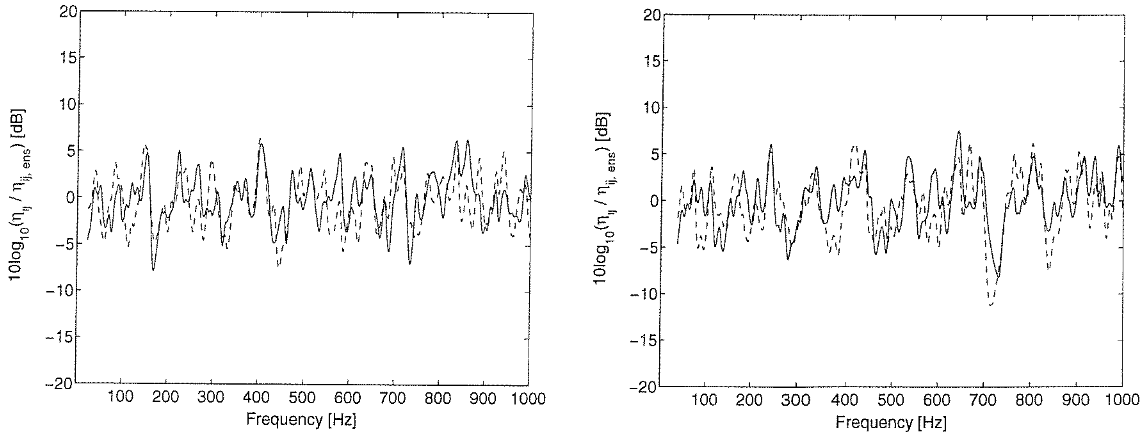

(e) $b = 0.63$ m

(f) $b = 0.50$ m

Figure 6.11 (a)-(f). The logarithmic CLF ratio $10\log_{10}\left(\hat{\eta}_{ij}/\eta_{ij,\ ens}\right)$ for various values of b, L_1 and L_2 (area ($S_1 = 0.5$ m^2, $S_2 = 1.0$ m^2), M_1 (= 0.53) and M_2 (= 1.6) are kept constant). —, $10\log_{10}\left(\hat{\eta}_{12}/\eta_{12,\ ens}\right)$; ---, $10\log_{10}\left(\hat{\eta}_{21}/\eta_{21,\ ens}\right)$.

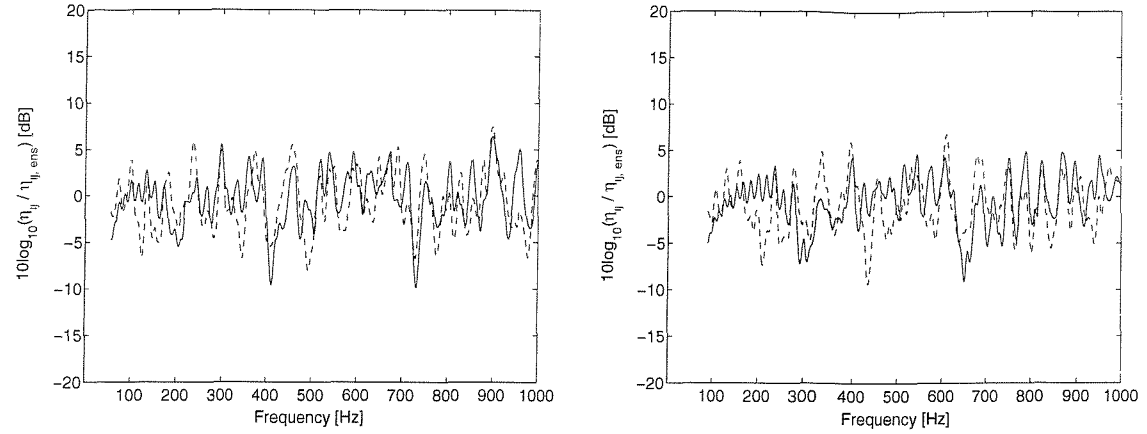

(g) $b = 0.40$ m (h) $b = 0.32$ m

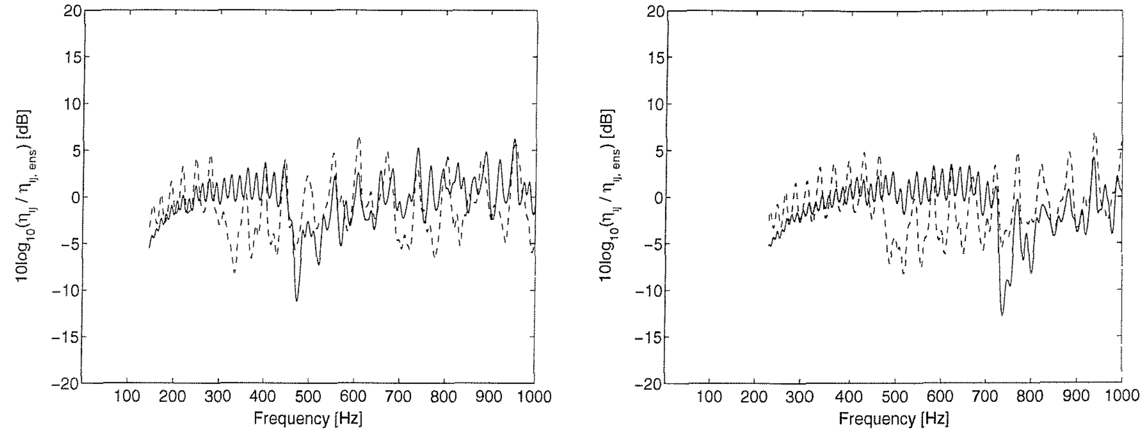

(i) $b = 0.25$ m (j) $b = 0.20$ m

Figure 6.11 (g)-(j). The logarithmic CLF ratio $10\log_{10}\left(\hat{\eta}_{ij}/\eta_{ij,\,ens}\right)$ for various values of b, L_1 and L_2 (area ($S_1 = 0.5$ m^2, $S_2 = 1.0$ m^2), M_1 (= 0.53) and M_2 (= 1.6) are kept constant). —, $10\log_{10}\left(\hat{\eta}_{12}/\eta_{12,\,ens}\right)$; ---, $10\log_{10}\left(\hat{\eta}_{21}/\eta_{21,\,ens}\right)$.

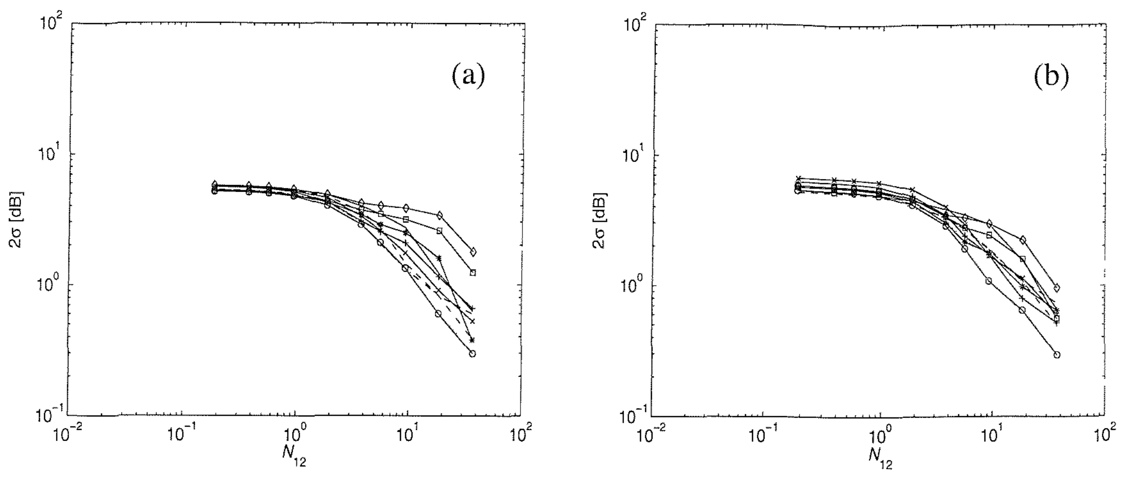

Figure 6.12. Variability of the effective CLF (2σ), (a) for η_{12} and (b) for η_{21}, for different values of b keeping plate areas and modal overlap factor constant. —, 1.58; ---, 1.26; -·-, 1.00; ····, 0.79; -o-, 0.63; -×-, 0.50; -+-, 0.40; -*-, 0.32; -□-, 0.25; -◇-,0.20 (b in metres).

6.5 An empirical model for the variability of the effective CLF

6.5.1 The variability of the effective CLF for finite plates

All of the previous results covering the extensive parameter variations are next considered together to establish appropriate parameters to describe the variability of the CLF and to quantify its confidence interval. Although the results up to now have been given in terms of 2σ, it is helpful at this point to work in terms of the variance, σ^2. Firstly the results for σ^2 of the logarithmic ratio of the frequency averaged effective CLF to the ensemble average CLF are plotted against the number of modes per band for the source plate N_{source} or the receiver plate N_{receiver}, as shown in Figure 6.13 (a). The results with no frequency averaging are plotted against the modal overlap factor for the source plate M_{source} or the receiver plate M_{receiver}, as shown in Figure 6.13 (b). No clear trend can be seen from these results, although σ^2 tends to fall with increasing N or M.

Next the results for σ^2 are plotted against $N_{12} = \sqrt{N_1 N_2}$ (the geometric mean number of modes per band), as shown in Figure 6.14 (a). These results are slightly less scattered than in the previous plot, Figure 6.13 (a). This result shows that the variability of the CLF σ^2 has a nonlinear relationship with N_{12} on log-log axes. The results for σ^2 are shown for the cases with no frequency averaging in Figure 6.14 (b). These are plotted against

$M_{12} = \sqrt{M_1 M_2}$ (the geometric mean modal overlap factor). These non-frequency averaged results show a linear relationship with M_{12} on log-log axes; from the slope of this relationship it is found that σ^2 is inversely proportional to M_{12}.

The values of σ^2 for low N_{12} are independent of N_{12} (see also Figures 6.5, 6.6, 6.8, 6.10 and 6.12) and are thus similar to those for no frequency averaging. By multiplying all data points in Figure 6.14 (a) by M_{12}, the results collapse to a similar level at low values of N_{12}. However it is found necessary also to shift the curves horizontally by a factor of $1/\sqrt{M_{12}}$ to collapse them to a single data set.

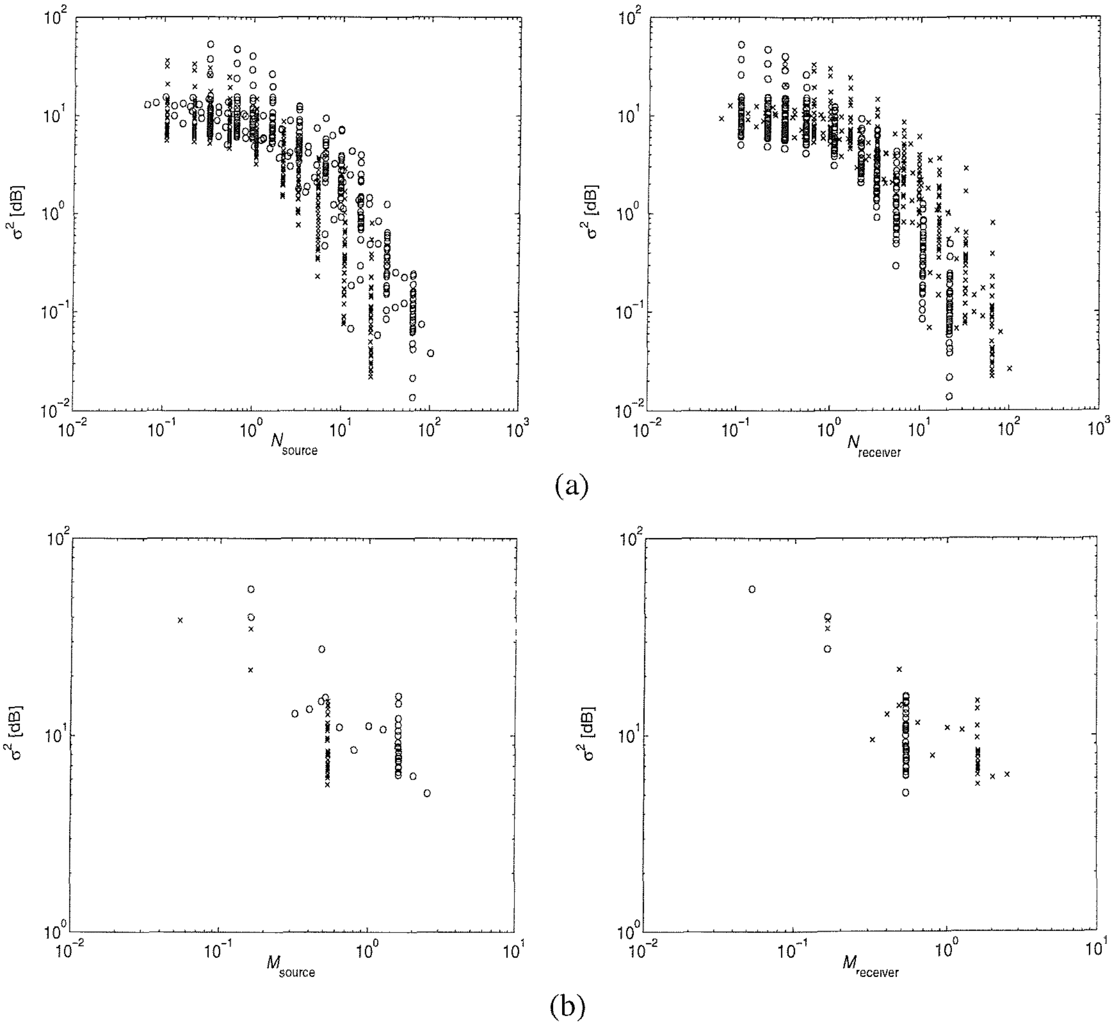

Figure 6.13. σ^2 of $10\log_{10}\left(\langle\hat{\eta}_{ij}\rangle/\eta_{ens}\right)$ for all sets of data plotted against (a) N_{source} and N_{receiver} when the effective CLFs are averaged over frequency bands (2, 4, 6, 10, 20, 40, 60, 100, 200, and 400 Hz) and (b) M_{source} and M_{receiver} when no frequency averaging is performed. Crosses denote results for η_{12} and circles denote those for η_{21}.

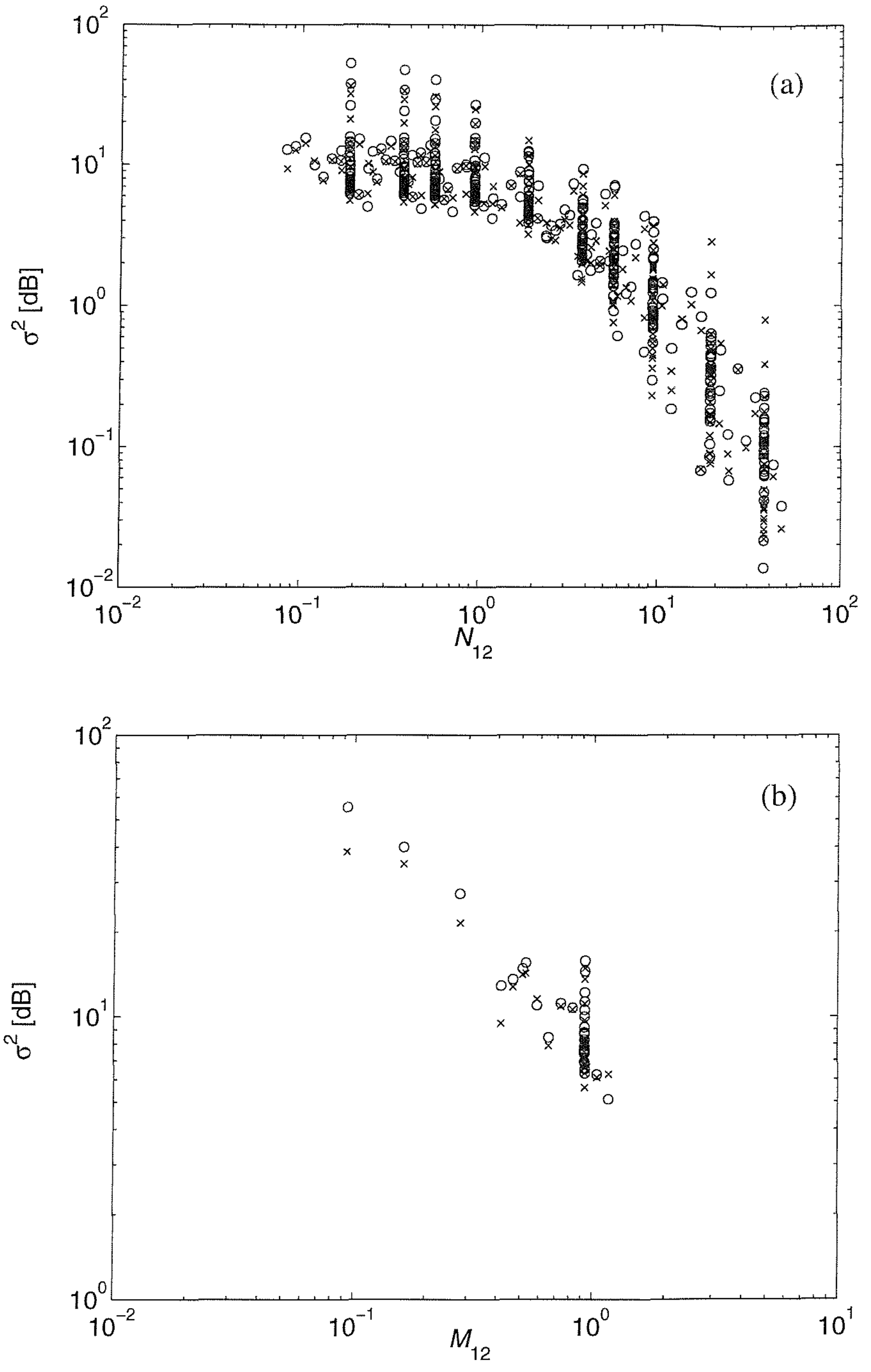

Figure 6.14. σ^2 of $10\log_{10}\left(\left\langle\hat{\eta}_{ij}\right\rangle/\eta_{ens}\right)$ for all sets of data plotted against (a) N_{12} when the effective CLFs are averaged over frequency bands (2, 4, 6, 10, 20, 40, 60, 100, 200, and 400 Hz) and (b) M_{12} when no frequency averaging is performed. Crosses denote results for η_{12} and circles denote those for η_{21}.

The result is shown in Figure 6.15 in which $\sigma^2 M_{12}$ is plotted against N_{12}^2/M_{12}. A formula has been established to fit three curves to the data in Figure 6.15: $\sigma^2 M_{12} = \dfrac{a}{1+bN_{12}^2/M_{12}}$ where a and b are constants for the three curves. Dividing through by M_{12} these can be expressed in the form

$$\sigma^2 = \frac{a}{M_{12}+bN_{12}^2}. \tag{6.1}$$

The first and third curves are fitted approximately as the minima and maxima of the ordinate value $\sigma^2 M_{12}$ as a function of N_{12}^2/M_{12} while the second curve corresponds to a line roughly through the centre of the data. The values of a and b are listed in Table 6.5.

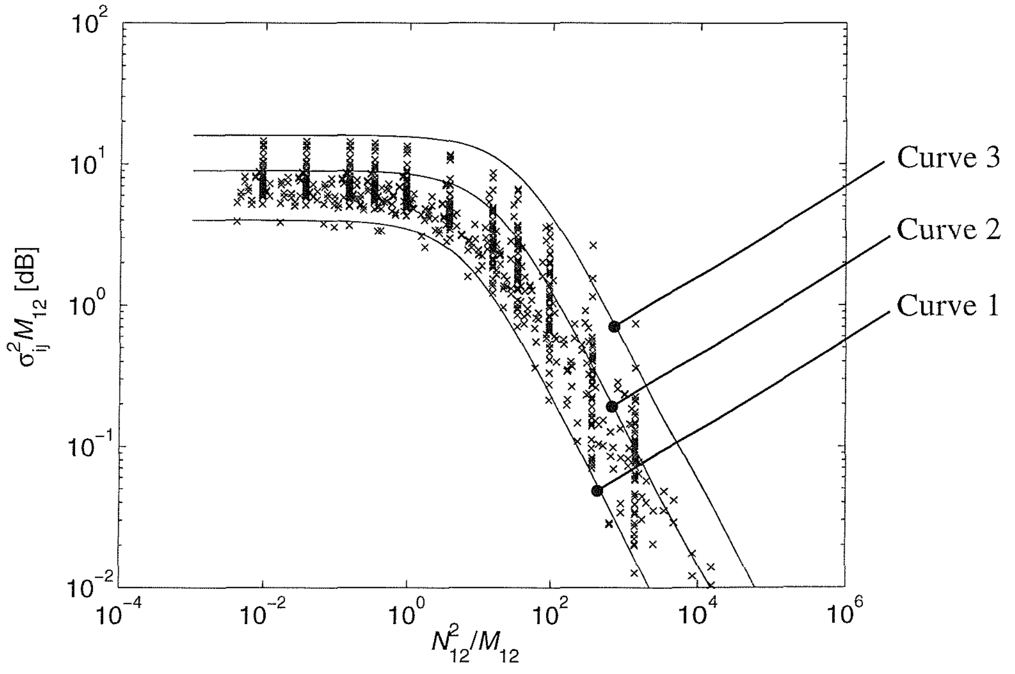

Figure 6.15. $\sigma^2 M_{12}$ plotted against N_{12}^2/M_{12} and three curves produced to quantify the variability of the CLF.

Using each of these curves rather than the original data points, a predicted confidence interval ($\pm 2\sigma$) for $10\log_{10}\left(\langle\hat{\eta}\rangle/\eta_{ens}\right)$ is determined for each pair of plates represented. In each case by comparing the DSM predictions with this predicted confidence interval, the percentage of frequency points falling inside this interval has been determined. Taking the average over all plates considered, it was found what confidence level each of the formulae represented. These are listed in Table 6.5. Of these, the second curve represents a 97.2% confidence interval for all sets of data and appears a suitable model.

Table 6.5. Percentage of points falling within $\pm 2\sigma$ limits defined by $\sigma^2 = \dfrac{a}{M_{12} + bN_{12}^2}$ for all sets of data.

Curve	a	b	Confidence interval (%)
1	4	1/6	82.3
2	9	1/16	97.2
3	16	1/36	99.7

6.5.2 New parameters to include cases of coupled finite and infinite plates

In order to apply the above concepts to the results for an infinite plate coupled to a finite plate (see Section 4.4) or a finite plate coupled to an infinite plate (see Section 4.5), the two parameters, M_{12} and N_{12}, cannot be used since the number of modes and modal densities for an infinite plate tend to infinity. The CLF ratio for a model with an infinite receiver plate and upper and lower bounds ($\pm 2\sigma$) obtained from equation (6.1) (with constants, $a = 9$ and $b = 1/16$) but using $2M_1$ and $2N_1$ instead of M_{12} and N_{12} are shown in Figure 6.16 (a). Figure 6.16 (b) shows the results of an infinite source plate coupled to a finite receiver plate for $n = 1$ along with bounds obtained from $2N_2$ and $2M_2$. The CLF results for the two semi-infinite plates with finite width $\eta_{12\infty}$ is used as a reference. In both cases these give reasonable upper and lower bounds for the CLF for those models. Therefore, instead of M_{12} and N_{12}, new parameters are sought which tend to $2M_1$ when $M_2 \to \infty$, $2M_2$ when $M_1 \to \infty$ but are close to M_{12} for $M_1 \approx M_2$.

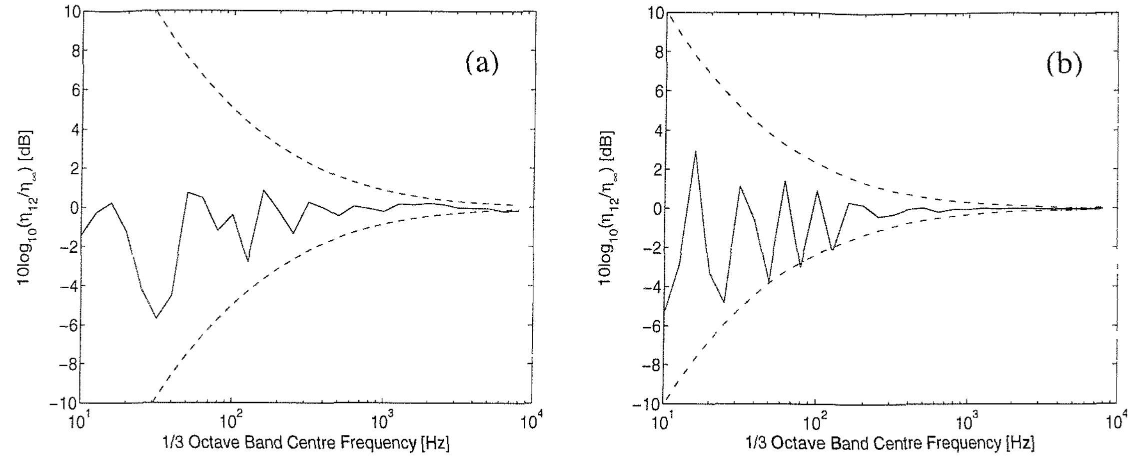

Figure 6.16. The effective CLFs and upper and lower bounds ($\pm 2\sigma$) for (a) a finite plate coupled to an infinite plate and (b) an infinite plate coupled to a finite plate for n = 1. —, $10\log_{10}\left(\hat{\eta}_{12}/\eta_{12\infty}\right)$; ---, upper and lower bounds obtained from equation (6.1) with $a = 9$ and b = 1/16 using $2M_1$ and $2N_1$ or $2M_2$ and $2N_2$ instead of M_{12} and N_{12}.

A new 'combined' modal overlap factor is therefore proposed, given by

$$M_{\text{comb}} = \frac{2M_1M_2}{M_1 + M_2}. \tag{6.2}$$

It may be noted that this satisfies $M_{\text{comb}} \approx M_{12}$ for $M_1 \approx M_2$, $M_{\text{comb}} = 2M_1$ for $M_2 \to \infty$, and $M_{\text{comb}} = 2M_2$ for $M_1 \to \infty$.

Similarly a new 'combined' number of modes in a band is proposed, given by

$$N_{\text{comb}} = \frac{2N_1N_2}{N_1 + N_2} \tag{6.3}$$

which satisfies $N_{\text{comb}} \approx N_{12}$ for $N_1 \approx N_2$, $N_{\text{comb}} = 2N_1$ for $N_2 \to \infty$, and $N_{\text{comb}} = 2N_2$ for $N_1 \to \infty$. Equations (6.2) and (6.3) are equivalent to the following relationships: $\frac{1}{M_{\text{comb}}} = \frac{1}{2}\left(\frac{1}{M_1} + \frac{1}{M_2}\right)$ and $\frac{1}{N_{\text{comb}}} = \frac{1}{2}\left(\frac{1}{N_1} + \frac{1}{N_2}\right)$, and thus reflect the fact that the smaller of the two values of N or M dominates the variability of the CLF.

Figure 6.17 shows N_{comb}/N_1 and N_{comb}/N_2 plotted against N_2/N_1. These are compared with N_{12}/N_1 and N_{12}/N_2. This plot shows that two values N_{comb} and N_{12} are close when

$N_1 \sim N_2$. The same plots also apply to M_{comb}, etc. The values of N_2/N_1 and M_2/M_1 considered in the parameter variations in Section 6.4 are limited to the range 0.6 to 4.74.

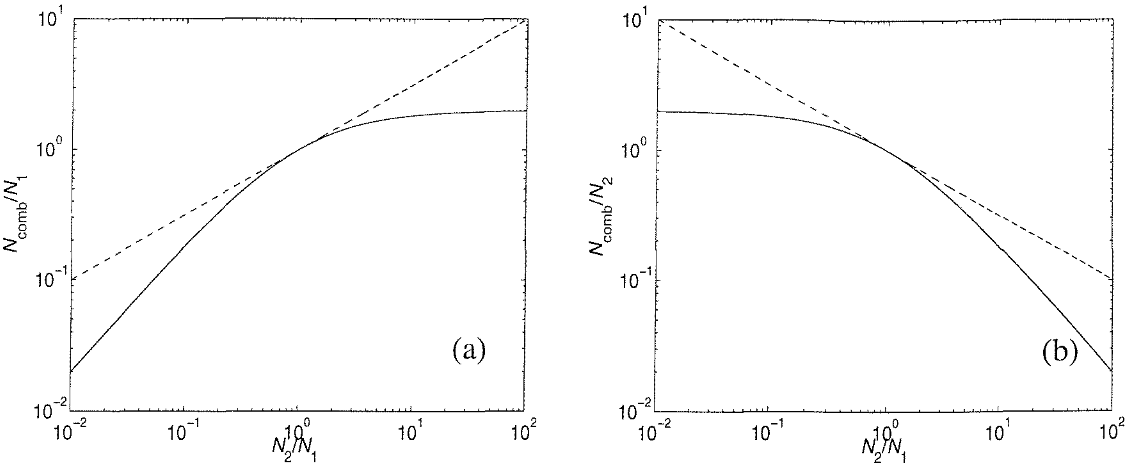

Figure 6.17. N_{comb}/N and N_{12}/N plotted against N_2/N_1. (a) —, N_{comb}/N_1; ---, N_{12}/N_1 and (b) —, N_{comb}/N_2; ---, N_{12}/N_2.

6.5.3 Derivation of empirical model

Using the same method as Section 6.5.1, a similar result is shown in Figure 6.18 in which $\sigma^2 M_{\text{comb}}$ is plotted against $N_{\text{comb}}^2 / M_{\text{comb}}$. Similarly, a formula has been established to fit three curves to the data in Figure 6.18: $\sigma^2 M_{\text{comb}} = \dfrac{c}{1 + dN_{\text{comb}}^2 / M_{\text{comb}}}$ where c and d are constants for the three curves. Dividing through by M_{comb} these can be expressed in the form

$$\sigma^2 = \frac{c}{M_{\text{comb}} + dN_{\text{comb}}^2}. \tag{6.4}$$

As above, the confidence intervals represented by each of these curves have been determined from the whole set of DSM results and from the results excluded the last two cases (the long narrow cases) in Table 6.4. These are listed in Table 6.6. If the long narrow cases are removed from the calculation, the percentage goes up slightly. Of these, the second curve is adopted as the 'empirical model' for the variability of the CLF:

$$\sigma^2 = \frac{6}{M_{\text{comb}} + N_{\text{comb}}^2 / 16}. \tag{6.5}$$

This represents a 95.7% confidence interval for all sets of data which are considered. It should be noted that this set covers the range of aspect ratios of 0.2 ~ 12.5 for one plate and 0.2 ~ 25 for the other plate. This model can be generally used to evaluate the uncertainty of the CLF of a two-coupled plate system at least within these limits. It is a refinement of the model in the previous section, that can now also be used to cover situations where one plate is infinite in length. However, it may be expected to fail if the plates become infinitely wide.

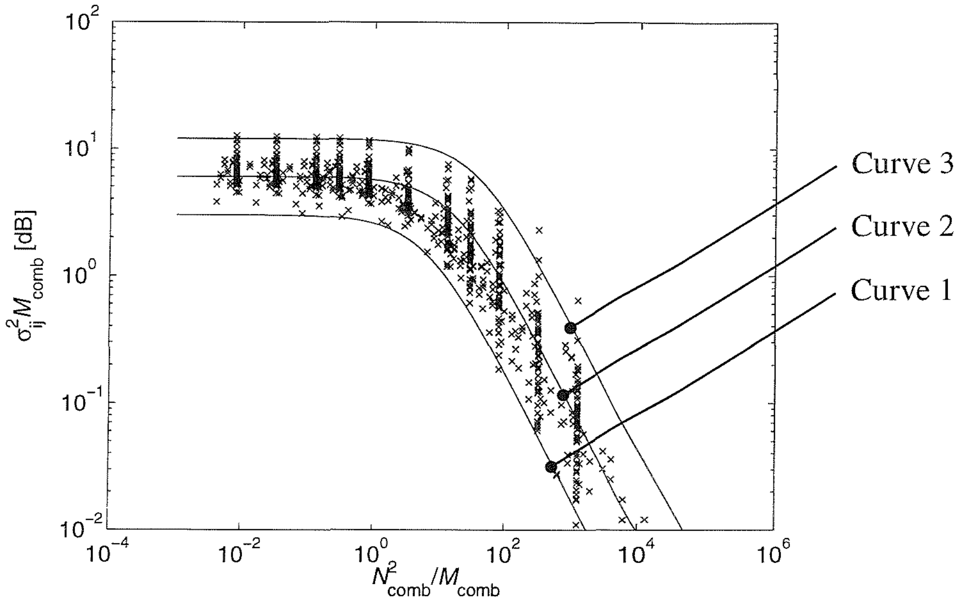

Figure 6.18. $\sigma^2 M_{\text{comb}}$ plotted against $N^2_{\text{comb}}/M_{\text{comb}}$ and three curves produced to quantify the variability of the CLF.

Table 6.6. Percentage of points falling within $\pm\sigma$ and $\pm 2\sigma$ limits defined by $\sigma^2 = \dfrac{c}{M_{\text{comb}} + dN^2_{\text{comb}}}$ for all sets of DSM results and for the results excluded the last two cases (the long narrow cases) in Table 6.4.

Curve	c	d	All sets of data		Excluding the long narrow cases	
			$\pm\sigma$	$\pm 2\sigma$	$\pm\sigma$	$\pm 2\sigma$
1	3	1/6	50.9	80.1	51.4	80.6
2	6	1/16	73.4	95.7	74.0	96.1
3	12	1/36	90.1	99.6	90.6	99.7

6.5.4 Comparison with previously published models

A similar investigation for two coupled plates, in which only the plate length ratio L_1/L_2 was varied, was performed by Mohammed [43]. He suggested a semi-empirical formula,

$$\left\{\frac{\sigma^2}{\langle\eta_{ij}\rangle^2}\right\} = \log_{10} c + 1.3\log_{10} M_{12} + 1.25\log_{10} N_{12} \tag{6.6}$$

where σ^2 is the variance of the CLF, $\langle\eta_{ij}\rangle$ is the mean value of the CLF and c is a constant which was determined by plotting the different sets of data and performing best straight line fits on log-log axes.

The current results, displayed in Figure 6.18, have been converted into the form used in Mohammed's model and are plotted in Figure 6.19. This graph shows that the current results cannot be represented by a straight line as suggested by Mohammed. Also the present data set far exceeds the number of configurations previously used [43]. The present model therefore seems more appropriate.

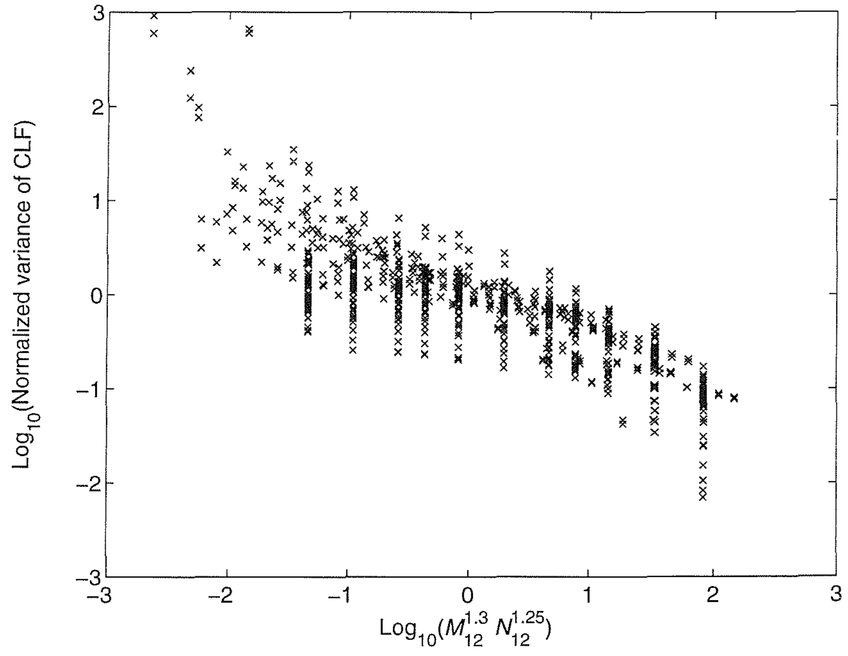

Figure 6.19. The normalised variance $\frac{\sigma^2}{\langle\hat{\eta}_{ij}\rangle}$ plotted against $(M_{12})^{1\,3}(N_{12})^{1\,25}$ based on the Mohammed's formula [43].

A general formula for the normalised variance in the CLFs is given by Lyon and DeJong [33],

$$\left\{\frac{\sigma^2}{\langle\eta_{ij}\rangle^2}\right\}=\frac{1}{\pi\omega\{\eta_1 n_1(\omega)+\eta_2 n_2(\omega)\}+\Delta\omega\{n_1(\omega)+n_2(\omega)\}}\frac{\langle\psi_1^4\rangle}{\langle\psi_1^2\rangle^2}\frac{\langle\psi_2^4\rangle}{\langle\psi_2^2\rangle^2} \tag{6.7}$$

where $\Delta\omega$ is the frequency spacing and ψ_1 and ψ_2 are the mode shapes of subsystem 1 and subsystem 2. If the data is taken in 1/3 octave bands and each plate is assumed to be simply supported, equation (6.7) is approximated by

$$\left\{\frac{\sigma^2}{\langle\eta_{ij}\rangle^2}\right\}=\frac{81}{16\omega\left[\pi\{\eta_1 n_1(\omega)+\eta_2 n_2(\omega)\}+0.231\{n_1(\omega)+n_2(\omega)\}\right]} \tag{6.8}$$

The logarithmic CLF ratio $10\log_{10}\left(\hat{\eta}_{12}/\eta_{12,ens}\right)$ obtained from the DSM for the baseline model used in Chapter 4 was compared with the upper and lower bounds obtained from $\pm2\sigma$ estimates based on the empirical model of equation (6.5) and based on equation (6.8) and these results are plotted in Figure 6.20.

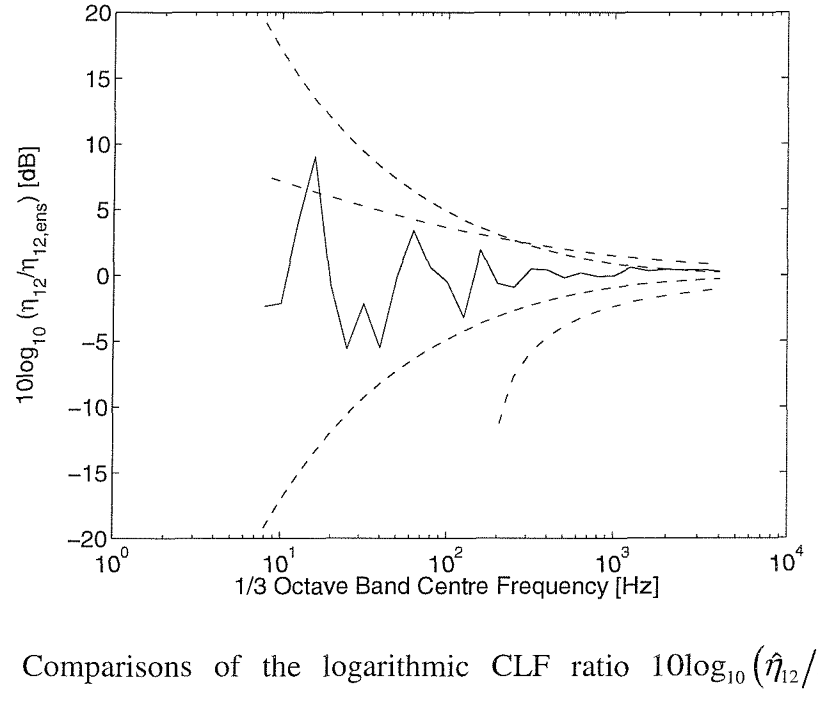

Figure 6.20. Comparisons of the logarithmic CLF ratio $10\log_{10}\left(\hat{\eta}_{12}/\eta_{12,ens}\right)$ for the baseline model obtained from the DSM with the upper and lower bounds based on the empirical model and equation (6.8). —, DSM result; ---, $\pm2\sigma$ estimate obtained from equation (6.5); -·-, $10\log_{10}\left(1\pm2\sigma/\langle\eta_{12}\rangle\right)$ estimate obtained from equation (6.8).

This shows that the DSM result calculated in 1/3 octave bands falls within the upper and lower bounds obtained from the empirical model proposed in this chapter over the whole frequency range. The result from equation (6.8) represents a good upper bound, whereas the lower bound is very low and it is not applicable at low frequencies because values inside the logarithm, $1-2\sigma/\langle\eta_{12}\rangle$, become negative below 200Hz. Strictly the distribution considered by Lyon and DeJong is not normal so that the 95% confidence interval is not simply $\pm 2\sigma$. However this has not been pursued further here.

6.5.5 Comparison with previous calculations

The results of the effective CLF found in the previous parameter variations, as described in Chapter 5, have been compared to the estimates of the confidence intervals based on equation (6.5). These results were in 1/3 octave bands and covered variations in thickness ratio, length ratio, and length-to-width ratio. The logarithmic ratio of the effective CLF to the ensemble average $10\log_{10}\left(\hat{\eta}_{ij}/\eta_{ij,\,ens}\right)$ was determined and these results are shown in Figure 6.21.

These $\pm 2\sigma$ estimates give better upper and lower bounds for the effective CLF than Craik's model considered in Chapter 5. The deviations at high frequencies in Figure 6.21 (a) are due to in-plane motion included in the DSM model but not in the ensemble average, as discussed in Section 5.2 (see Figure 5.2). The results for three cases ($L_2 = 1.26$, 0.5, 0.4m) exceed the upper bound at low modal overlap as shown in Figure 6.21 (b). These peaks correspond to the first resonance of the receiver plate investigated in Table 5.4. However, they exceed the present bounds by less than they exceeded Craik's bounds in Figure 5.6, even though the present figure is based on the ensemble average which will tend to increase the CLF ratio at low frequencies.

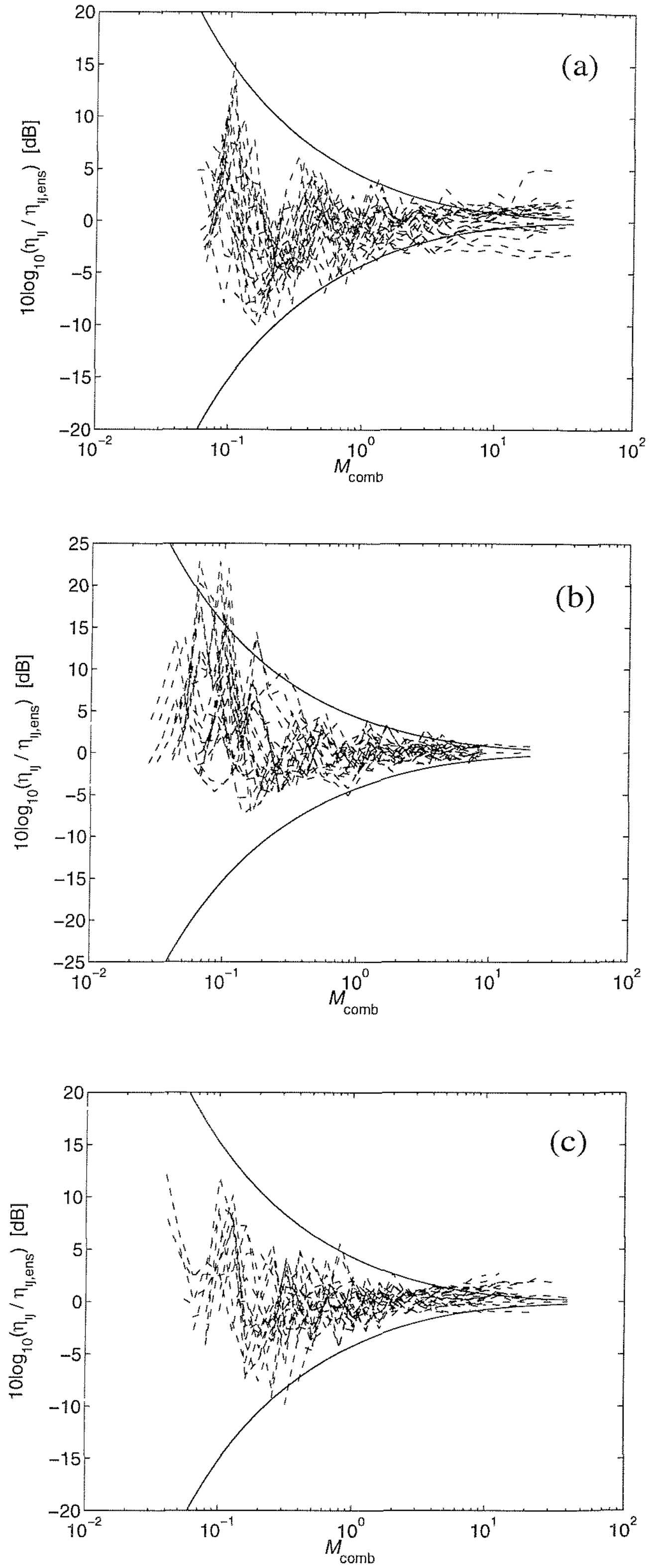

Figure 6.21. Logarithmic CLF ratio $10\log_{10}\left(\hat{\eta}_{ij}/\eta_{ij,\,ens}\right)$ obtained from Chapter 5 and plotted against M_{comb} results in 1/3 octave bands. (a) varying thickness ratio, (b) varying length ratio, and (c) varying length-to-width ratio. ---, $10\log_{10}\left(\hat{\eta}_{12}/\eta_{12,\,ens}\right)$; -·-, $10\log_{10}\left(\hat{\eta}_{21}/\eta_{21,\,ens}\right)$; —, $\pm 2\sigma$ estimate based on equation (6.5).

6.6 Statistical investigation of CLF

6.6.1 Tests for normal distribution

If a population of data is normally distributed, the probability distribution function is a bell-shaped curve which is symmetric with respect to the mean and the cumulative frequency function is an S-shaped curve. The Chi-square test, often called χ^2 goodness of fit test, can also be used to check whether data is normally distributed. An alternative test often used as a supplement to the χ^2 test is to study the skewness, which is a relative measure of the symmetry of the distribution function. The kurtosis, a higher order statistical moment, is another measure of the shape of a distribution. This is a measure of flatness or peakedness of the distribution. For a normal distribution one expects the skewness to be 0 and the kurtosis to be equal to 3.

In this section these various tests are applied to the logarithmic ratio of the frequency averaged effective CLF to the ensemble average CLF. If this is normally distributed, the distribution of the CLF is said to be log-normal. The probability distribution function is investigated for two cases. These correspond to averaging over 20 Hz and 200 Hz bandwidths for the baseline model, as shown in Figure 6.1. Figure 6.22 shows the probability distribution function and cumulative frequency function for the former case.

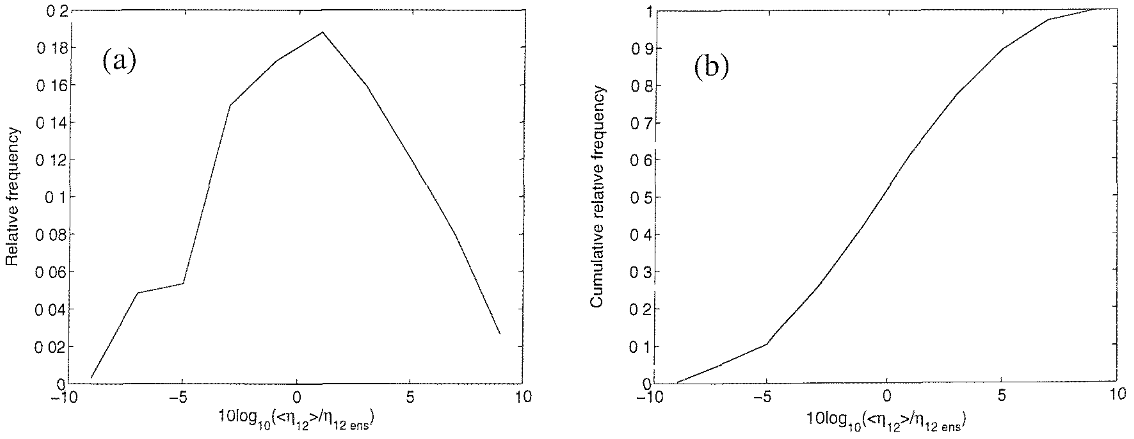

Figure 6.22. The probability distribution of the logarithmic CLF ratio $10\log_{10}\left(\langle\hat{\eta}_{ij}\rangle/\eta_{ij\ ens}\right)$ averaged over 20 Hz frequency bands: (a) relative frequency and (b) cumulative relative frequency.

These functions resemble those for a normal distribution, but this needs to be determined by a test of normality. Similarly Figure 6.23 shows the results for the 200 Hz averaging.

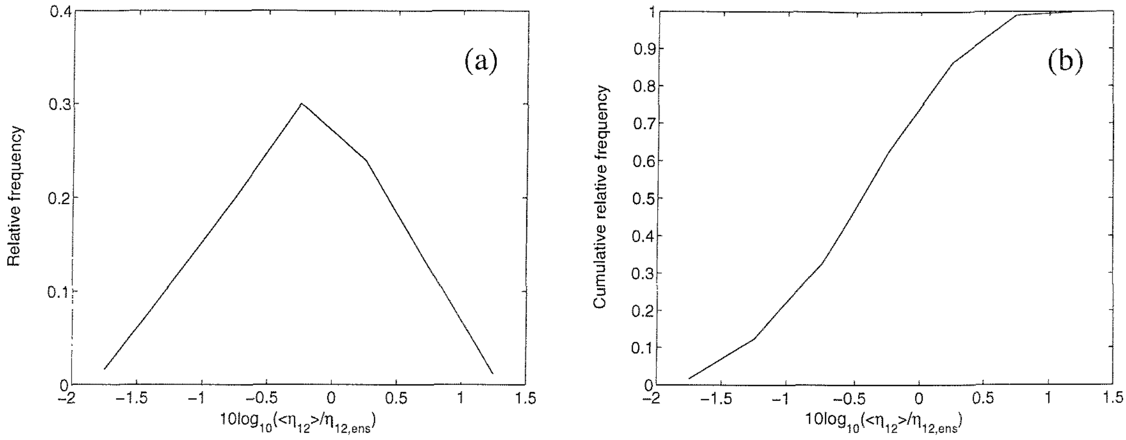

Figure 6.23. The probability distribution of the logarithmic CLF ratio $10\log_{10}\left(\left\langle\hat{\eta}_{ij}\right\rangle/\eta_{ij,\,ens}\right)$ averaged over 200 Hz frequency band: (a) relative frequency and (b) cumulative relative frequency.

A Chi-square test for the hypothesis that the population for the 20 Hz bandwidth results is normal is shown in Table 6.7. In the table, x_j is the dB interval of the sample, Φ are the values of the distribution function obtained from a statistical table [90], p_j is the probability of a sample occurring in the interval, b_j is the number of sample values in the interval, e_j is the theoretically expected number in the interval if the distribution was normal, and $(\chi_0)_j^2 = (b_j - e_j)^2/e_j$. The overall value χ_0^2 is given by $\sum_{j=1}^{K}(\chi_0)_j^2$. c is the value of the Chi-square distribution obtained from a table [90] with the given values of the distribution function and number of degrees of freedom $K-1$, where K is the number of intervals. As $\chi_0^2 > c$, the hypothesis is rejected.

A Chi-square test for the 200 Hz frequency band results is shown in Table 6.8 and the result also rejects the hypothesis that the population is normal.

Table 6.7. A Chi-square test for the logarithmic CLF ratio $10\log_{10}\left(\langle\hat{\eta}_{ij}\rangle/\eta_{ij,ens}\right)$ averaged over 20 Hz frequency bands. Mean $\mu = 0.82$, standard deviation $\sigma = 3.84$, number of samples $n = 973$, and degrees of freedom = 8.

x_j	$\frac{X_j-\mu}{\sigma}$	$\Phi\left(\frac{X_j-\mu}{\sigma}\right)$	$e_j = np_j$	b_j	$(\chi_0)_j^2$
-∞ ... -6	-∞ ... -1.77	0.0000 ... 0.0384	37.36	50	4.27
-6 ... -4	-1.77 ... -1.25	0.0384 ... 0.1056	65.39	52	2.74
-4 ... -2	-1.25 ... -0.73	0.1056 ... 0.2327	123.67	145	3.68
-2 ... 0	-0.73 ... -0.21	0.2327 ... 0.4168	179.13	168	0.69
0 ... 2	-0.21 ... 0.31	0.4168 ... 0.6217	199.37	183	1.34
2 ... 4	0.31 ... 0.83	0.6217 ... 0.7967	170.28	155	1.37
4 ... 6	0.83 ... 1.35	0.7967 ... 0.9115	111.70	117	0.25
6 ... 8	1.35 ... 1.87	0.9115 ... 0.9693	56.24	77	7.66
8 ... ∞	1.87 ... ∞	0.9693 ... 1.0000	29.87	26	0.50

$\chi_0^2 = \sum_{j=1}^{K} \frac{(b_j - e_j)^2}{e_j} = 22.5$, $c = 15.51$ as the solution of $P(\chi^2 \leq c) = 95\%$.

Table 6.8. A Chi-square test for the logarithmic CLF ratio $10\log_{10}\left(\langle\hat{\eta}_{ij}\rangle/\eta_{ij,ens}\right)$ averaged over 200 Hz frequency bands. Mean $\mu = -0.21$, standard deviation $\sigma = 0.62$, number of samples $n = 793$, and degrees of freedom = 6.

x_j	$\frac{X_j-\mu}{\sigma}$	$\Phi\left(\frac{X_j-\mu}{\sigma}\right)$	$e_j = np_j$	b_j	$(\chi_0)_j^2$
-∞ ... -1.5	-∞ ... -2.08	0.0000 ... 0.0188	14.91	13	0.24
-1.5 ... -1.0	-2.08 ... -1.27	0.0188 ... 0.1020	65.98	85	5.48
-1.0 ... -0.5	-1.27 ... -0.47	0.1020 ... 0.3192	172.24	159	1.02
-0.5 ... 0	-0.47 ... 0.34	0.3192 ... 0.6331	248.92	238	0.48
0 ... 0.5	0.34 ... 1.15	0.6331 ... 0.8749	191.75	190	0.02
0.5 ... 1.0	1.15 ... 1.95	0.8749 ... 0.9744	78.90	99	5.12
1.0 ... ∞	1.95 ... ∞	0.9744 ... 1.0000	20.30	9	6.29

$\chi_0^2 = 18.65$, $c = 12.59$ as the solution of $P(\chi^2 \leq c) = 95\%$.

As a result of the Chi-square test for the logarithmic CLF ratio $10\log_{10}\left(\langle\hat{\eta}_{ij}\rangle/\eta_{ij,\,ens}\right)$ averaged over the 20 Hz or 200 Hz frequency bands, the probability distributions for the two cases appear not to be a normal distribution.

As a supplement to the Chi-square test, the skewness and kurtosis are considered. A measure of the amount of the skewness in a population is given by Snedecor and Cochran [91]

$$\gamma_1 = \frac{\sum_{j=1}^{N}\left(x_j-\mu\right)^3/N}{\sigma^3} \tag{6.9}$$

where x_j is the sample value, μ is the sample mean, N is the number of samples, and σ is the standard deviation. The term $\left(x_j-\mu\right)^3$ in the numerator of equation (6.9) is called the third moment about the mean. For a normal distribution, the skewness γ_1 is zero. If γ_1 is positive, the distribution has extreme values in the upper half of the frequency distribution curve and the distribution is positively skewed or skewed to the right [92].

The kurtosis is given by [91]

$$\gamma_2 = \frac{\sum_{j=1}^{N}\left(x_j-\mu\right)^4/N}{\sigma^4}. \tag{6.10}$$

The term $\left(x_j-\mu\right)^4$ in the numerator of equation (6.10) is called the fourth moment about the mean. For a normal distribution, the kurtosis γ_2 is 3, *i.e.* $\gamma_2 - 3 = 0$. If γ_2 is greater than 3, the distribution is peaked. If γ_2 is less than 3, the distribution function has a flatter top than the normal.

Figure 6.24 shows the skewness and kurtosis for the logarithmic CLF ratio, $10\log_{10}\left(\langle\hat{\eta}_{12}\rangle/\eta_{12,\,ens}\right)$ or $10\log_{10}\left(\langle\hat{\eta}_{21}\rangle/\eta_{21,\,ens}\right)$. This is plotted against the bandwidth used in frequency averaging (from 10 Hz to 400 Hz) for all datasets of parameter variations as described in Section 6.4. All results of the skewness lie between –2 and +2. The mean value of the skewness for the logarithmic CLF ratio is –0.11 for both $10\log_{10}\left(\langle\hat{\eta}_{12}\rangle/\eta_{12,\,ens}\right)$ and $10\log_{10}\left(\langle\hat{\eta}_{21}\rangle/\eta_{21,\,ens}\right)$. This means that the distribution of the data is slightly negatively skewed from their mean value. The standard deviations of the skewness are greater than the expected value for a normal distribution as given by [91], $\sqrt{6/N} = 0.15$ where N (= 252) is the number of samples.

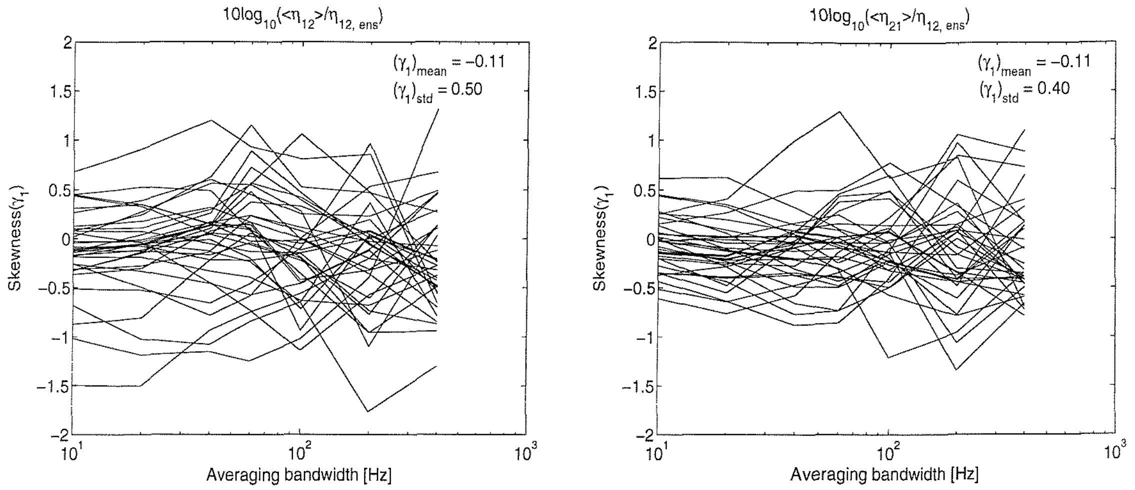

(a) skewness

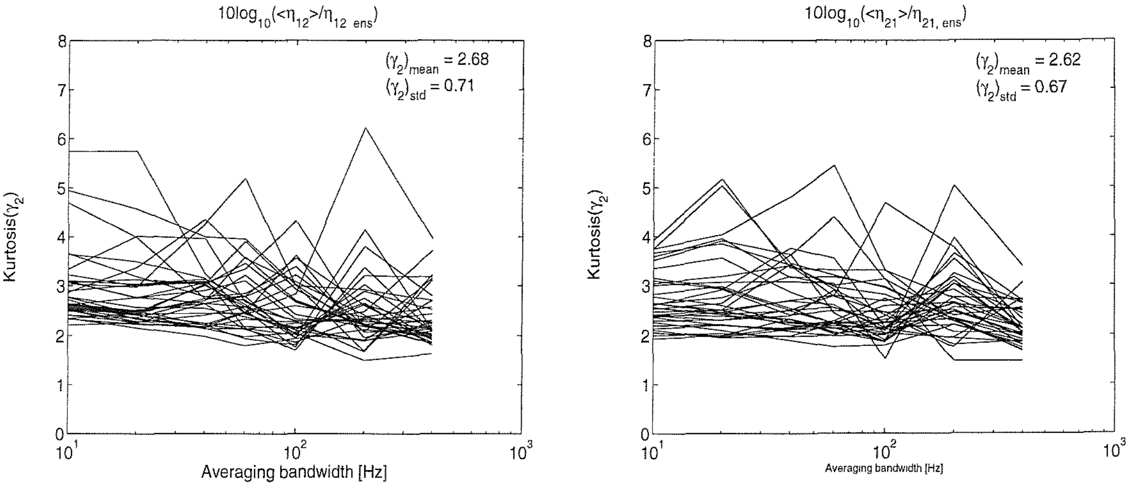

(b) kurtosis

Figure 6.24. Skewness and kurtosis for the logarithmic CLF ratio, $10\log_{10}\left(\langle\hat{\eta}_{12}\rangle/\eta_{12,\,ens}\right)$ or $10\log_{10}\left(\langle\hat{\eta}_{21}\rangle/\eta_{21,\,ens}\right)$, plotted against frequency bandwidth from 10 Hz to 400 Hz for all datasets of parameter variations: (a) skewness and (b) kurtosis.

The mean values of γ_2–3 for the logarithmic CLF ratio, $10\log_{10}\left(\langle\hat{\eta}_{12}\rangle/\eta_{12,\,ens}\right)$ and $10\log_{10}\left(\langle\hat{\eta}_{21}\rangle/\eta_{21,\,ens}\right)$, are –0.32 and –0.38. This means that the distribution of the data has a slightly flatter top compared to the normal. The standard deviations of γ_2–3 are greater than the expected value for a normal distribution as given by [91], $\sqrt{24/N}=0.31$.

As a result of the Chi-square test, skewness and kurtosis, the CLF ratios in dB, either $10\log_{10}\left(\langle\hat{\eta}_{12}\rangle/\eta_{12,\,ens}\right)$ or $10\log_{10}\left(\langle\hat{\eta}_{21}\rangle/\eta_{21,\,ens}\right)$, are unlikely to be normally distributed. Nevertheless, they are not greatly different from normal and for simplicity normal distributions will continue to be assumed.

6.6.2 Test for interdependence of CLFs

In the empirical model above, the variability of η_{12} and η_{21} has been considered without regard to their interdependence. In this section the degree to which the two variables, η_{12} and η_{21}, are linearly related is investigated. For this purpose, a normalised variance ratio is defined by $\sigma_d^2/(\sigma_{12}\sigma_{21})$, where σ_d^2 is the variance of the difference between $10\log_{10}\left(\langle\hat{\eta}_{21}\rangle/\eta_{21,\,ens}\right)$ and $10\log_{10}\left(\langle\hat{\eta}_{12}\rangle/\eta_{12,\,ens}\right)$ and σ_{12} and σ_{21} are the standard deviations of the two logarithmic CLF ratios respectively.

Figure 6.25 shows the variance ratio, $\sigma_d^2/(\sigma_{12}\sigma_{21})$, for the four groups of results obtained from the parameter variations described in Section 6.4: (a) results for three different levels of damping ($\eta_1=\eta_2$) and for two sets of unequal damping ($\eta_1\neq\eta_2$), (b) results for 11 different thickness ratios (h_1/h_2), (c) results for 10 different length ratios (L_1/L_2) and (d) results for 10 different length-to-width ratios (L_1/b). In each case $\sigma_d^2/(\sigma_{12}\sigma_{21})$ is plotted against the 'combined' number of modes in a band N_{comb}, as defined in equation (6.3). If they are dependent on each other the variance ratios should lie well below 1 but in some cases in Figure 6.25 (d) they are greater than 1. The variance ratio for all datasets is shown again in Figure 6.26 (a).

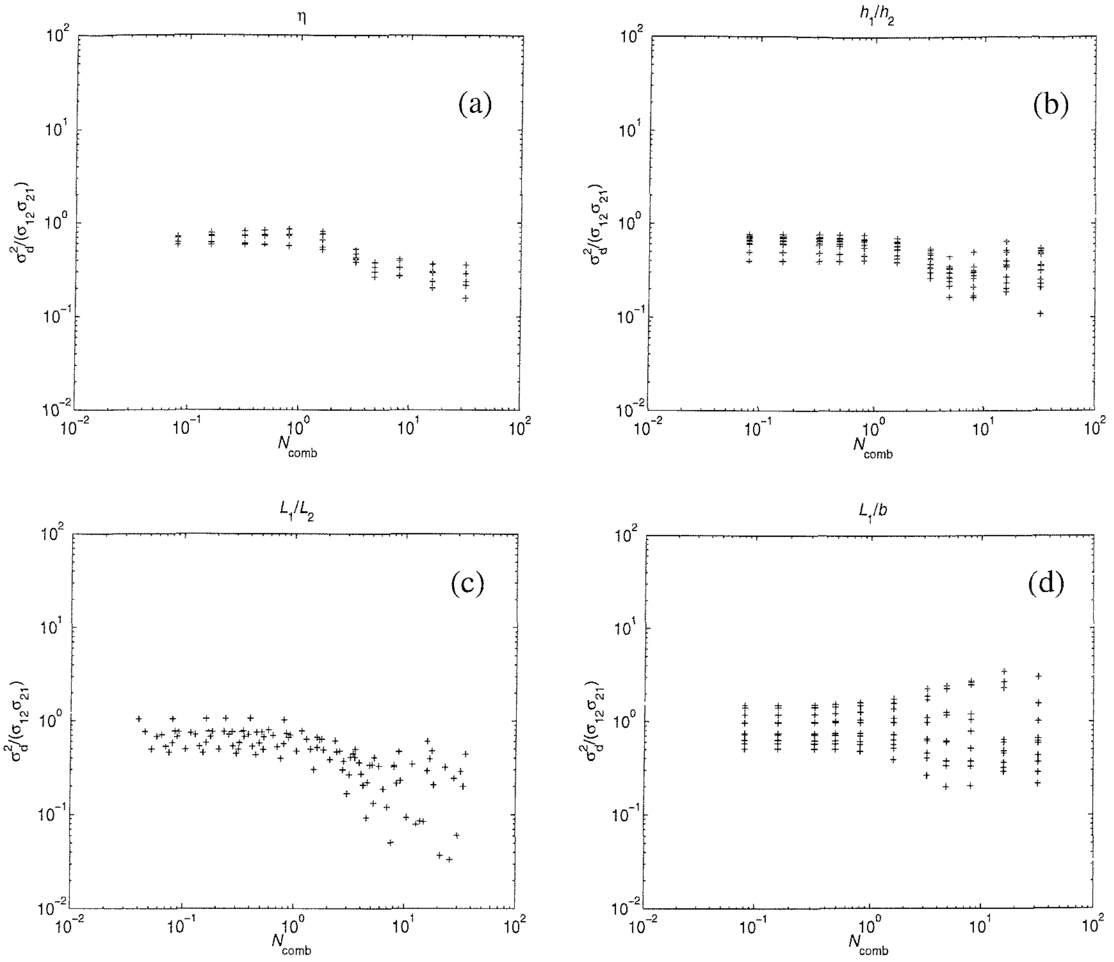

Figure 6.25. Variance ratio $\sigma_d^2/(\sigma_{12}\sigma_{21})$ for four groups of results from the parameter variations: (a) results for three different levels of damping ($\eta_1 = \eta_2$) and for two sets of unequal damping ($\eta_1 \neq \eta_2$), (b) results for 11 different thickness ratios (h_1/h_2), (c) results for 10 different length ratios (L_1/L_2) and (d) results for 10 different length-to-width ratios (L_1/b), plotted against the combined number of modes N_{comb}.

Another parameter that can be used is the correlation coefficient given by [91]

$$\rho = \frac{\text{cov.}}{\sigma_{12}\sigma_{21}}. \qquad (6.9)$$

The numerator of the correlation coefficient is the population covariance of the two variables, given by [91]

$$\text{cov.} = \frac{\sum (X_{12} - \mu_{12})(X_{21} - \mu_{21})}{N}, \qquad (6.10)$$

where X_{12} and X_{21} are the two variables, *i.e.* $10\log_{10}\left(\langle\hat{\eta}_{12}\rangle/\eta_{12,\,ens}\right)$ and $10\log_{10}\left(\langle\hat{\eta}_{21}\rangle/\eta_{21,\,ens}\right)$, and μ_{12} and μ_{21} are their sample means. The covariance of the two variables is zero when they are independent of each other. The correlation coefficient is a non-dimensional number that lies between –1 and +1. It is shown in Figure 6.26 (b).

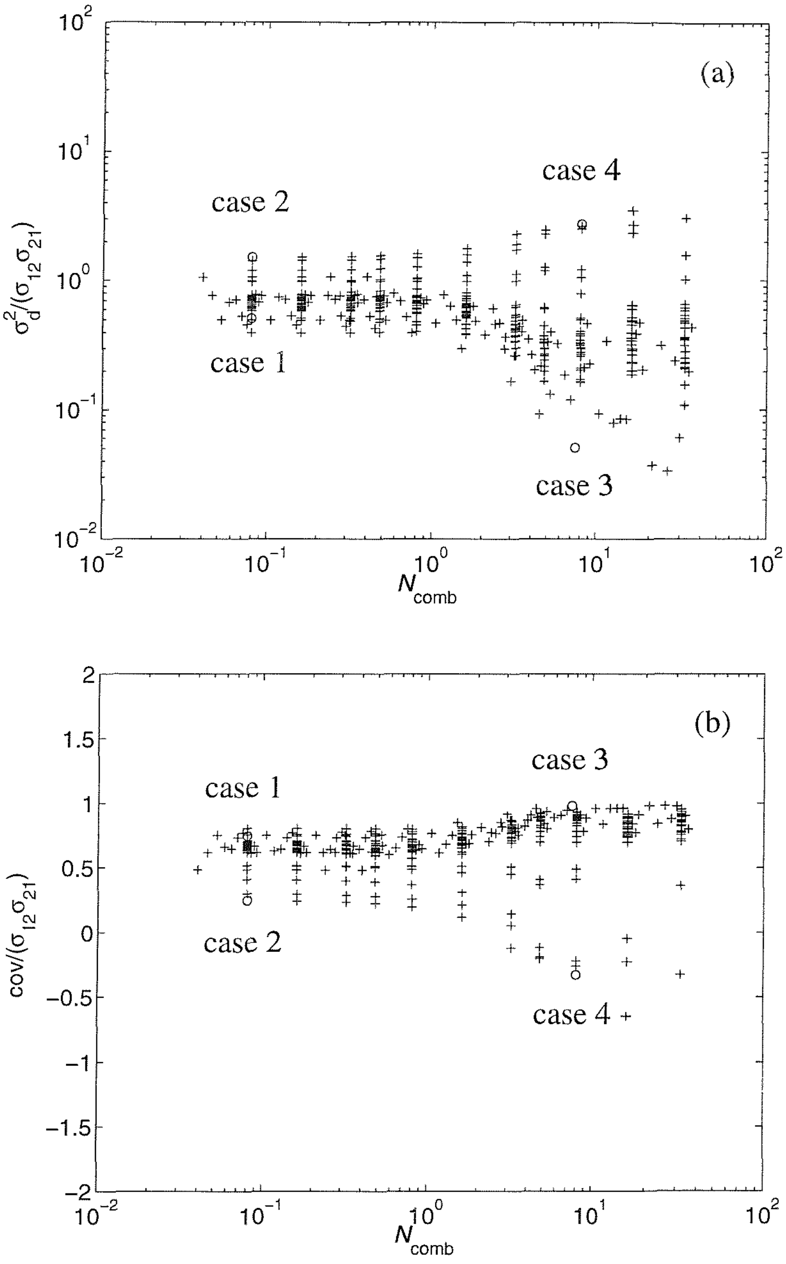

Figure 6.26. (a) The variance ratio $\sigma_d^2/\left(\sigma_{12}\sigma_{21}\right)$ for all cases of parameter variations plotted against N_{comb} and (b) correlation coefficient, covariance/$(\sigma_{12}\sigma_{21})$, plotted against N_{comb}.

If the absolute value of the correlation coefficient is close to unity, the two variables will show a straight line or an ellipse in a scatter diagram in which one variable is plotted against the other. Conversely there will be no clear relationship between them if the absolute value of ρ is less than about 0.5 [91].

Most of the correlation coefficients in Figure 6.26 (b) are positive and close to unity indicating that in these situations η_{12} and η_{21} are well correlated. Cases 1-4, marked as circles in Figure 6.26, were identified as being extreme values in the correlation coefficient as well as in the normalised variance given in Figure 6.26 (a). Cases 1 and 3 correspond to low variance in the difference, while the corresponding correlation coefficients show a high level of correlation, fairly close to unity. Conversely cases 2 and 4 correspond to high variance in the difference, with case 2 showing apparently poor positive correlation whilst case 4 shows slight negative correlation; large values of one variable are associated with small values of the other variable. These are better understood by inspection of the corresponding values of the coupling loss factor, plotted against each other and separately against frequency, as shown in Figures 6.27-6.30.

Figure 6.27 shows the CLF ratios in dB, $10\log_{10}\left(\langle\hat{\eta}_{12}\rangle/\eta_{12,\,ens}\right)$ and $10\log_{10}\left(\langle\hat{\eta}_{21}\rangle/\eta_{21,\,ens}\right)$ for case 1 ($h_1 = 3$ mm, $h_2 = 2$ mm, $L_1 = 0.32$ m, $L_2 = 0.63$ m, $b = 1.58$ m, no frequency averaging). These are plotted against each other (a) and against frequency, (b) and (c). The results appear reasonably correlated when η_{12} is plotted against η_{21}, *i.e.* the results lie mostly on a diagonal line. When plotted against frequency they appear to have some similar fluctuations, although with detail differences.

Figure 6.28 shows the results for case 2 ($h_1 = 3$ mm, $h_2 = 2$ mm, $L_1 = 2.5$ m, $L_2 = 5.0$ m, $b = 0.2$ m, no frequency averaging). These are also plotted against each other (a) and against frequency, (b) and (c). These appear uncorrelated when η_{12} is plotted against η_{21}. The CLF ratio versus frequency appears correlated above approximately 734 Hz. This is the cut-on frequency of plate 1 for transverse order $n = 2$. Below that frequency there are systematic differences. It may be noted that these plates are very narrow and are effectively one-dimensional at low frequencies. Here the results η_{ens} are not reliable.

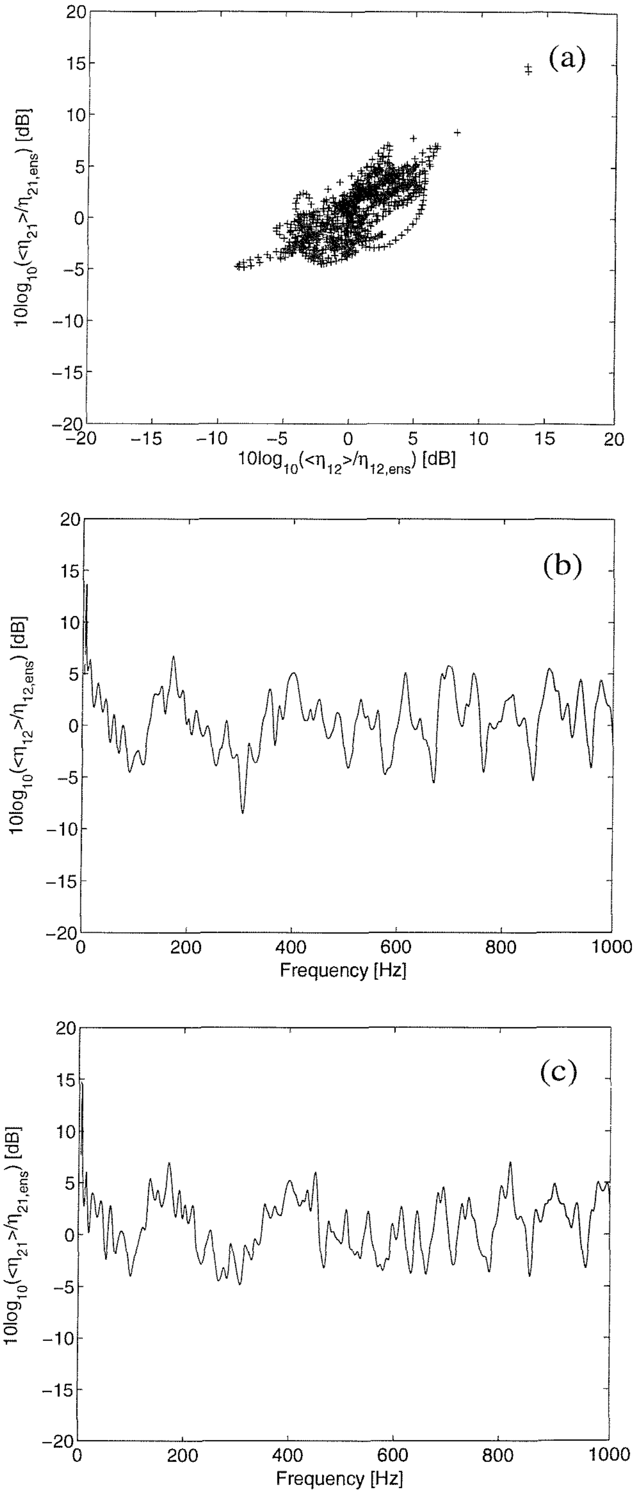

Figure 6.27. Logarithmic CLF ratio for case 1 ($h_1 = 3$ mm, $h_2 = 2$ mm, $L_1 = 0.32$ m, $L_2 = 0.63$ m, $b = 1.58$ m, no frequency averaging), plotted (a) $10\log_{10}\left(\langle\hat{\eta}_{21}\rangle/\eta_{21,ens}\right)$ against $10\log_{10}\left(\langle\hat{\eta}_{12}\rangle/\eta_{12,ens}\right)$, (b) $10\log_{10}\left(\langle\hat{\eta}_{12}\rangle/\eta_{12,ens}\right)$ against frequency, and (c) $10\log_{10}\left(\langle\hat{\eta}_{21}\rangle/\eta_{21,ens}\right)$ against frequency.

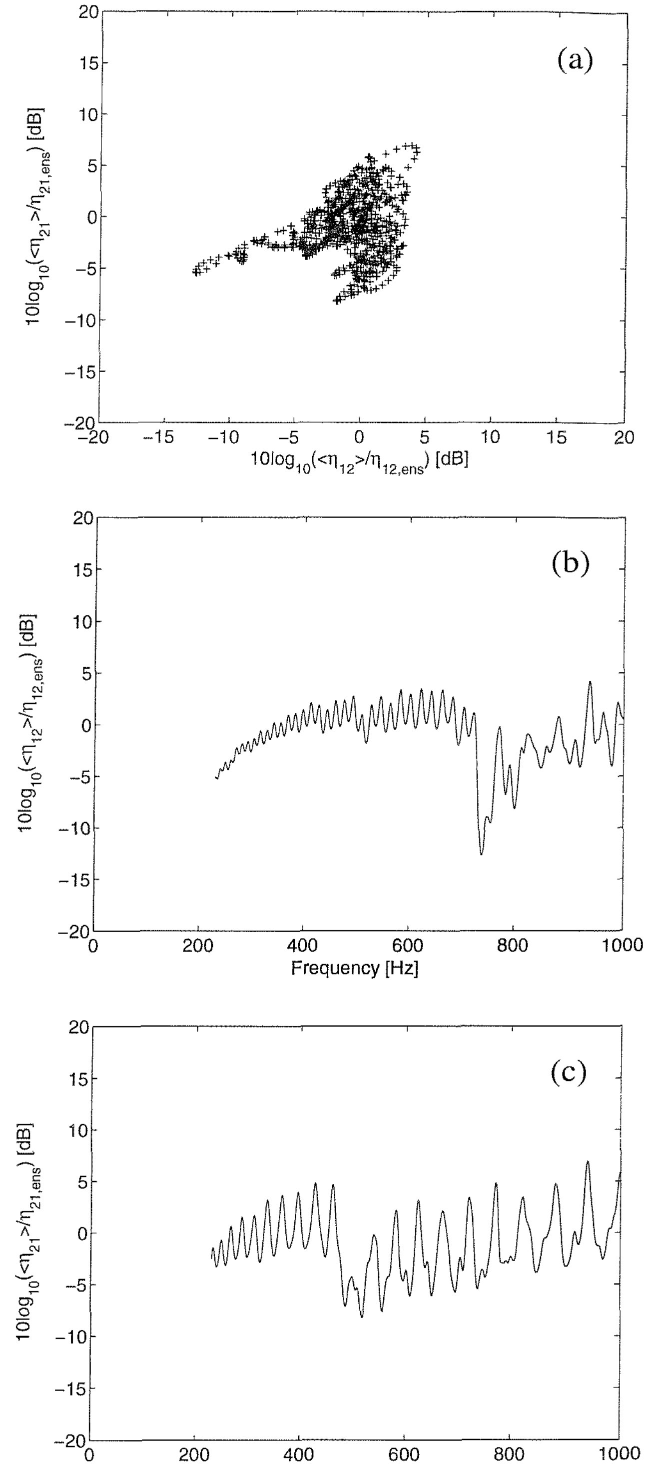

Figure 6.28. Logarithmic CLF ratio for case 2 ($h_1 = 3$ mm, $h_2 = 2$ mm, $L_1 = 2.5$ m, $L_2 = 5.0$ m, $b = 0.2$ m, no frequency averaging), plotted (a) $10\log_{10}\left(\langle\hat{\eta}_{21}\rangle/\eta_{21,ens}\right)$ against $10\log_{10}\left(\langle\hat{\eta}_{12}\rangle/\eta_{12,ens}\right)$, (b) $10\log_{10}\left(\langle\hat{\eta}_{12}\rangle/\eta_{12,ens}\right)$ against frequency, and (c) $10\log_{10}\left(\langle\hat{\eta}_{21}\rangle/\eta_{21,ens}\right)$ against frequency.

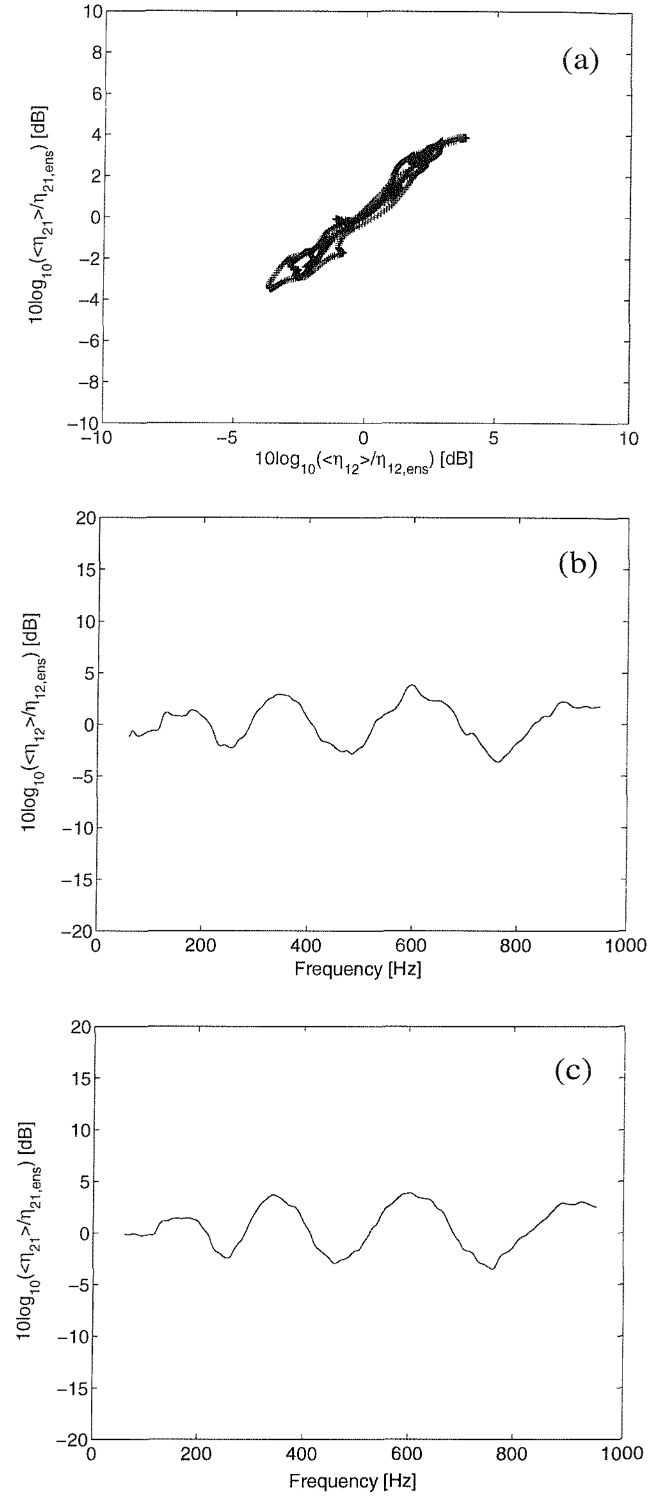

Figure 6.29. Logarithmic CLF ratio for case 3 ($h_1 = 3$ mm, $h_2 = 2$ mm, $L_1 = 0.5$ m, $L_2 = 0.79$ m, $b = 1.0$ m, 100 Hz bands averaging), plotted (a) $10\log_{10}\left(\langle\hat{\eta}_{21}\rangle/\eta_{21,ens}\right)$ against $10\log_{10}\left(\langle\hat{\eta}_{12}\rangle/\eta_{12,ens}\right)$, (b) $10\log_{10}\left(\langle\hat{\eta}_{12}\rangle/\eta_{12,ens}\right)$ against frequency, and (c) $10\log_{10}\left(\langle\hat{\eta}_{21}\rangle/\eta_{21,ens}\right)$ against frequency.

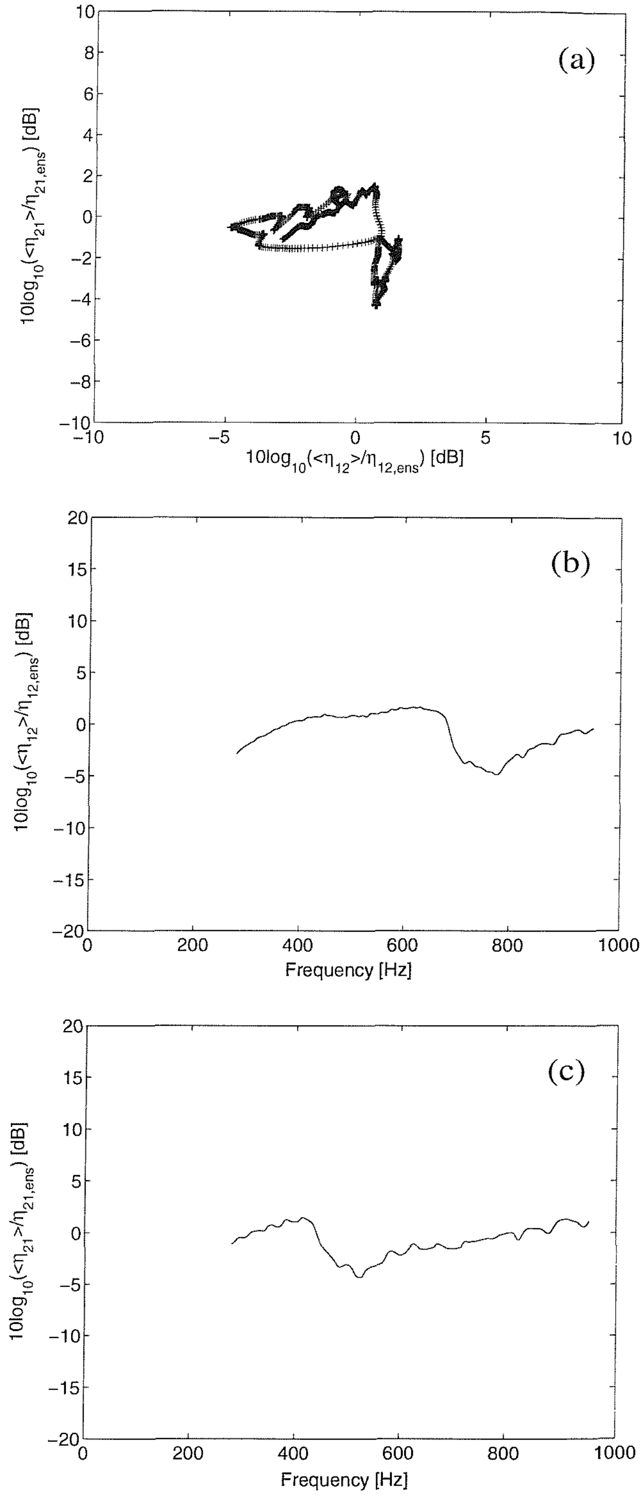

Figure 6.30. Logarithmic CLF ratio for case 4 ($h_1 = 3$ mm, $h_2 = 2$ mm, $L_1 = 2.5$ m, $L_2 = 5.0$ m, $b = 0.2$ m, 100 Hz bands averaging), plotted (a) $10\log_{10}\left(\langle\hat{\eta}_{21}\rangle/\eta_{21,ens}\right)$ against $10\log_{10}\left(\langle\hat{\eta}_{12}\rangle/\eta_{12,ens}\right)$, (b) $10\log_{10}\left(\langle\hat{\eta}_{12}\rangle/\eta_{12,ens}\right)$ against frequency, and (c) $10\log_{10}\left(\langle\hat{\eta}_{21}\rangle/\eta_{21,ens}\right)$ against frequency.

Figure 6.29 shows the results for case 3 ($h_1 = 3$ mm, $h_2 = 2$ mm, $L_1 = 0.5$ m, $L_2 = 0.79$ m, $b = 1.0$ m, 100 Hz bands averaging), plotted against each other (a) and against frequency, (b) and (c). The result of η_{12} versus η_{21} shows very good correlation with most points on a diagonal within a narrow band. η_{12} and η_{21} plotted against frequency are very similar curves.

Figure 6.30 shows the results for case 4 ($h_1 = 3$ mm, $h_2 = 2$ mm, $L_1 = 2.5$ m, $L_2 = 5.0$ m, $b = 0.2$ m, 100 Hz bands averaging), plotted against each other (a) and against frequency, (b) and (c). The result of η_{12} versus η_{21} shows 'intermediate' (not poor or good) correlation. η_{12} and η_{21} plotted against frequency show some similarity with case 2 but the frequency averaging has removed much of the fluctuation. Again this system has very narrow plates, leading to a breakdown in the approximations used in determining η_{ens}.

In summary, in 89.1% of all cases considered the absolute value of the correlation coefficient is greater than and equal to 0.5, *i.e.* $|\rho| \geq 0.5$. The cases with poor correlation ($|\rho| < 0.5$) are mostly long narrow plates for which this indicates a problem with the ensemble average CLF η_{ens} rather than the independence of η_{12} and η_{21}.

6.7 Conclusions

In this chapter, the variability of the coupling loss factor (CLF) for a system of two coupled rectangular plates has been examined and quantified using a systematic parameter variation. The ensemble average CLF given by Wester and Mace [50] was used to improve the estimate of the average CLF for all cases, providing a good basis for studying the variability. An empirical model for the variability of the CLF has been developed using these results.

Firstly, narrow band energies and powers were calculated for a large number of configurations using the dynamic stiffness method. The modal overlap factor was kept constant versus frequency by using a loss factor inversely proportional to frequency. The effective CLFs $\langle \hat{\eta}_{ij} \rangle$ were obtained from these energies averaged over frequency bands. The effects of frequency and modal overlap were separated by using frequency averages at a series of constant bandwidths rather than 1/3 octave averages.

Secondly, the logarithmic ratio of the effective CLF to the ensemble average, $10\log_{10}\left(\langle\hat{\eta}_{ij}\rangle/\eta_{ij,\,ens}\right)$, was determined and the variance σ^2 was obtained over the whole frequency region for each case to express the variability of the effective CLF compared to the ensemble average. An empirical model was developed to express the dependence of the variance σ^2 on the modal overlap factors and numbers of modes in a frequency band. This is given by

$$\sigma^2 = \frac{6}{M_{\mathrm{comb}} + N_{\mathrm{comb}}^2/16}$$

where $M_{\mathrm{comb}} = \dfrac{2M_1M_2}{M_1+N_2}$ and $N_{\mathrm{comb}} = \dfrac{2N_1N_2}{N_1+N_2}$.

It has been established that this represents a 95.7% confidence interval for all sets of data which are considered. These covered a range of aspect ratios of 0.2 ~ 12.5 for one plate and of 0.2 ~ 25 for the other plate. This model has been developed for a system of two coupled rectangular plates and can be used to evaluate the uncertainty of the CLF of that system. However, it is not known whether other types of system can be represented by the same model. This should be the subject of further research.

Thirdly, these results have been compared with the previously published models suggested by Mohammed [43] and Lyon and DeJong [33]. The present data set far exceeds the number of configurations previously used by Mohammed and shows that the variability depends on the modal overlap factor M at low values of the number of modes in a frequency band N and on N at high values. Moreover, the two parameters, M_{comb} and N_{comb}, are more appropriate than the geometric mean values, M_{ij} and N_{ij} used by Mohammed, as the former are applicable in the limit of a semi-infinite source or receiver plate as well as for two finite plates. From the comparison of the logarithmic CLF ratio obtained from the DSM results in dB, $10\log_{10}\left(\langle\hat{\eta}_{12}\rangle/\eta_{12,\,ens}\right)$, with the upper and lower bounds based on the current model and Lyon and DeJong's formula [33], the bounds from the empirical model performed better than those from the latter formula. The present model therefore seems more reliable.

Finally, a statistical investigation has been carried out into the distribution of $10\log_{10}\left(\langle\hat{\eta}_{12}\rangle/\eta_{12,\,ens}\right)$ or $10\log_{10}\left(\langle\hat{\eta}_{21}\rangle/\eta_{21,\,ens}\right)$, in order to test whether they are normally distributed and are independent each other. As a result of the study, it is found that they are unlikely to be normally distributed. Nevertheless a normal distribution remains a reasonable approximation (this means that the CLF is log-normally distributed). The logarithmic CLF ratio from subsystem 1 to subsystem 2 and that from subsystem 2 to subsystem 1 are found not generally to be independent of each other, although the degree of correlation varies from one case to another.

CHAPTER 7

EXPERIMENTAL VALIDATION USING TWO PLATES JOINED BY BOLTS

7.1 Introduction

Experiments have been performed in order to validate the empirical model of variability of the CLF for a two-plate system obtained in Chapter 6, in a different practical situation. It is not the intention to validate the DSM calculations as such, as this is a generally accepted technique.

This chapter describes these experimental studies. The system studied consists of two coplanar plates joined by bolts. All outer edges of the plates have free boundary conditions for simplicity. Although this differs from the two rectangular plates coupled at right angles with opposite edges simply supported that were considered in the development of the empirical model, the experimental study provides a validation of the effectiveness of the empirical model. Indeed its use in a slightly different situation gives additional benefit to this validation. Although experimental studies on simply supported plates are possible [93] they involve greater practical difficulties than the use of free edges.

Initially an investigation was performed on an existing two-plate system [94] with equal thicknesses ($h_1 = h_2 = 2.93$ mm) joined at right angles by a thicker bracket (8 mm). The experimental CLFs for this system were not in good agreement with the analytical results. It was identified that this was due to the thicker bracket constraining the joint, particularly in the corresponding analytical model with simple supports at its ends. Moreover, the two plates with equal thicknesses have similar modal energy. These results are not presented here. Instead, another two-plate system was considered in which two plates are directly joined by bolts in the same plane. These two plates have different thicknesses ($h_1 = 2.93$ mm, $h_2 = 0.90$ mm) and damping patches were attached in an attempt to avoid a situation of strong coupling.

A point force was applied to positions on one plate and then on the other plate. The vibration of the source plate and the receiver plate was measured to give an estimate of the mean kinetic energy for each plate. Ten forcing points and ten response points on each plate were used in the experiment. From the confidence interval for the effective CLF investigated in Chapter 4, it is known that this will introduce a moderate uncertainty, which is quantified in Section 7.3.2.2 below. The DLF for the two uncoupled plates was obtained using the decay rate method. The CLFs were subsequently evaluated from the experiments using the SEA power balance equations and the total kinetic energy measured.

An analytical model of this system is also developed for comparison, as it differs from those considered earlier. The effective CLF of this system was investigated by using the DSM, in the same way as described in Section 4.2 and these analytical results were compared with experimental results. Finally, the variability of the experimental CLF as a function of frequency has been investigated and compared to results from the empirical model described in Chapter 6.

7.2 Description of the plates

7.2.1 Experimental model

The system on which measurements were performed consisted of two large aluminium plates, joined by eight bolts, as shown in Figure 7.1. The experimental configuration of the measurement is shown in the photograph in Figure 7.2 (a). Figure 7.2 (b) shows the connection area of the plates. The other holes are present to allow a different experimental configuration in which two plates are connected at right angles by a thicker bracket.

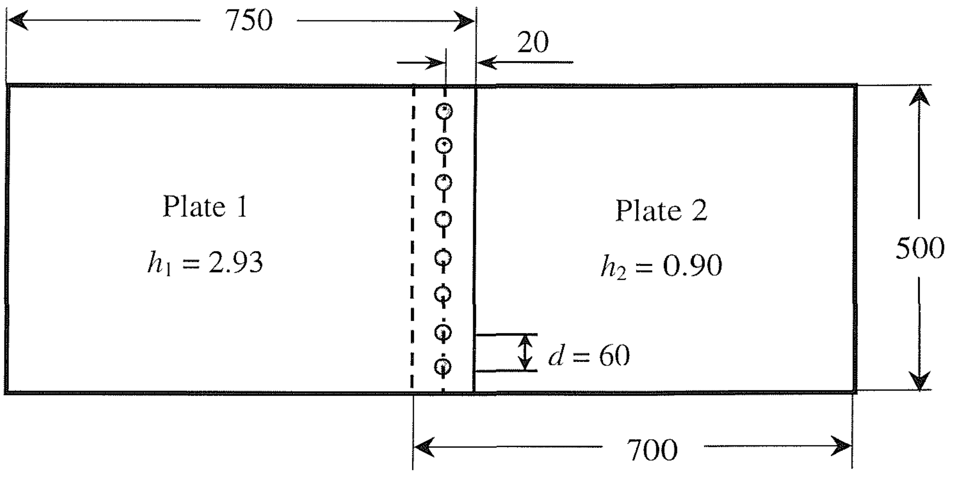

Figure 7.1. Two coplanar aluminium plates coupled by eight bolts (bolt spacing $d = 60$ mm). All dimensions are in millimetres.

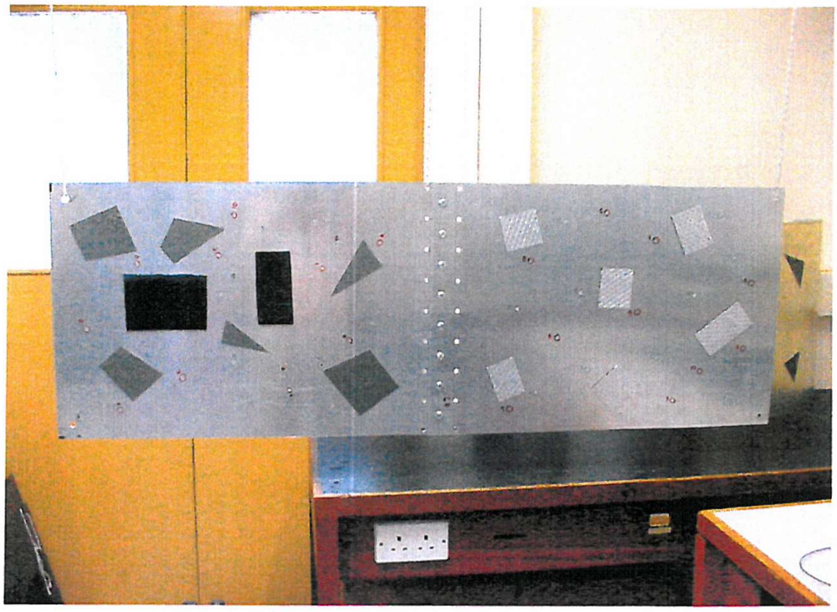

(a) Test structure of two plates joined by bolts

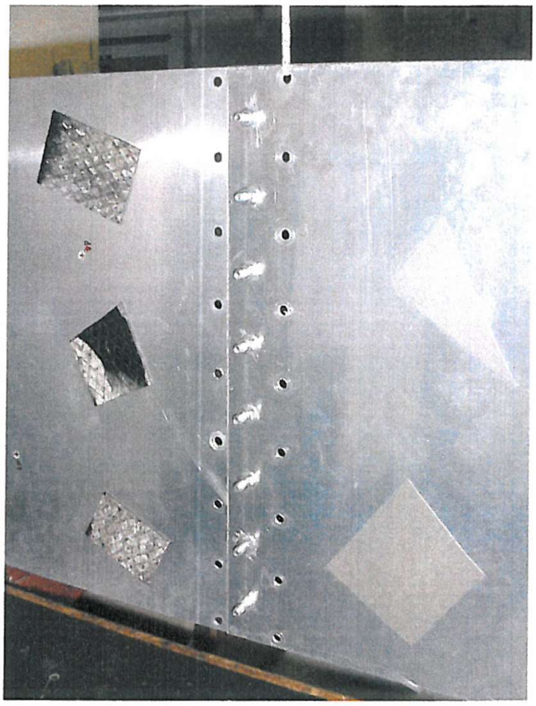

(b) Bolts connection area

Figure 7.2. Experimental structure of two-plate system joined by single line of bolts.

This structure was suspended using three elastic ropes to approximate free-free boundary conditions. The dimensions and properties of the plates are listed in Table 7.1.

Table 7.1. Dimensions and properties of the plates.

Parameter	Plate 1	Plate 2
Length L (mm)	750	700
Width b (mm)	500	500
Thickness h (mm)	2.93	0.90
Modal density $n(\omega)$	0.0064	0.019
Average modal spacing Δ (Hz)	25.0	8.25
Young's modulus E (N/m^2)	7.24×10^{10}	7.24×10^{10}
Poisson's ratio μ	0.333	0.333
Material density ρ (kg/m^3)	2.794×10^3	2.794×10^3

If the DLF is very low, equipartition of modal energy [33] may occur between two subsystems. This may also result in an inaccurate result for the CLF due to strong coupling. Since the bare aluminium plate has low damping, unconstrained layer damping patches were attached on both sides of the plates as shown in Figure 7.2 (a) and (b) in order to increase the DLF.

7.2.2 Analytical model

This system was modelled using the DSM, as shown in Figure 7.3. The bolts, including nuts and washers, were considered at the joint in the model as a distributed mass (total 0.173 kg) and a moment of inertia (1.296×10^{-5} kg·m^2). In the model two opposite longitudinal edges are simply supported, as required for application of the DSM. This model is used to obtain a calculated effective CLF for comparison with the experimental results.

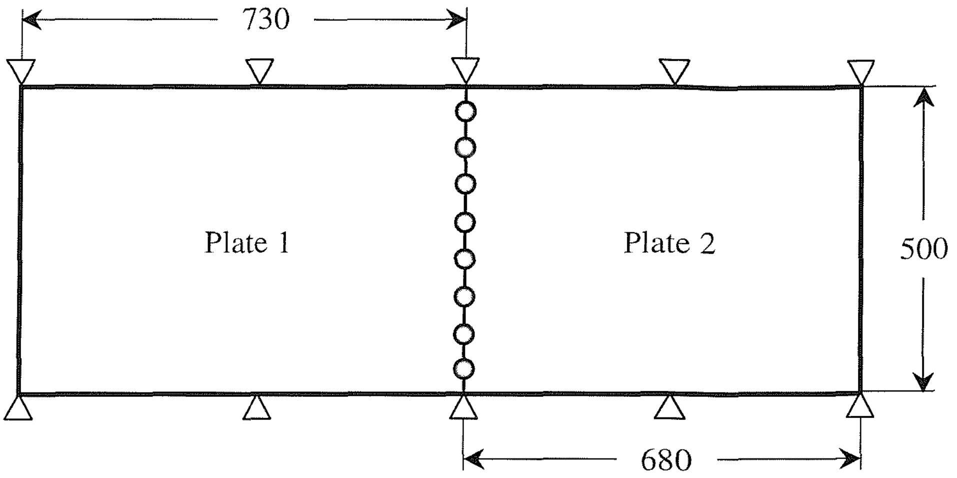

Figure 7.3. Analytical model of the two plates. This system is divided into two subsystems ignoring the overlapping parts from the joint. All dimensions are in millimetres. Circles denote the distributed mass (M_b = 0.346 kg/m) of the bolts.

7.3 Experimental determination of the CLF

The DLF and the vibrational kinetic energy were measured for the coupled plate configuration. These are all the values necessary in order to obtain the experimental CLFs using equation (3.13). The DLFs for the two uncoupled plates were obtained by using the decay rate method. The DLF results for four different response points were arithmetically averaged. The accelerations of the source plate and the receiver plate were measured, when a point force was applied to one plate and then the other plate in turn. These were used to give the spatially averaged mean kinetic energy for each plate. Ten forcing points and ten response points for each plate were randomly selected and used in the experiment. The uncertainty introduced by using ten forcing and response points is further discussed in Section 7.3.2.2.

7.3.1 Damping Loss Factor (DLF)

The measurement of the DLF was conducted on the two uncoupled plates. In this measurement the decay rate method, which is based on the transient response of a resonant mode with linear damping, was used. This method can be applied to the measurement of the average damping of a group of resonant modes in a frequency band [33].

7.3.1.1 Instrumentation

The instrumentation used in the measurement of the DLF consisted of an impact hammer, an accelerometer, a charge amplifier, a band pass filter, and a signal analyser as listed in Table 7.2. Figure 7.4 shows the schematic diagram of the test instrumentation and the numbers in the figure represent the equipment listed in Table 7.2. The experimental configuration of the measurement is shown in the photograph in Figure 7.5. After the excitation due to the impact hammer was applied, the response signals of the accelerometers were conditioned by the charge amplifiers, band pass filtered and then acquired by the signal analyser. The band pass filter was set to a selection of 1/3 octave bands, centred on the frequencies 63, 125, 250, 500, 1000, 2000, 4000 and 8000 Hz.

Table 7.2. Equipment used for the measurement of DLFs.

Equipment		Maker/Model	Serial Number
1	Impact Hammer	B & K Type 8202	1271063
2	Accelerometer	B & K Type 4375	1239001
3	Charge Amplifier	B & K Type 2635	1827830
4	Band Pass Filter	Kemo Type VBF8	2209541
5	Signal Analyser	HP 3566A	2911A00263

7.3.1.2 DLF measurements

The transient acceleration response due to the impact was recorded in the time domain and stored in the personal computer for further processing. For the purpose of obtaining better estimates of the decay slope, the original acceleration signals were Hilbert transformed [95] in MATLAB. A plot of a typical example of the transformed data is shown in Figure 7.6.

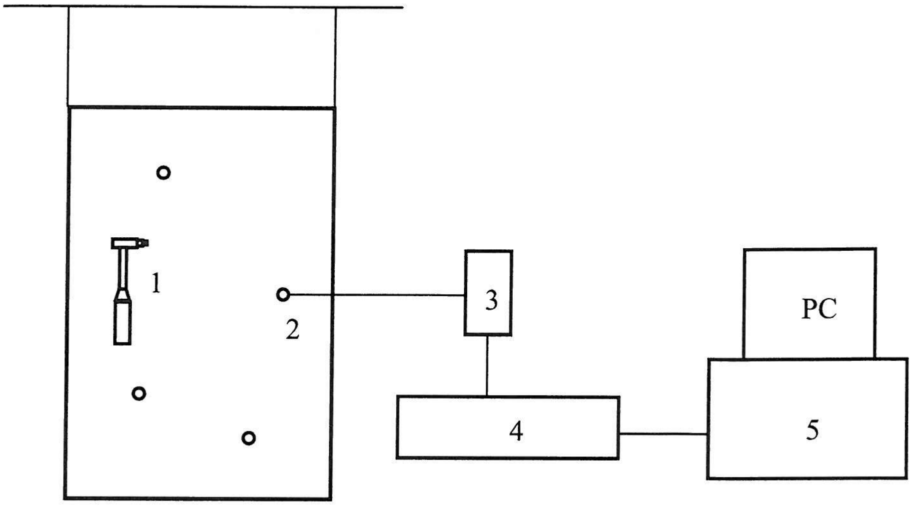

Figure 7.4. Instrumentation used for the measurement of the DLF. (Numbers refer to items in Table 7.2).

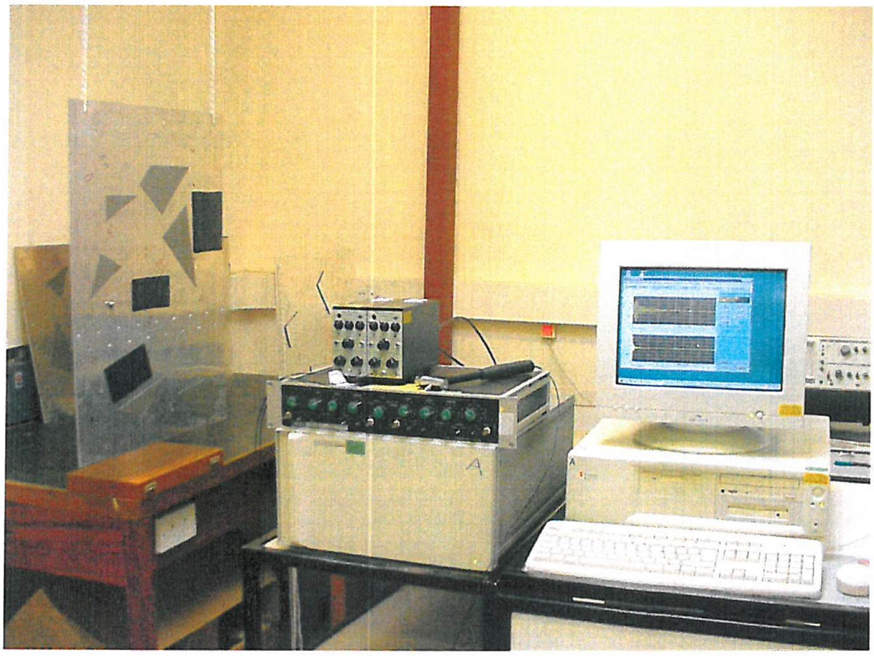

Figure 7.5. Experimental configuration for the measurement of DLF.

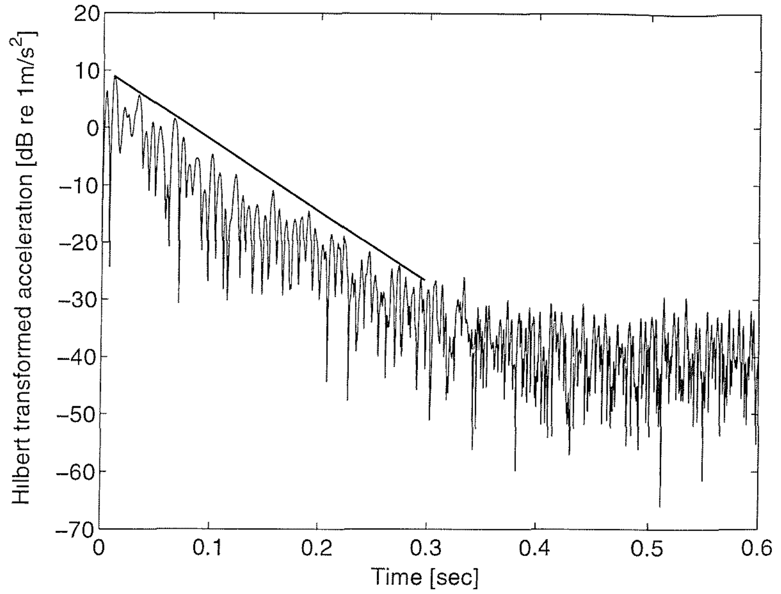

Figure 7.6. Example of the decay slope in a 1/3 octave band centred on 500 Hz processed from time history data.

The DLF is given by [33]

$$\eta = \frac{2.2}{f_c T_{60}} \tag{7.1}$$

where f_c is the centre frequency of a frequency band and T_{60} is defined as the time taken for the response amplitude to decay by 60 dB after initial excitation. The value of T_{60} is extrapolated from the initial decay slope when the response signal is plotted as log-rms amplitude vs. linear time. The DLFs for four response points were examined in the selected 1/3 octave frequency bands and then the results for the four points were arithmetically averaged. The decay time of the bandpass filter T_{60} was checked ($(T_{60})_{125\text{Hz}} = 0.08$ and $(T_{60})_{1\text{kHz}} = 0.01$) and found to be much shorter than the higher damped plate ($(T_{60})_{125\text{Hz}} = 0.54$ and $(T_{60})_{1\text{kHz}} = 0.05$), so that the decay of the response signal was not due to the filter. Table 7.3 shows the centre frequencies used in the experiment and the averaged DLFs for the two uncoupled plates. Figure 7.7 shows a graphical plot of the DLFs.

Table 7.3. The average DLFs obtained for the two uncoupled plates.

1/3 Octave Band Centre Frequency (Hz)	η_1	η_2
63	0.014	0.036
125	0.013	0.033
250	0.012	0.030
500	0.010	0.038
1000	0.011	0.041
2000	0.012	0.030
4000	0.018	0.032
8000	0.018	0.026
Mean	0.014	0.033

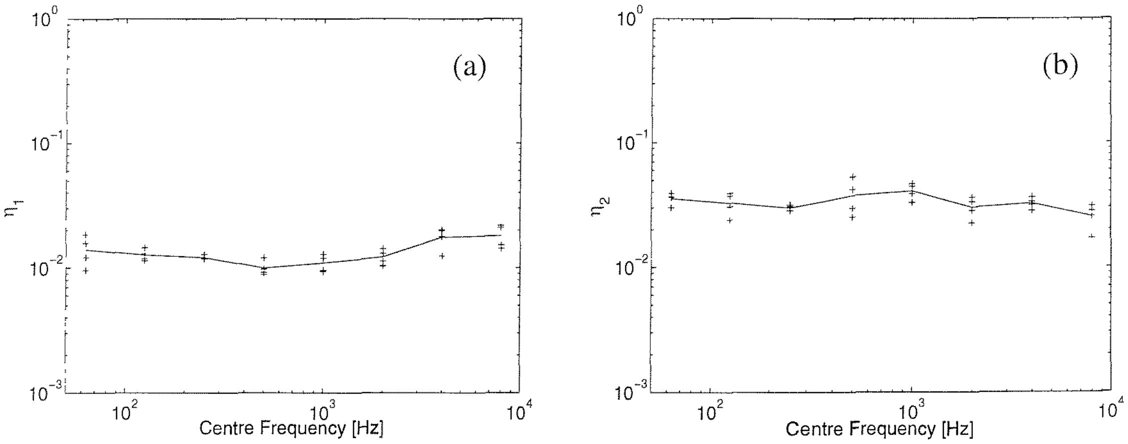

Figure 7.7. The DLFs measured (a) for the thicker plate (h_1 = 2.93 mm) and (b) for the thinner plate (h_2 = 0.9 mm). +, the DLF at each response point; —, the averaged DLF.

7.3.2 Vibrational energy

7.3.2.1 Instrumentation

The instrumentation used in the measurement of the vibration energy consisted of an instrumented force impact hammer with steel tip which should give usable results in the 0 – 7 kHz range, accelerometers, charge amplifiers and a signal analyser as listed in Table 7.4. Figure 7.8 shows a schematic diagram of the test instrumentation; the numbers represent the equipment listed in Table 7.4. The experimental configuration of the measurement is shown in the photograph in Figure 7.9.

Table 7.4. Equipment used for measurement of energy.

Equipment		Make/Model	Serial Number
1	Impact Hammer	B & K Type 8202	1271063
2	Accelerometer 1	B & K Type 4375	1239001
3	Accelerometer 2	B & K Type 4375	0987160
4	Accelerometer 3	B & K Type 4374	2209540
5	Accelerometer 4	B & K Type 4374	2209541
6	Charge Amplifier 1	B & K Type 2635	1827830
7	Charge Amplifier 2	B & K Type 2635	777627
8	Charge Amplifier 3	B & K Type 2635	1318160
9	Charge Amplifier 4	B & K Type 2635	814962
10	Charge Amplifier 5	B & K Type 2635	777629
11	Signal Analyser (Hewlett Packard)	HP 3566A	2911A00263

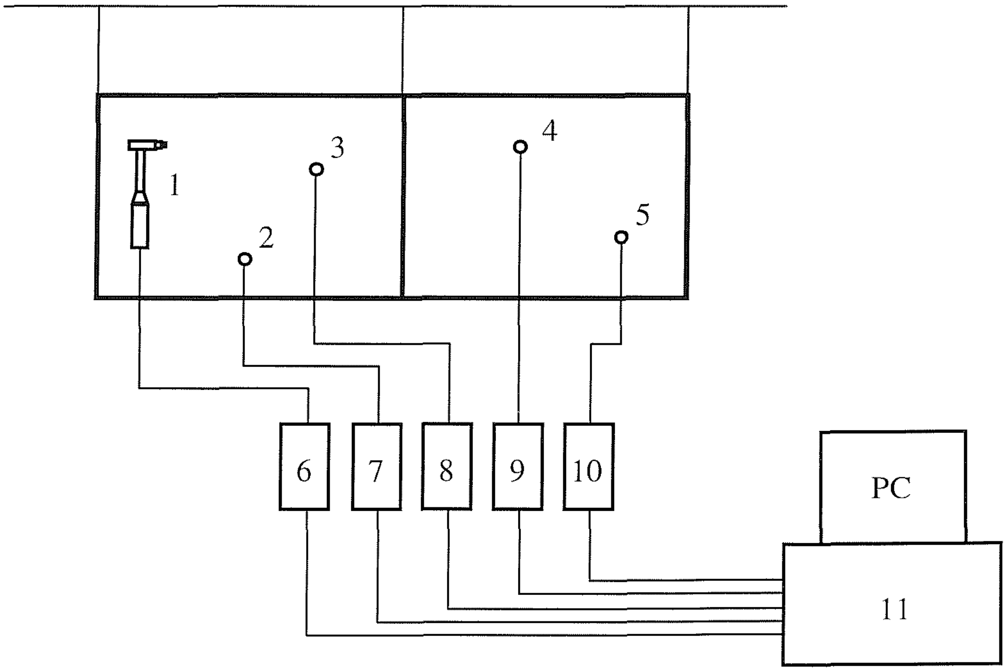

Figure 7.8. Instrumentation used for the measurement of vibrational energy and input force. (Numbers refer to items in Table 7.4).

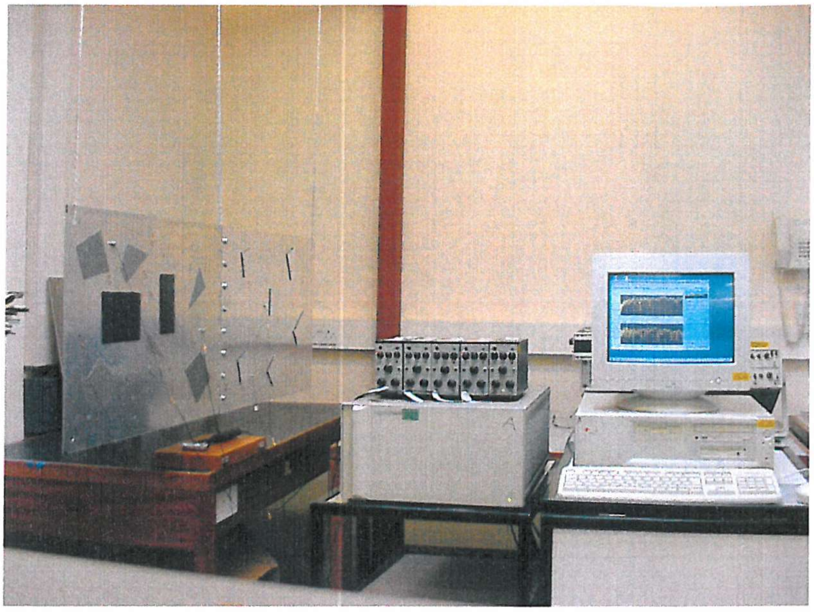

Figure 7.9. Experimental configuration for the measurement of vibrational energy and input force.

The applied force was measured by the force transducer in the impact hammer. This was passed to the signal analyser through a charge amplifier, which can amplify the signal. The response signals of the accelerometers were also passed to the analyser via charge amplifiers. The built-in lower and upper frequency limits of the charge amplifiers were set to 2 Hz and 10 kHz. Additionally, anti-aliasing filters are incorporated in the acquisition hardware of the Hewlett Packard signal analyser.

It is noted that the measurement error due to the transducer mass must be checked beforehand. The measurement error is given by

$$error = 20\log_{10}\left|\frac{Z_p + Z_a}{Z_p}\right| \tag{7.2}$$

where Z_p ($=8\sqrt{\rho hD}$ from [48]) is the impedance of the plate, Z_a ($=j\omega M_a$) is the impedance of the accelerometer and M_a is the mass of the accelerometer. In order to estimate the measurement error, the impedances of the two plates (approximated as infinite plates) and two accelerometers were compared and are shown in Figure 7.10. This figure shows that the thicker plate is not significantly affected by transducer mass below

10 kHz, but that an error of around 3 dB on the thinner plate can be expected at 7 kHz, where the impedances of the thinner plate and the lighter accelerometer are equal. If the heavier accelerometer were used on the lighter plate this frequency would be lowered to 1.7 kHz. Therefore two accelerometers of B & K Type 4375 (2.6 g) were used for vibration measurement of the thicker plate ($h_1 = 2.93$ mm) and two accelerometers of B & K Type 4374 (0.65 g) were used for the thinner plate ($h_2 = 0.9$ mm).

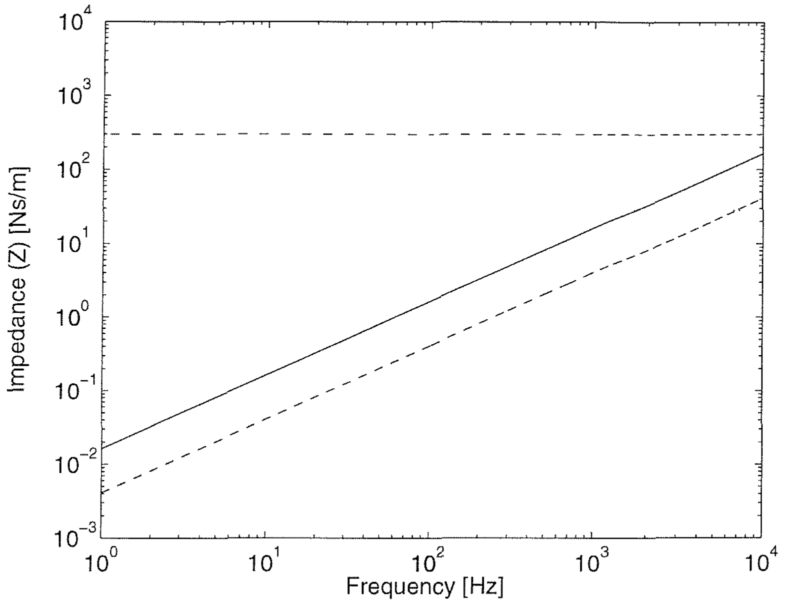

Figure 7.10. Impedance of infinite plates and transducers. -·-, plate 1 ($h_1 = 2.93$mm); , plate 2 ($h_2 = 0.9$mm); —, B & K Type 4375 accelerometer (2.6g); ---, B & K Type 4374 accelerometer (0.65g).

Based on this information, the experimental data were measured up to 6.4 kHz. However, the input power spectral density was found to drop by around 20 dB from its maximum value by 2 kHz and consequently the coherence of the signals also falls at high frequencies, as shown in Figure 7.11. Therefore, the data analyses were limited to the range up to 2 kHz. At this frequency the measurement error introduced by the mass loading from the accelerometers is limited to about 0.4 dB.

The frequency resolution was chosen to ensure that several points lay within the half-power bandwidth (ηf) of the plate modes. A typical value of the DLF is $\eta_1 = 0.01$ for the thicker plate and $\eta_2 = 0.03$ for the thinner plate. Therefore, two sets of experiments were performed, one in the low frequency range (0 to 400 Hz), with 0.125 Hz resolution, and another in the high frequency range (0 to 6.4 kHz), with 2 Hz resolution. The experimental data were analysed separately in the two frequency ranges, 25-400 Hz and 400-2000 Hz. The lower limit was chosen based on the theoretical first cut-on frequency of the thicker plate (29 Hz). The final results were combined to cover the frequency range from 25 to 2000 Hz.

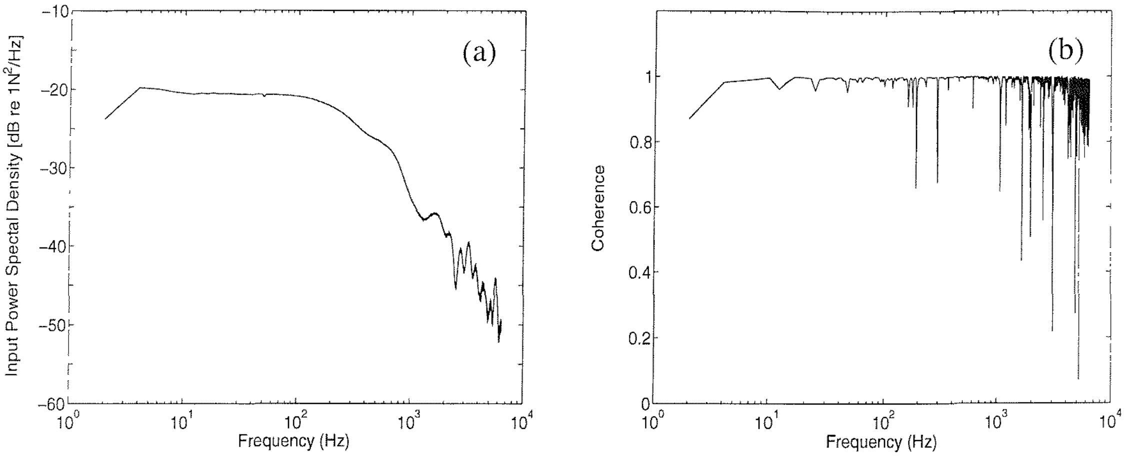

Figure 7.11. Examples of data; (a) input power spectral density for plate 1 and (b) the coherence of the signals.

7.3.2.2 Measurements

An impact point force, perpendicular to the surface of the plate, was applied to the source plate. The frequency response functions of acceleration due to the point force were measured at 2 response points for the source plate and at 2 points for the receiver plate simultaneously. A total of ten forcing points, randomly chosen for each plate, were sequentially excited and the vibration was measured using the four accelerometers. Then the accelerometers were moved and measurements were repeated until ten response points on each plate had been measured. For each forcing point on the thicker plate (plate 1) the response at each position on both plates was measured using a single impact. For excitation on the thinner plate (plate 2) an average of 3 impacts was used as the results were found to be less stable.

The uncertainty in the CLF estimate introduced by the number of forcing points and response points used was discussed in Chapter 4. For 10 forcing points the 90% confidence interval was found to be about ±1.5 dB. This corresponds to $\pm 1.645\,\sigma_f$ for a normal distribution [90] where σ_f is the standard deviation due to the number of forcing points. Hence the variance due to the forcing points, ${\sigma_f}^2$, is 0.83. The uncertainty of the experimental CLF introduced by using ten forcing points and ten response points is estimated by $\sigma^2 = {\sigma_f}^2 + {\sigma_r}^2$ where ${\sigma_r}^2$ is the variance due to the number of response points. It is assumed that ${\sigma_f}^2 = {\sigma_r}^2$ by reciprocity. This gives σ= 1.3 dB, *i.e.* the 95% confidence interval due to the number of forcing and response points is ±2.6 dB.

7.3.2.3 Spatially averaged kinetic energy

The temporally and spatially averaged mean square velocity for a unit force was obtained from the frequency response functions of acceleration for a unit force,

$$\left\langle \frac{\overline{v^2}}{\overline{F^2}} \right\rangle_{ij} = \frac{\sum_{m=1}^{10} \sum_{n=1}^{10} \left| \frac{a_m}{F_n} \right|_{ij}^2}{100\,\omega^2} \tag{7.3}$$

where i is the plate number which is excited, j is that for which vibration is measured, m is the number of response point on plate j and n is the number of excitation point on plate i. In order to compare the experimental data with the analytical results, the normalised data were used in the calculation of vibrational energy.

For a uniform plate the maximum spatially averaged kinetic energy in a cycle normalised by the mean square force is given by [39]

$$\frac{E_{ij}}{\overline{F^2}} = m_j \left\langle \frac{\overline{v^2}}{\overline{F^2}} \right\rangle_{ij} \tag{7.4}$$

where m_j is the mass of plate j and $\left\langle \overline{v^2} / \overline{F^2} \right\rangle_{ij}$ is the spatially averaged mean square velocity of plate j normalised by the mean square force. It is assumed that the mean total energy is equal to the maximum kinetic energy over a cycle, which will be the case where sufficient modes are present in a frequency band. Figure 7.12 shows the spatially averaged kinetic energy normalised by the mean square force for excitation on plate 1 and plate 2 respectively. Finally, these results were averaged over 1/3 octave frequency bands to yield the 1/3 octave band energies and these were used in equation (3.13) to give the experimental CLFs.

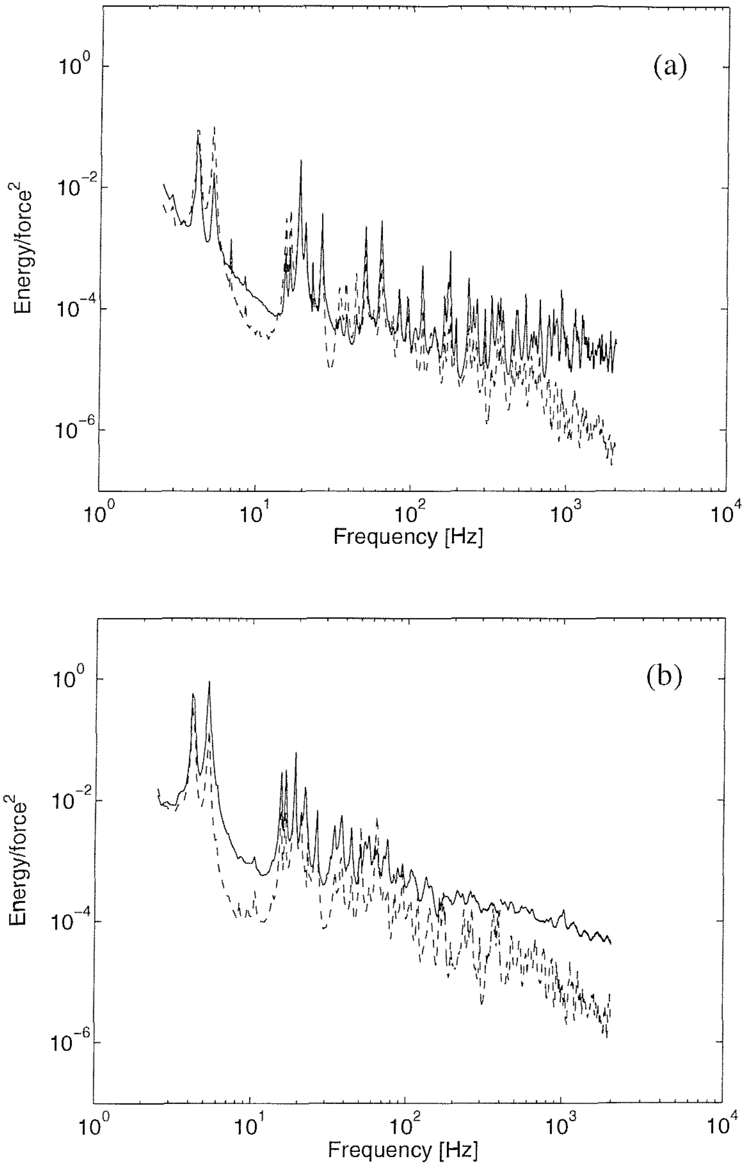

Figure 7.12. Spatially averaged maximum kinetic energy normalised by mean square force $E_{ij}/\overline{F^2}$ when excitation was applied to (a) plate 1 and (b) plate 2 respectively: —, normalised kinetic energy for the source plate; ---, normalised kinetic energy for the receiver plate.

7.3.3 Experimental results for CLF

The experimental CLF was obtained by substituting the spatially averaged kinetic energies and the measured DLFs into equation (3.13). In order to get the effective CLF using all ten forcing points, all sets of kinetic energies were averaged over the number of forcing points and then were averaged over the number of response points as in equation (7.3) before the calculation of the CLF. Results are shown in Figure 7.13.

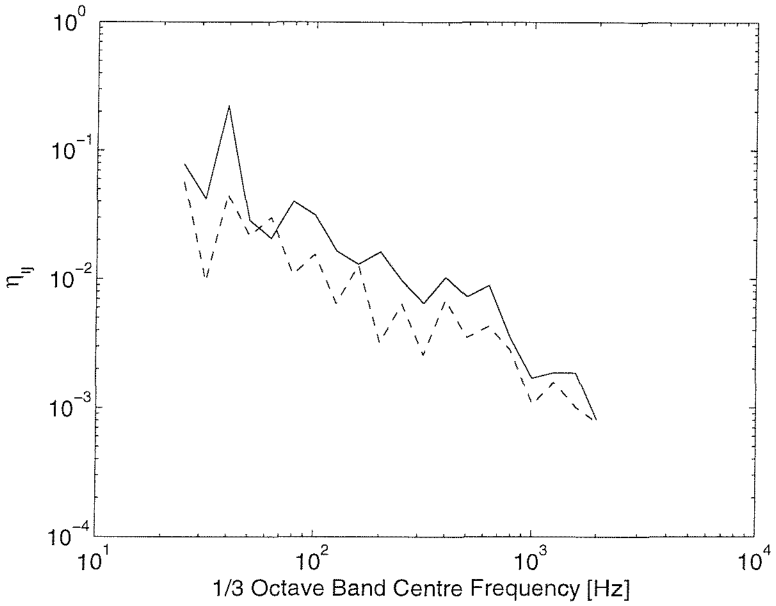

Figure 7.13. The experimental CLFs $\hat{\eta}_{ij}$ for the two-plate system. The damping values obtained from the experimental data as shown in Table 7.3 are used in calculating the CLF. —, η_{12}; ---, η_{21}.

The sensitivity of the results to the DLF values used was investigated, as also shown in Figure 7.14. For this comparison, nominal damping values ($\eta_1 = 0.01$ and $\eta_2 = 0.03$) were used in calculating the CLF from the experimental data and these were adjusted by doubling the values for plate 1, by doubling the values for plate 2 and by doubling both values. It is observed that the damping value of the receiver plate has more effect than that of the source plate. These results show the same trend as the damping effect on the ensemble average CLF results described in Chapter 3 (see Figure 3.3).

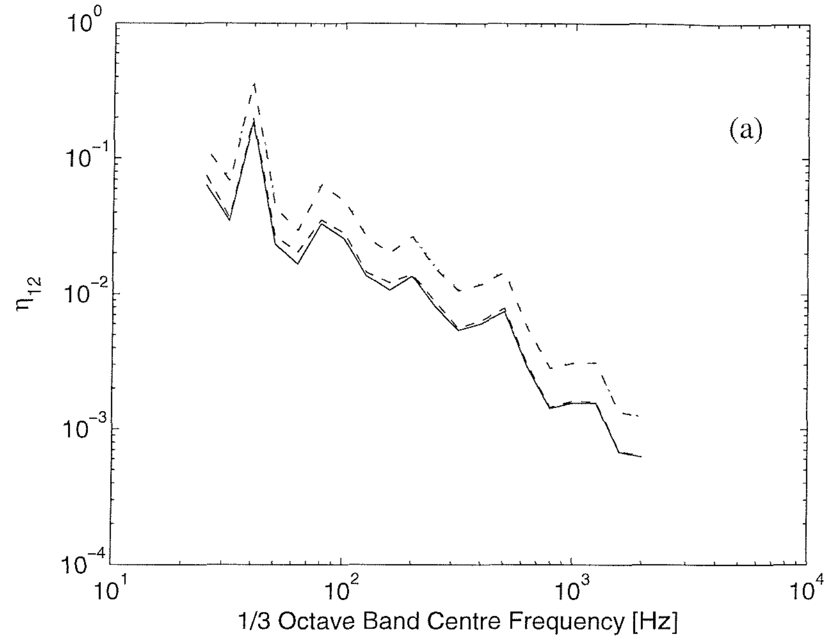

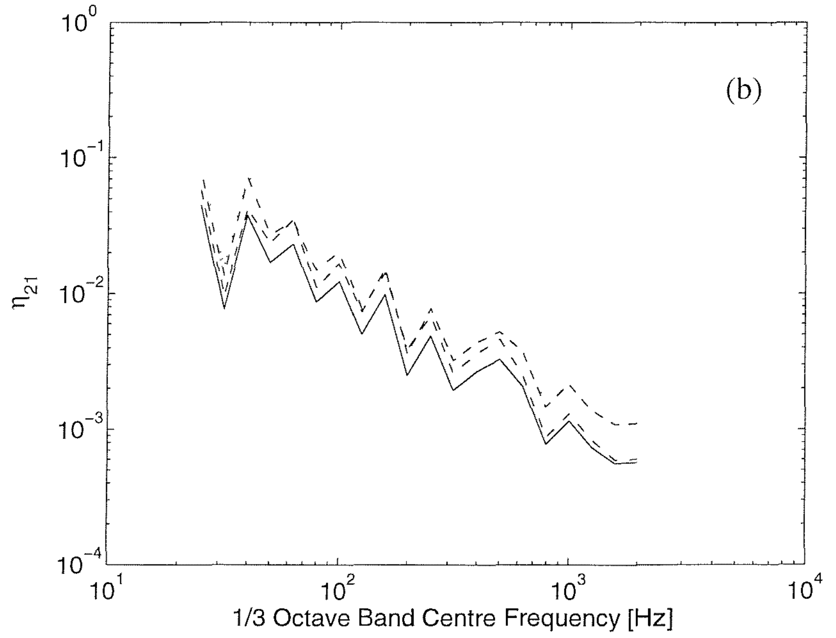

Figure 7.14. The effect of the DLF on the experimental CLFs $\hat{\eta}_{ij}$ for the two-plate system. The damping values used in calculating the CLF from the experimental data were adjusted by doubling the values for plate 1, by doubling the values for plate 2 and by doubling both values. —, $\eta_1 = 0.01$, $\eta_2 = 0.03$; ---, $\eta_1 = 0.02$, $\eta_2 = 0.03$; -·-, $\eta_1 = 0.01$, $\eta_2 = 0.06$; ·····, $\eta_1 = 0.02$, $\eta_2 = 0.06$.

7.4 Analytical CLF determination

7.4.1 Empirical model

The analytical CLF obtained from two semi-infinite plates, $\eta_{ij\infty}$ described in Section 3.4, cannot be used for the two coplanar plates, since the transmission efficiency in equation (3.21) is based on a right-angled or simply supported joint. Similarly $\eta_{ij,\,ens}$ in equation (3.24) is based on a simply supported joint.

The CLFs for bolt connected plate structures of similar material are given by [96],

$$\eta_{ij} = \left(\frac{2}{3}\right)^{1/4} \frac{b}{S_i} \left(\frac{h_i c_L}{\omega}\right)^{1/2} \frac{h_i^{3/2} h_j^{3/2}}{\left(h_i^{3/2} + h_j^{3/2}\right)^2} \quad \text{for } \lambda_b > d \ \ (\textit{Line connection}) \tag{7.5}$$

$$\eta_{ij} = \frac{4N}{\sqrt{3}} \frac{h_i c_L}{\omega S_i} \frac{h_i^2 h_j^2}{\left(h_i^2 + h_j^2\right)^2} \quad \text{for } \lambda_b < d \ \ (\textit{Point connection}) \tag{7.6}$$

where $c_L \left(= \sqrt{E/\rho(1-\mu^2)}\right)$ is the longitudinal wavespeed, λ_b is the smaller bending wavelength of two plates, b is the length of the connection, N is the number of bolts, and d is the bolt spacing, assumed constant.

An approximate result for the CLF of two plates joined in the same plane can be obtained by using equation (3.17) and the transmission efficiency at normal incidence given by Cremer and Heckl [48]

$$\tau_{12}(0) = \left[\frac{2\sqrt{\chi\psi}(1+\chi)(1+\psi)}{\chi(1+\psi)^2 + 2\psi\left(1+\chi^2\right)}\right]^2 \tag{7.7}$$

where $\chi = \sqrt{h_2/h_1}$ and $\psi = \left(h_1/h_2\right)^2$ for joints where the two plates have the same material properties but different thicknesses. The result for the normal incidence was regarded by Craik [49] as a good approximation to within 1 dB of the angular averaged values for $\chi > 1$.

Figure 7.15 shows a comparison of the CLFs for the two coplanar plates obtained from equations (3.17) and (7.7), the results obtained from equations (7.5) and (7.6), and the semi-infinite results for a right-angled connection. The CLFs for the semi-infinite plates joined at right angles are much smaller than other two results: the CLFs results for the two coplanar plates obtained from equation (7.7) by 10 dB for η_{12} and η_{21}, and those results obtained from equations (7.5) and (7.6) by 7 dB for η_{12} and 9 dB for η_{21}, respectively. It will be noted that equation (7.5) does not satisfy the consistency relation (equation (3.9)). For the simply supported joint, since only the bending moment at the joint is able to transmit energy, the energy transmission for the right-angled plates can be smaller than that for the coplanar plates for which both the bending moment and the internal force at the joint can transmit energy.

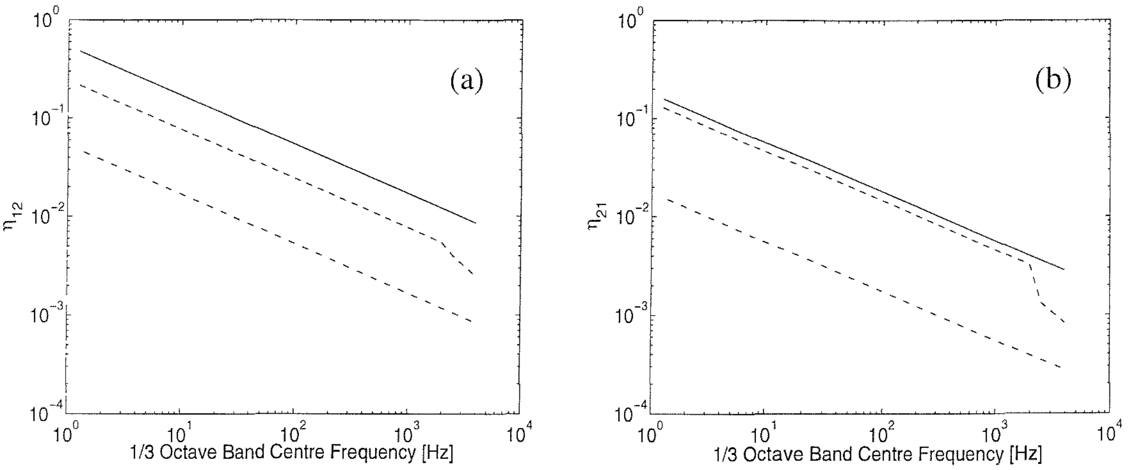

Figure 7.15. The CLFs (a) η_{12} and (b) η_{21}: —, the CLFs for the two coplanar plates obtained from equations (3.17) and (7.7); ---, the CLFs for the two coplanar plates obtained from equations (7.5) and (7.6); -·-, the CLFs for the semi-infinite plates joined at right angles.

According to equations (7.5) and (7.6), the connection between the two plates may change from a line connection to a point connection when the smaller bending wavelength of two plates equals the bolt spacing, $\lambda_b = d$. These frequencies for the two plates are 7970 Hz for plate 1 (thick plate) and 2450 Hz for plate 2 (thin plate) respectively. In both figures the curves obtained from equations (7.5) and (7.6) drop at about 2500 Hz which the bending wavelength of the thinner plate is equal to the bolt spacing. Note that the mass of bolts is not included in equations (7.5) and (7.6).

The transmission efficiencies for the above three cases shown in Figure 7.15 were calculated as a function of thickness ratio where all the plates have the same material properties. These are shown in Figure 7.16. The corresponding transmission efficiency for the CLFs obtained from equations (7.5) and (7.6) is extracted from equation (3.17). This result is symmetrical as shown in that figure, whereas other two results are non-symmetrical. Also note that the transmission efficiency for the two plates joined in the same plane has a maximum value of 1 when the thicknesses of the two plates are equal.

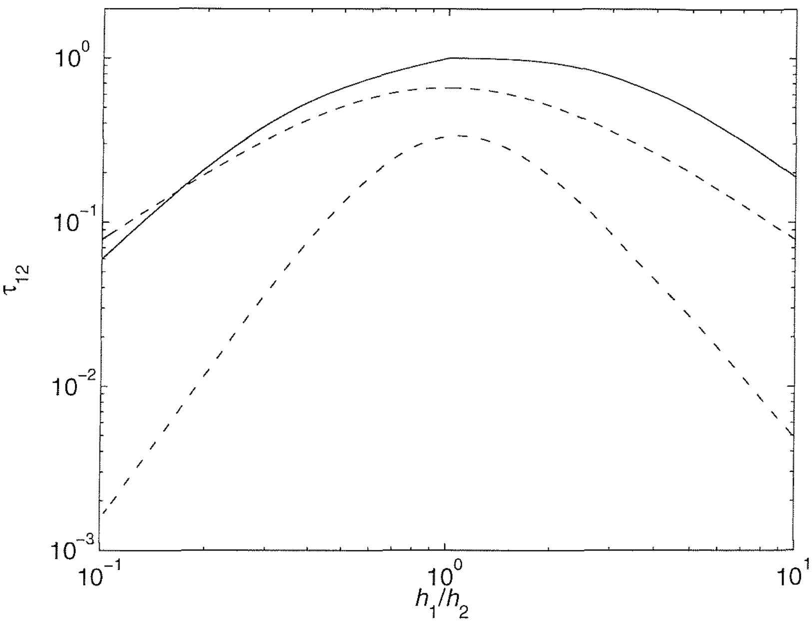

Figure 7.16. The angular averaged transmission efficiency: —, the approximate result obtained from equation (7.7); ---, τ_{12} extracted from the CLF equation (7.5); -·-, $\tau_{12,d}$ for the two semi-infinite plates joined at right angles.

7.4.2 DSM model

The dynamic response of this system can be obtained by the DSM. In Chapters 2 and 4, models for a two-plate system have been developed and used to estimate the 'effective' CLF. Using the same method, the equations of motion of this system can be solved to yield the dynamic response of the structure, from which the effective CLF can be found.

In a previous investigation on two finite plates in Chapter 4, it has been shown that if 400 excitation points are used in the source plate to simulate a 'rain-on-the-roof' type excitation the effect of the number of forcing points is limited to ±0.1 dB. A harmonic point excitation is therefore applied at 400 randomly chosen points, avoiding edges. For each forcing point, the source plate is separated into two parts at the longitudinal position of the applied force. Each point force excites vibration in many different transverse orders, n, across the plate width. For a given frequency, all such components whose cut-on frequency is below the frequency under consideration have been included.

First, to make an analytical model, the dynamic stiffness matrix for each plate was produced, and then assembled for the whole system. The two-plate system is shown in Figure 7.17. Plate 1 is separated into two sub-plates, 1_a and 1_b, when a point force F is applied to plate 1 at an intermediate position.

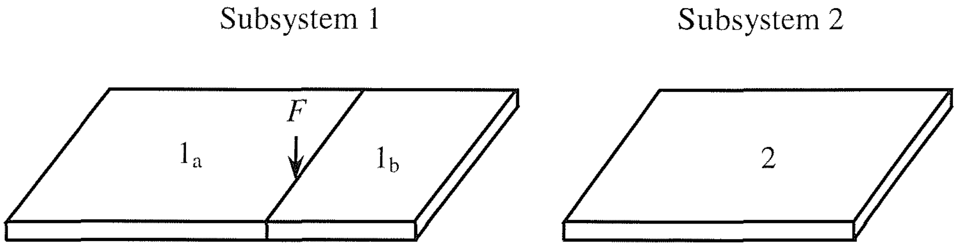

Figure 7.17. Two-subsystem model. Plate 1 is separated into two sub-plates, 1_a and 1_b, at the position of the point force F.

The dynamic stiffness matrix for a single plate was given in Chapter 2. The global dynamic stiffness matrix, $\mathbf{K}_{tot}$, of the total system can be derived by assembling the dynamic stiffness matrices of the three plates. An equally distributed mass (0.346 kg/m) and moment of inertia (2.59×10^{-5} kg·m^2/m) due to the bolts are included in the global matrix in the appropriate elements of the matrix at the common edge. The reduced dynamic stiffness matrix, $\mathbf{K}_r$, for flexural motion of transverse order n, is an 8×8 frequency-dependent matrix. The response can be obtained from $\mathbf{K}_r^{-1}\mathbf{F}$, where $\mathbf{F}$ is an applied force vector, for every frequency. The response of the subsystems was integrated analytically over the length and width of the plate for each transverse order n to give an accurate measure of its strain energy and summed over n at each frequency. In the calculation of the CLF, the bending strain energy was calculated for each sub-plate and then summed for each subsystem. This process was repeated for each excitation point on plate 1 and then for excitation points on plate 2.

7.4.3 Results from DSM model

As in the previous chapters the term 'effective' CLF $\hat{\eta}_{ij}$ is used for the individual realisation to distinguish it from the ensemble average CLF η_{ij}. The effective CLF can be evaluated using equation (3.13). In equation (3.13) the consistency relation of the CLFs, $n_1\eta_{12} = n_2\eta_{21}$, is not assumed. If η_1 and η_2 are known then the only unknowns are $\hat{\eta}_{12}$ and $\hat{\eta}_{21}$. In principle, one only needs excitation applied to one subsystem, but for numerical accuracy excitation is applied separately to both subsystems. The DLFs obtained from the experiment, which were described in Section 7.3.1, were used in the calculation of the dissipated power.

The effective CLFs obtained from equation (3.13) for the DSM model are shown in Figure 7.18 and these results are compared with the analytical results based on equation (7.7) and the results obtained from equations (7.5) and (7.6). The influence of the mass of the bolts at the joint was investigated and is also shown in Figure 7.18.

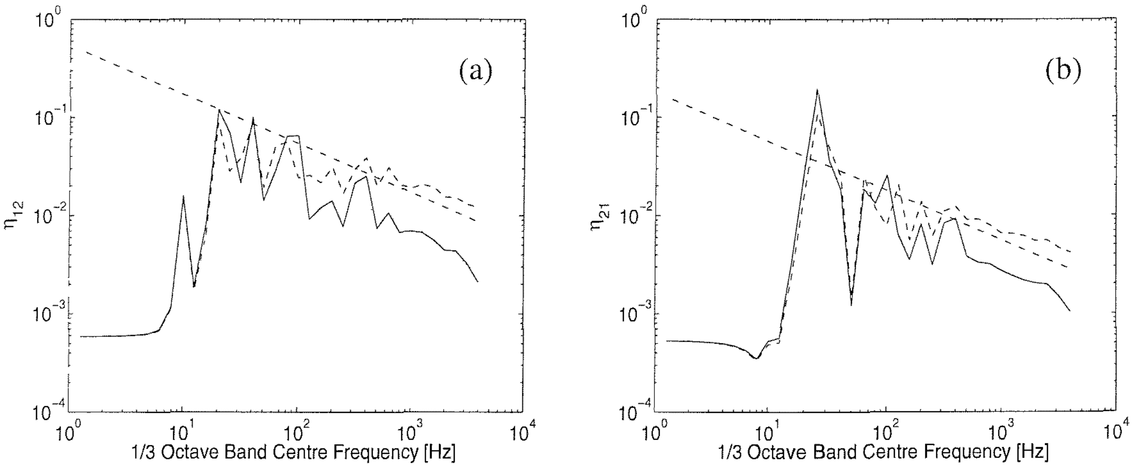

Figure 7.18. The influence of the bolts on the effective CLFs, (a) $\hat{\eta}_{12}$ (from thick to thin) and (b) $\hat{\eta}_{21}$ (from thin to thick) for the two-plate system. —, the effective CLFs when the bolts are considered in the model; ---, the effective CLFs when the bolts are not considered; -·-, the results based on equation (7.7); ·····, the results from equations (7.5) and (7.6).

When the influence of the bolts are considered in the DSM model, the effective CLF $\hat{\eta}_{12}$ (from thick to thin plate) tends toward the result obtained from equations (7.5) and (7.6) above the first cut-on frequency of the thicker plate, $f_{\text{cut-on}} = 29$ Hz. However the result for $\hat{\eta}_{21}$ (from thin to thick plate) shows that the effective CLF is generally somewhat lower than the result from the formulae below 2 kHz.

If the bolts are not considered in the model, the effective CLFs fluctuate against the result obtained from equations (7.5) and (7.6) below 300 Hz, whereas the predicted results are greater than the result based on equation (7.7) above 300 Hz.

Since the two plates are coupled in-line by bolts, no in-plane motion is introduced by the out-of-plane excitation. The results for the effective CLFs are identical whether or not in-plane terms are included in the DSM model.

7.4.4 Comparison between measured and predicted CLFs

The experimental CLFs obtained in Section 7.3.3 were compared with the analytical results predicted using strain and kinetic energies and are shown in Figure 7.19. Discrepancies between the experimental CLFs and the analytical results are quite likely to have been caused by the different boundary conditions between experiment and analysis. Also the use of kinetic energy in the experiment will cause errors at low frequencies, as discussed in Chapter 2. However, when the estimated uncertainty of ±2.6 dB in the experimental CLFs due to the limited number of force and response positions is considered (see Section 7.3.2.2), the experimental CLFs coincide reasonably well with the analytical results apart from around 50 Hz and above 800 Hz. There are no modes in the analytical model in the 50 Hz band. The remaining error may be occurred by the energy dissipation in the joint as the two plates are joined by bolts.

Since ensuring agreement between analysis and experiment was not the main aim of this study, the level of agreement found in Figure 7.19 is considered acceptable. The main aim is, rather, to study the variability of the CLF, quantitatively as well as qualitatively, using the empirical model (equation (6.5)) developed in Chapter 6.

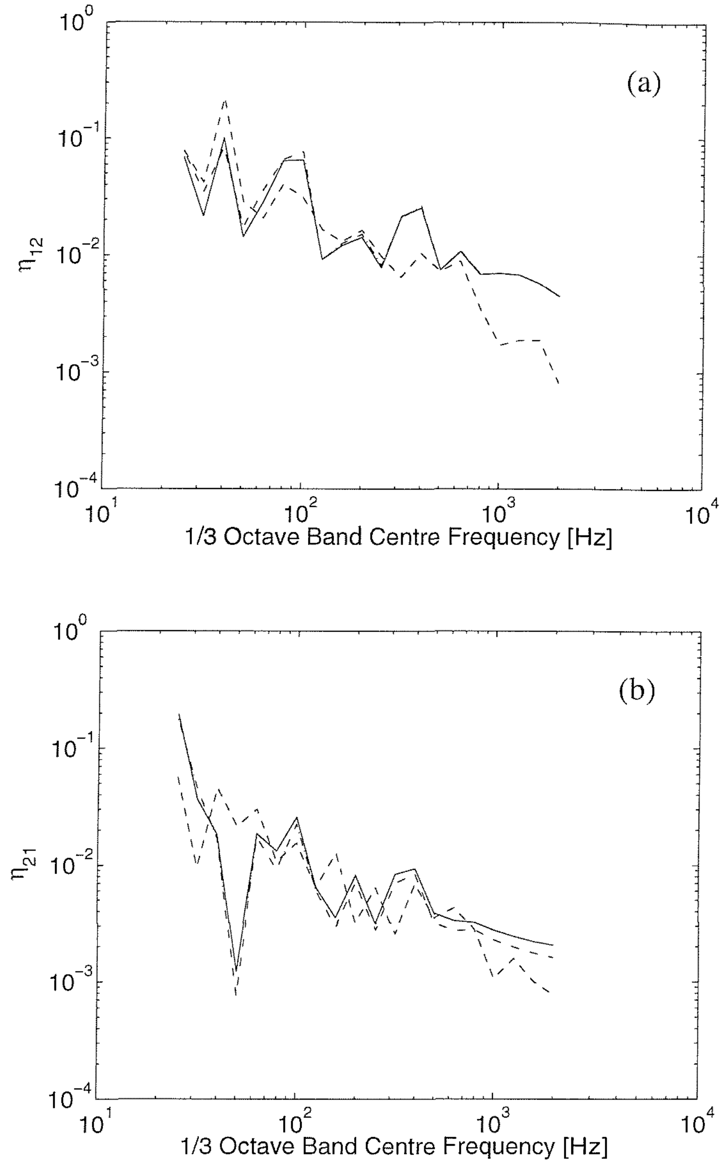

Figure 7.19. Comparison of the experimental CLFs with the analytical results: (a) $\hat{\eta}_{12}$ and (b) $\hat{\eta}_{21}$. —, analytical CLF predicted using strain energy; -·-, analytical CLF predicted using kinetic energy; ---, experimental CLF.

7.5 The variability of the experimental CLF

In order to investigate the variability in the experimental CLF, the original experimental data were averaged over various different frequency bandwidths: *i.e.* 20, 40, 60, 100, 200 and 400 Hz, rather than 1/3 octave bands. The expected variability 2σ (in dB) for these frequency bandwidths was obtained from equation (6.5) and is shown in Figure 7.20 using analytical estimates of M_{comb} and N_{comb}. The values of 2σ are frequency dependent as M_{comb} dominates the variability for low frequency bandwidth and varies with frequency. The variability decreases as the frequency bandwidth increases and that of the 400 Hz frequency average result is shown to be less than 1 dB. Since there was no reliable theoretical curve to use as a reference point, the 400 Hz frequency average result was used as a reference to obtain a normalised CLF from the experimental data.

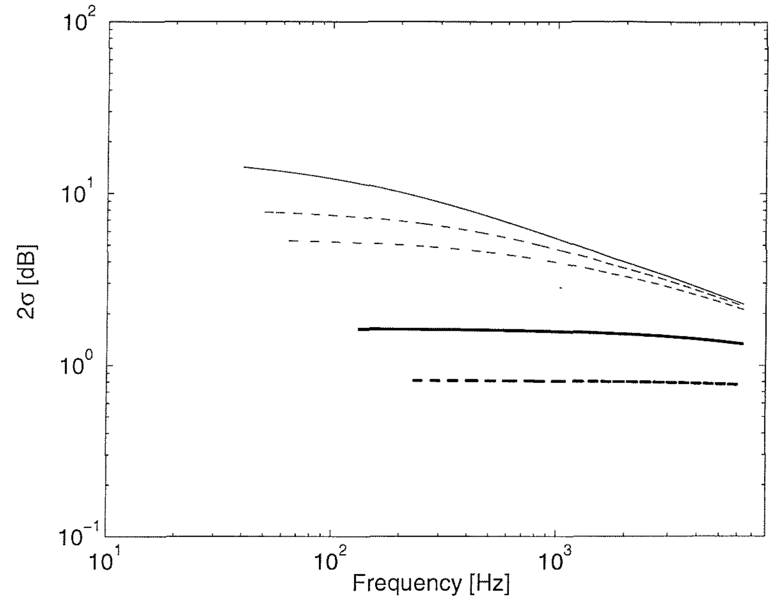

Figure 7.20. The expected variability 2σ (in dB) of the effective CLF for various different frequency bandwidths. —, 20 Hz; ---, 40 Hz; -·-, 60 Hz; ·····, 100 Hz; —, 200 Hz; - - -, 400 Hz using the empirical model.

The measured CLF ratio, based on Δf = 20, 40, 60, 100 and 200 Hz frequency bandwidths, $10\log_{10}\left(<\hat{\eta}_{ij,\Delta f}>/<\hat{\eta}_{ij,400\mathrm{Hz}}>\right)$ was obtained. This is compared in Figure 7.21 with the $\pm 2\sigma$ estimates obtained from equation (6.5). Note that the frequency range is limited by the use of the 400 Hz average as a reference. The percentage of the frequency points falling within these bounds was determined and is listed in Table 7.5. In each case the $\pm 2\sigma$ bands are shown to be good upper and lower limits for the experimental CLF ratio.

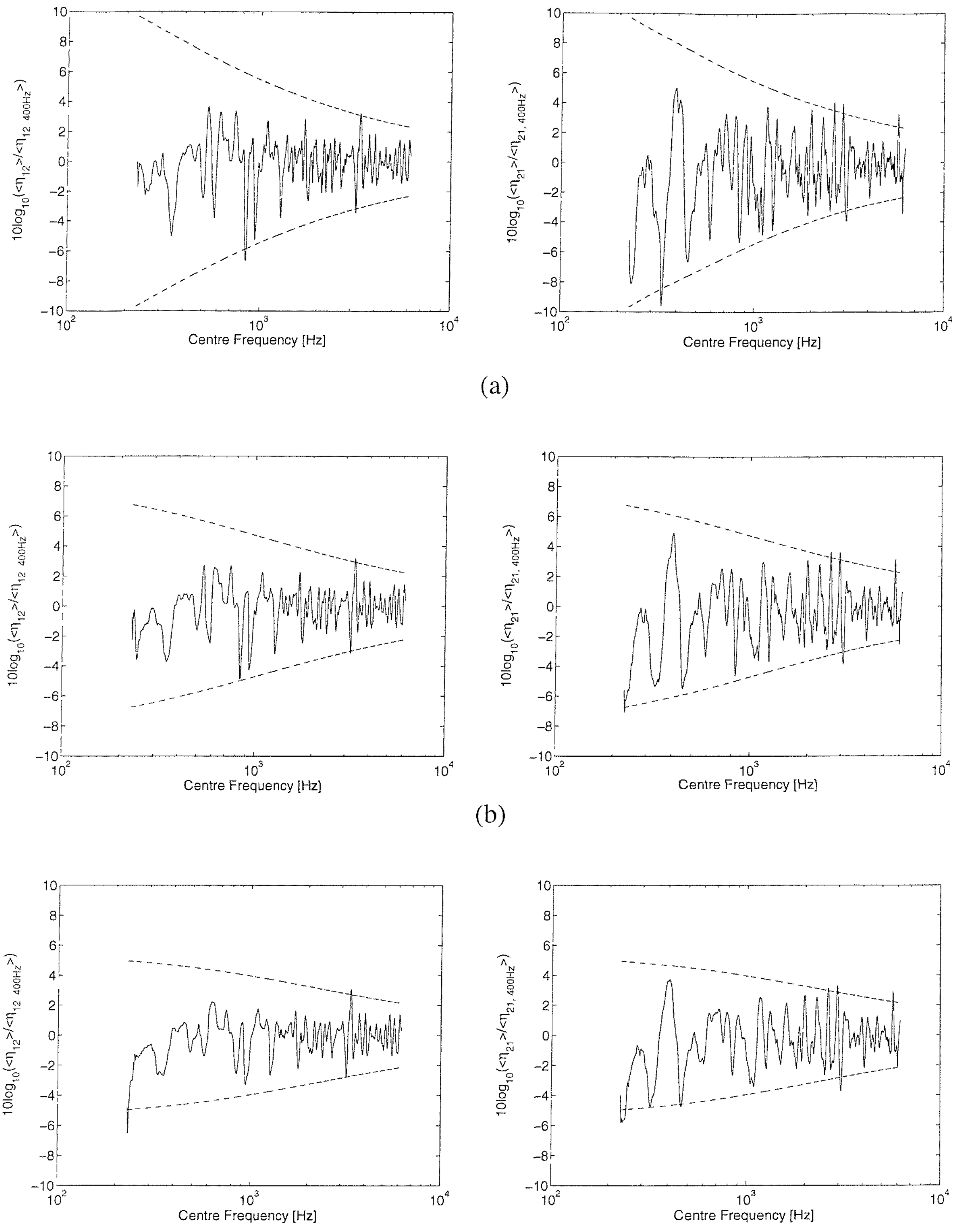

(a)

(b)

(c)

Figure 7.21 (a) - (c). The measured CLF ratio averaged for frequency bandwidth of (a) 20 Hz, (b) 40 Hz, and (c) 60 Hz, and the predicted $\pm 2\sigma$ bands obtained from equation (6.5). —, $10\log_{10}\left(<\hat{\eta}_{ij,\Delta f}>/<\hat{\eta}_{ij,400Hz}>\right)$; ---, $\pm 2\sigma$.

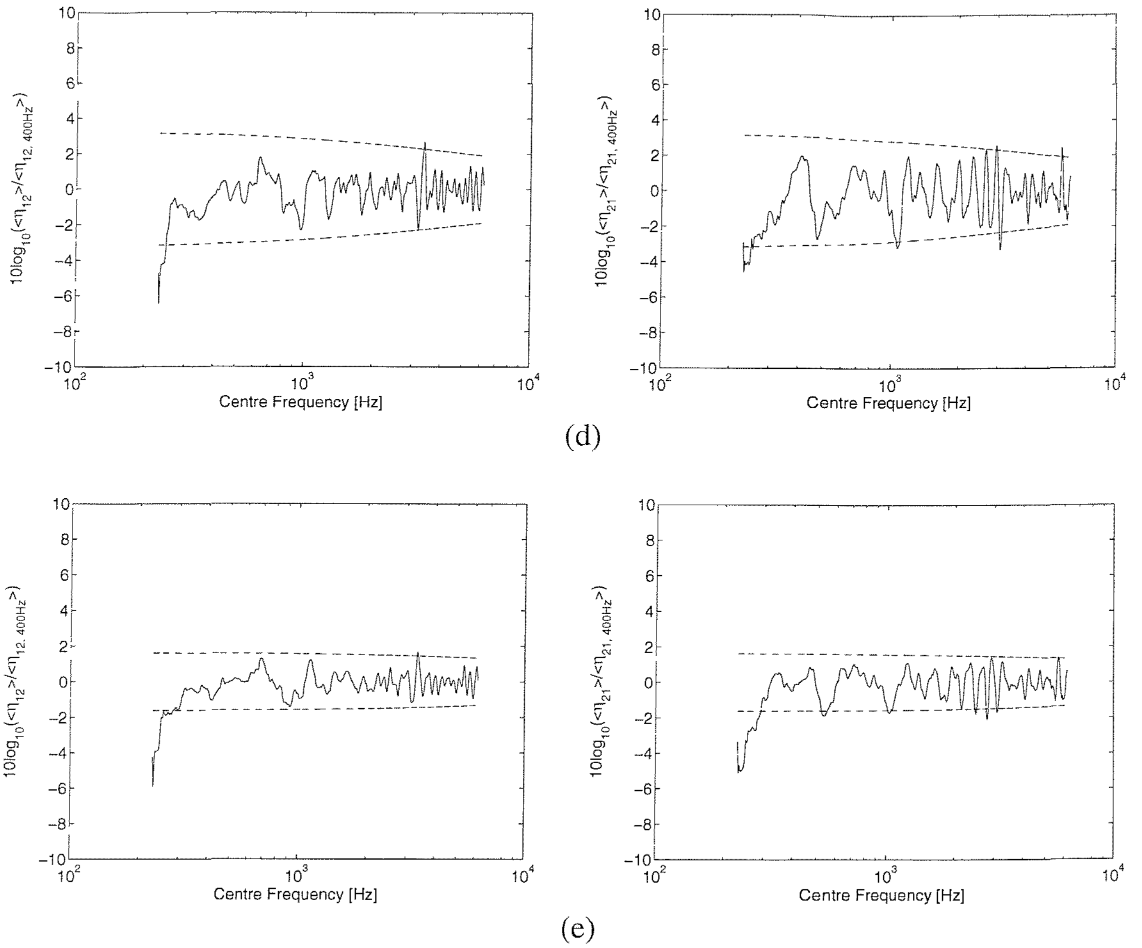

(d)

(e)

Figure 7.21 (d) - (e). The measured CLF ratio averaged for frequency bandwidth of (d) 100 Hz and (e) 200 Hz, and the predicted $\pm 2\sigma$ bands obtained from equation (6.5). —, $10\log_{10}\left(<\hat{\eta}_{ij,\,\Delta f}>/<\hat{\eta}_{ij,\,400Hz}>\right)$; ---, $\pm 2\sigma$.

Table 7.5. Percentage of points falling within $\pm\sigma$ and $\pm 2\sigma$ bands for the experimental CLF ratio.

Band	$10\log_{10}\left(<\hat{\eta}_{12}>/<\hat{\eta}_{12,\,400\mathrm{Hz}}>\right)$	$10\log_{10}\left(<\hat{\eta}_{21}>/<\hat{\eta}_{21,\,400\mathrm{Hz}}>\right)$
$\pm\sigma$	85.2 %	73.2 %
$\pm 2\sigma$	98.9 %	96.0 %

* Values falling within $\pm\sigma$ and $\pm 2\sigma$ for a normal distribution are 68.3 % and 95.4 % respectively.

7.6 Conclusions

From the results of experimental and analytical work for two coplanar plates joined by bolts, described in this chapter, the following conclusions can be drawn:

(a) Considering the estimated uncertainty of the experimental CLFs, the experimental CLF estimates agreed reasonably well with the analytical results above 30 Hz, although the results around 50 Hz and above 800 Hz were not so good. Some discrepancies may be caused by the different boundary conditions between experiment and analysis and the use of kinetic energy in the experiment.

(b) Since the main aim is to study the variability of the CLF, quantitatively as well as qualitatively, using the empirical model developed in Chapter 6, the level of agreement found is considered acceptable. This conclusion supports the argument that the analytical results obtained in the previous chapters are also acceptable.

(c) Over 95% of the experimental CLF values fell within the $\pm 2\sigma$ bounds predicted by the empirical model developed in Chapter 6. This conclusion suggests that the empirical model obtained from two plates joined at right angles may be applicable to other geometries.

CHAPTER 8

CONSEQUENCES FOR SEA MODELS

8.1 Introduction

In Chapter 3 the SEA framework was introduced and some of the methods to evaluate the CLF were discussed. In the remaining chapters the behaviour of two coupled rectangular plates has been investigated using the DSM. The effective CLF for a particular realisation of two coupled rectangular plates has been evaluated and shown to fluctuate significantly at low modal overlap, relative to the ensemble average CLF or the semi-infinite result. An empirical model for the confidence interval of the effective CLF, in terms of the modal overlap factor and the number of modes in a frequency band, has been derived and finally shown to agree with results from an experimental study.

However, SEA predictions give results in terms of average response energies in the subsystems. These results will depend on the input power values, the modal densities, and the DLFs as well as the CLFs. This chapter discusses briefly the consequences of the variation in the CLF for the subsequent SEA predictions. The variation of the CLF is obtained from the empirical model developed in Chapter 6. In order to investigate the sensitivity of the resulting SEA prediction, a Monte Carlo simulation is used. The ratio between the energy of the receiver plate and that of the source plate, obtained from the SEA equations, is compared with results directly obtained from the DSM model of the system.

As the variability of the CLF has only been considered for two directly coupled rectangular plates, the present work is also limited to a two-plate system. Other systems could be considered in a similar manner.

8.2 Monte Carlo simulation

8.2.1 Method

In order to investigate the effect of variations in the CLF on the results of an SEA prediction, consider an SEA model of the baseline two-plate structure used in Chapter 4 ($h_1 = 3$ mm, $L_1 = 0.5$ m, $h_2 = 2$ mm, $L_2 = 1.0$ m, $b = 1.0$ m and $\eta_1 = \eta_2 = 0.1$: see Figure 4.1). Calculations are performed initially in 1/3 octave bands. The results will be considered in terms of the ratio of the energy of the receiver E_{receiver} to that of the source plate E_{source}.

When power is injected to plate 1 in a frequency band centred at ω, the energies of the two plates determined by the power balance equations, (3.1) and (3.2), are given by

$$\begin{Bmatrix} E_1^1 \\ E_2^1 \end{Bmatrix} = \frac{1}{\omega}\begin{bmatrix} \eta_1 + \eta'_{12} & -\eta'_{21} \\ -\eta'_{12} & \eta_2 + \eta'_{21} \end{bmatrix}^{-1} \begin{Bmatrix} P_{1,\mathrm{in}}^1 \\ 0 \end{Bmatrix} \tag{8.1}$$

where η'_{12} and η'_{21} are the CLFs. In the present case these are considered to be perturbed relative to the ensemble average result of Section 3.5. These CLFs are determined by using the estimated standard deviation σ of the logarithmic CLF ratio, $10\log_{10}\left(\hat{\eta}_{ij}/\eta_{ij,ens}\right)$, in dB. The estimated σ is obtained from the empirical model given by equation (6.5) and is shown in Figure 8.1 for this baseline situation. The CLFs η'_{ij} are given by

$$\eta'_{12} = 10^{\Delta\eta_{12}/10}\eta_{12,ens} \tag{8.2}$$

and

$$\eta'_{21} = 10^{\Delta\eta_{21}/10}\eta_{21,ens}\,. \tag{8.3}$$

where the perturbation of the CLF with respect to the relevant ensemble value, $\Delta\eta_{ij}$, is obtained according to a Monte Carlo simulation. This is an empirical method that uses computer-generated random numbers to obtain large numbers of samples from any specified distribution. In the present work, the normally distributed random numbers for 1000 samples were obtained using a MATLAB built-in function, 'randn' with zero mean and standard deviation σ. Two extreme cases were considered for the perturbation of the CLF: one is where the variations $\Delta\eta_{12}$ and $\Delta\eta_{21}$ are totally dependent and the other where they are considered to be independent. The former requires the same relative variation,

$\Delta\eta_{12} = \Delta\eta_{21}$, whilst in the latter case $\Delta\eta_{12} \neq \Delta\eta_{21}$ in which each one is normally distributed and randomly chosen independently.

Finally the energies for the two plates are calculated by solving equation (8.1) for each of the 1000 sets of η'_{ij}, and the distribution of $E_{\text{receiver}} / E_{\text{source}}$ is obtained.

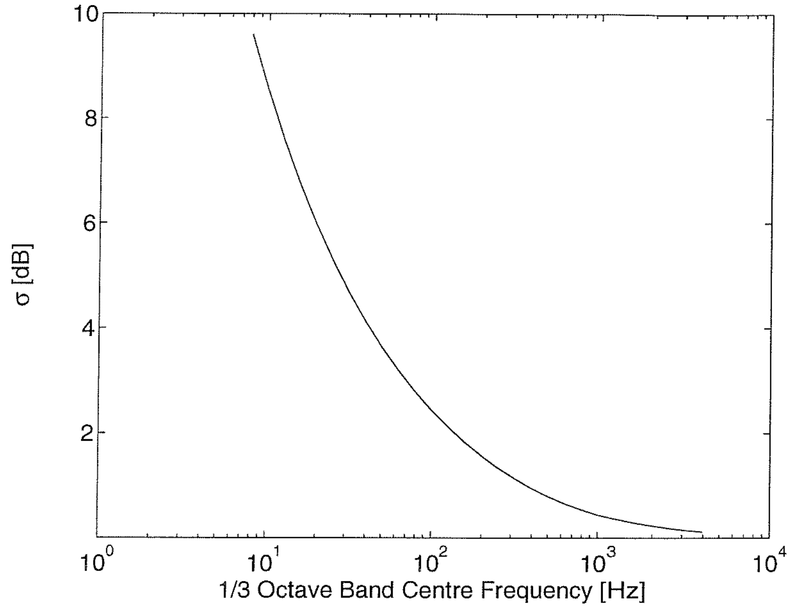

Figure 8.1. The estimated standard deviation σ of $10\log_{10}\left(\hat{\eta}_{ij}/\eta_{ij,\,ens}\right)$ obtained from the empirical model for the variability of the effective CLF in equation (6.5) for the parameters of the baseline model of two plates.

8.2.2 Results in 1/3 octave bands

For the case where $\Delta\eta_{12}$ and $\Delta\eta_{21}$ are dependent, the result is shown in Figure 8.2. This shows the mean value of the perturbed SEA simulations, the prediction obtained using the ensemble average CLF $\eta_{ij,\,ens}$ and the energy ratio calculated by the DSM. Also shown is a range of ±*s*, where *s* is the standard deviation of the energy ratio in dB obtained from the perturbed SEA simulations. The DSM result is approximately bounded by the range ±*s* of the mean SEA simulations across the whole frequency range. The mean value of the simulations and the result obtained using the ensemble average CLF $\eta_{ij,\,ens}$ differ slightly at the lower frequencies. This may be caused by non-linear components which occur in the inversion of the loss factor matrix in the process of solving equation (8.1); consequently the results of the energy ratio are not normally distributed although $\Delta\eta_{ij}$ are normally distributed. The difference between the mean SEA simulations and the prediction using the ensemble average CLF reduces as frequency increases. In practice this difference is only significant when $\pm s$ is greater than about ±5dB. Where $\pm s$ is greater than this it is probably inappropriate to use SEA as the results are too unreliable for practical application.

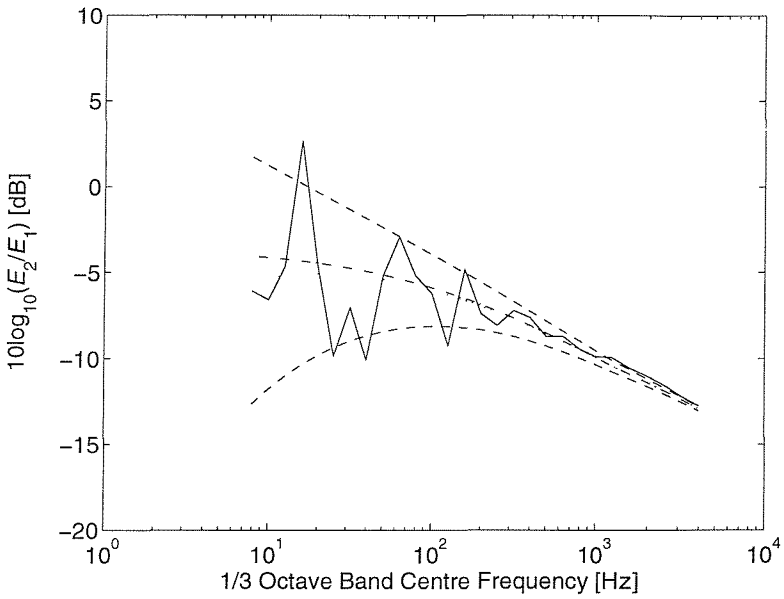

Figure 8.2. The energy ratio in dB, $10\log_{10}(E_2/E_1)$, for two plates when $\Delta\eta_{12}$ and $\Delta\eta_{21}$ are dependent. —, DSM; -·-, prediction using $\eta_{ij,ens}$; ·····, mean value of perturbed SEA simulations; ---, $\pm s$ from perturbed SEA simulations.

The skewness and kurtosis of the Monte Carlo results for $10\log_{10}(E_2/E_1)$ were investigated and are shown in Figure 8.3. The distribution of the logarithmic energy ratio is negatively skewed below 250Hz, with respect to a normal distribution. The value of (kurtosis-3) is close to zero for most of the frequency range but below 12.5Hz the distribution is peaked. As frequency increases, the skewness and (kurtosis-3) are small and close to their expected standard deviation for a normal distribution, as given by Snedecor and Cochran [91].

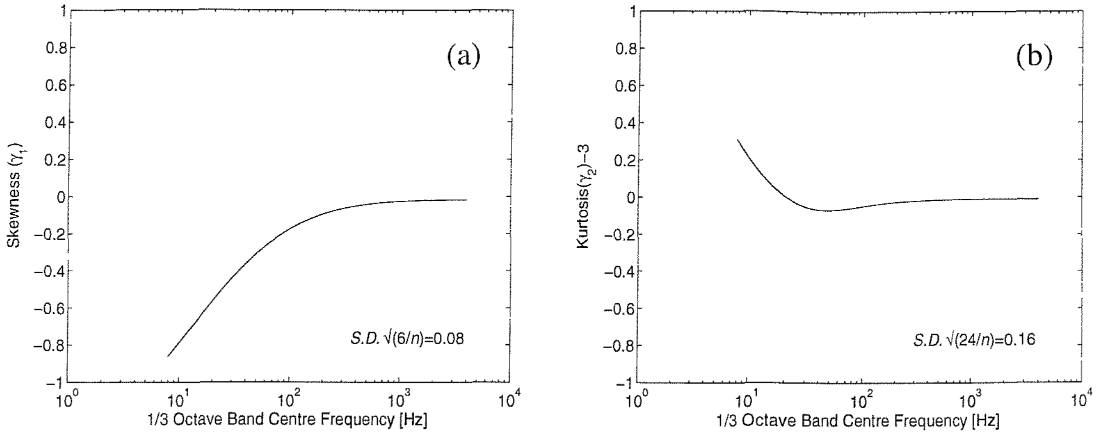

Figure 8.3. (a) skewness and (b) (kurtosis-3) for $10\log_{10}(E_2/E_1)$ from Monte Carlo simulations when $\Delta\eta_{12}$ and $\Delta\eta_{21}$ are dependent. The expected standard deviation (S.D.) of each quantity for a normal distribution is given by Snedecor and Cochran [91].

When $\Delta\eta_{12}$ and $\Delta\eta_{21}$ are assumed to be independent, the mean values and the standard deviation of the energy ratio in dB are as shown in Figure 8.4. Again the result obtained from the DSM is shown for comparison.

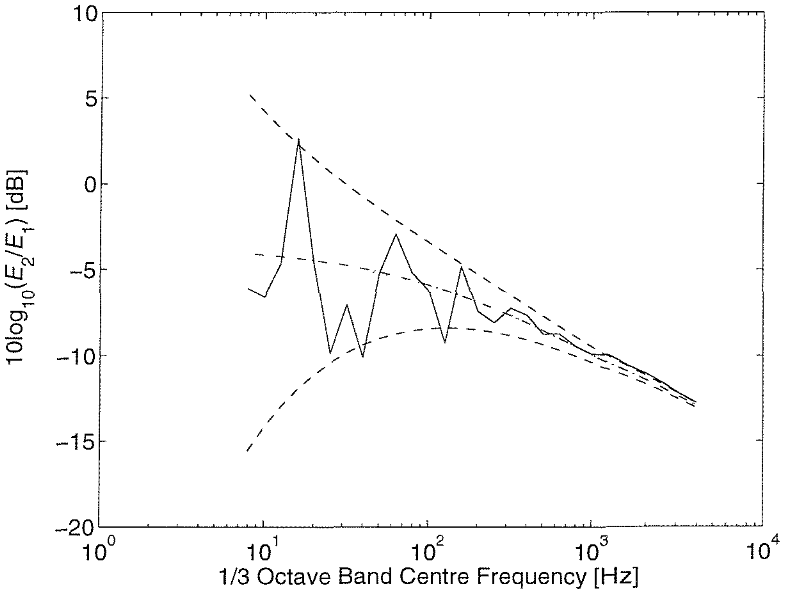

Figure 8.4. The energy ratio in dB, $10\log_{10}(E_2/E_1)$, for two plates when $\Delta\eta_{12}$ and $\Delta\eta_{21}$ are independent. —, DSM; -·-, prediction using $\eta_{ij,\,\mathrm{ens}}$; ·····, mean value of perturbed SEA simulations; ---, ±s from perturbed SEA simulations.

The DSM energy ratio again falls approximately within ±s of the simulation over the whole frequency range, but the bounds at low frequency are wider than the previous result in Figure 8.2. At the lower frequencies the skewness and (kurtosis-3) are smaller than the previous results, as shown in Figure 8.5.

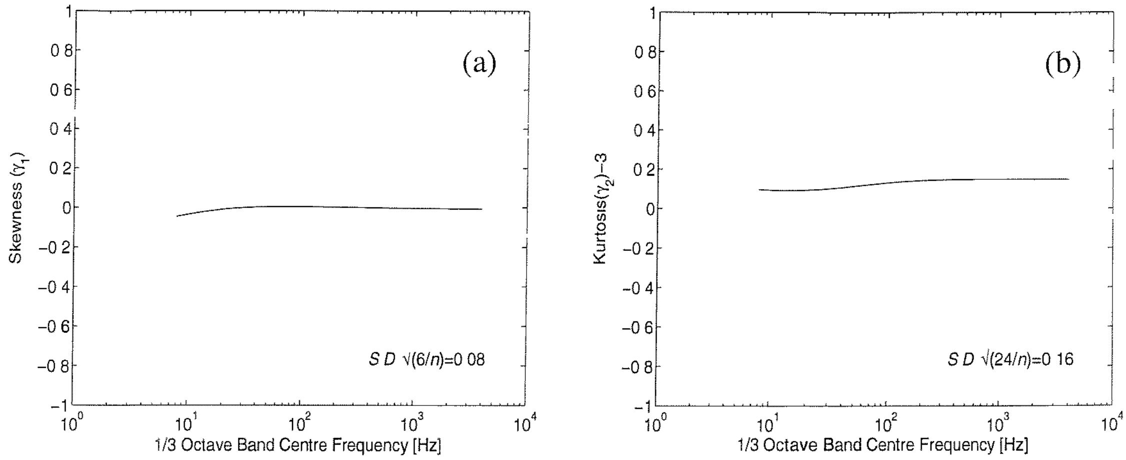

Figure 8.5. (a) skewness and (b) (kurtosis-3) for $10\log_{10}(E_2/E_1)$ from Monte Carlo simulations when $\Delta\eta_{12}$ and $\Delta\eta_{21}$ are independent. The expected standard deviation (S.D.) of each quantity for a normal distribution is given by Snedecor and Cochran [91].

It is found in the present case that the estimated standard deviation σ obtained from the empirical model for the variability of the effective CLF is similar to the standard deviation s of the energy ratio in dB when $\Delta\eta_{12}$ and $\Delta\eta_{21}$ are independent. This is shown in Figure 8.6. When $\Delta\eta_{12}$ and $\Delta\eta_{21}$ are treated as dependent the resulting standard deviation s of the energy ratio is somewhat lower than σ. The standard deviations all decrease as frequency (or modal overlap) increases.

8.2.3 Results for constant modal overlap factor

Since the damping values of the two plates in the above calculations were kept constant as $\eta_1 = \eta_2 = 0.1$, the modal overlap factors for the two plates varied with frequency.

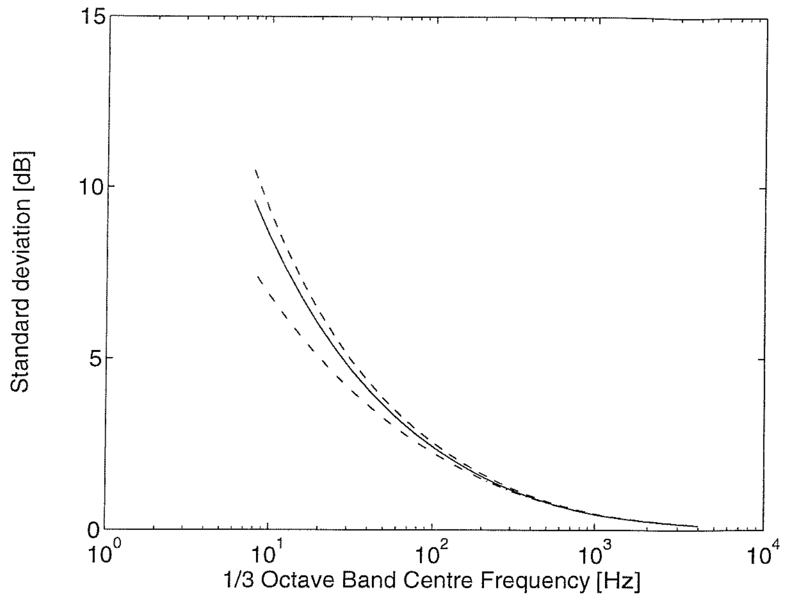

Figure 8.6. Standard deviations in dB obtained from the empirical model (Figures 8.1) and Monte Carlo simulations (Figures 8.2 and 8.4). —, σ obtained from empirical model; -·-, s when $\Delta\eta_{12}$ and $\Delta\eta_{21}$ are dependent ; ---, s when $\Delta\eta_{12}$ and $\Delta\eta_{21}$ are independent.

Three different levels of frequency-dependent DLF (low damping = $1/f$, medium damping = $3/f$, and high damping = $10/f$), as used in Section 6.4.1.2, were next considered in order to give a constant modal overlap factor. The bounds $\pm s$ of the SEA simulation were obtained by Monte Carlo simulation with $\Delta\eta_{12}$ and $\Delta\eta_{21}$ dependent or independent, as before. The energies for the two plates were evaluated by the DSM and were averaged over overlapping frequency bands. In this section 20 Hz and 200 Hz bands are considered as examples.

The results of the energy ratio averaged over 20 Hz and 200 Hz bands are shown in Figures 8.7 - 8.10. Figures 8.7 and 8.8 show the results obtained when it is assumed that $\Delta\eta_{12}$ and $\Delta\eta_{21}$ are dependent. Results are plotted of the energy ratio in dB, $10\log_{10}(E_2/E_1)$, for the two plates. Results are given for the three different levels of DLF: (a) low damping ($M_{\mathrm{comb}} = 0.08$), (b) medium damping ($M_{\mathrm{comb}} = 0.24$) and (c) high damping ($M_{\mathrm{comb}} = 0.80$), where M_{comb} is the combined modal overlap factor given by equation (6.2).

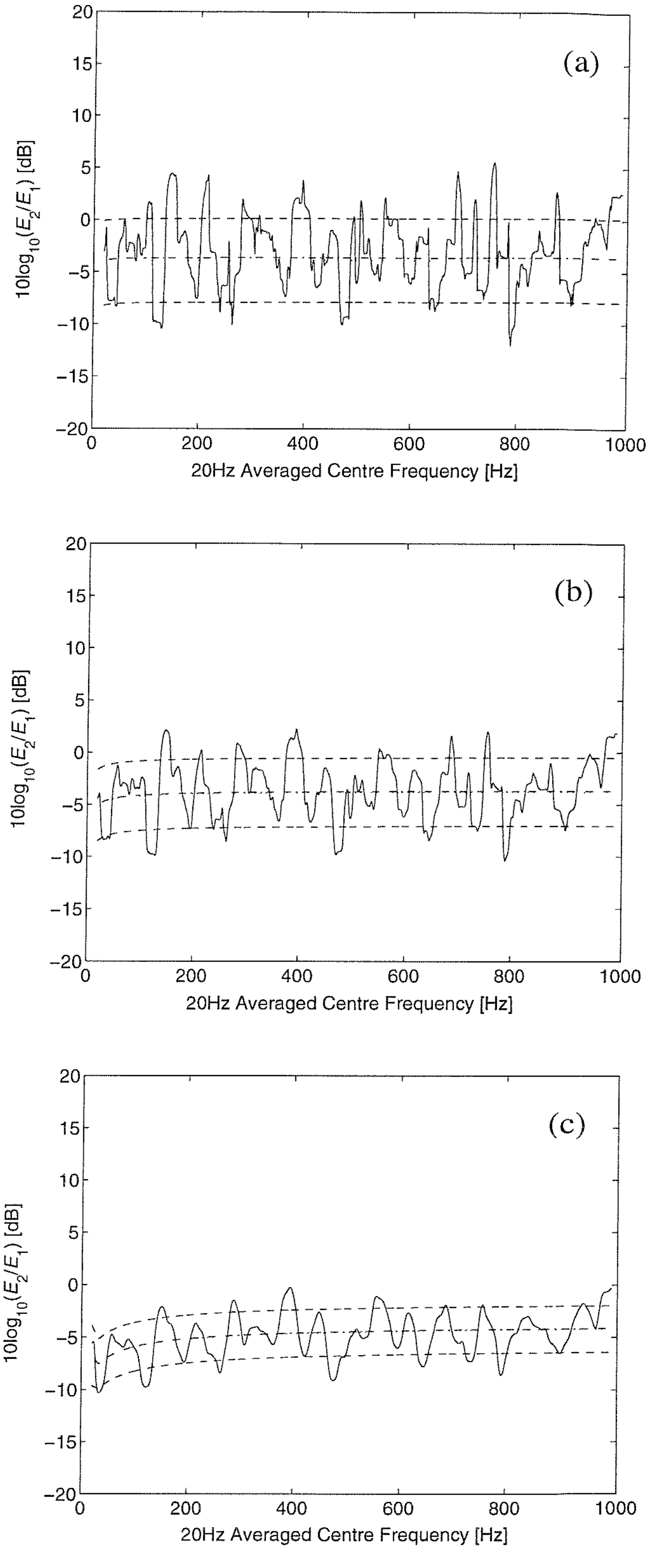

Figure 8.7. The energy ratio averaged over 20 Hz bands in dB, $10\log_{10}(E_2/E_1)$, when $\Delta\eta_{12}$ and $\Delta\eta_{21}$ are considered dependent: (a) low damping ($M_{\text{comb}} = 0.08$), (b) medium damping ($M_{\text{comb}} = 0.24$) and (c) high damping ($M_{\text{comb}} = 0.80$). —, DSM; -·-, prediction using $\eta_{ij,\,ens}$; ·····, mean value of simulation; ---, ±s of simulation.

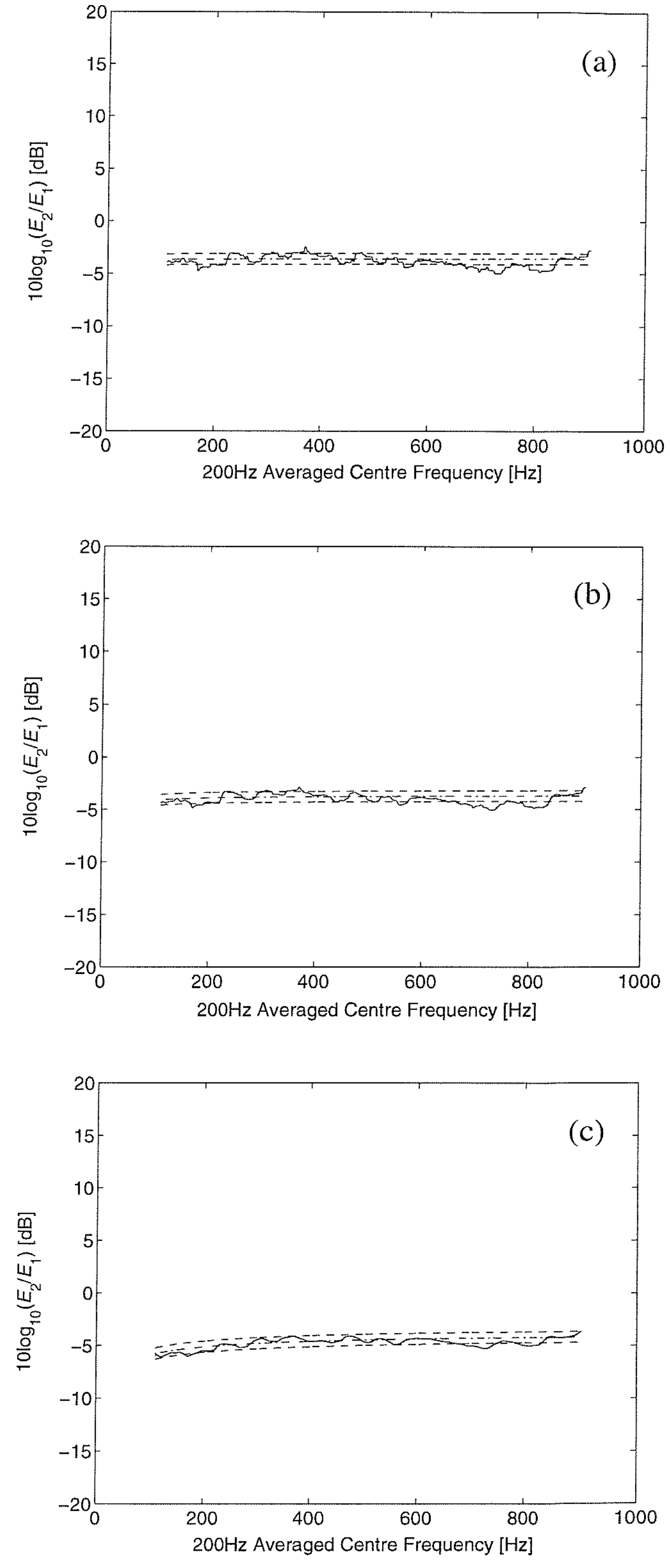

Figure 8.8. The energy ratio averaged over 200 Hz bands in dB, $10\log_{10}(E_2/E_1)$, when $\Delta\eta_{12}$ and $\Delta\eta_{21}$ are considered dependent: (a) low damping ($M_{\text{comb}} = 0.08$), (b) medium damping ($M_{\text{comb}} = 0.24$) and (c) high damping ($M_{\text{comb}} = 0.80$). —, DSM; -·-, prediction using $\eta_{ij,\,ens}$; ·····, mean value of simulation; ---, ±s of simulation.

As the modal overlap factor increases, the bounds ±*s* of the SEA simulation decrease. When $\Delta\eta_{12}$ and $\Delta\eta_{21}$ are assumed independent, the bounds ±*s* of the SEA simulation are larger than those obtained when $\Delta\eta_{12}$ and $\Delta\eta_{21}$ are assumed dependent, as shown in Figures 8.9 and 8.10. It is noted that for a 20 Hz bandwidth *M* is important in determining the bounds, whilst for a 200 Hz bandwidth *N* is important, rather than *M*.

The percentage of the values of the energy ratio obtained from the DSM falling within the range ±*s* dB of the SEA simulation was investigated and is listed in Table 8.1. In most cases the number of points is similar to the expected 68 % for a normal distribution for the dependent case, slightly more points falling in the range for the independent assumption.

Table 8.1. The percentage of the values of the exact energy ratio obtained from the DSM falling between the upper and lower bounds ±*s* dB of the perturbed SEA simulations.

Model	Baseline model	Low damping model		Medium damping model		High damping model	
$\Delta\eta_{12}$, $\Delta\eta_{21}$	1/3 octave bands	20 Hz	200 Hz	20 Hz	200 Hz	20 Hz	200 Hz
Dependent	64	73.1	61.2	73.3	63.3	72.5	81.2
Independent	68	81.4	72.8	82.6	75.0	79.2	86.1

Table 8.2 compares the various standard deviations. σ is the expected standard deviation of the CLF ratio from the model of Chapter 6, *s* is the standard deviation of the perturbed SEA results. By subtracting the mean of the perturbed SEA results from the DSM results, these may be averaged over frequency, yielding the standard deviation s'. These results are given for the three levels of damping and two frequency bandwidths considered. The values of *s* for the perturbed SEA simulations are similar to those for σ, the estimated standard deviation for the CLF. The difference $(s - s')$ for the 20 Hz bandwidth decreases as the DLF increases, whereas for the 200 Hz bandwidth it increases with increasing the DLF; nevertheless, the standard deviation of the perturbed SEA results *s* is very small.

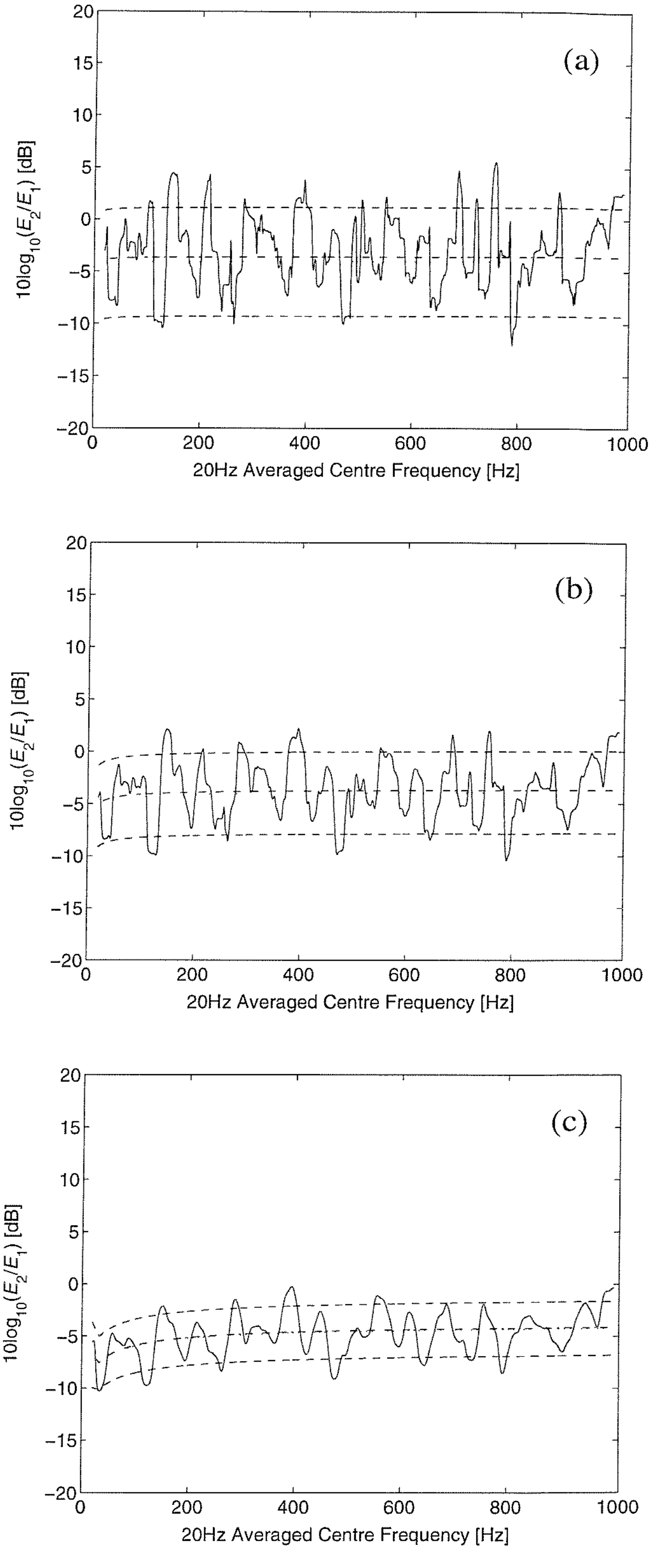

Figure 8.9. The energy ratio averaged over 20 Hz bands in dB, $10\log_{10}(E_2/E_1)$, when $\Delta\eta_{12}$ and $\Delta\eta_{21}$ are considered independent: (a) low damping ($M_{\mathrm{comb}} = 0.08$), (b) medium damping ($M_{\mathrm{comb}} = 0.24$) and (c) high damping ($M_{\mathrm{comb}} = 0.80$). —, DSM; -·-, prediction using $\eta_{ij,\,ens}$; ·····, mean value of simulation; ---, ±s of simulation.

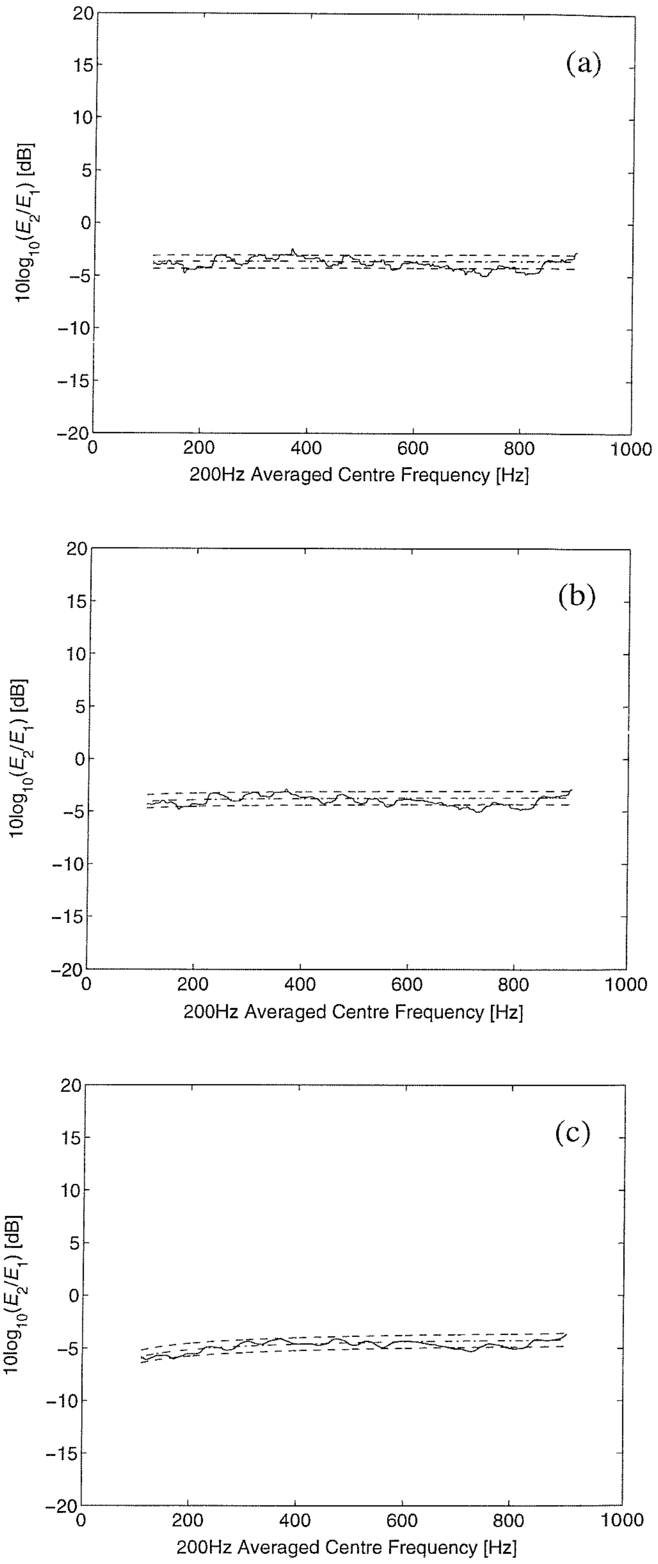

Figure 8.10. The energy ratio averaged over 200 Hz bands in dB, $10\log_{10}(E_2/E_1)$, when $\Delta\eta_{12}$ and $\Delta\eta_{21}$ are considered independent: (a) low damping ($M_{\mathrm{comb}} = 0.08$), (b) medium damping ($M_{\mathrm{comb}} = 0.24$) and (c) high damping ($M_{\mathrm{comb}} = 0.80$). —, DSM; -·-, prediction using $\eta_{ij,\,ens}$; ·····, mean value of simulation; ---, ±*s* of simulation.

Table 8.2. The standard deviations (σ of the CLF obtained from the empirical model for the variability of the effective CLF, s of the perturbed SEA simulations and s' of DSM results) for three different damping models.

Frequency band	$\Delta\eta_{12}$, $\Delta\eta_{21}$	damping	σ	s	s'	$s-s'$
20 Hz	Dependent	low	4.99	4.02	3.52	0.50
		medium	3.87	3.29	2.84	0.45
		high	2.50	2.19	1.96	0.23
	Independent	low	4.99	5.23	3.52	1.71
		medium	3.87	3.92	2.84	1.08
		high	2.50	2.60	1.96	0.64
200 Hz	Dependent	low	0.61	0.51	0.52	-0.01
		medium	0.61	0.51	0.50	0.01
		high	0.60	0.52	0.36	0.16
	Independent	low	0.61	0.62	0.52	0.10
		medium	0.61	0.64	0.50	0.14
		high	0.60	0.61	0.36	0.25

8.2.4 Investigation of coupling strength

The ratio of the effective CLF $\hat{\eta}_{ij}$ to the DLF for the source plate η_i is an indication of the coupling strength [88]; *i.e.* if the ratio is greater than 1, then the subsystems may be considered 'strongly coupled'. These ratios were investigated and are shown in Figures 8.11 and 8.12. The models considered are the baseline model in 1/3 octave bands as well as results averaged over 20 Hz and 200 Hz frequency bands for the three levels of damping. For the 1/3 octave model (Figure 8.11), which has a constant loss factor η, the two plates are only strongly coupled at low frequencies. For the three cases of the different damping values averaged over 20 Hz frequency bands (Figure 8.12 (a), (c) and (e)), the two plates are strongly coupled at some frequencies. The results for 200 Hz bands (for which η is frequency dependent) seem relatively insensitive to the damping values (Figure 8.12 (b), (d) and (f)) and lie below 1; the two plates may be considered weakly coupled.

Another indication of the coupling strength is the coupling parameter $\gamma(k_x)$ defined by Wester and Mace [50]: when the gamma value is positive and much less than unity, the subsystems can be considered weakly coupled, otherwise they can be considered not weakly coupled. Determining the coupling parameter $\gamma(k_y)$ for normal incidence, using equation (3.25), it was found to be below unity for $f > 175$ Hz for the baseline model. For the three cases for which the damping is frequency dependent, the gamma values were above unity for the low and medium damping cases and below unity only when the frequency is between 20 and 60 Hz for the high damping case. Since these gamma values are based on the ensemble average [50], the corresponding gamma values in the realisations and the frequency averaged investigations; *e.g.* 1/3 octave, 20 Hz and 200 Hz bands, in Figures 8.11 and 8.12, cannot be directly compared.

From these two measures of coupling strength it is seen that the cases considered include both weak and strong coupling. It may therefore be concluded that the bounds $\pm s$ obtained from the perturbed SEA simulations give a good approximation to the actual variations $\pm s'$, irrespective of the coupling strength (see Figures 8.7 and 8.9).

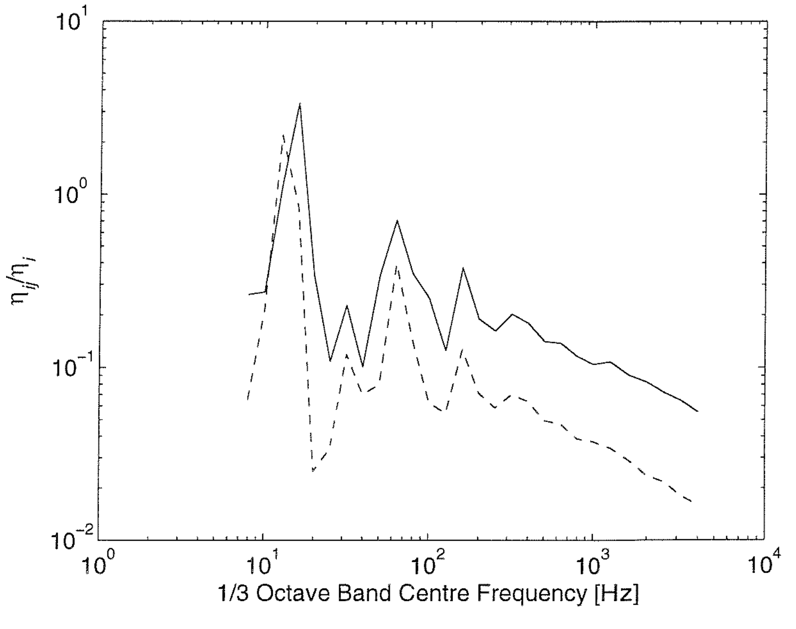

Figure 8.11. The ratio of the effective CLF $\hat{\eta}_{ij}$ to the DLF for the source plate η_i for the baseline model in 1/3 octave bands. —, $\hat{\eta}_{12}/\eta_1$; ---, $\hat{\eta}_{21}/\eta_2$.

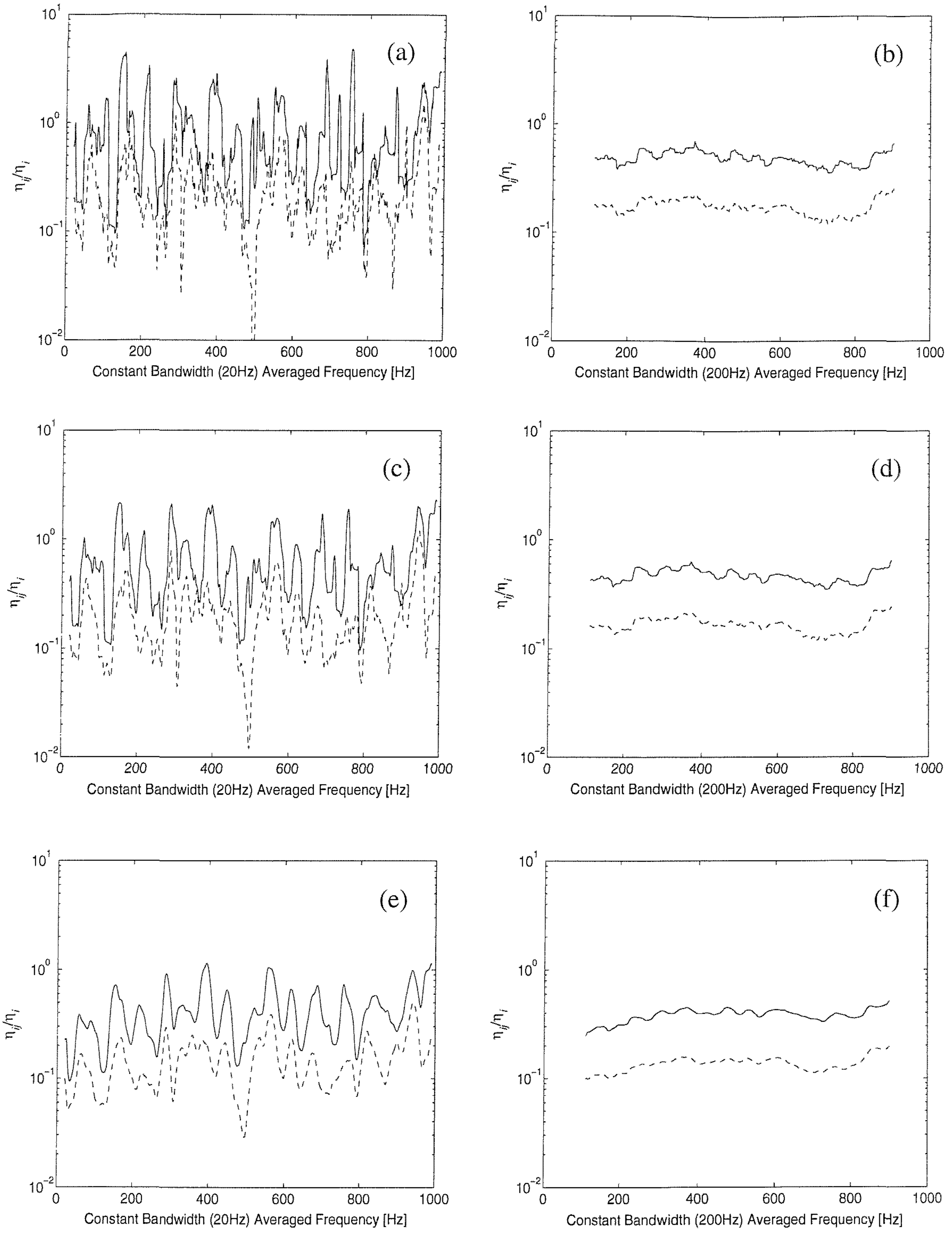

Figure 8.12. The ratio of the effective CLF $\hat{\eta}_{ij}$ to the DLF for the source plate η_i: low damping model ((a) 20 Hz bands, (b) 200 Hz bands); medium damping model ((c) 20 Hz bands, (d) 200 Hz bands); high damping model ((e) 20 Hz bands, (f) 200 Hz bands). —, $\hat{\eta}_{12}/\eta_1$; ---, $\hat{\eta}_{21}/\eta_2$.

8.3 Concluding remarks

SEA predictions for a two-plate system were obtained by perturbing the CLF according to the previously developed empirical model. The following conclusions can be drawn from these results.

The standard deviation ($\pm\sigma$) of the CLF results corresponds approximately to the standard deviation ($\pm s$) of the consequent energy ratios. Both standard deviations depend on the modal overlap factor and frequency average bandwidth. If the frequency average is carried out over a large bandwidth, the effect of the modal overlap factor on the standard deviation becomes small.

The bounds $\pm s$ obtained from the perturbed SEA simulations give a good approximation to the actual variations in the DSM results even in the case of strong coupling.

The mean value of the SEA simulations deviates from the result obtained using the ensemble average CLF below a frequency where the standard deviation ($\pm s$) of the energy ratio is greater than about ±5 dB. This frequency could in any case be seen as a lower limit for application of SEA, below which the results are unreliable.

It is noted that the empirical model developed in this research was obtained from the limited cases of two coupled rectangular plates. The empirical model can be used to find the variability of the effective CLFs for a system of two coupled subsystems or to estimate the resulting variability of the SEA prediction for that system. However, it is not known how to apply the empirical model to a multi-subsystem model. In particular, the CLFs for the multi-subsystem model will not be independent, as some modal behaviour affects η_{ij} for a given receiver subsystem j for all other subsystems i.

CHAPTER 9

CONCLUSIONS

9.1 Introduction

This research was undertaken to investigate variability in the CLF using two coupled rectangular plates as an example and to develop an empirical model to quantify the uncertainties in the CLF. The DSM was used in order to obtain the exact dynamic response for the particular structures across a wide frequency range. Extensive parameter studies have been performed to determine the variability of the CLF. An empirical model describing the variability of the CLF was developed and validated. The subsequent confidence intervals for SEA predictions using this variability were investigated using Monte Carlo simulation. Results and conclusions drawn from this research are summarised here, followed by recommendations for future work.

9.2 Summary of results and conclusions

9.2.1 Background research and theory

A number of relevant research studies and complementary approaches applicable to the solution of dynamic problems in the mid to high frequency range have been reviewed and were presented in Chapter 1. This highlighted the difficulties and, in particular, the uncertainties which are present in SEA due to variability in the coupling loss factors.

In Chapter 2 the theoretical predictions of the dynamic response of a uniform plate to an applied harmonic point force were described and the DSM models were developed. This was extended to two coupled plates, with a line connection at the joint.

It was demonstrated that for reliable results, all half-sine orders with a cut-on frequency below the frequency of analysis should be included.

The input power for a point force has been compared with the dissipated power. It was clarified that the strain energy should be used, at least in the low and medium frequency range, since significant errors occur in the dissipated power calculation if kinetic energy is used when hysteretic losses are introduced.

In-plane motion has also been considered for two coupled plates in an L shape configuration. Although the in-plane motion has only a small effect in the examples considered, it may be important for large structures or multi-plate structures.

The theoretical background of the SEA framework was presented in Chapter 3. Various methods to evaluate the effective CLF, the ensemble average CLF and the CLF based on semi-infinite plates, were discussed. Previously published theoretical upper and lower bounds were reviewed for comparison with the variability of the CLF to be evaluated in the following chapters.

9.2.2 Analytical CLF determination and the modal behaviour of the two plates

Various analytical models were presented in Chapter 4 in order to evaluate the effective CLFs and to investigate the influence of the modal behaviour of the source or receiver plate or both. In order to isolate the effects on the variability of the way in which the systems are excited, a sensitivity investigation was performed. Confidence intervals were obtained for six different sized sets of forcing points. It was seen that the confidence intervals are large for small numbers of forcing points and reduce as more points are taken. They are not strongly dependent on frequency. As the number of forcing points increases, the effective CLF estimates become more reliable, so that for a 90% confidence interval of ±1.5 dB at least ten points should be taken. For 400 forcing points it can be expected that the uncertainty will be reduced to ±0.25 dB. By reciprocity the same is expected to apply to the number of response positions used.

The effective CLFs, for finite plate realisations, were calculated using three different methods, *i.e.* based on the actual mode count, the asymptotic modal density and matrix-inversion from a 'numerical experiment'. Of these, the latter was found to be more reliable. These results were compared with the CLF obtained from semi-infinite plates.

The effective CLF for finite plates fluctuated considerably relative to the CLF based on semi-infinite plates at low frequencies and agreed well with the semi-infinite plate results at high frequencies. It was also shown that the consistency relationship ($n_1\eta_{12} = n_2\eta_{21}$) is satisfied by the predicted CLF at high frequencies, although at low frequencies considerable variation is found.

Although the effective CLF results converged to those of an infinite plate at high frequencies, some discrepancies remained. The effect of the plate thickness on the high frequency asymptotic behaviour was investigated in terms of the transmission efficiency τ_{ij}. Good agreement was found for dissimilar thicknesses, but for similar thicknesses it was found necessary to introduce a correction to the infinite plate by a factor of $2/(2-\tau)$. The remaining discrepancy between the effective CLF and the semi-infinite result was attributed to the influence of in-plane motion in the finite plate results and its neglect in the semi-infinite plate results.

The relationship was investigated between peaks and troughs in the effective CLF and in the ratio between the energy of the receiver plate and that of the source plate, and these were related to the modal behaviour of the plates. The effective CLF estimates and the energy ratio at low frequencies, in the region of the first few modes, contain peaks which correspond to the uncoupled modes of the receiver plate. Such peaks do not appear at resonances of the source plate.

The variability in the effective CLF, or the transmission efficiency, due to the modal behaviour of both the source and receiver plates has been examined using a systematic investigation involving both finite-width semi-infinite and finite plates.

The transmission efficiencies were evaluated between a semi-infinite source plate and a finite receiver plate with different thickness ratios. At low frequencies, the transmission efficiency oscillates considerably around that for two semi-infinite plates, converging as frequency increases. The peaks and troughs in the transmission efficiency correspond to the modal behaviour of the receiver plate. The uncoupled finite plate could be approximated using either simply supported or clamped boundary condition at the interface, which represent two extremes between which the coupled plate may be considered to lie.

A finite source plate coupled to a semi-infinite receiver plate was considered to investigate the influence of the modal behaviour of the source plate. At low frequencies, the effective

CLF fluctuates around the CLF for two semi-infinite plates, but it is relatively smooth compared to the fluctuations for a semi-infinite source plate coupled to a finite receiver plate. These fluctuations in the effective CLF are found to be due to the predominance of particular angles of incidence corresponding to the source plate modes, rather than due to the direct influence of the modal behaviour of the source plate.

Therefore it was found that the modal behaviour of both the source and receiver plates affects the energy transmission between two subsystems, rather than only that of the receiver plate as asserted by Craik *et al.* [44]. Nevertheless, the results were found to be more sensitive to the DLF of the receiver plate than that of the source plate.

9.2.3 Variability of the CLF

In order to quantify the variability of the effective CLF, a wide range of parameter investigations was performed using finite plate simulations which incorporate variations in both modal density and modal overlap, either together or separately.

Chapter 5 presented an initial parametric investigation on the variability of the effective CLF, performed using DSM. The parameters varied were: (i) the plate thickness ratio, (ii) the length ratio, (iii) the length-to-width ratio of the two plates and (iv) the damping loss factors. In each case, the modal density and the DLF were constant with frequency, whilst the modal overlap factor increased with increasing frequency. Results were presented in one-third octave bands. The ratio of the effective CLFs for finite plates to the CLF based on semi-infinite plates was determined and compared with Craik's upper and lower bounds.

At low modal overlap the effective CLFs fluctuated considerably, whereas the variability generally reduced as frequency increased. The results fall within a slightly wider range than Craik's upper and lower bounds, although these bounds are shown to be useful indications of the variability in the CLF. However, they do not account for remaining variability when the modal overlap is greater than about 0.4. Better agreement occurs when the modal overlap of both subsystems is taken into account, rather than that of the receiver alone, as originally proposed by Craik.

A further parametric investigation was performed in Chapter 6. Two parameters, the average number of modes in a frequency band N and the modal overlap factor M, were considered as independent control parameters. The ensemble average CLF discussed in Section 3.5, instead of the CLF based on semi-infinite plates, was used to provide a more consistent basis for comparisons. Results were determined in overlapping frequency bands of constant bandwidth. The ratio of the frequency averaged effective CLF to the ensemble average CLF expressed in dB was obtained and the mean over all centre frequencies and the standard deviation σ were determined. The mean was found to be close to 0 dB, whilst the range of $\pm 2\sigma$ reduces as the bandwidth increases.

The variance σ^2 of each case was investigated to find the variability of the effective CLF in terms of two new parameters, the 'combined' modal overlap factor $M_{\text{comb}} = 2/(M_1^{-1}+M_2^{-1})$ and the 'combined' number of modes $N_{\text{comb}} = 2/(N_1^{-1}+N_2^{-1})$. The two parameters as proposed are also applicable for the limiting cases of an infinite plate coupled to a finite plate. An empirical formula for the variance of the effective CLF in dB was derived in terms of M_{comb} and N_{comb}:

$$\sigma^2 = \frac{6}{M_{\text{comb}} + N_{\text{comb}}^2/16}.$$

It was shown that the empirical model provides improved confidence intervals of the CLF compared to the previously published estimates [33, 43]. The estimates of confidence intervals based on the empirical model were also compared with the results of the effective CLF for various parameter variations obtained from Chapter 5. These estimates gave better upper and lower bounds for the effective CLF than Craik's model discussed in Chapter 5.

Statistical investigations were carried out to review the distribution of the effective CLF and the interdependence of η_{12} and η_{21}. As a result of the Chi-square test and a study of the skewness and kurtosis, the probability distributions for the logarithmic CLF ratio are unlikely to be strictly normally distributed. Nevertheless, for simplicity a normal distribution remains a reasonable approximation. It was found that η_{12} and η_{21} are not independent of each other, although the degree of correlation varies from one case to another.

9.2.4 Validation of the CLF variability and SEA consequences

Experimental validation of the empirical model on two coplanar plates joined by bolts was presented in Chapter 7. In the experimental study, the measured vibrations were averaged over ten forcing points and ten response points. The experimental and analytical CLFs were investigated and were discussed in relation to the empirical model for the variability of the effective CLF developed in Chapter 6.

The experimental CLF estimates agreed reasonably well with the analytical results above 30 Hz, although the results around 50 Hz and above 800 Hz were not so good. Some discrepancies may be caused by the different boundary conditions between experiment and analysis and the use of kinetic energy in the experiment. Since the main aim is to study the variability of the CLF, quantitatively as well as qualitatively, the level of agreement found was considered acceptable.

It was shown that over 95% of the experimental CLF values fell within the $\pm 2\sigma$ bounds based on the empirical model developed in Chapter 6. This suggests that the empirical model obtained from two plates joined at right angles may be applicable to other geometries.

The consequences for SEA predictions of the variation in the CLF were presented in Chapter 8. The variation in the CLF was obtained from the estimated standard deviation σ based on the empirical model for the variability of the effective CLF developed in Chapter 6. A Monte Carlo simulation was used to investigate the effect of perturbing of the CLF with respect to the relevant ensemble value. The energy ratio between the receiver plate and the source plate obtained from the SEA equations was compared with the exact analytical DSM results.

From the results in 1/3 octave bands, it was found that about 65% of the exact energy ratio results falls within ± one standard deviation (s) of the perturbed SEA simulations. The mean value of the SEA simulations diverges from the result obtained using the ensemble average CLFs at low frequencies. This occurs at frequencies where the standard deviation of the energy ratio is greater than about ±5dB. This frequency could be seen, in any case, as a lower limit for application of SEA, below which the results are too unreliable.

From the results for 20 Hz and 200 Hz bandwidths and constant modal overlap factors, are greater percentage of the values of the exact energy ratio fall within the range $\pm s$ from the perturbed SEA simulations, particularly when the modal overlap factor and frequency bandwidth are large. As the modal overlap factor increases, the bounds of the SEA simulation decrease slightly. It was shown that the SEA predictions are more reliable when the modal overlap factor (or the DLF) and frequency bandwidth are large. This corresponds to a fundamental hypothesis of the application of SEA. For a small bandwidth the effect of the modal overlap factor on the bounds is large, whereas for a large bandwidth the number of modes in a frequency band is important, not the modal overlap factor.

The variability ($\pm\sigma$) of the effective CLF is similar to the variability ($\pm s$) of the subsequent energy ratios (both expressed in dB). When the CLFs are assumed to be independent of each other, the bounds $\pm s$ obtained from the SEA simulation are slightly larger than those obtained when they are assumed to be dependent. The bounds obtained from the perturbed SEA simulations give a good approximation to the actual variations even in the case of strong coupling.

9.3 Recommendations for future research

This project has investigated the variability of the effective CLF for two rectangular plates. An empirical formula for the variability of the CLF, to assist in quantifying the uncertainty of the SEA predictions, has been derived. It is not possible without further investigation to generalise this result to structures consisting of different geometry or made up of multiple subsystems. Generally, real built-up structures such as an automotive vehicle have arbitrary geometry and complicated connections between subsystems. SEA is a useful method to predict the structural vibration and sound in those complex structures at mid to high frequencies, although other variant methods can also be used to obtain the dynamic response of complex structures. It would be possible to evaluate the variability of the CLF and to quantify the uncertainty of the SEA predictions using the same methodology as in this research. Some suggestions of particular relevance to an automotive vehicle are as follows.

An automotive vehicle consists of hundreds of panels, beam-like structures and pre-assembled substructures. Especially body panels are pressed into the required geometry from thin and flat rolled plates. Corrugations and stiffeners are usually added into panels to improve the rigidity of thin plates and these panels are assembled by spot welding or bolted connections. Most of the panels form a curved and complex geometry rather than a flat and rectangular shape. There are a number of junction areas, *i.e.* roof to windshield joint, centre pillar to floor panel joint and floor to bulkhead joint, etc., with various connection types from point coupling to line coupling. Most of these connections are formed by more than three subsystems of beams and plates. Accordingly, it is necessary to consider the confidence interval for curved and multi-subsystem structures of these various types.

SEA can be used to evaluate not only structural vibration but also interior noise inside vehicles at mid to high frequencies. In order to quantify the reliability of results from the SEA predictions, an investigation of the confidence interval of the coupling between the structure and the acoustic cavity is also required. Since an SEA model for automotive vehicles is typically constructed using hundreds of subsystems, it should be considered to what extent the confidence interval for each substructure affects that for the total system. An enclosed box structure with an acoustic cavity would be a good example case extending the work to consider the influence of individual CLF variability as well as multiple CLF variabilities on the sensitivity in the response in the final SEA prediction. Moreover, since the CLFs for multiple subsystem models will not be independent, effect on the SEA prediction requires attention.

REFERENCES

[1] I. Yamazaki and T. Inoue 1989 *SAE Paper 891996*. An application of structural-acoustic coupling analysis to boom analysis.

[2] N. Basavanhalli, R. Sommers, L. Brooks, F. Zweng, W. A. Kargus IV 1995 *SAE Paper 951092*. Reduction of passenger car road noise using computational analysis.

[3] W. Stokes, J. Bretl, A. Crewe, W. S. Park, J. Y. Lee and M. S. Lee 1997 *Proceedings of SAE Noise and Vibration Conference, Traverse City, Michigan*. Computer simulation of in-vehicle boom noise.

[4] P. Hynna, P. Klinge and J. Vuoksinen 1995 *Journal of Sound and Vibration* **180**(4), 583-607. Prediction of structure-borne sound transmission in large welded ship structures using statistical energy analysis.

[5] B. M. Gibbs and C. L. S. Gilford 1976 *Journal of Sound and Vibration* **49**(2), 267-286. The use of power flow methods for the assessment of sound transmission in building structures.

[6] G. Fraser 1998 *Ph.D. Thesis, Heriot-Watt University, Edinburgh, UK.* Structure-borne sound in motor-vehicles using Statistical Energy Analysis.

[7] T. Bharj, N. Lalor and G. Stimpson 2000 *European Conference on Vehicle Noise and Vibration 2000, London, UK, IMechE C577/016/2000*, 217-226. An experimental SEA model of a car constructed from very few measurements.

[8] J.C. Wohlever and R. J. Bernhard 1992 *Journal of Sound and Vibration* **153**, 1-19. Mechanical energy flow models of rods and beams.

[9] O. M. Bouthier and R. J. Bernhard 1995 *Journal of Sound and Vibration* **182**(1), 129-147. Simple models of energy flow in vibrating membranes.

[10] O. M. Bouthier and R. J. Bernhard 1995 *Journal of Sound and Vibration* **182**(1), 149-166. Simple models of the energetics of transversely vibrating plates.

[11] A. Carcaterra and A. Sestieri 1995 *Journal of Sound and Vibration* **188**(2), 269-282. Energy density equations and power flow in structures.

[12] F. Han, R. J. Bernhard and L. G. Mongeau 1997 *Journal of Sound and Vibration* **208**(5), 841-859. Energy flow analysis of vibrating beams and plates for discrete random excitations.

[13] F. Han, L. G. Mongeau and R. J. Bernhard 1998 *Journal of Fluids and Structures* **12**, 315-333. Energy flow analysis of beams and plates for random distributed loading.

[14] D.J. Nefke and S.H. Sung, 1987 *Statistical Energy Analysis, ASME Publication, NCA-3*, 47-54. Power flow finite element analysis of dynamics systems: basic theory and application to beams.

[15] N. Vlahopoulos, X. Zhao and T. Allen 1999 *Journal of Sound and Vibration* **220**(1), 135-154. An approach for evaluating power transfer coefficients for spot-welded joints in an energy finite element formulation.

[16] X. Zhao and N. Vlahopoulos 2000 *Journal of Sound and Vibration* **237**(2), 181-202. A hybrid finite element formulation for mid-frequency analysis of systems with excitation applied on short members.

[17] N. Vlahopoulos and X. Zhao 2001 *Journal of Sound and Vibration* **242**(3), 445-473. An investigation of power flow in the mid-frequency range for systems of co-linear beams based on a hybrid finite element formulation.

[18] R.S. Langley 1992 *Journal of Sound and Vibration* **159**, 483-502. A wave intensity technique for the analysis of high frequency vibrations.

[19] R. S. Langley and A. N. Bercin 1997 in *Statistical Energy Analysis; an Overview, with Applications in Structural Dynamics* (A. J. Keane and W. G. Price, editors), 59-69. Cambridge University Press. Originally published in Philosophical Transactions of the Royal Society of London, series A, volume 346, 429-554, (1994). Wave intensity analysis of high frequency vibrations.

[20] K. H. Heron 1997 in *Statistical Energy Analysis; an Overview, with Applications in Structural Dynamics* (A. J. Keane and W. G. Price, editors), 71-80. Cambridge University Press. Originally published in Philosophical Transactions of the Royal Society of London, series A, volume 346, 429-554, (1994). Advanced statistical energy analysis.

[21] L. Maxit and J.-L. Guyader 1999 *Proceedings of Sixth International Congress on Sound and Vibration, Copenhagen, Denmark*, 2257-2264. Statistical modal energy distribution analysis (S.M.E.D.A.).

[22] J.-L. Guyader 1999 *Proceedings of Sixth International Congress on Sound and Vibration, Copenhagen, Denmark*, 59-84. State of art of energy methods used for vibroacoustic prediction.

[23] A.J. Keane and W.G. Price (editors) 1997 *Statistical Energy Analysis: an Overview, with Applications in Structural Dynamics*, Cambridge University Press. Philosophical Transactions of the Royal Society of London, series A, volume 346, 429-554, Published by The Royal Society (1994).

[24] F.J. Fahy and W.G. Price (editors) 1999 *IUTAM Symposium on Statistical Energy Analysis*, Proceedings of the IUTAM Symposium held in Southampton, U.K., London: Kluwer Academic Publishers.

[25] SEANET 2000 BRITE/EURAM Thematic Network Project, BRRT-CT98-5088. First year activity report.

[26] SEANET 2001 BRITE/EURAM Thematic Network Project, BRRT-CT98-5088. Deliverable D2: Synthesis report.

[27] G. B. Warburton 1976 *The Dynamical Behaviour of Structures*. Oxford: Pergamon Press; second edition.

[28] R. S. Langley 1989 *Journal of Sound and Vibration* **135**(2), 319-331. Application of the dynamic stiffness method to the free and forced vibrations of aircraft panels.

[29] R. S. Langley 1990 *Journal of Sound and Vibration* **136**(3), 439-452. Analysis of power flow in beams and frameworks using the direct-dynamic stiffness method.

[30] R. S. Langley 1992 *Journal of Sound and Vibration* **156**(3), 521-540. A dynamic stiffness technique for the vibration analysis of stiffened shell structures.

[31] ESDU 1997 *Item No. 97033, ESDU International plc. London, UK.* Methods for analysis of the dynamic response of structures.

[32] R.H. Lyon and G. Maidanik 1962 *Journal of the Acoustical Society of America* **34**(5), 623-639. Power flow between linearly coupled oscillators.

[33] R. H. Lyon and R. G. DeJong 1995 *Theory and Application of Statistical Energy Analysis*. Boston: Butterworth-Heinemann; second edition.

[34] J. Woodhouse 1981 *Applied Acoustics* **14**, 455-469. An introduction to statistical energy analysis of structural vibration.

[35] C. B. Burroughs, R. W. Fisher and F. R. Kern 1997 *Journal of the Acoustical Society of America* **101**(4), 1779-1789. An introduction to statistical energy analysis.

[36] F. J. Fahy 1998 *Acoustics Bulletin March / April, 5-11.* An introduction to statistical energy analysis.

[37] F. J. Fahy 1997 in *Statistical Energy Analysis; an Overview, with Applications in Structural Dynamics* (A. J. Keane and W. G. Price, editors), 1-18. Cambridge University Press. Originally published in Philosophical Transactions of the Royal Society of London, series A, volume 346, 429-554, (1994). Statistical energy analysis: a critical overview.

[38] ESDU 1999 *Item No. 99009, ESDU International plc. London, UK.* An introduction to Statistical Energy Analysis.

[39] D.J. Thompson 2000 *Lecture Notes on MSc. Sound and Vibration Studies, ISVR, University of Southampton, Southampton, UK.* High frequency structural vibration.

[40] SEANET 2000 *BRITE/EURAM Thematic Network Project, BRRT-CT98-5088.* Statistical Energy Analysis: A guide for potential users.

[41] B. R. Mace 1993 *Journal of Sound and Vibration* **166**(3), 429-461. The statistical energy analysis of two continuous one-dimensional subsystems.

[42] F. J. Fahy and A. D. Mohammed 1992 *Journal of Sound and Vibration* **158**(1), 45-67. A study of uncertainty in application of SEA to coupled beam and plate systems, part I: Computational experiments.

[43] A. D. Mohammed 1990 *Ph.D. Thesis, University of Southampton, Southampton, UK.* A study of uncertainty in applications of Statistical Energy Analysis.

[44] R. J. M. Craik, J. A. Steel and D. I. Evans 1991 *Journal of Sound and Vibration* **144**(1), 95-107. Statistical energy analysis of structure-borne sound transmission at low frequencies.

[45] B. R. Mace 1992 *Journal of Sound and Vibration* **154**(2), 289-319. Power flow between two continuous one-dimensional subsystems: a wave solution.

[46] B. R. Mace 1992 *Journal of Sound and Vibration* **154**(2), 321-341. The statistics of power flow between two continuous one-dimensional subsystems.

[47] B. R. Mace 1992 *Journal of Sound and Vibration* **159**(2), 305-325. Power flow between two coupled beams.

[48] L. Cremer, M. Heckl and E. E. Ungar 1988 *Structure-borne Sound.* New York: Springer-Verlag; second edition.

[49] R. J. M. Craik 1996 Sound transmission through buildings using Statistical Energy Analysis. Gower Publishing Ltd.

[50] E. C. N. Wester and B. R. Mace 1996 *Journal of Sound and Vibration* **193**(4), 793-822. Statistical energy analysis of two edge-coupled rectangular plates: Ensemble averages.

[51] C. Simmons 1991 *Journal of Sound and Vibration* **144**(2), 215-227. Structure-borne sound transmission through plate junctions and estimates of SEA coupling loss factors using the finite element method.

[52] J. A. Steel and R. J. M. Craik 1994 *Journal of Sound and Vibration* **178**(4), 553-561. Statistical energy analysis of structure-borne sound transmission by finite element methods.

[53] C. R. Fredo 1997 *Journal of Sound and Vibration* **199**(4), 645-666. A SEA-like approach for the derivation of energy flow coefficients with a finite element model.

[54] L. Maxit and J.-L. Guyader 2001 *Journal of Sound and Vibration* **239**(5), 907-930. Estimation of SEA coupling loss factors using a dual formulation and FEM modal information, part I: Theory.

[55] D. Karnopp 1966 *Journal of the Acoustical Society of America* **40**, 380-384. Coupled vibratory-system analysis, using the dual formulation.

[56] L. Maxit and J.-L. Guyader 2001 *Journal of Sound and Vibration* **239**(5), 931-948. Estimation of SEA coupling loss factors using a dual formulation and FEM modal information, part II: Numerical applications.

[57] D. A. Bies and S. Hamid 1980 *Journal of Sound and Vibration* **70**(2), 187-204. *In Situ* determination of loss and coupling loss factors by the power injection method.

[58] F. F. Yap and J. Woodhouse 1996 *Journal of Sound and Vibration* **197**(3), 351-371. Investigation of damping effects on statistical energy analysis of coupled structures.

[59] E. Skudrzyk 1980 *Journal of the Acoustical Society of America* **67**(4), 1105-1135. The mean-value method of predicting the dynamic response of complex vibrations.

[60] R.S. Langley and K.H. Heron 1990 *Journal of Sound and Vibration* **143**, 241-253. Elastic wave transmission through plate/beam junctions.

[61] H. Nishino and M. Ohlrich 2000 *Proceedings of NOVEM Conference, Lyon, France*. Prediction of medium frequency vibration by wave intensity analysis.

[62] A. Carcaterra and L. Adamo 1996 *Structural Acoustics Energy Methods in Vibro-acoustics – V School, Zakopane Poland*, 41-51. Wave energy propagation in vibrating systems, part I: theory.

[63] A. Carcaterra and L. Adamo 1996 *Structural Acoustics Energy Methods in Vibro-acoustics – V School, Zakopane Poland*, 53-65. Wave energy propagation in vibrating systems, part II: experiments.

[64] R.S. Langley 1995 *Journal of Sound and Vibration* **182**(4), 637-657. On the vibrational conductivity approach to high frequency dynamics for two-dimensional structural components.

[65] C. Soize 1993 *Journal of the Acoustical Society of America* **94**, 849-865. A model and numerical method in the medium frequency range for vibroacoustic predictions using the theory of structural fuzzy.

[66] R.S. Langley and P.G. Bremner 1999 *Journal of the Acoustical Society of America* **105**, 1657-1671. A hybrid method for the vibration analysis of complex structural-acoustic systems.

[67] S. Finnveden 1997 *Journal of Sound and Vibration* **199**(1), 125-154. Spectral finite element analysis of the vibration of straight fluid-filled pipes with flanges.

[68] F. Birgersson 2000 *MSc. Thesis, ISVR, The University of Southampton, Southampton, UK*. Modelling with the dynamic stiffness and the spectral finite element methods for distributed sources.

[69] S. Finnveden, F. Birgersson and N.S. Ferguson 2001 *Proceedings of Inter-noise 2001, The Hague, The Netherlands*. Modelling with the spectral FEM for turbulence excitation of cylindrical pipes.

[70] K.M. Ahmida and J.R.F. Arruda 2001 *International Journal of Solids and Structures* 38 1669-1679. Spectral element-based prediction of active power flow in Timoshenko beams.

[71] C. Boisson, J.-L. Guyader, P. Millot and C. Lesueur 1982 *Journal of Sound and Vibration* **81**(1), 93-105. Energy transmission in finite coupled plates, part II: application to an L shaped structure.

[72] A. Biran and M. Breiner 1995 *MATLAB for Engineers*. Addison-Wesley Publishing Company Inc.

[73] The Math Works, Inc. 1995 The Student Edition of MATLAB, Version 4 User's Guide.

[74] S. Timoshenko and S. Woinowsky-Krieger 1959 *Theory of Plates and Shells*. New York: McGraw-Hill; second edition.

[75] D. J. Mead 1982 in *Noise and Vibration* (R.G. White and J.G. Walker editors). Chapter 9: Structural wave motion. Chichester: Ellis Horwood.

[76] P. G. Craven and B. M. Gibbs 1981 *Journal of Sound and Vibration* **77**(3), 417-427. Sound transmission and mode coupling at junctions of thin plates, part I: representation of the problem.

[77] A. N. Bercin and R. S. Langley 1996 *Computers & Structures* **59(5)**, 869-875. Application of the Dynamic Stiffness Technique to the In-plane Vibrations of Plate Structures.

[78] R. Szilard 1974 *Theory and Analysis of Plates: Classical and Numerical Methods*. New Jersey: Pretice-Hall, Inc.

[79] W. S. Park, D. J. Thompson and N. S. Ferguson 1999 *ISVR Technical Memorandum* No.846, *ISVR, University of Southampton, Southampton, UK.* The power balance of beams and plates using the Dynamic Stiffness Method.

[80] D. J. Gorman 1982 *Free Vibration Analysis of Rectangular Plates*. New York: Elsevier.

[81] E. Eichler 1964 *Journal of the Acoustical Society of America* **36**(2), 344-348. Plate-edge admittance.

[82] C. Kauffmann 1998 *Journal of the Acoustical Society of America* **103**(4), 1874-1884. Input mobilities and power flows for edge-excited, semi-infinite plates.

[83] A. N. Bercin 1996 *Journal of Sound and Vibration* **191**(5), 661-680. An assessment of the effects of in-plane vibrations on the energy flow between coupled plates.

[84] R. H. Lyon 1986 *Noise Control Engineering Journal* **26**(1), 22-27. In-plane contribution to structural noise transmission.

[85] B. R. Mace 1994 *Journal of Sound and Vibration* **178**(1), 95-112. On the statistical energy analysis hypothesis of coupling power proportionality and some implications of its failure.

[86] W. S. Park, D. J. Thompson and N. S. Ferguson 2000 *ISVR Technical Memorandum* No.856, *ISVR, University of Southampton, Southampton, UK.* Sources of error and confidence intervals for SEA parameters of two coupled rectangular plates.

[87] E. Sarradj 2000 *Proceedings of NOVEM 2000, Lyon, France (CD-ROM).* The uncertain relationship between transmission coefficient and coupling loss factor.

[88] P.W. Smith, Jr. 1979 *Journal of the Acoustical Society of America* **65**(3), 695-698. Statistical models of coupled dynamical systems and the transition from weak to strong coupling.

[89] A.T. Moorhouse and B.M. Gibbs 1995 *Applied Acoustics* **45** 227-245. Calculation of the mean and maximum mobility for concrete floors.

[90] E. Kreyszig 1979 *Advanced Engineering Mathematics Volume I & II.* John Wiley & Sons Inc.; fourth edition.

[91] G.W. Snedecor and W.G. Cochran 1967 *Statistical methods.* The Iowa State University Press; 6th edition.

[92] M. Fogiel 1978 *The statistics problem solver.* Research and Education Association.

[93] B.M. Gibbs and Y. Shen 1987 *Journal of Sound and Vibration* **112**(3), 469-485. The predicted and measured bending vibration of an L-combination of rectangular thin plates.

[94] I. Boorer 2001 *Undergraduate Project, ISVR, University of Southampton, Southampton, UK.* An investigation into the variability of experimental statistical energy analysis evaluation.

[95] T.P. Krauss, L. Shure and J.N. Little 1994 *Signal Processing Toolbox User's Guide.* The Math Works, Inc.

[96] N.S. Ferguson 2000 *Lecture Notes on MSc. Sound and Vibration Studies, ISVR, University of Southampton, Southampton, UK.* Advanced Measurement Techniques - Statistical Energy Analysis Laboratory.

APPENDIX A.

ANALYTICAL INTEGRATION OF STRAIN ENERGY

In calculating the energy of each plate, an analytical integration has been performed to give good accuracy. The displacements and their derivatives are obtained from the dynamic stiffness approach.

A.1. The strain energy for flexural vibration

The strain energy for flexural vibration is given by [27]

$$E_{strain,f} = \frac{D}{2}\int_0^b \int_0^L \left[\left(\frac{\partial^2 w}{\partial x^2} \right)^2 + \left(\frac{\partial^2 w}{\partial y^2} \right)^2 + 2\mu \frac{\partial^2 w}{\partial x^2}\frac{\partial^2 w}{\partial y^2} + 2(1-\mu)\left(\frac{\partial^2 w}{\partial x \partial y} \right)^2 \right] dxdy \qquad \text{(A.1)}$$

where D is the flexural rigidity ($= Eh^3/12(1\text{-}\mu^2)$, E is the Young's modulus, h is the thickness of the plate, μ is the Poisson's ratio, respectively), b is the width of the plate, L is the length of the plate and w is the out-of-plane deflection amplitude which is a real value dependent on time t. Equation (A.1) represents the instantaneous strain energy in a cycle.

The time averaged strain energy is given by

$$\overline{E}_{strain,f} = \frac{1}{T}\int_0^T E_{strain,f}(t)dt\,. \qquad \text{(A.2)}$$

Each term in the strain energy oscillates at frequency 2ω from 0 to maximum at each location. Different locations may have their maximum value at different times, but the time integral $\int dt$ can be taken inside the $\iint dxdy$. Then the four terms can be evaluated separately, *e.g.* for the first term

$$\begin{aligned} \frac{1}{T}\int_0^T \left[\int_0^b \int_0^L \left(\frac{\partial^2 w}{\partial x^2} \right)^2 dxdy \right] dt &= \int_0^b \int_0^L \left[\frac{1}{T}\int_0^T \left(\frac{\partial^2 w}{\partial x^2} \right)^2 dt \right] dxdy \\ &= \frac{1}{2}\int_0^b \int_0^L \left| \frac{\partial^2 W_n}{\partial x^2} \right|^2 dxdy \end{aligned} \qquad \text{(A.3)}$$

where W_n is the out-of-plane displacement amplitude. For a rectangular plate which is simply supported along two opposite edges (see Figure 2.1), W_n may be taken to be of the form

$$W_n(x,y) = \sum_{n=1}^{n_{\max}} \sum_{m=1}^{4} A_{nm} e^{k_{nm}x} \sin(k_n y) \tag{A.4}$$

where the complex A_{nm} terms are four unknown constants of integration, which can be found by ensuring that the solution satisfies the boundary conditions at the ends. The k_{nm} terms are the four complex trace wavenumbers in the x direction, k_n ($=n\pi y/b$) is the trace wavenumber in the y direction and n is the number of half-sine waves along the transverse edge.

The first term of the integral in equation (A.1) can be rewritten in the form

$$\frac{1}{2}\int_0^b \int_0^L \left| \frac{\partial^2 W_n}{\partial x^2} \right|^2 dxdy = \frac{1}{2}\int_0^b \int_0^L \left(\frac{\partial^2 W_n}{\partial x^2} \right) \left(\frac{\partial^2 W_n}{\partial x^2} \right)^* dxdy \tag{A.5}$$

where
$$\frac{\partial^2 W_n}{\partial x^2} = \sum_{n=1}^{n_{\max}} \sum_{m=1}^{4} A_{nm} k_{nm}^2 e^{k_{nm}x} \sin(k_n y) \tag{A.6}$$

and * denotes the complex conjugate.

Substituting equation (A.6) into equation (A.5),

$$\begin{aligned} &\frac{1}{2}\int_0^b \int_0^L \left[\left(\sum_n \sum_m A_{nm} k_{nm}^2 e^{k_{nm}x} \right) \left(\sum_{n'} \sum_{m'} A_{n'm'}^* k_{n'm'}^{*2} e^{k_{n'm'}^* x} \right) \sin(k_n y) \sin(k_{n'} y) \right] dxdy \\ &= \frac{b}{4} \sum_n \sum_m \sum_{m'} \frac{A_{nm} A_{nm'}^* k_{nm}^2 k_{nm'}^{*2}}{k_{nm} + k_{nm'}^*} \left\{ e^{(k_{nm}+k_{nm'}^*)L} - 1 \right\} \end{aligned} \tag{A.7}$$

where $\int_0^b \sin(k_n y) \sin(k_{n'} y)\, dy = \frac{b}{2}$ if $n = n'$, and 0 if $n \neq n'$.

The second term of the integral in equation (A.1) can be rewritten as

$$\frac{1}{2}\int_0^b \int_0^L \left| \frac{\partial^2 W_n}{\partial y^2} \right|^2 dxdy = \frac{1}{2}\int_0^b \int_0^L \left(\frac{\partial^2 W_n}{\partial y^2} \right) \left(\frac{\partial^2 W_n}{\partial y^2} \right)^* dxdy \tag{A.8}$$

where
$$\frac{\partial^2 W_n}{\partial y^2} = -\sum_{n=1}^{n_{\max}} \sum_{m=1}^{4} k_n^2 A_{nm} e^{k_{nm}x} \sin(k_n y). \tag{A.9}$$

Substituting equation (A.9) into equation (A.8),

$$\begin{aligned}&\frac{1}{2}\int_0^b\int_0^L\left[\left(-\sum_n\sum_m k_n^2 A_{nm}e^{k_{nm}x}\right)\left(-\sum_{n'}\sum_{m'} k_n^2 A_{n'm'}^{*}e^{k_{nm}x}\right)\sin(k_n y)\sin(k_{n'}y)\right]dxdy\\&=\frac{b}{4}\sum_n\sum_m\sum_{m'}\frac{k_n^4 A_{nm}A_{nm'}^{*}}{k_{nm}+k_{nm'}^{*}}\left\{e^{(k_{nm}+k_{nm'}^{*})L}-1\right\}.\end{aligned} \tag{A.10}$$

The third term of the integral in equation (A.1) can be rewritten as

$$\mu\int_0^b\int_0^L \mathrm{Re}\left[\left(\frac{\partial^2 W_n}{\partial x^2}\right)\left(\frac{\partial^2 W_n}{\partial y^2}\right)^{*}\right]dxdy. \tag{A.11}$$

Substituting equations (A.6) and (A.9) into equation (A.11),

$$\begin{aligned}&\mu\int_0^b\int_0^L \mathrm{Re}\left[\left(\sum_n\sum_m A_{nm}k_{nm}^2 e^{k_{nm}x}\right)\left(-\sum_{n'}\sum_{m'} k_{n'}^2 A_{n'm'}^{*}e^{k_{n'm'}x}\right)\sin(k_n y)\sin(k_{n'}y)\right]dxdy\\&=-\frac{b\mu}{2}\sum_n\sum_m\sum_{m'}k_n^2\,\mathrm{Re}\left[\frac{A_{nm}A_{nm'}^{*}k_{nm}^2}{k_{nm}+k_{nm'}^{*}}\left\{e^{(k_{nm}+k_{nm'}^{*})L}-1\right\}\right].\end{aligned} \tag{A.12}$$

The last term of the integral in equation (A.1) can be rewritten as

$$(1-\mu)\int_0^b\int_0^L\left|\frac{\partial^2 W_n}{\partial x\partial y}\right|^2 dxdy=(1-\mu)\int_0^b\int_0^L\left(\frac{\partial^2 W_n}{\partial x\partial y}\right)\left(\frac{\partial^2 W_n}{\partial x\partial y}\right)^{*}dxdy \tag{A.13}$$

where

$$\frac{\partial^2 W_n}{\partial x\partial y}=\sum_{n=1}^{n_{\max}}\sum_{m=1}^{4}k_n A_{nm}k_{nm}e^{k_{nm}x}\cos(k_n y). \tag{A.14}$$

Substituting equation (A.14) into equation (A.13),

$$\begin{aligned}&(1-\mu)\int_0^b\int_0^L\left[\left(\sum_n\sum_m k_n A_{nm}k_{nm}e^{k_{nm}x}\right)\left(\sum_{n'}\sum_{m'}k_{n'}A_{n'm'}^{*}k_{n'm'}^{*}e^{k_{n'm'}^{*}x}\right)\cos(k_n y)\cos(k_{n'}y)\right]dxdy\\&=\frac{b(1-\mu)}{2}\sum_n\sum_m\sum_{m'}\frac{k_n^2 A_{nm}A_{nm'}^{*}k_{nm}k_{nm'}^{*}}{k_{nm}+k_{nm'}^{*}}\left\{e^{(k_{nm}+k_{nm'}^{*})L}-1\right\}.\end{aligned} \tag{A.15}$$

The time averaged strain energy for flexural vibration can be obtained analytically from equations (A.7), (A.10), (A.12) and (A.15). Therefore, the maximum strain energy $(E_{strain,f})_{\max}$ which is twice the time averaged strain energy, is given by

$$
\begin{aligned}
(E_{strain\ f})_{\max} = \frac{Db}{4}\Bigg[& \sum_{n}\sum_{m}\sum_{m'} \frac{A_{nm}A_{nm'}k_{nm}^{2}k_{nm'}^{*2}}{k_{nm}+k_{nm'}^{*}}\left\{e^{(k_{nm}+k_{nm}^{*})L}-1\right\}+ \\
& \sum_{n}\sum_{m}\sum_{m'} \frac{k_{n}^{4}A_{nm}A_{nm'}^{*}}{k_{nm}+k_{nm'}^{*}}\left\{e^{(k_{nm}+k_{nm'}^{*})L}-1\right\}- \\
& 2\mu\sum_{n}\sum_{m}\sum_{m'} k_{n}^{2}\,\mathrm{Re}\left[\frac{A_{nm}A_{nm'}^{*}k_{nm}^{2}}{k_{nm}+k_{nm'}^{*}}\left\{e^{(k_{nm}+k_{nm'}^{*})L}-1\right\}\right]+ \\
& 2(1-\mu)\sum_{n}\sum_{m}\sum_{m'} \frac{k_{n}^{2}A_{nm}A_{nm'}^{*}k_{nm}k_{nm'}^{*}}{k_{nm}+k_{nm'}^{*}}\left\{e^{(k_{nm}+k_{nm'}^{*})L}-1\right\}\Bigg] \\
= \frac{Db}{4}\mathrm{Re} & \left(\sum_{n}\sum_{m}\sum_{m'} \frac{A_{nm}A_{nm'}^{*}}{k_{nm}+k_{nm'}^{*}}\left\{e^{(k_{nm}+k_{nm'}^{*})L}-1\right\}\left\{\begin{matrix} k_{nm}^{2}k_{nm'}^{*2}+k_{n}^{4}+2\mu k_{nm}^{2}+ \\ 2(1-\mu)k_{n}^{2}k_{nm}k_{nm'}^{*} \end{matrix}\right\}\right).
\end{aligned}
\tag{A.16}
$$

A.2. The strain energy for in-plane vibration

The instantaneous strain energy for in-plane vibration is given by [27]

$$
E_{strain,i} = \frac{Eh}{2(1-\mu^{2})}\int_{0}^{b}\int_{0}^{L}\left[\left(\frac{\partial u}{\partial x}\right)^{2}+\left(\frac{\partial v}{\partial y}\right)^{2}+2\mu\frac{\partial u}{\partial x}\frac{\partial v}{\partial y}+\frac{(1-\mu)}{2}\left(\frac{\partial u}{\partial y}+\frac{\partial v}{\partial x}\right)^{2}\right]dxdy \tag{A.17}
$$

where u and v are the longitudinal and transverse deflection, respectively, which are real valued functions of t.

If the boundary conditions are simply-supported along the longitudinal edges, the in-plane deflections, the longitudinal deflection U and the transverse deflection V, may be written as [76]

$$
U_{n}(x,y)=\sum_{n=1}^{n_{\max}}\left\{\begin{bmatrix}\lambda_{n1} & \lambda_{n2}\end{bmatrix}\begin{bmatrix}C_{n1}e^{\lambda_{n1}x} \\ C_{n2}e^{\lambda_{n2}x}\end{bmatrix}+\begin{bmatrix}k_{n} & k_{n}\end{bmatrix}\begin{bmatrix}C_{n3}e^{\lambda_{n3}x} \\ C_{n4}e^{\lambda_{n4}x}\end{bmatrix}\right\}\sin(k_{n}y) \tag{A.18}
$$

$$
V_{n}(x,y)=\sum_{n=1}^{n_{\max}}\left\{\begin{bmatrix}k_{n} & k_{n}\end{bmatrix}\begin{bmatrix}C_{n1}e^{\lambda_{n1}x} \\ C_{n2}e^{\lambda_{n2}x}\end{bmatrix}+\begin{bmatrix}\lambda_{n3} & \lambda_{n4}\end{bmatrix}\begin{bmatrix}C_{n3}e^{\lambda_{n3}x} \\ C_{n4}e^{\lambda_{n4}x}\end{bmatrix}\right\}\cos(k_{n}y) \tag{A.19}
$$

where the complex C_{nr} terms are four unknown constants of integration. The λ_{nr} terms are determined by

$$
\lambda_{n1,n2}=\pm\sqrt{k_{n}^{2}-k_{L}^{2}} \quad \text{and} \quad \lambda_{n3,n4}=\pm\sqrt{k_{n}^{2}-k_{T}^{2}} \tag{A.20}
$$

where $k_{L}^{2}=\rho\omega^{2}(1-\mu^{2})/E$ and $k_{T}^{2}=2\rho\omega^{2}(1+\mu)/E$.

The four terms in equation (A.17) can be evaluated separately by taking the time average, as described in Section A.1.

The first term of the integral in equation (A.17) can be rewritten as

$$\frac{1}{2}\int_0^b\int_0^L\left|\frac{\partial U_n}{\partial x}\right|^2 dxdy=\frac{1}{2}\int_0^b\int_0^L\left(\frac{\partial U_n}{\partial x}\right)\left(\frac{\partial U_n}{\partial x}\right)^* dxdy \tag{A.21}$$

where $$\frac{\partial U_n}{\partial x}=\sum_{n=1}^{n_{\max}}\left\{\begin{bmatrix}\lambda_{n1} & \lambda_{n2}\end{bmatrix}\begin{bmatrix}C_{n1}\lambda_{n1}e^{\lambda_{n1}x}\\ C_{n2}\lambda_{n2}e^{\lambda_{n2}x}\end{bmatrix}+\begin{bmatrix}k_n & k_n\end{bmatrix}\begin{bmatrix}C_{n3}\lambda_{n3}e^{\lambda_{n3}x}\\ C_{n4}\lambda_{n4}e^{\lambda_{n4}x}\end{bmatrix}\right\}\sin(k_n y) \tag{A.22}$$

and $*$ denotes the complex conjugate.

Substituting equation (A.22) into equation (A.21),

$$\begin{aligned}
&\frac{1}{2}\int_0^b\int_0^L\Bigg[\left\{\sum_n\left(C_{n1}\lambda_{n1}^2e^{\lambda_{n1}x}+C_{n2}\lambda_{n2}^2e^{\lambda_{n2}x}+k_nC_{n3}\lambda_{n3}e^{\lambda_{n3}x}+k_nC_{n4}\lambda_{n4}e^{\lambda_{n4}x}\right)\right\}\\
&\qquad\left\{\sum_{n'}\left(C_{n'1}^*\lambda_{n'1}^{*2}e^{\lambda_{n'1}^*x}+C_{n'2}^*\lambda_{n'2}^{*2}e^{\lambda_{n'2}^*x}+k_{n'}C_{n'3}^*\lambda_{n'3}^*e^{\lambda_{n'3}^*x}+k_{n'}C_{n'4}^*\lambda_{n'4}^*e^{\lambda_{n'4}^*x}\right)\right\}\sin(k_ny)\sin(k_{n'}y)\Bigg]dxdy\\
&=\frac{b}{4}\sum_n\Bigg[\left|C_{n1}\right|^2\left|\lambda_{n1}\right|^4\frac{\mathrm{e}^{2\mathrm{Re}(\lambda_{n1})L}-1}{2\mathrm{Re}(\lambda_{n1})}+\left|C_{n2}\right|^2\left|\lambda_{n2}\right|^4\frac{\mathrm{e}^{2\mathrm{Re}(\lambda_{n2})L}-1}{2\mathrm{Re}(\lambda_{n2})}+\\
&\qquad k_n^2\left|C_{n3}\right|^2\left|\lambda_{n3}\right|^4\frac{\mathrm{e}^{2\mathrm{Re}(\lambda_{n3})L}-1}{2\mathrm{Re}(\lambda_{n3})}+k_n^2\left|C_{n4}\right|^2\left|\lambda_{n4}\right|^4\frac{\mathrm{e}^{2\mathrm{Re}(\lambda_{n4})L}-1}{2\mathrm{Re}(\lambda_{n4})}+\\
&\qquad 2\mathrm{Re}\Bigg\{C_{n1}C_{n2}^*\lambda_{n1}^2\lambda_{n2}^{*2}\frac{\mathrm{e}^{(\lambda_{n1}+\lambda_{n2}^*)L}-1}{\lambda_{n1}+\lambda_{n2}^*}+C_{n1}C_{n3}^*\lambda_{n1}^2\lambda_{n3}^*k_n\frac{\mathrm{e}^{(\lambda_{n1}+\lambda_{n3}^*)L}-1}{\lambda_{n1}+\lambda_{n3}^*}+\\
&\qquad\qquad C_{n1}C_{n4}^*\lambda_{n1}^2\lambda_{n4}^*k_n\frac{\mathrm{e}^{(\lambda_{n1}+\lambda_{n4}^*)L}-1}{\lambda_{n1}+\lambda_{n4}^*}+C_{n2}C_{n3}^*\lambda_{n2}^2\lambda_{n3}^*k_n\frac{\mathrm{e}^{(\lambda_{n2}+\lambda_{n3}^*)L}-1}{\lambda_{n2}+\lambda_{n3}^*}+\\
&\qquad\qquad C_{n2}C_{n4}^*\lambda_{n2}^2\lambda_{n4}^*k_n\frac{\mathrm{e}^{(\lambda_{n2}+\lambda_{n4}^*)L}-1}{\lambda_{n2}+\lambda_{n4}^*}+C_{n3}C_{n4}^*\lambda_{n3}\lambda_{n4}^*k_n^2\frac{\mathrm{e}^{(\lambda_{n3}+\lambda_{n4}^*)L}-1}{\lambda_{n3}+\lambda_{n4}^*}\Bigg\}\Bigg].
\end{aligned} \tag{A.23}$$

where $\int_0^b\sin(k_ny)\sin(k_{n'}y)\,dy=\frac{b}{2}$ if $n = n'$.

The second term of the integral in equation (A.17) can be rewritten as

$$\frac{1}{2}\int_0^b\int_0^L\left|\frac{\partial V_n}{\partial y}\right|^2 dxdy=\frac{1}{2}\int_0^b\int_0^L\left(\frac{\partial V_n}{\partial y}\right)\left(\frac{\partial V_n}{\partial y}\right)^* dxdy \tag{A.24}$$

where $$\frac{\partial V_n}{\partial y} = -\sum_{n=1}^{n_{\max}} k_n \left\{ \begin{bmatrix} k_n & k_n \end{bmatrix} \begin{bmatrix} C_{n1} e^{\lambda_{n1} x} \\ C_{n2} e^{\lambda_{n2} x} \end{bmatrix} + \begin{bmatrix} \lambda_{n3} & \lambda_{n4} \end{bmatrix} \begin{bmatrix} C_{n3} e^{\lambda_{n3} x} \\ C_{n4} e^{\lambda_{n4} x} \end{bmatrix} \right\} \sin(k_n y)\,. \tag{A.25}$$

Substituting equation (A.25) into equation (A.24),

$$\begin{aligned}
&\frac{1}{2}\int_0^b \int_0^L \Bigg[k_n^2 \left\{ \sum_n \left(k_n C_{n1} e^{\lambda_{n1} x} + k_n C_{n2} e^{\lambda_{n2} x} + C_{n3} \lambda_{n3} e^{\lambda_{n3} x} + C_{n4} \lambda_{n4} e^{\lambda_{n4} x} \right) \right\} \\
&\qquad \left\{ \sum_{n'} \left(k_{n'} C^*_{n'1} e^{\lambda^*_{n'1} x} + k_{n'} C^*_{n'2} e^{\lambda^*_{n'2} x} + C^*_{n'3} \lambda^*_{n'3} e^{\lambda^*_{n'3} x} + C^*_{n'4} \lambda^*_{n'4} e^{\lambda^*_{n'4} x} \right) \right\} \sin(k_n y) \sin(k_{n'} y) \Bigg] dxdy \\
&= \frac{b}{4} \sum_n k_n^2 \Bigg[k_n^2 \left| C_{n1} \right|^2 \frac{\mathrm{e}^{2\mathrm{Re}(\lambda_{n1})L} - 1}{2\mathrm{Re}(\lambda_{n1})} + k_n^2 \left| C_{n2} \right|^2 \frac{\mathrm{e}^{2\mathrm{Re}(\lambda_{n2})L} - 1}{2\mathrm{Re}(\lambda_{n2})} + \\
&\qquad \left| C_{n3} \right|^2 \left| \lambda_{n3} \right|^2 \frac{\mathrm{e}^{2\mathrm{Re}(\lambda_{n3})L} - 1}{2\mathrm{Re}(\lambda_{n3})} + \left| C_{n4} \right|^2 \left| \lambda_{n4} \right|^2 \frac{\mathrm{e}^{2\mathrm{Re}(\lambda_{n4})L} - 1}{2\mathrm{Re}(\lambda_{n4})} + \\
&\qquad 2\mathrm{Re} \Bigg\{ k_n^2 C_{n1} C^*_{n2} \frac{\mathrm{e}^{(\lambda_{n1} + \lambda^*_{n2})L} - 1}{\lambda_{n1} + \lambda^*_{n2}} + k_n C_{n1} C^*_{n3} \lambda^*_{n3} \frac{\mathrm{e}^{(\lambda_{n1} + \lambda^*_{n3})L} - 1}{\lambda_{n1} + \lambda^*_{n3}} + \\
&\qquad\qquad k_n C_{n1} C^*_{n4} \lambda^*_{n4} \frac{\mathrm{e}^{(\lambda_{n1} + \lambda^*_{n4})L} - 1}{\lambda_{n1} + \lambda^*_{n4}} + k_n C_{n2} C^*_{n3} \lambda^*_{n3} \frac{\mathrm{e}^{(\lambda_{n2} + \lambda^*_{n3})L} - 1}{\lambda_{n2} + \lambda^*_{n3}} + \\
&\qquad\qquad k_n C_{n2} C^*_{n4} \lambda^*_{n4} \frac{\mathrm{e}^{(\lambda_{n2} + \lambda^*_{n4})L} - 1}{\lambda_{n2} + \lambda^*_{n4}} + C_{n3} C^*_{n4} \lambda_{n3} \lambda^*_{n4} \frac{\mathrm{e}^{(\lambda_{n3} + \lambda^*_{n4})L} - 1}{\lambda_{n3} + \lambda^*_{n4}} \Bigg\} \Bigg].
\end{aligned} \tag{A.26}$$

The third term of the integral in equation (A.17) can be rewritten as

$$\mu \int_0^b \int_0^L \mathrm{Re} \left\{ \left(\frac{\partial U_n}{\partial x} \right) \left(\frac{\partial V_n}{\partial y} \right)^* \right\} dxdy\,. \tag{A.27}$$

Substituting equations (A.22) and (A.25) into equation (A.27),

$$
\begin{aligned}
&\mu\int_0^b\int_0^L\Bigg[\Bigg\{\sum_n\Big(C_{n1}\lambda_{n1}^2e^{\lambda_{n1}x}+C_{n2}\lambda_{n2}^2e^{\lambda_{n2}x}+k_nC_{n3}\lambda_{n3}e^{\lambda_{n3}x}+k_nC_{n4}\lambda_{n4}e^{\lambda_{n4}x}\Big)\Bigg\}\\
&\qquad\Bigg\{\sum_{n'}(-k_{n'})\Big(k_{n'}C_{n'1}^*e^{\lambda_{n'1}^*x}+k_{n'}C_{n'2}^*e^{\lambda_{n'2}^*x}+C_{n'3}^*\lambda_{n'3}^*e^{\lambda_{n'3}^*x}+C_{n'4}^*\lambda_{n'4}^*e^{\lambda_{n'4}^*x}\Big)\Bigg\}\sin(k_ny)\sin(k_{n'}y)\Bigg]dxdy\\
&=-\frac{\mu b}{2}\sum_n k_n\,\mathrm{Re}\Bigg[\left|C_{n1}\right|^2\lambda_{n1}^2k_n\frac{\mathrm{e}^{2\mathrm{Re}(\lambda_{n1})L}-1}{2\mathrm{Re}\left(\lambda_{n1}\right)}+\left|C_{n2}\right|^2\lambda_{n2}^2k_n\frac{\mathrm{e}^{2\mathrm{Re}(\lambda_{n2})L}-1}{2\mathrm{Re}\left(\lambda_{n2}\right)}+\\
&\qquad\left|C_{n3}\right|^2\left|\lambda_{n3}\right|^2k_n\frac{\mathrm{e}^{2\mathrm{Re}(\lambda_{n3})L}-1}{2\mathrm{Re}\left(\lambda_{n3}\right)}+\left|C_{n4}\right|^2\left|\lambda_{n4}\right|^2k_n\frac{\mathrm{e}^{2\mathrm{Re}(\lambda_{n4})L}-1}{2\mathrm{Re}\left(\lambda_{n4}\right)}+\\
&\qquad C_{n1}C_{n2}^*\lambda_{n1}^2k_n\frac{\mathrm{e}^{\left(\lambda_{n1}+\lambda_{n2}^*\right)L}-1}{\lambda_{n1}+\lambda_{n2}^*}+C_{n1}C_{n3}^*\lambda_{n1}^2\lambda_{n3}^*\frac{\mathrm{e}^{\left(\lambda_{n1}+\lambda_{n3}^*\right)L}-1}{\lambda_{n1}^*+\lambda_{n3}^*}+\\
&\qquad C_{n1}C_{n4}^*\lambda_{n1}^2\lambda_{n4}^*\frac{\mathrm{e}^{\left(\lambda_{n1}+\lambda_{n4}^*\right)L}-1}{\lambda_{n1}+\lambda_{n4}^*}+C_{n2}C_{n1}^*\lambda_{n2}^2k_n\frac{\mathrm{e}^{\left(\lambda_{n2}+\lambda_{n1}^*\right)L}-1}{\lambda_{n2}+\lambda_{n1}^*}+\\
&\qquad C_{n2}C_{n3}^*\lambda_{n2}^2\lambda_{n3}^*\frac{\mathrm{e}^{\left(\lambda_{n2}+\lambda_{n3}^*\right)L}-1}{\lambda_{n2}+\lambda_{n3}^*}+C_{n2}C_{n4}^*\lambda_{n2}^2\lambda_{n4}^*\frac{\mathrm{e}^{\left(\lambda_{n2}+\lambda_{n4}^*\right)L}-1}{\lambda_{n2}+\lambda_{n4}^*}+\\
&\qquad C_{n3}C_{n1}^*\lambda_{n3}k_n^2\frac{\mathrm{e}^{\left(\lambda_{n3}+\lambda_{n1}^*\right)L}-1}{\lambda_{n3}+\lambda_{n1}^*}+C_{n3}C_{n2}^*\lambda_{n3}k_n^2\frac{\mathrm{e}^{\left(\lambda_{n3}+\lambda_{n2}^*\right)L}-1}{\lambda_{n3}+\lambda_{n2}^*}+\\
&\qquad C_{n3}C_{n4}^*\lambda_{n3}\lambda_{n4}^*k_n\frac{\mathrm{e}^{\left(\lambda_{n3}+\lambda_{n4}^*\right)L}-1}{\lambda_{n3}+\lambda_{n4}^*}+C_{n4}C_{n1}^*\lambda_{n4}k_n^2\frac{\mathrm{e}^{\left(\lambda_{n4}+\lambda_{n1}^*\right)L}-1}{\lambda_{n4}+\lambda_{n1}^*}+\\
&\qquad C_{n4}C_{n2}^*\lambda_{n4}k_n^2\frac{\mathrm{e}^{\left(\lambda_{n4}+\lambda_{n2}^*\right)L}-1}{\lambda_{n4}+\lambda_{n2}^*}+C_{n4}C_{n3}^*\lambda_{n4}\lambda_{n3}^*k_n\frac{\mathrm{e}^{\left(\lambda_{n4}+\lambda_{n3}^*\right)L}-1}{\lambda_{n4}+\lambda_{n3}^*}\Bigg\}\Bigg]
\end{aligned}
\tag{A.28}
$$

The last term of the integral in equation (A.17) can be rewritten as

$$
\frac{(1-\mu)}{4}\int_0^b\int_0^L\left|\frac{\partial U_n}{\partial y}+\frac{\partial V_n}{\partial x}\right|^2dxdy=\frac{(1-\mu)}{4}\int_0^b\int_0^L\left(\frac{\partial U_n}{\partial y}+\frac{\partial V_n}{\partial x}\right)\left(\frac{\partial U_n}{\partial y}+\frac{\partial V_n}{\partial x}\right)^*dxdy \tag{A.29}
$$

where
$$
\frac{\partial U_n}{\partial y}=\sum_{n=1}^{n_{\max}}k_n\left\{\begin{bmatrix}\lambda_{n1} & \lambda_{n1}\end{bmatrix}\begin{bmatrix}C_{n1}e^{\lambda_{n1}x}\\ C_{n2}e^{\lambda_{n2}x}\end{bmatrix}+\begin{bmatrix}k_n & k_n\end{bmatrix}\begin{bmatrix}C_{n3}e^{\lambda_{n3}x}\\ C_{n4}e^{\lambda_{n4}x}\end{bmatrix}\right\}\cos(k_ny) \tag{A.30}
$$

and

$$
\frac{\partial V_n}{\partial x}=\sum_{n=1}^{n_{\max}}\left\{\begin{bmatrix}k_n\lambda_{n1} & k_n\lambda_{n2}\end{bmatrix}\begin{bmatrix}C_{n1}e^{\lambda_{n1}x}\\ C_{n2}e^{\lambda_{n2}x}\end{bmatrix}+\begin{bmatrix}\lambda_{n3}^2 & \lambda_{n4}^2\end{bmatrix}\begin{bmatrix}C_{n3}e^{\lambda_{n3}x}\\ C_{n4}e^{\lambda_{n4}x}\end{bmatrix}\right\}\cos(k_ny). \tag{A.31}
$$

Substituting equations (A.30) and (A.31) into equation (A.29),

$$
\begin{aligned}
&\frac{1-\mu}{4}\int_0^b\int_0^L\Bigg[\left\{\sum_n\left(2k_nC_{n1}\lambda_{n1}e^{\lambda_{n1}x}+2k_nC_{n2}\lambda_{n2}e^{\lambda_{n2}x}+C_{n3}(k_n^2+\lambda_{n3}^2)e^{\lambda_{n3}x}+C_{n4}(k_n^2+\lambda_{n4}^2)e^{\lambda_{n4}x}\right)\right\}\\
&\qquad\left\{\sum_{n'}\left(2k_{n'}C^*_{n'1}\lambda^*_{n'1}e^{\lambda^*_{n'1}x}+2k_{n'}C^*_{n'2}\lambda^*_{n'2}e^{\lambda^*_{n'2}x}+C^*_{n'3}(k_{n'}^2+\lambda^{*2}_{n'3})e^{\lambda^*_{n'3}x}+C^*_{n'4}(k_{n'}^2+\lambda^{*2}_{n'4})e^{\lambda^*_{n'4}x}\right)\right\}\cos(k_ny)\cos(k_{n'}y)\Bigg]dxdy\\
&=\frac{(1-\mu)b}{8}\sum_n\Bigg[4k_n^2\left|C_{n1}\right|^2\left|\lambda_{n1}\right|^2\frac{\mathrm{e}^{2\mathrm{Re}(\lambda_{n1})L}-1}{2\mathrm{Re}(\lambda_{n1})}+4k_n^2\left|C_{n2}\right|^2\left|\lambda_{n2}\right|^2\frac{\mathrm{e}^{2\mathrm{Re}(\lambda_{n2})L}-1}{2\mathrm{Re}(\lambda_{n2})}+\\
&\qquad\left|C_{n3}\right|^2\left|k_n^2+\lambda_{n3}\right|^2\frac{\mathrm{e}^{2\mathrm{Re}(\lambda_{n3})L}-1}{2\mathrm{Re}(\lambda_{n3})}+\left|C_{n4}\right|^2\left|k_n^2+\lambda_{n4}\right|^2\frac{\mathrm{e}^{2\mathrm{Re}(\lambda_{n4})L}-1}{2\mathrm{Re}(\lambda_{n4})}+\\
&\qquad 2\mathrm{Re}\Bigg\{4k_n^2C_{n1}C^*_{n2}\lambda_{n1}\lambda^*_{n2}\frac{\mathrm{e}^{(\lambda_{n1}+\lambda^*_{n2})L}-1}{\lambda_{n1}+\lambda^*_{n2}}+2k_nC_{n1}C^*_{n3}\lambda_{n1}(k_n^2+\lambda^{*2}_{n3})\frac{\mathrm{e}^{(\lambda_{n1}+\lambda^*_{n3})L}-1}{\lambda_{n1}+\lambda^*_{n3}}+\\
&\qquad 2k_nC_{n1}C^*_{n4}\lambda_{n1}(k_n^2+\lambda^{*2}_{n4})\frac{\mathrm{e}^{(\lambda_{n1}+\lambda^*_{n4})L}-1}{\lambda_{n1}+\lambda^*_{n4}}+2k_nC_{n2}C^*_{n3}\lambda_{n2}(k_n^2+\lambda^{*2}_{n3})\frac{\mathrm{e}^{(\lambda_{n2}+\lambda^*_{n3})L}-1}{\lambda_{n2}+\lambda^*_{n3}}+\\
&\qquad 2k_nC_{n2}C_{n4}\lambda_{n2}(k_n^2+\lambda^{*2}_{n4})\frac{\mathrm{e}^{(\lambda_{n2}+\lambda^*_{n4})L}-1}{\lambda_{n2}+\lambda^*_{n4}}+C_{n3}C^*_{n4}(k_n^2+\lambda_{n3}^2)(k_n^2+\lambda^{*2}_{n4})\frac{\mathrm{e}^{(\lambda_{n3}+\lambda^*_{n4})L}-1}{\lambda_{n3}+\lambda^*_{n4}}\Bigg\}\Bigg].
\end{aligned}
\tag{A.32}
$$

The maximum strain energy for in-plane vibration can be obtained analytically from equations (A.23), (A.26), (A.28) and (A.32).

APPENDIX B.

COUPLING TWO PLATES USING DSM

B.1 Dynamic Stiffness Matrix for a coupled plate system

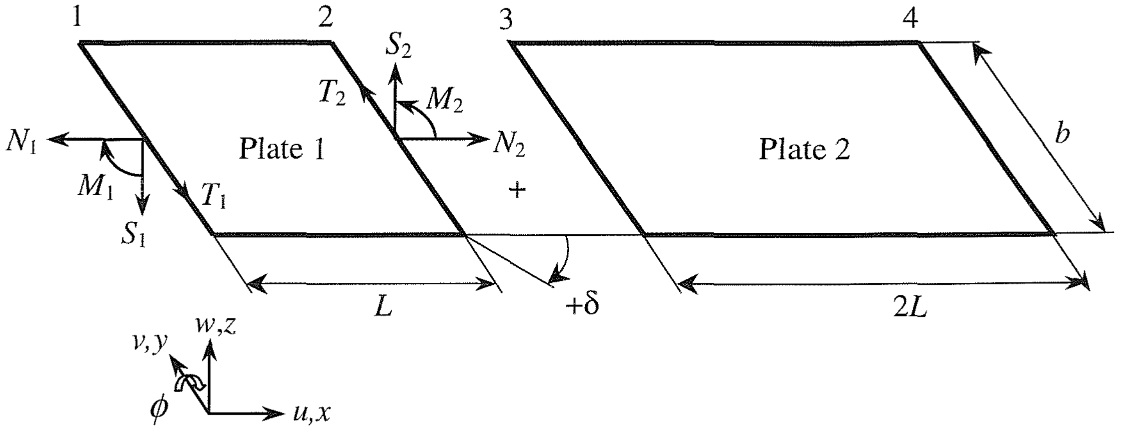

For the flexural vibration for plate 1 and plate 2, $\mathbf{F}_{f1} = \mathbf{K}_{f1}\,\mathbf{u}_{f1}$ and $\mathbf{F}_{f2} = \mathbf{K}_{f2}\,\mathbf{u}_{f2}$

where

$$\mathbf{F}_{f1}{}^{T} = \{-S_1 \quad M_1 \quad S_2 \quad -M_2\}, \tag{B.1}$$

$$\mathbf{F}_{f2}{}^{T} = \{-S_3 \quad M_3 \quad S_4 \quad -M_4\}, \tag{B.2}$$

$$\mathbf{u}_{f1}{}^{T} = \{w_1 \quad \phi_1 \quad w_2 \quad \phi_2\}, \tag{B.3}$$

$$\mathbf{u}_{f2}{}^{T} = \{w_3 \quad \phi_3 \quad w_4 \quad \phi_4\} \tag{B.4}$$

and the dynamic stiffness matrix for flexure, $\mathbf{K}_{f1}$ and $\mathbf{K}_{f2}$, is defined in equation (2.41).

For the in-plane vibration for plate 1 and plate 2, $\mathbf{F}_{t1} = \mathbf{K}_{t1}\,\mathbf{u}_{t1}$ and $\mathbf{F}_{t2} = \mathbf{K}_{t2}\,\mathbf{u}_{t2}$

where

$$\mathbf{F}_{t1}{}^{T} = \{-N_1 \quad -T_1 \quad N_2 \quad T_2\}, \tag{B.5}$$

$$\mathbf{F}_{t2}{}^{T} = \{-N_3 \quad -T_3 \quad N_4 \quad T_4\}, \tag{B.6}$$

$$\mathbf{u}_{t1}{}^{T} = \{u_1 \quad v_1 \quad u_2 \quad v_2\}, \tag{B.7}$$

$$\mathbf{u}_{t2}{}^{T} = \{u_3 \quad v_3 \quad u_4 \quad v_4\} \tag{B.8}$$

and the dynamic stiffness matrix for in-plane motion, $\mathbf{K}_{t1}$ and $\mathbf{K}_{t2}$, is defined in equation (2.52).

Assembling the dynamic stiffness matrices for flexure and in-plane motion and multiplying the transformation matrix given in Appendix B.2, the force-displacement relationship for a coupled plate system can be obtained from

$$\mathbf{F}_p = \mathbf{K}_p \mathbf{u}_p, \tag{B.9}$$

where

$$\mathbf{F}_p = \mathbf{T}_p^T \begin{bmatrix} \mathbf{F}_{f1} \\ \mathbf{F}_{f2} \\ \mathbf{F}_{t1} \\ \mathbf{F}_{t2} \end{bmatrix}, \ \mathbf{u}_p = \mathbf{T}_p^T \begin{bmatrix} \mathbf{u}_{f1} \\ \mathbf{u}_{f2} \\ \mathbf{u}_{t1} \\ \mathbf{u}_{t2} \end{bmatrix} \text{ and } \mathbf{K}_p = \mathbf{T}_p^T \begin{bmatrix} \mathbf{K}_{f1} & 0 & 0 & 0 \\ 0 & \mathbf{K}_{f2} & 0 & 0 \\ 0 & 0 & \mathbf{K}_{t1} & 0 \\ 0 & 0 & 0 & \mathbf{K}_{t2} \end{bmatrix} \mathbf{T}_p.$$

B.2 Transformation Matrix $\mathbf{T}_p$ for a coupled plate system

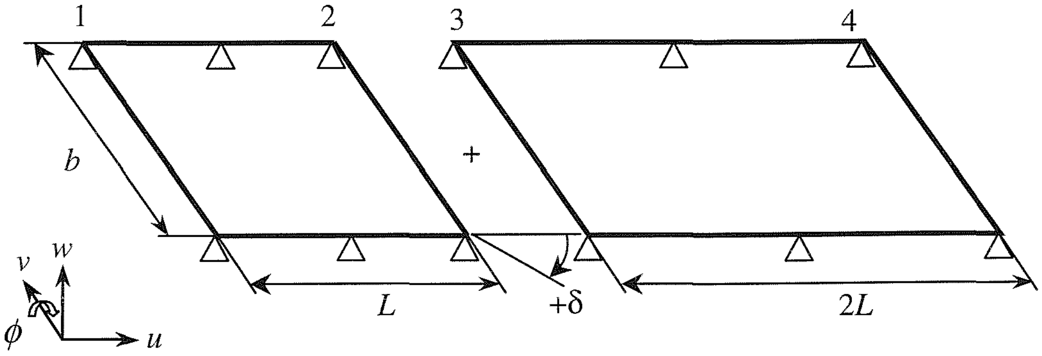

The continuity conditions at the joint $x = L$,

$$w_2 = w_3 \cos\delta - u_3 \sin\delta \tag{B.10}$$

$$u_2 = w_3 \sin\delta + u_3 \cos\delta \tag{B.11}$$

$$v_2 = v_3 \tag{B.12}$$

$$\phi_2 = \phi_3. \tag{B.13}$$

Take as the independent displacements,

$$\{w_1,\ \phi_1,\ w_2,\ \phi_2,\ w_4,\ \phi_4,\ u_1,\ v_1,\ u_2,\ v_2,\ u_4,\ v_4\}. \tag{B.14}$$

Then the transformation matrix $\mathbf{T}_p$ is given by,

$$\mathbf{T}_p = \begin{array}{cccccccccccc|c}
w_1 & \phi_1 & w_2 & \phi_2 & w_4 & \phi_4 & u_1 & v_1 & u_2 & v_2 & u_4 & v_4 & \\
\hline
1 & . & . & . & . & . & . & . & . & . & . & . & w_1 \\
. & 1 & . & . & . & . & . & . & . & . & . & . & \phi_1 \\
. & . & 1 & . & . & . & . & . & . & . & . & . & w_2 \\
. & . & . & 1 & . & . & . & . & . & . & . & . & \phi_2 \\
. & . & \cos\delta & . & . & . & . & . & \sin\delta & . & . & . & w_3 \\
. & . & . & 1 & . & . & . & . & . & . & . & . & \phi_3 \\
. & . & . & . & 1 & . & . & . & . & . & . & . & w_4 \\
. & . & . & . & . & 1 & . & . & . & . & . & . & \phi_4 \\
. & . & . & . & . & . & 1 & . & . & . & . & . & u_1 \\
. & . & . & . & . & . & . & 1 & . & . & . & . & v_2 \\
. & . & . & . & . & . & . & . & 1 & . & . & . & u_2 \\
. & . & . & . & . & . & . & . & . & 1 & . & . & v_2 \\
. & . & -\sin\delta & . & . & . & . & . & \cos\delta & . & . & . & u_3 \\
. & . & . & . & . & . & . & . & . & 1 & . & . & v_3 \\
. & . & . & . & . & . & . & . & . & . & 1 & . & u_4 \\
. & . & . & . & . & . & . & . & . & . & . & 1 & v_4
\end{array}$$

(B.15)

which gives

$$\mathbf{u}_p = \mathbf{T}_p{}^T \mathbf{u}_{(p1+p2)} \tag{B.16}$$

where $\mathbf{u}_p = \{w_2 \quad \phi_1 \quad w_2 \quad \phi_2 \quad w_4 \quad \phi_4 \quad u_1 \quad v_1 \quad u_2 \quad v_2 \quad u_4 \quad v_4\}^T$ and

$\mathbf{u}_{(p1+p2)} = \{w_1 \quad \phi_1 \quad w_2 \quad \phi_2 \quad w_3 \quad \phi_3 \quad w_4 \quad \phi_4 \quad u_1 \quad v_1 \quad u_2 \quad v_2 \quad u_3 \quad v_3 \quad u_4 \quad v_4\}^T$.

Similarly, the forces at the interface $x = L$ are related by

$$\overline{S}_2 = S_2 - S_3 \cos\delta + N_3 \sin\delta \tag{B.17}$$

$$\overline{N}_2 = N_2 - S_3 \sin\delta - N_3 \cos\delta \tag{B.18}$$

$$\overline{M}_2 = M_2 - M_3 \tag{B.19}$$

where $\overline{S}_2$, $\overline{N}_2$ and $\overline{M}_2$ are the externally applied forces. The external forces $\mathbf{F}_p$ thus satisfy $\mathbf{F}_p = \mathbf{T}_p{}^{\mathrm{T}} \mathbf{F}_{(p1+p2)}$.

APPENDIX C.

DYNAMIC STIFFNESS MATRIX FOR A SEMI-INFINITE PLATE

An undamped semi-infinite plate, as shown in Figure C.1, is assumed to be simply supported along two opposite edges ($y = 0$ and $y = b$).

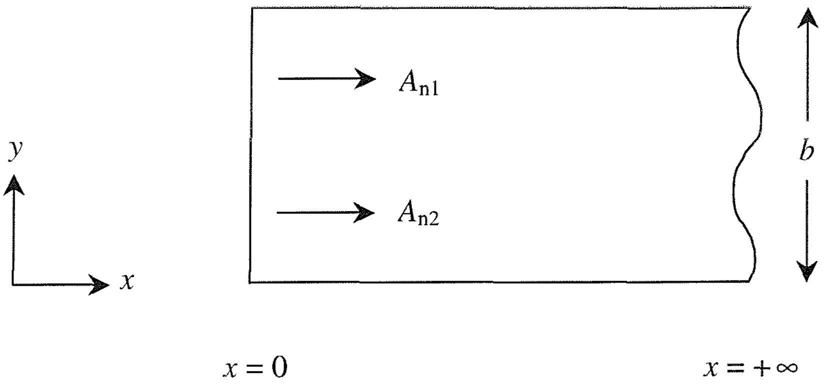

Figure C.1. A semi-infinite plate of finite width, *b*.

The deflection for flexural vibration may be taken to be of the form

$$W_n(x) = \sum_{r=1}^{2} A_{nr} e^{k_{nr} x}, \tag{C.1}$$

where the A_{nr} terms are two unknown constants of integration which can be found by ensuring that the solution satisfies the boundary conditions at the left-hand edge of the plate and the k_{nr} terms are the positive-going nearfield and propagating waves ($k_{n1,\,n2} = -\sqrt{k_n^2 \pm k^2}$, $k = \left(\rho h \omega^2 / D\right)^{1/4}$ and $k_n = n\pi / b$).

Upon introducing the flexural displacement vector for longitudinal direction

$$\mathbf{u}_{nf}^T = \{W_n(0) \quad W_n'(0)\}, \tag{C.2}$$

then

$$\begin{aligned} W_n(0) &= A_{n1} + A_{n2} \\ W_n'(0) &= k_{n1}A_{n1} + k_{n2}A_{n2} \end{aligned}, \tag{C.3}$$

or in matrix form

$$\mathbf{u}_{nf} = \begin{bmatrix} 1 & 1 \\ k_{n1} & k_{n2} \end{bmatrix} \begin{Bmatrix} A_{n1} \\ A_{n2} \end{Bmatrix}, \tag{C.4}$$

$$\mathbf{u}_{nf} = \mathbf{p}_{1n}\mathbf{A}_n, \tag{C.5}$$

where $\mathbf{A}_n^T = \{A_{n1} \quad A_{n2}\}$ and

$$\mathbf{p}_{1n} = \begin{bmatrix} 1 & 1 \\ k_{n1} & k_{n2} \end{bmatrix}. \tag{C.6}$$

Equation (C.1) may be used to derive a relationship between the displacements and forces at the left-hand end of the plate, and thus the dynamic stiffness matrix of the plate for flexural vibrations with transverse modeshape $\sin(k_n y)$ for each *n*. The longitudinal shear force $S_n(x)$ and bending moment $M_n(x)$ along the free edges may be written as [74]

$$S_n = -D\left[W_n''' - (2-\mu)k_n^2 W_n'\right], \tag{C.7}$$

$$M_n = -D\left[W_n'' - \mu k_n^2 W_n\right], \tag{C.8}$$

where D is the flexural rigidity ($= Eh^3/12(1-\mu^2)$)and μ is the Poisson's ratio.

Upon introducing the restoring force vector

$$\mathbf{F}_{nf}^T = \{-S_n(0) \quad M_n(0)\}, \tag{C.9}$$

where $$-S_n(0) = D\left[\sum_{r=1}^{2}(k_{nr})^3 A_{nr} - (2-\mu)k_n^2\left\{\sum_{r=1}^{2}k_{nr}A_{nr}\right\}\right] \tag{C.10}$$

and $$M_n(0) = -D\left[\sum_{r=1}^{2}(k_{nr})^2 A_{nr} - \mu k_n^2 \sum_{r=1}^{2} A_{nr}\right], \tag{C.11}$$

this allows $\mathbf{F}_{nf}$ to be written in terms of $\mathbf{A}_n$:

$$\mathbf{F}_{nf} = \mathbf{p}_{2n}\mathbf{A}_n \tag{C.12}$$

where

$$\mathbf{p}_{2n} = D\begin{bmatrix} (k_{n1})^3 - (2-\mu)k_n^2 k_{n1} & (k_{n2})^3 - (2-\mu)k_n^2 k_{n2} \\ -(k_{n1})^2 + \mu k_n^2 & -(k_{n2})^2 + \mu k_n^2 \end{bmatrix} \tag{C.13}$$

and $\mathbf{K}_{inf}$ is the dynamic stiffness matrix of the semi-infinite plate for flexural vibrations.

From equation (C.5), $\mathbf{A}_n = \mathbf{p}_{1n}^{-1}\mathbf{u}_{nf}$, equation (C.9) can be rewritten in matrix form,

$$\mathbf{F}_{nf} = \mathbf{p}_{2n}\mathbf{A}_n = \mathbf{p}_{2n}\mathbf{p}_{1n}^{-1}\mathbf{u}_{nf} = \mathbf{K}_{inf}\mathbf{u}_{nf}\,. \tag{C.14}$$

Hence

$$\mathbf{K}_{inf} = \mathbf{p}_{2n}\mathbf{p}_{1n}^{-1}\,. \tag{C.15}$$